ARISTOTLE UNIVERSITY OF THESSALONIKI / CERN

Contribution to the search for solar axions in the CAST experiment

Theodoros Vafeiadis

November 2012

ΑΡΙΣΤΟΤΕΛΕΙΟ ΠΑΝΕΠΙΣΤΗΜΙΟ ΘΕΣΣΑΛΟΝΙΚΗΣ / CERN

Συμβολή στην έρευνα των ηλιακών αξιονίων στο πείραμα CAST

Θεόδωρος Βαφειάδης

Νοέμβριος 2012

Summary

The CERN Axion Solar Telescope (CAST) is an implementation of the axion helioscope with the highest sensitivity to date. In the present thesis the results of the analysis of one of the Micromegas detectors in CAST (sunrise side) for the 2009 and 2010 data taking periods are presented.

A new detector lab has been realized at CERN (162 S-065) with a variable energy calibration system based on an X-ray beam line built at the Max-Planck-Institut für extraterrestrische Physik/Garching (MPE). The purpose of this work is to calibrate for the first time the present and future CAST detectors, in a number of energies and test the efficiency of the software selection criteria.

The results of the measurements in the lab were used in the analysis of the data acquired in 2009 and 2010 with the sunrise Micromegas detector of CAST. The data are consistent with no axion signal, thus a limit in the coupling constant of axions to photons is extracted in the axion mass range 0.655 -1.01 eV/c^2:

$$g_{\alpha\gamma} \leq 3.9\times10^{-10}\ \mathrm{GeV}^{-1} \text{ at } 95\%\ \mathrm{CL}$$

which is expected to be slightly improved by the contribution of the rest of the detectors.

Περίληψη

Παρόλο που το Standard Model είναι μια παγιωμένη θεωρία και η ισχύς του έχει επιβεβαιωθεί πειραματικά σε μεγάλο βαθμό, εγείρει κάποια αναπάντητα αινίγματα, όπως το πρόβλημα της παραβίασης της CP συμμετρίας στις ισχυρές αλληλεπιδράσεις. Η QCD, προβλέπει μια παραβίαση της συμμετρίας CP που δεν έχει επιβεβαιωθεί πειραματικά. Μια λύση στο πρόβλημα εισήχθη από τους Peccei και Quinn το 1977 [1], που πρότειναν την διατήρηση της συμμετρίας CP υπό την παρουσία ενός ψευδοβαθμωτού σωματιδίου, του αξιονίου, επεκτείνοντας την ιδέα του 't Hooft [2,3].

Αξιόνια μπορούν να παραχθούν στον ήλιο με το μηχανισμό Primakoff [21]. Η διαφορική ροή των ηλιακών αξιονίων στη γη, λαμβάνοντας υπόψη τη μέση απόσταση ήλιου-γης υπολογίστηκε [57] λαμβάνοντας υπόψη το τελευταίο ηλιακό μοντέλο [58] του 2004:

$$\frac{d\Phi_a}{dE_a} = g_{10}^2\, 6.02 \cdot 10^{10}\, E_a^{2.481}\, e^{-\frac{E_a}{1.205}}\, [\mathrm{cm^{-2}s^{-1}keV^{-1}}] \tag{1}$$

Όπου $g_{10} = g_{a\gamma}/10^{-10}\ \mathrm{GeV}^{-1}$ και οι ενέργειες είναι σε keV.

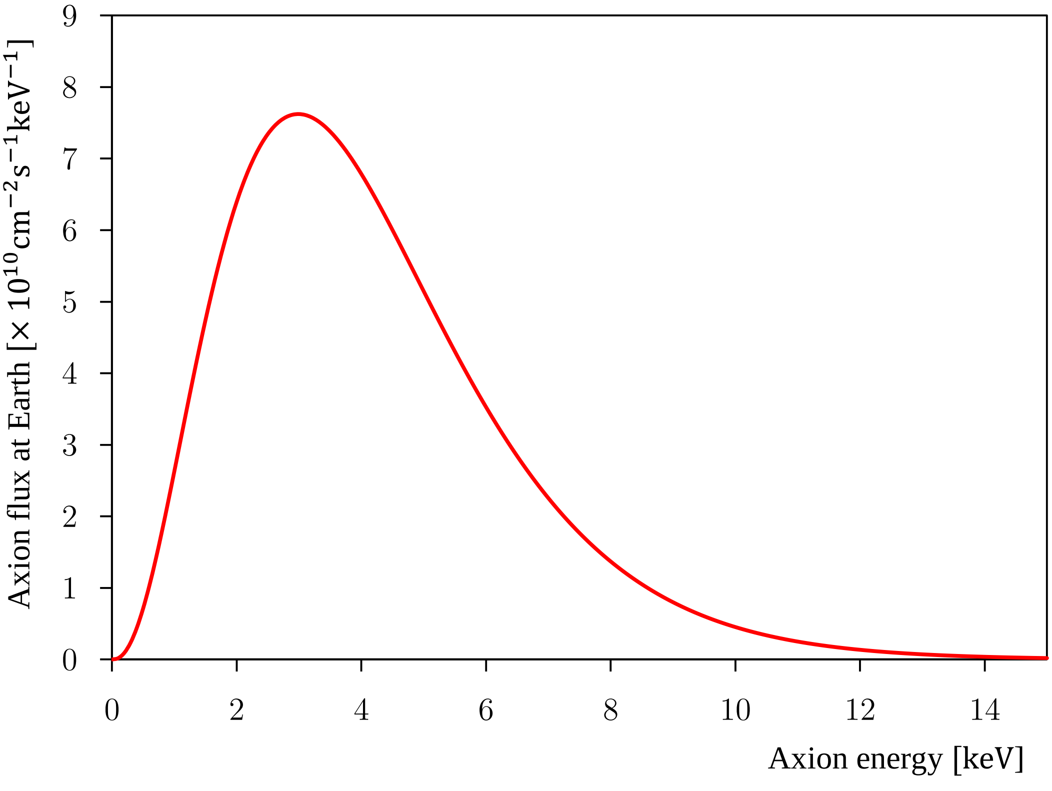

Σχήμα 1: Η ροή αξιονίων στη γη, από το τελευταίο ηλιακό μοντέλο [58]. Η μέγιστη ένταση είναι στα ~3 keV και η μέση ενέργεια είναι $\langle E_a \rangle$=4.2 keV.

Το Τηλεσκόπιο Ηλιακών Αξιονίων στο CERN (CAST), είναι μια εφαρμογή ενός ηλιοσκοπίου αξιονίων με τη μεγαλύτερη μέχρι στιγμής ευαισθησία. Η αρχή ανίχνευσης του είναι το φαινόμενο Primakoff: Ένα εισερχόμενο αξιόνιο επιδρά με ένα δυνητικό φωτόνιο από το κάθετο μαγνητικό πεδίο του μαγνήτη του τηλεσκοπίου και μετατρέπεται σε ένα πραγματικό φωτόνιο που μεταφέρει την ενέργεια και ορμή του αρχικού αξιονίου όταν αξιόνιο και φωτόνιο βρίσκονται σε σύμπτωση. Σχηματική αναπαράσταση της παραπάνω αρχής φαίνεται στο Σχήμα 1.

Το κύριο εξάρτημα του CAST είναι ένας δίπολος πρωτότυπος μαγνήτης 10 μέτρων από το LHC, που μπορεί να παράγει πεδίο 9 T [61]. Αυτός ο πρωτότυπος μαγνήτης κατασκευάστηκε να είναι ευθύς κ όχι κυρτός όπως οι υπόλοιποι μαγνήτες του LHC. Οι δύο κοιλότητές του έχουν άνοιγμα 43 mm.

Αυτός ο πρωτότυπος μαγνήτης του LHC βρίσκεται εγκατεστημένος σε μια κινούμενη πλατφόρμα που του επιτρέπει να κινείται από -8° έως +8° στην κάθετη διεύθυνση και από -40 έως +40 μοίρες στην οριζόντια, επιτρέποντάς τον να ακολουθεί τον ήλιο περίπου 1.5 ώρες στην ανατολή και 1.5 ώρες στη δύση καθ’ όλη τη διάρκεια του χρόνου.

Δύο διαφορετικοί τύποι ανιχνευτών ακτίνων X, χαμηλού υποστρώματος (τρεις Micromegas και ένας CCD) είναι τοποθετημένοι σε κάθε άκρο των δύο κοιλοτήτων του μαγνήτη, με σκοπό να ανιχνεύσουν αξιόνια αποκλειστικά όταν ο μαγνήτης ακολουθεί τον ήλιο. Τις υπόλοιπες ώρες της μέρας ο μαγνήτης μένει στάσιμος σε μια οριζόντια θέση και λαμβάνονται μετρήσεις υποστρώματος.

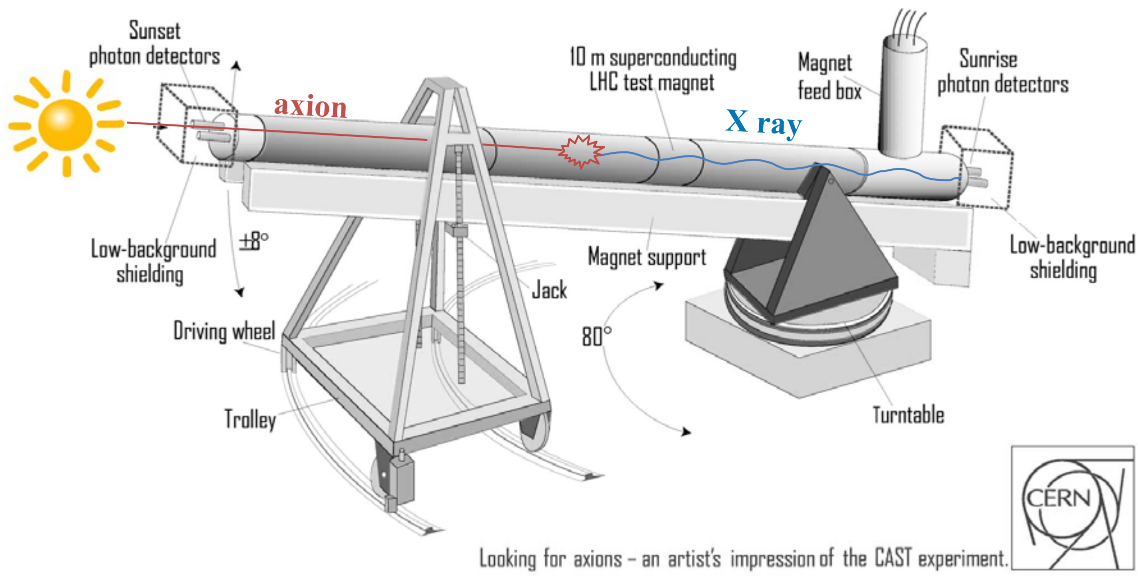

Σχήμα 2: Σχηματική αναπαράσταση της αρχής ανίχνευσης αξιονίων από το πείραμα CAST.

Κατά τη διάρκεια των περιόδων λήψης δεδομένων του CAST όλες οι γενιές ανιχνευτών Micromegas χρησιμοποιήθηκαν. Στην αρχή της Φάσης I (2003) και της Φάσης II (λήψης δεδομένων με ^{4}He στο εσωτερικό των κοιλοτήτων – 2005 και 2006) ανιχνευτές Micromegas συμβατικής τεχνολογίας χρησιμοποιήθηκαν στην ανατολική μεριά του μαγνήτη.

Κατά τη διακοπή για συντήρηση του 2007, για την προετοιμασία για τη Φάση II με ^{3}He στο εσωτερικό των κοιλοτήτων, έγινε μια πλήρης αναθεώρηση των γραμμών των ανιχνευτών που επέτρεψε την εγκατάσταση ανιχνευτών Micromegas τεχνολογίας bulk και microbulk σε τρία από τα τέσσερα άκρα των κυλινδρικών κοιλοτήτων του μαγνήτη.

Οι ανιχνευτές Micromegas τεχνολογίας microbulk αποδείχθηκαν η καλύτερη επιλογή για τις πειραματικές συνθήκες του CAST. Η χρήση λίγων υλικών, η χαμηλή εγγενής ακτινοβολία τους και η καλύτερη ενεργειακή διακριτική ικανότητά τους, τους κάνει άριστους για πειράματα ανίχνευσης σωματιδίων με χαμηλούς ρυθμούς. Συνδυάζουν όλα τα πλεονεκτήματα των ανιχνευτών bulk με βελτιωμένη απόδοση ομοιομορφία και σταθερότητα. Οι ανιχνευτές microbulk στο CAST έχουν φτάσει ενεργειακή διακριτική ικανότητα καλύτερη από 12% FWHM, σε αντίθεση με τους bulk που δεν μπορούν να φτάσουν τιμές μικρότερες από 14% FWHM. Από το 2008 τρεις από τις τέσσερις γραμμές του πειράματος καταλαμβάνονται από ανιχνευτές τεχνολογίας microbulk.

Κατά τη διάρκεια λήψης δεδομένων με ανιχνευτές Micromegas, τρεις τύποι δεδομένων λαμβάνονται. (μέτρηση επιπέδου μηδενικού σήματος, βαθμονόμησης και υποστρώματος). Τα δυαδικά αρχεία που αποθηκεύονται από το σύστημα λήψης δεδομένων του ανιχνευτή Micromegas στην ανατολική πλευρά του πειράματος πρέπει να αποκωδικοποιηθούν και να εξαχθούν από αυτά όλες οι απαραίτητες πληροφορίες. Ένα γεγονός που καταγράφεται από τον ανιχνευτή αποτελείται από το σήμα που καταγράφεται από τα strips και από 2500 δείγματα από τον παλμό που καταγράφεται από το mesh. Οι δύο βασικές ομάδες πληροφοριών είναι η χωρική πληροφορία που προέρχεται από τα X και Y strips και η χρονική πληροφορία που προέρχεται από το σήμα που συλλέγεται στο mesh.

Αφού εξαχθεί η πληροφορία, εφαρμόζεται ένας αλγόριθμος για την επιλογή γεγονότων, για να διαχωριστούν τα γεγονότα που προέρχονται από ακτίνες X, από τα υπόλοιπα, όπως κοσμικά μιόνια και ακτίνες γ υψηλής ενέργειας, που είναι και οι κύριες πηγές υποστρώματος στο CAST, με ρυθμό περίπου 1 Hz. Οι ακτίνες X με ενέργειες μικρότερες των 10 keV παράγουν πρωτογενή ιονισμό περιορισμένο σε λιγότερο από 1 mm. Αφού διαπεράσει την περιοχή ενίσχυσης του ανιχνευτή, το φορτίο θα έχει μικρό risetime και μέγιστη διασπορά 5 mm. Τα μιόνια και τα πολύ ενεργειακά φωτόνια γ θα έχουν πολύ πιο πλατύς παλμούς. Για αυτό και τα χαρακτηριστικά του παλμού τους είναι πολύ διαφορετικά στο ενεργειακό εύρος ενδιαφέροντος (2-7 keV), κάνοντας τα εύκολα αναγνωρίσιμα.

Για να καθοριστεί η επίδοση της επιλογής γεγονότων στην αναγνώριση των ακτίνων X ένα νέο εργαστήριο εξοπλίστηκε στο CERN, που περιλαμβάνει ένα σύστημα βαθμονόμησης μεταβλητής ενέργειας. Το σύστημα αυτό βασίζεται στη γραμμή ακτίνων X που κατασκευάσθηκε στο ινστιτούτο Max-Planck-Institut für extraterrestrische Physik/Garching (MPE). Σκοπός του εγχειρήματος αυτού είναι να βαθμονομηθούν για πρώτη φορά οι τωρινοί και μελλοντικοί ανιχνευτές που θα χρησιμοποιηθούν στο CAST σε μια πληθώρα ενεργειών μεταξύ 2 και 10 keV. Η μελέτη αυτή είναι απαραίτητη για την ανάλυση δεδομένων γιατί είναι ο μόνος τρόπος να οριστεί η απόδοση του λογισμικού επιλογής γεγονότων στο ενεργειακό εύρος ενδιαφέροντος.

Στην παρούσα εργασία έγινε ανάλυση των δεδομένων των περιόδων 2009 και 2010 με τον ανιχνευτή Micromegas της ανατολικής πλευράς του πειράματος CAST. Η περίοδος λήψης δεδομένων του 2009, διήρκησε από τις 13 Ιουλίου έως τις 8 Δεκεμβρίου. Σε αυτή την περίοδο το CAST κάλυψε 247 βήματα πίεσης (από το #420 έως το #647) που αντιστοιχούν σε πίεση στις κοιλότητες του μαγνήτη από 37.5 mbar στους 1.8 K έως 65.2 mbar στους 1.8 K. Το εύρος μαζών αξιονίου που καλύφθηκε είναι 0.66-0.88 eV/c^2. Ο ανιχνευτής M9 που λάμβανε τα δεδομένα στο διάστημα αυτό έδειξε μια σταθερή απόδοση.

Μετά την εφαρμογή των κριτηρίων επιλογής και λαμβάνοντας υπόψη τους χρόνους που ο μαγνήτης ακολουθούσε τον ήλιο, τα αποτελέσματα της ανάλυσης για το 2009, φαίνονται στον παρακάτω πίνακα.

	Tracking	**Background**
Time (h)	190.4	3478.8
Counts	421	7961
Mean background (2-7 keV) (keV^{-1}cm^{-2} s^{-1})	(8.08±0.39)×10^{-6}	(8.36±0.09)×10^{-6}

Πίνακας 2: Σύνοψη της επίδοσης του ανιχνευτή Micromegas της ανατολικής πλευράς για το 2009.

Η περίοδος λήψης δεδομένων του 2010 ξεκίνησε στις 5 Μαΐου πολύ αργότερα από ότι ήταν προγραμματισμένο. Ο λόγος ήταν η αναπάντεχη καθυστέρηση στη συντήρηση των κρυογενικών συστημάτων του CAST.

Η πρώτη περίοδος λήψης δεδομένων κράτησε από τις 5 Μαΐου έως τις 7 Αυγούστου. Αφιερώθηκε στην κάλυψη κενών που δημιουργήθηκαν στη σάρωση των μαζών του αξιονίου λόγω μιας διαρροής που εμφανίστηκε κατά τη διάρκεια του 2008. Για να είναι βέβαιο ότι θα καλυφτούν επιτυχώς όλα τα κενά, κάθε κενό επεκτάθηκε ώστε να περιλαμβάνει 2 έως 3 βήματα πριν και μετά. Σαν αποτέλεσμα το CAST ξαναεπισκέφθηκε 142 βήματα πίεσης.

Η περίοδος λήψης δεδομένων με νέα βήματα πίεσης διήρκησε από τις 10 Αυγούστου έως τις 30 Νοεμβρίου. Σε αυτή την περίοδο 126 νέα βήματα πίεσης καλύφθηκαν (από το #602 έως το #729). Αυτά τα βήματα πίεσης αντιστοιχούν σε πίεσης στις κοιλότητες του μαγνήτη από 65.1 mbar στους 1.8K έως 82.52 mbar στους 1.8 K κ μάζες αξιονίων από 0.85 eV/c^2 έως 1.01 eV/c^2. Ο ανιχνευτής M11 παρουσίασε εξαιρετική σταθερότητα, ιδίως μετά από μια εκτενή αναβάθμιση που έλαβε χώρα τον Απρίλιο. Τα αποτελέσματα συνοψίζονται στον παρακάτω πίνακα:

	Tracking	**Background**
Time (h)	196.6	4496
Counts	443	10552
Mean background (2-7 keV) ($keV^{-1}cm^{-2}s^{-1}$)	$(8.24\pm0.4)\times10^{-6}$	$(8.58\pm0.09)\times10^{-6}$

Πίνακας 3: Σύνοψη της επίδοσης του ανιχνευτή Micromegas της ανατολικής πλευράς για το 2010.

Τα αποτελέσματα της ανάλυσης των δεδομένων που καταγράφτηκαν από τον ανιχνευτή Micromegas της ανατολικής μεριάς του πειράματος CAST χρησιμοποιήθηκαν για να υπολογιστεί ένα όροι για την $g_{\alpha\gamma}$. Το μήκος συνοχής και η πυκνότητα του αέριου μέσου εντός των κοιλοτήτων του μαγνήτη, σα συνάρτηση της μετρούμενης πίεσης $P_{1.8}$ λήφθηκαν από τις τελευταίες προσομοιώσεις CFD.

Η εξαγωγή του ορίου έγινε με τη μεγιστοποίηση της συνάρτησης Πιθανότητας. Το αποτέλεσμα λαμβάνεται με την ολοκλήρωση της Βαεσιανής πιθανότητας από 0 έως 95%. Στην παρούσα εργασία ένα όριο στην $g_{\alpha\gamma}$ υπολογίζεται στο εύρος μαζών αξιονίου 0.655 -1.01 eV/c^2 και είναι:

$$g_{\alpha\gamma} \leq 3.9\times10^{-10}\ \mathrm{GeV}^{-1} \text{ at } 95\%\ \mathrm{CL} \tag{2}$$

Το οποίο θα βελτιωθεί από τη συνεισφορά και των υπολοίπων ανιχνευτών του πειράματος.

Acknowledgements

From October 2007 until December 2009 I have been given the opportunity, in the grounds of my PhD thesis, to work for the CAST experiment, being at CERN more than 50% of the time in total. In January 2010 I was selected as a doctoral student at CERN, to work for CAST. Being full time at CERN gave me the opportunity of a "closer look" at the way it operates, and meet, integrate and collaborate with personnel from various Departments. I find this teamwork most instructive, due to their methodology, level of knowledge, experience and expertise, and therefore extremely satisfactory.

In a small experiment like CAST very quickly you realise that apart from your main projects, you have to get involved with all the aspects of the experiment. This is something that as far as experience goes is unparalleled. The CAST experiment is the ideal place to work as a phD student of experimental physics.

Of course this work would have not been possible without Martyn's efforts. His interest in my projects and his patience and help were crucial factors for their completion. His motivation – at times stress – and his perfectionism could only have influenced me positively.

Thomas was a great teacher with a vast knowledge of the Micromegas detectors and Biljana was always eager, despite being busy, to discuss, guide me and explain the theory behind the axions. Both with their corrections and indications contributed greatly to the present thesis.

Cenk was a big help and support and together with Nuno created a very stimulating and enjoyable working environment. The experience of Nuno, his calm attitude and his knowledge were a strong help to this journey.

Great gratitude goes to Jean-Michel, the vacuum expert of CAST, with whom every discussion was educative and he was always available to assist.

It was a real privilege to work with the CASTers, but above all it was a great pleasure. I should mention Stephan, Iannis, Esther, Theopisti, Igor, Thodoros G., Silvia, Idan, Inaki, Javier, Asun, JuanAn, Alfredo, Jaime and Julia as well and thank them for enriching this excellent experience.

I would specially like to thank Konstantin for the opportunity he gave me to work at CAST and Christos who, in September 2007, boldly told me "In one month you will go to CERN" and has been encouraging and helping me, together with Tassos, ever since.

Last but not least, my family deserves a big thank you, perhaps a medal. Valia and Vincent have shown, especially the last year, a big amount of patience and they were supporting me and motivating me to finish. The grandparents and Dora were the backstage heroes that in the past few months were in turns constantly living with us, to help and give me more time to work. In my first steps at CERN, Despina offered me a big support with her hospitality and her valuable advice and assisted me to integrate in the local society.

To Valia and Vincent

Contents

1. The trigger for axions

Contents

1.1 Introduction

Although the Standard Model is a well-established theory and its validity has been verified to great extend from many experiments, it is giving rise to some yet unresolved puzzles, such as the strong CP problem. QCD, the non-abelian gauge theory of the strong interactions, predicts a violation of the CP symmetry which has never been experimentally verified. One solution to the strong CP problem was introduced by Peccei and Quinn in 1977 [1], who proposed the conservation of the CP symmetry in the presence of a pseudoscalar particle, the axion, expanding to the idea of 't Hooft [2,3]. He stressed that the physics of a theory with non-trivial vacuum topology, such as QCD, requires an additional parameter Θ in its Lagrangian.

1.2 The Strong CP problem and the axion

The dynamics of the interactions of quarks and gluons, in the framework of QCD are described by the Lagrangian:

$$\mathcal{L}_{\mathrm{QCD}} = -\sum_f \bar{q}\left(\gamma^\mu \frac{1}{i} D_\mu + m_f\right) q_f - \frac{1}{4} G_a^{\mu\nu} G_{\mu\nu}^a \tag{1.1}$$

where q_f are the quark fields for f flavors of quarks, m_f the quark masses and G_a the gluon field tensor, with a being the gluon color index.

In the limit $m_f \to 0$ there is a global symmetry $G = U(f)_R \times U(f)_L$ which corresponds to the freedom of the arbitrary chiral rotations of the quarks with each other. Since m_u and m_d are relatively small compared to the dynamical scale of the theory one could consider the above symmetry as $G = U(2)_R \times U(2)_L$. It's vectorial subgroup, $U(1)_V$ (with $V = L + R$, the baryon number) is also an exact symmetry. However the axial subgroup $U(1)_A$ (with $A = L - R$, spin alignment) is not a symmetry in QCD. As a consequence of the breaking of this symmetry, a pseudoscalar particle should exist, with vanishing mass in the limit of m_u and $m_d \to 0$ corresponding to the Nambu-Goldstone boson of the $U(1)_A$ symmetry. This is known as the $U(1)_A$ problem, the solution of which created yet another one [4].

Since QCD has a non-trivial vacuum topology, its vacuum state is a superposition of n vacuum states:

$$|\Theta\rangle = \sum_n \exp(-in\Theta)\,|n\rangle \tag{1.2}$$

where the angle Θ is an arbitrary parameter and $|\Theta\rangle$ is called the Θ-vacuum.

The effect of the Θ-vacuum can be introduced in the Lagrangian of the QCD as an additional term:

$$\mathcal{L}_{QCD} = \mathcal{L} + \mathcal{L}_{\Theta} \tag{1.3}$$

with:

$$\mathcal{L}_{\Theta} = \Theta \frac{g_s^2}{32\pi^2} G_{\mu\nu}^a \tilde{G}_a^{\mu\nu} \tag{1.4}$$

Where g_s is the coupling constant. Taking into account the electroweak interactions:

$$\mathcal{L}_{\mathrm{QCD}} = \mathcal{L}_{\mathrm{pert.}} + \bar{\Theta} \frac{g_s^2}{32\pi^2} G_{\mu\nu}^a \tilde{G}_a^{\mu\nu} \tag{1.5}$$

with:

$$\bar{\Theta} = \Theta + Arg\,\det\mathcal{M} \tag{1.6}$$

with the effective Θ term, $\bar{\Theta}$, containing the quark mass matrix $\mathcal{M}$.

Due to this topology and the chirality breakdown of QCD it was shown [2, 3] that $U(1)_A$ is not a symmetry of QCD, so no Nambu-Goldstone boson of the $U(1)_A$ symmetry has to exist. On the other hand the introduction of the $\bar{\Theta}$ leads to a very big neutron electric dipole moment

$$d_n \sim e\bar{\Theta}\ , \tag{1.7}$$

unless the parameter $\bar{\Theta}$ is very small ($\leq 10^{-9}$).

Since $\bar{\Theta}$ is a free parameter, it should be equally probable to get any value. The strong CP problem is the reason why the combination with the electroweak parameters should result in such a small $\bar{\Theta}$ [5].

A solution to this problem was proposed by Peccei and Quinn in 1977. They proposed a spontaneously broken global chiral symmetry, $U(1)_{PQ}$ [1] for the full Lagrangian (eq.

1.5). In the presence of such a symmetry the CP problem can be solved since $\bar{\Theta}$ can be made a dynamical variable with a classical potential that is minimized when $\bar{\Theta} = 0$. An associated Nambu-Goldstone boson is thus created, the axion [6, 7].

The additional term to the Lagrangian can be then written:

$$\mathcal{L}_a = \bar{\Theta} \frac{a}{f_a} \xi \frac{g_s^2}{32\pi^2} G_a^{\mu\nu} \tilde{G}_{\mu\nu}^a \tag{1.8}$$

Where a is the axion field, ξ is a model dependant constant and f_a the Peccei Quinn scale. The presence of the term $\mathcal{L}_a$ in the Lagrangian provides an effective potential V_{eff} for the axion field, which has minimum [4] when:

$$\langle \alpha \rangle = -\frac{f_a}{\xi} \bar{\Theta} \tag{1.9}$$

In the minimum of V_{eff}, the axion mass does not vanish and has a value:

$$m_a^2 = \langle \frac{\partial^2 V_{\text{eff}}}{\partial a^2} \rangle = -\frac{\xi}{f_a} \frac{g^2}{32\pi^2} \frac{\partial}{\partial a} \langle G_a^{\mu\nu} \tilde{G}_{\mu\nu}^a \rangle \tag{1.10}$$

Thus the QCD with the addition of the $U(1)_{\text{PQ}}$ does not contain a CP violating term, but instead the interactions of a pseudo scalar particle with non-vanishing mass, which are characterized by the Peccei Quinn scale f_a.

1.3 Axion dynamics

1.3.1 Axion models

The solution of the CP problem by Peccei-Quinn, works for any value of the Peccei Quinn scale f_a, thus leading to a large range of axion masses ($m_a \propto 1/f_a$) and couplings ($g_a \propto 1/f_a$) [4]. Several models have been proposed, that can be split in two categories, depending on the size of f_a: visible models, for small f_a thus large axion mass, and invisible models, for large f_a and small axion mass.

1.3.1.1 Visible axion models

A variety of axion models [8,9] and indeed the one originally proposed by Peccei and Quinn [10] resulted from the assumption that the Peccei-Quinn scale f_a is related to the electroweak scale $f_{\mathrm{weak}} \sim 250$ GeV. The resulting weak scale axions will be light and long lived, since they can only decay through the $a \rightarrow 2\gamma$ process. These axions (also known as PQWW axions) are excluded through astrophysical considerations [11] and the non-observation of the process:

$$K^+ \rightarrow \pi^+ a \tag{1.11}$$

Indeed the theoretical value of the branching ratio is given by [12]:

$$BR(K^+ \rightarrow \pi^+ a) \geq 3.5 \times 10^{-5} \tag{1.12}$$

comparing this with the experimental limit:

$$BR(K^+ \rightarrow \pi^+ a) \leq 1.4 \times 10^{-6} \tag{1.13}$$

one can exclude the visible axions.

1.3.1.2 Invisible axion models

Quickly after the visible axions were ruled out, new models with $f_a \gg f_{weak}$ were introduced. In these models the properties of axions are closely related to those of neutral pions. The two photon interaction is the one that has played a key role in their development [13]:

$$\mathcal{L}_{a\gamma} = -\frac{1}{4} g_{a\gamma} F_{\mu\nu} \tilde{F}^{\mu\nu} a = g_{a\gamma} \boldsymbol{E} \cdot \boldsymbol{B}\, a \tag{1.14}$$

where F is the electromagnetic field strength tensor, $\tilde{F}$ its dual and $\boldsymbol{E}$ and $\boldsymbol{B}$ the electric and magnetic fields, respectively. The coupling constant of this interaction is:

$$g_{a\gamma} = \frac{\alpha}{2\pi f_a}\left(\frac{E}{N} - \frac{2}{3}\frac{4+z+w}{1+z+w}\right) \tag{1.15}$$

where α is the fine structure constant and E and N, are the electromagnetic and color anomaly of the axial current, associated with the axion field, defined as:

$$E \equiv 2\sum_j X_j Q_j^2 D_j \quad , \quad N \equiv \sum_j X_j \tag{1.16}$$

with Q_j being the electric charge and X_j the PQ charge. D_j=1 for leptons and D_j=3 for quarks. $z = m_u/m_d$ and $w = m_u/m_s$ are the quark-mass ratios. Simplifying eq. (1.15), taking into account that $w << z$, one gets:

$$g_{a\gamma} = \frac{\alpha}{2\pi}\left(\frac{E}{N} - \frac{2}{3}\frac{4+z}{1+z}\right)\frac{1+z}{\sqrt{z}}\frac{m_a}{m_\pi f_\pi} \tag{1.17}$$

The first model introduced was by Kim, Shifman, Vainshtein and Zakharov - KSVZ [14,15]. They proposed a (very) heavy quark which carries the Peccei-Quinn charge and does not participate in interactions with electrons at tree level. The axion interacts only through this new quark. In the standard KSVZ model the ratio E/N is equal to zero.

On the other hand in a grand unified model such as DFSZ (Dine-Fischler-Srednicki-Zhitiniskii) [16,17] axions couple to ordinary quarks and leptons, thus giving E/N=8/3 and a value of $g_{a\gamma}$:

$$g_{a\gamma}^{\mathrm{DFSZ}} \approx -0.75\frac{\alpha}{2\pi f_a} \tag{1.18}$$

Although these are the two generic cases, E/N is not known and for a fixed f_a a broad range of $g_{a\gamma}$ is possible [18].

This linear relation between $g_{a\gamma}$ and m_a in eq. (1.17) defines the 'axion line' for a given axion model in the $g_{a\gamma} - m_a$ parameter space.

1.3.2 Axion couplings

1.3.2.1 Coupling to gluons

The chiral anomaly of the $U(1)_{\mathrm{PQ}}$ symmetry implies that the axion can interact with gluons. The Lagrangian of the interaction is:

$$\mathcal{L}_{aG} = \frac{\alpha_s}{8\pi f_a} G_a^{\mu\nu}\tilde{G}_{\mu\nu}^a \quad a \tag{1.19}$$

with a, the axion field and $\alpha_s = g_s^2/4\pi$. This interaction can be described with a Feynman diagram as seen in Figure 1.1:

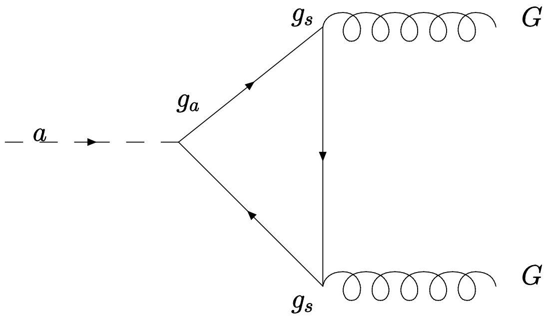

Figure 1.1: The Feynman diagram of the axion coupling to gluons. $\boldsymbol{g_s}$ is the strong coupling constant and $\boldsymbol{g_a}$ the axion to fermion coupling constant.

The coupling of the axion to gluons can be used to extract a rough estimate of its mass:

$$m_a^2 = \frac{f_\pi^2 m_\pi^2}{f_a^2} \frac{z}{(1+z+w)(1+z)} \,, \tag{1.20}$$

as a function of the pion mass and the ratios of quark masses.

For m_π = 135 MeV, f_π = 93 MeV and taking into account the values of z and w frequently used in the axion literature, $z = 0.56$ and $w = 0.028$ [19, 20], one can extract:

$$m_a = \frac{f_\pi \; m_\pi}{f_a} \frac{z^{1/2}}{1+z} = 0.6\text{eV} \frac{10^7\text{GeV}}{f_a} \tag{1.21}$$

1.3.2.2 Coupling to photons

The coupling of axions to photons has two contributions: through the coupling to neutral pions which then decay to photons, Figure 1.2(a), and via the Primakoff effect [21] through which the axions can couple to two photons, Figure 1.2(b).

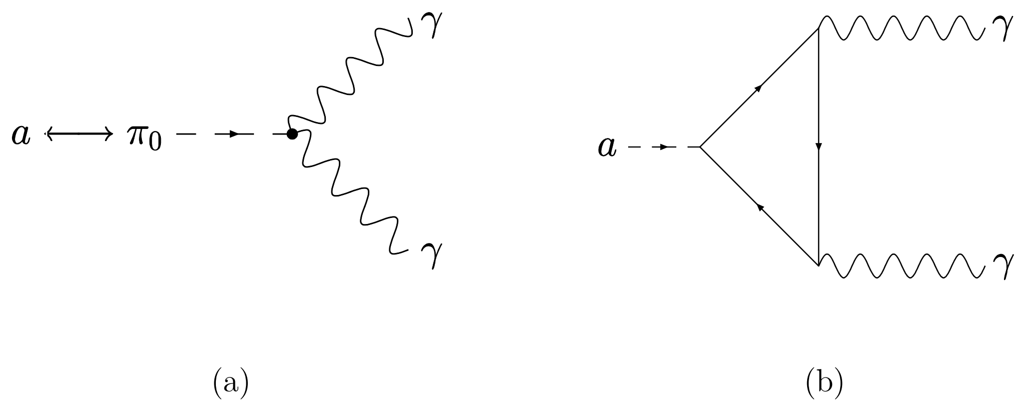

Figure 1.2: The coupling of axions to photons (a) via the coupling to pions and (b) via a triangle loop of fermions that carry the Peccei-Quinn charge (Primakoff effect).

The Lagrangian of this coupling is given by eq. (1.14) and the coupling constant is given by eq. (1.17). Taking into account the ratios of quark masses one gets:

$$g_{a\gamma} = \frac{\alpha}{2\pi f_a}\left(\frac{E}{N} - 1.93 \pm 0.08\right) \tag{1.22}$$

1.3.2.3 Coupling to fermions

The interaction with fermions is model dependant. The Lagrangian of a coupling of axions to fermions is

$$\mathcal{L}_{af} = \frac{g_{af}}{2m_f}\overline{\Psi}_f\ \gamma^\mu\gamma_5\Psi_f\partial_\mu a \tag{1.23}$$

where Ψ_f is the fermion field, m_f the fermion mass and g_{af} the coupling constant of this interaction:

$$g_{af} = \frac{C_f m_f}{f_a} \tag{1.24}$$

with C_f is the effective Peccei-Quinn charge, a model dependent quantity.

In hadronic models, like KSVZ, axions do not interact with fermions at tree level, although in the DSFZ model the coupling to electrons at tree level is allowed, giving a non-zero value to the model dependent term C_e, whereas the coupling to nucleons is allowed in both theories, yielding different coupling constants though, due to the different values of C_n and C_p [22].

1.4 Axions as dark matter candidates

The composition of the dark matter in the universe is still a mystery and the Standard Model does not predict a particle, which could be a dark matter candidate. On the other hand, a viable candidate, the axion, arises from the Peccei-Quinn solution to the strong CP problem [23].

Axions satisfy the general criteria for becoming a cold dark matter candidate. There can be large populations of axions in the universe, big enough to provide the required dark matter energy density. Despite the axion's small mass [5, 17], axion dark matter is non-relativistic, as they are produced from equilibrium through three mechanisms: vacuum realignment [24, 25, 26], string decay [27, 28, 29] and domain wall decay [30, 31, 32].

The axions are long lived, weakly interacting, color and charge neutral [33]. If we consider that the lifetime of the axion is governed by the $a \rightarrow \gamma\gamma$ decay, we get [34]:

$$\tau_a \approx 4.6 \times 10^{40} \mathrm{s} \left(\frac{E}{N} - 1.95\right)^2 \left(\frac{f_a/N}{10^{10} GeV}\right)^5 \tag{1.25}$$

Setting E/N=0, with $\frac{f_a}{N} \geq 3\times10^5$ GeV (a value favoured from the cosmological and astrophysical constraints) one finds that $\tau_a > t_0$, with the age of the Universe estimated at t_0~14 Gyrs.

1.5 Astrophysical constraints

The stars like the Sun have the proper conditions to create axions via the Primakoff effect. The axion production will compete with the production of photons. Since the photons are strongly trapped, their radiation pressure acts as a counterbalance for the gravitational pressure. Introducing a new energy loss channel, will accelerate a star's evolution, so the coupling of the axion can be limited by calculations based on the lifetime of appropriate stellar objects.

1.5.1 Globular cluster stars

The most stringent constraint for the axion to photon coupling today is due to the horizontal branch (HB) stars, which are in their helium burning phase, in globular clusters, Figure 1.3. Globular clusters are a population of gravitationally linked stars with the same age. The ones presently known have masses a bit below the one of the Sun. An average lifetime of the HB stars can be measured relatively to the red giant evolutionary time scale by the ratio of the number observed in the HB phase to those in the red giant phase. In other words after exhaustion of the core-hydrogen burning but before the helium flash. The helium burning lifetime, agrees with the expected value within 10% [35].

From the helium burning lifetime one can derive an upper limit for a Primakoff production of axions produced by the interaction of a real plus a virtual photon: $\gamma + (A, Z) \rightarrow a + (A, Z)$. This limit is:

$$g_{a\gamma} < 10^{-10}\ \mathrm{GeV}^{-1} \tag{1.26}$$

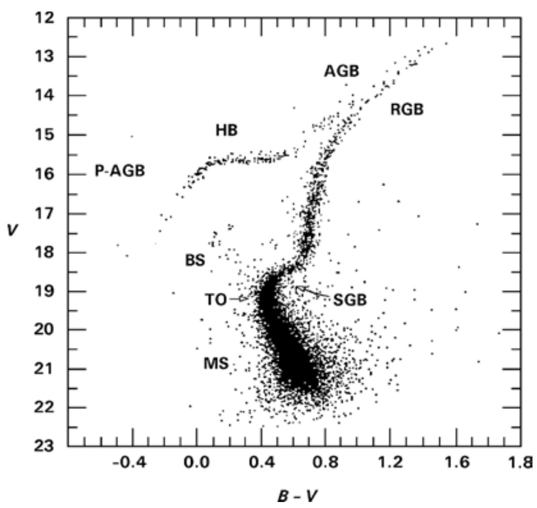

Figure 1.3: Color magnitude diagram of a globular cluster [22]. The vertical axis is the Visual brightness of the star (V) and the horizontal, the difference between blue and visual brightness (B-V), which is related to the surface temperature of the star. (blue stars are towards the left). The different types of stars shown are: MS (main sequence) - core hydrogen burning, BS (blue stragglers), TO (main-sequence turnoff) - central hydrogen is exhausted, SGB (subgiant branch) - hydrogen burning in a thick shell, RGB (red-giant branch) - hydrogen burning in a thin shell with a growing core until helium ignites, HB (horizontal branch) - helium burning in the core and hydrogen burning in a shell, AGB (asymptotic giant branch) - helium and hydrogen shell burning, P-AGB (post-asymptotic giant branch) - final evolution from the AGB to the white-dwarf stage.

1.5.2 White dwarf cooling

White dwarfs are another class of astronomical objects that provide limits for the axion energy loss channels, through their evolution. They are the remnants of stars with original mass several times the mass of the Sun. When they ascend the asymptotic giant branch (AGB, see Figure 1.3) they lose most of their mass. Their degenerate carbon-oxygen core is simply cooling down. Their cooling rate could also increase by the Bremsstrahlung channel $e^- + (A, Z) \rightarrow e^- + (A, Z) + a$. Their cooling speed can be estimated by the period decrease $\dot{P}/P$, allowing one to set a limit to the energy losses through the axion channel [22]:

$$g_{ae} < 1.3\times10^{-13}\ \text{GeV}^{-1} \tag{1.27}$$

With 95% CL. This is the most restrictive limit for the electron coupling of axions.

1.5.3 SN1987a

The strictest bounds on the g_{aN}, from axions produced by nucleon-nucleon bremsstrahlung ($N + N \rightarrow N + N + a$) is supplied by the observations of the Super Nova 1987a. When the massive star collapsed to a protoneutron star, this channel could have competed with the neutrino emission [23]. The fact that the neutrino signal observed in 1987, equally shared between IMB and Kamiokande Cherenkov detectors (19 neutrinos in 10 seconds) was in good agreement with the models. It yields a coupling constant in the regime [35]:

$$3\times10^{-10}\ \text{GeV}^{-1} \leq g_{aN} \leq 3\times10^{-7}\ \text{GeV}^{-1} \tag{1.28}$$

This range corresponds to the free streaming regime, as seen in Figure 1.4. For higher coupling constants than the range in eq. (1.28), the axions cannot escape from the core.

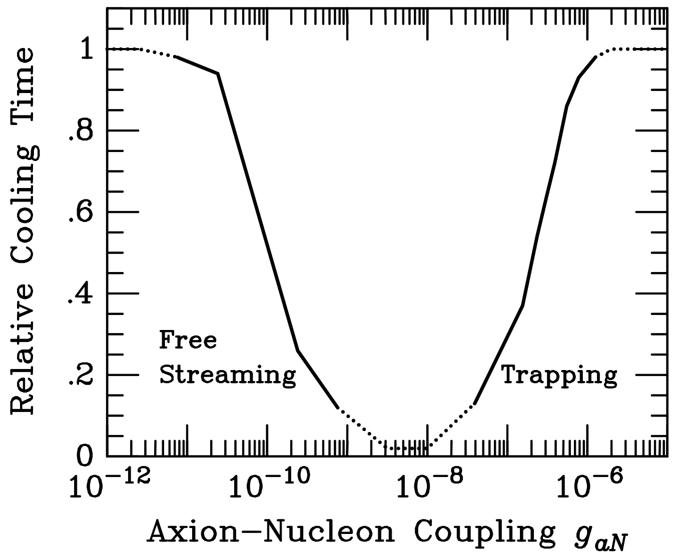

Figure 1.4: Relative duration of the neutrino burst of a Super Nova, as a function of the axion to nucleon coupling. The left side corresponds to axions that are emitted freely from the entire core and the right side to axions that cannot escape from the core.

1.6 Cosmological constraints

The astrophysical constraints are interesting if considered together with the cosmological ones. A lower limit for the axion mass can be set by the requirement not to "overclose" the universe with axions. Searching for a cosmological mass limit, one has to distinguish between two generic scenarios:

Inflation occurred after the Peccei-Quinn symmetry breaking

In this case the initial axion field takes a constant value [36]:

$$a_i = f_a \Theta_i \tag{1.29}$$

With Θ_i the initial misalignment of the Θ parameter and $0 \leq \Theta < \pi$. Since Θ_i is an unknown parameter, one cannot extract a strict cosmological limit for m_a. There is however the possibility to derive Θ_i through the limits set by inflation-induced quantum fluctuations which lead to temperature fluctuations of the cosmic microwave background. Such a limit could be set [37] and axions can have any mass below 1 meV.

Inflation did not occur at all or it occurred after the Peccei-Quinn symmetry breaking

The axions after acquiring mass, through a string mechanism, in the QCD phase transition, they quickly become non-relativistic, thus part of the cold dark matter. Following Battye and Shellard [38], the energy of the axionic strings turns into axions, restricting the axion mass to $m_a \geq 10^{-4}$ eV, whereas following Sikivie et al [39, 40] it goes more into kinetic axion energy, thus not increasing the density of relic axions significantly allowing for smaller masses of the axion, $m_a \geq 10^{-6}$ eV.

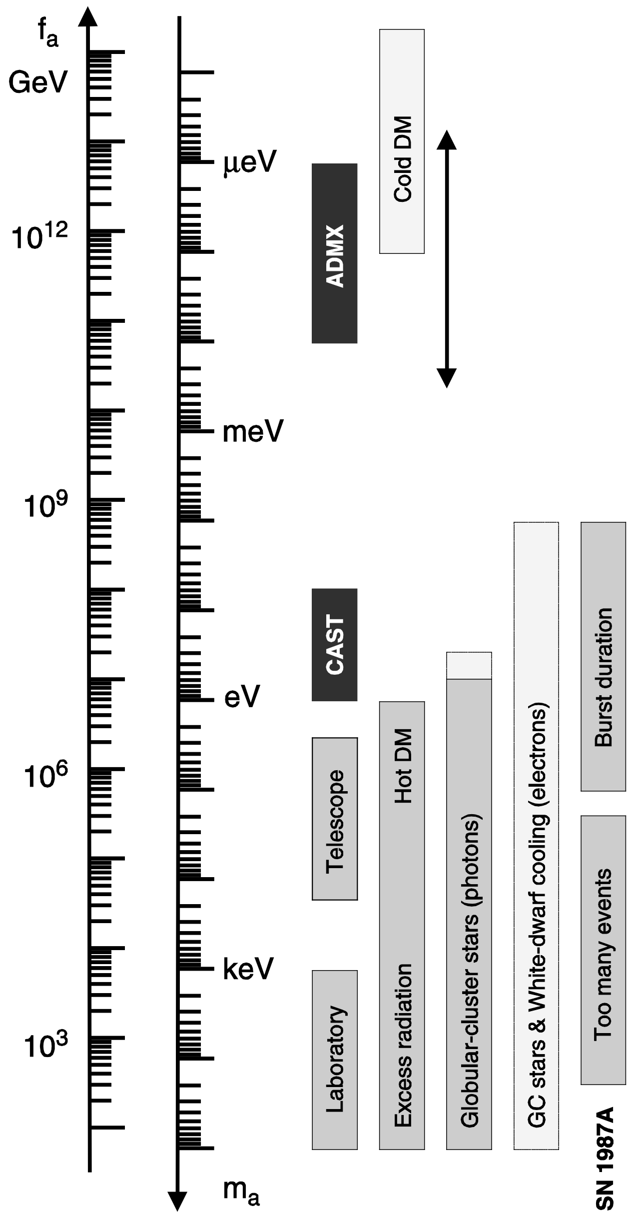

Figure 1.5: Excluded axion mass regions from the astrophysical and cosmological constraints [22].

1.7 Axion experiments

Although a very good candidate to solve many unanswered questions, axion remains yet to be discovered. A big step towards this direction was made by Sikivie [41] in 1983, when he proposed a search strategy for detecting the axion, based on its coupling to two photons. In this scheme, axions convert into two photons, via a Primakoff interaction, in the presence of a strong magnetic field. Several implementations have immediately started taking shape constraining the coupling constant $g_{a\gamma}$.

1.7.1 Galactic halo axion searches

The so called Haloscopes are searching for galactic halo axions mainly with electromagnetic cavities, permeated by a strong magnetic field. When the frequency of the magnetic field of the cavity equals the mass of the axion then the galactic halo axions' conversion to resonance photons is enhanced. The photon signal is then measured by sensitive microwave receivers, which record the excess of photons due to a conversion inside the cavity. Since the limits of axion mass are very wide, a large range of frequencies must be explored [42].

The first of these experiments was carried out by a collaboration of the University of Rochester, Brookhaven National Laboratory and Fermi National Accelerator Laboratory, (RBF). It covered the axion mass range: 4.5 μeV $< m_a <$ 16.3 μeV.

Another microwave cavity experiment, done almost in parallel was carried out at the University of Florida (UF) and covered the ranges 5.46-5.95 μeV and 7.46-7.60 μeV [42].

A second generation experiment, the ADMX, (Axion Dark Matter eXperiment) was conceived and built at the Lawrence Livermore National Laboratory (LLNL). Currently it is housed at the Center of Experimental Physics and Astrophysics in the University of Washington. The experiment is about to commission the Phase 2 of the program (2012) with significant upgrades, going deeper into the model region, as seen in Figure 1.6. In Phase 1, the masses of the axion that were excluded were [43,44]: 2.9 μeV $< m_a <$ 3.53 μeV.

The smaller CARRACK I experiment, in Kyoto, uses Rydberg atoms (atoms excited to a very high state) to detect the microwave photons that would result from axion conversion. Their results exclude axions with masses in a narrow range around 10 μeV. This experiment is being upgraded to CARRACK II, which intends to probe the range between 2 and 50 μeV with sensitivity to cover a wide coupling constant range.

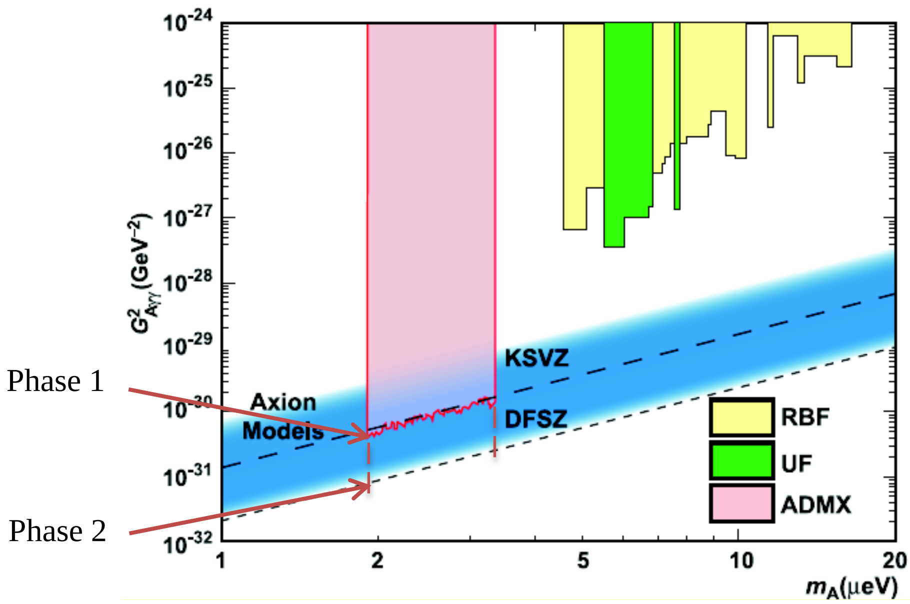

Figure 1.6: The excluded axion mass region of Phase 1 and the projected Sensitivity of Phase 2 of the ADMX experiment. The RBF and UF results are also shown.

1.7.2 Laser axion searches

Their general principle is that axions are produced through the interaction of polarized photon beams with the virtual photons of a magnetic field through the process:

$$\gamma + \gamma_{\text{virtual}} \rightarrow a \tag{1.30}$$

These experiments are not focused only on the axion search but they can provide a test of QED or search for any other scalar, pseudoscalar particle that couples to photons. The laser experiments can be divided in two categories:

1.7.2.1 *"Photon regeneration" or "shining light through the wall" experiments*

A polarized laser beam is travelling through a transverse magnetic field and hits into an absorber, the "wall". Only axions created in the magnetic field will be able to propagate through the wall. A second magnetic field behind the wall reconverts the axions to photons which are then detected, as seen in Figure 1.7.

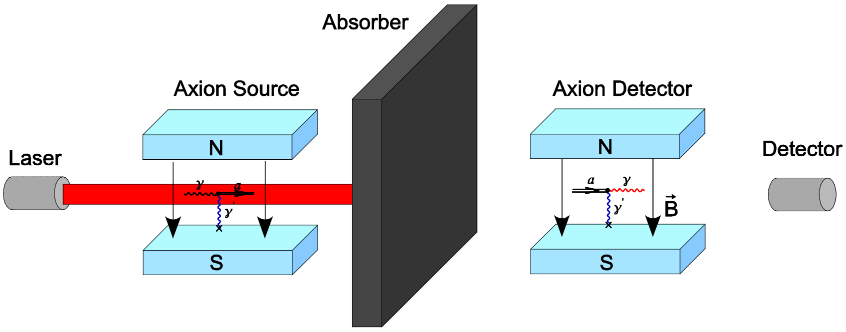

Figure 1.7: Schematic representation of the principal of operation of "Photon regeneration" or "light shining through the wall experiments" [45].

The pioneering experiment based on this technique was performed by the Brookhaven-Fermilab-Rutherford-Trieste (BFRT) collaboration. Since no signal from photon regeneration was found, they set the upper limit of the coupling constant at $g_{a\gamma} <$ 6.7×10^{-7} GeV^{-1} for axion mass $m_a < 10^{-3}$ eV [46,47].

Several experiments of this principle are running and presently taking data. The ALPs experiment at DESY, with a HERA dipole magnet, searching for axion like particles, the GammeV at Fermilab, with a Tevatron magnet, searching for evidence of a meV axion-like particle to disprove the PVLAS signal, and the OSQAR experiment at CERN, which is two experiments in one:

- Experiment which performs optical precision measurements for axions and axion-like particles (ALPs),
- QED test and photon regeneration experiment.

The two experiments are integrated in the same LHC superconducting dipole magnet therefore they can provide solid results via mutual cross-checks.

1.7.2.2 Polarization experiments

This kind of experiments are indirect detection type experiments. They are based on the theoretical assumption that scalar and pseudoscalar particles, which couple to photons, can affect their polarization in vacuum, through a transverse magnetic field. If the original photon was linearly polarized, with an angle with respect to the magnetic field direction, after the interaction with the particle it will have gained a rotation (Linear Dichroism) and an ellipticity (Linear Birefringence), Figure 1.8.

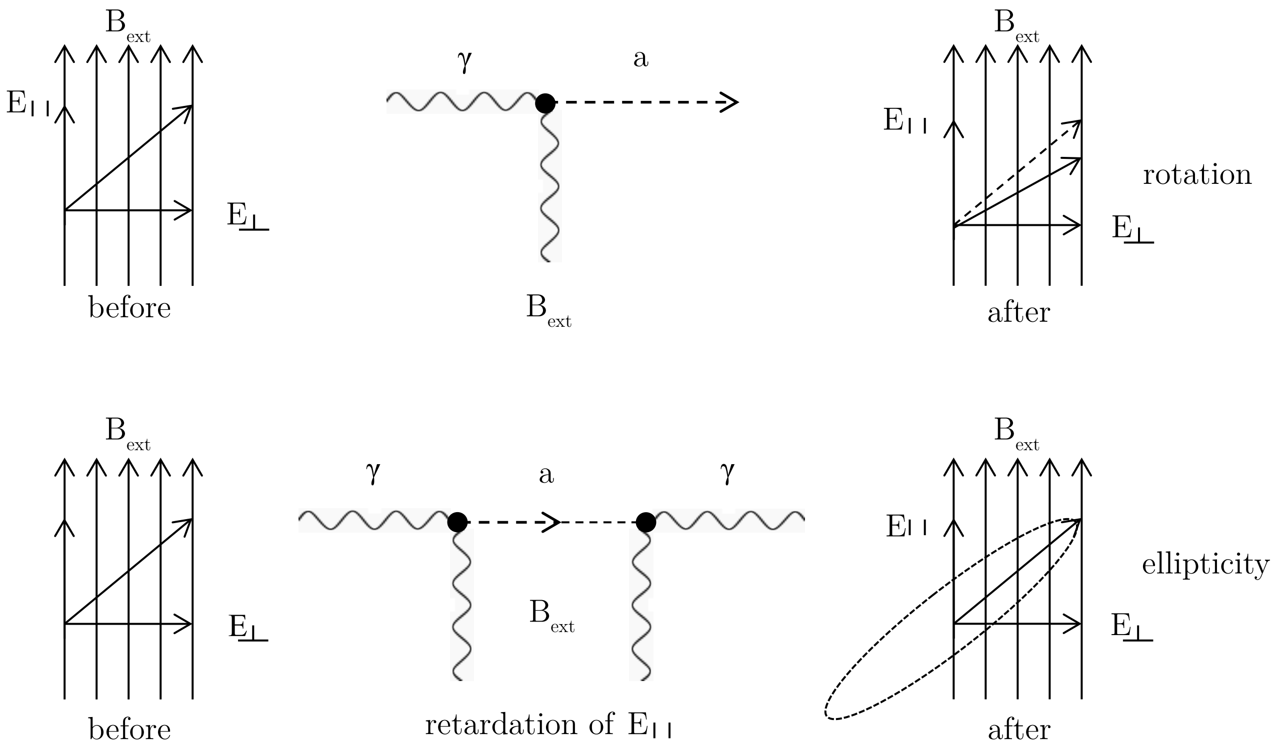

Figure 1.8: Up: Linear Dichroism. Down: Linear Birefringence.

BFRT has used the same magnets as with the shining light through the wall experiment, to search for both effects, setting a limit for the axion coupling constant of $g_{a\gamma} < 3.6\times10^{-7}$ GeV^{-1} for masses $m_a < 5\times10^{-4}$ eV [48]. PVLAS in 2006 claimed an experimental observation of a rotation of the polarization plane of light propagating through a transverse magnetic field [49], which has been excluded by several experiments including PVLAS itself.

1.7.3 Solar axion searches

From Earth, the most important source of astrophysical axions is the Sun. Axions can be produced in the core, via their coupling to photons, in the presence of the fluctuating electromagnetic field of the plasma. Due to their weak interaction with matter they escape the Sun and reach the Earth. In order to detect solar axions, two techniques have been developed.

1.7.3.1 Bragg diffraction experiments

The idea was originally proposed by E. A. Paschos and K. Zioutas [50]. An axion can convert to photons, via the inverse Primakoff effect, in the vicinity of the intense Coulomb field of nuclei in a crystal lattice. The crystal can either be used as an axion converter and detector or as a focal optical device, with a detector in its focal plane.

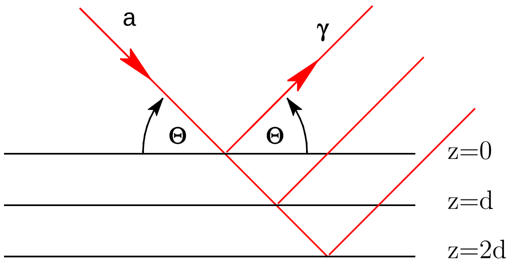

Figure 1.9: If the Bragg law is fulfilled the resulting photons from different lattices of the material will combine constructively and result to an enhanced signal, propagating in known angle.

Two collaborations, COSME [51] and SOLAX [52], both using Germanium detectors, have provided bounds to the axion to photon coupling, which are independent of the mass of the axion:

$$g_{a\gamma} < 2.7\times10^{-9}\ \mathrm{GeV}^{-1}\ \text{(SOLAX)} \tag{1.31}$$

$$g_{a\gamma} < 2.8\times10^{-9}\ \mathrm{GeV}^{-1}\ \text{(COSME)} \tag{1.32}$$

DAMA, using NaI(Tl) crystals as detector material provided the limit [53]:

$$g_{a\gamma} < 1.7\times10^{-9}\ \mathrm{GeV}^{-1} \tag{1.33}$$

Although the main advantage of the Bragg diffraction experiments is that the limits they provide are independent of the mass of the axion, they cannot reach the sensitivity of the axion helioscopes.

1.7.3.2 Axion Helioscope experiments

This kind of experiments is based on the idea presented by Sikivie [41] and their main element is a powerful magnet. They are the most sensitive axion experiments in the mass range of 10^{-5} eV $\leq m_a \leq 1$ eV. In the transverse magnetic field of this magnet, axions couple to virtual photons, and convert into photons, via the inverse Primakoff effect. The resulting photons, that have the same energy spectrum as the original axions, scaled down by the conversion probability, can eventually be detected by placing an X-ray detector in the end of the magnetic field area as shown in Figure 1.10.

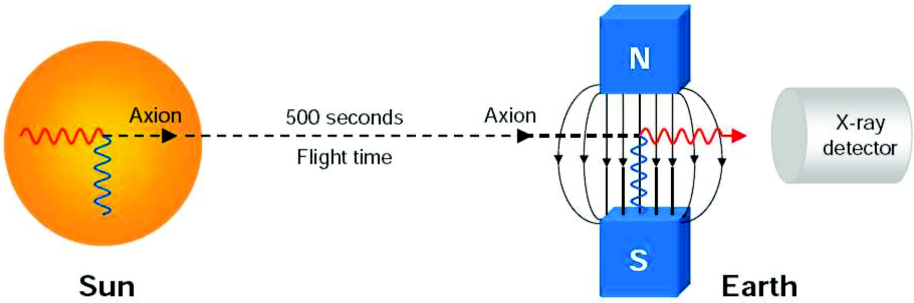

Figure 1.10: Principal of detection of an axion helioscope.

The first axion helioscope was created at the beginning of the 90s by Lazarus *et al.* [54]. It visited two axion mass regions, setting a limit of $g_{a\gamma} \leq 3.6\times10^{-9}$ GeV^{-1} for $m_a \leq 0.03$ eV and $g_{a\gamma} \leq 7.7\times10^{-9}$ GeV^{-1} for 0.03 eV $\leq m_a \leq 0.11$ eV . The Tokyo Axion Helioscope achieved a higher sensitivity and set a stricter limit [55], $g_{a\gamma} \leq 6\times10^{-10}$ GeV^{-1} for $m_a \leq 0.03$ eV.

Last but not least, the CERN Axion Solar Telescope (CAST), which is the implementation of the axion helioscope with the highest sensitivity to date, will be reviewed in detail in chapter 2.

2. The CERN Axion Solar Telescope experiment

Contents

2.1 The solar axions

The term of the Lagrangian in eq. (1.14) points to a production of axions and axion like particles due to the fluctuations of $\boldsymbol{E} \cdot \boldsymbol{B}$, i.e. in the thermal plasma of the Sun. $\boldsymbol{E}$ is provided by the charged particles of the medium and $\boldsymbol{B}$ comes from the propagating thermal photons. This is the Primakoff effect [21]. The Feynman diagram is shown in Figure 2.1 (left) where a photon converts into an axion in the electric field of a charged particle. If one takes into account the stellar energy loss limits for the other interactions of axions, the solar fluxes derived from them would be much smaller than the one from the Primakoff production. Therefore the Primakoff effect is considered as the only production process and the axions are considered not to couple to electrons at tree level [56].

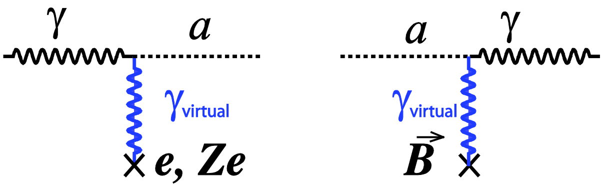

Figure 2.1 Feynman diagram of the Primakoff production (left) and the inverse process in the presence of a magnetic field (right).

The differential flux of solar axions seen from Earth, taking into account the mean distance of Earth and Sun, is calculated in [57]. Considering the latest solar model [58] from 2004:

$$\frac{d\Phi_a}{dE_a} = g_{10}^2 \, 6.02 \cdot 10^{10} \, E_a^{2.481} \, e^{-\frac{E_a}{1.205}} \, [\mathrm{cm^{-2} s^{-1} keV^{-1}}] \tag{2.1}$$

Where $g_{10} = g_{a\gamma}/10^{-10}$ GeV and the energies are in keV. The comparison of this calculation with a previous one [59], which was based on a solar model from 1982 [60], yields that the axion flux prediction depends only slightly on the solar mode. In Figure 2.2, the latest solar model is plotted.

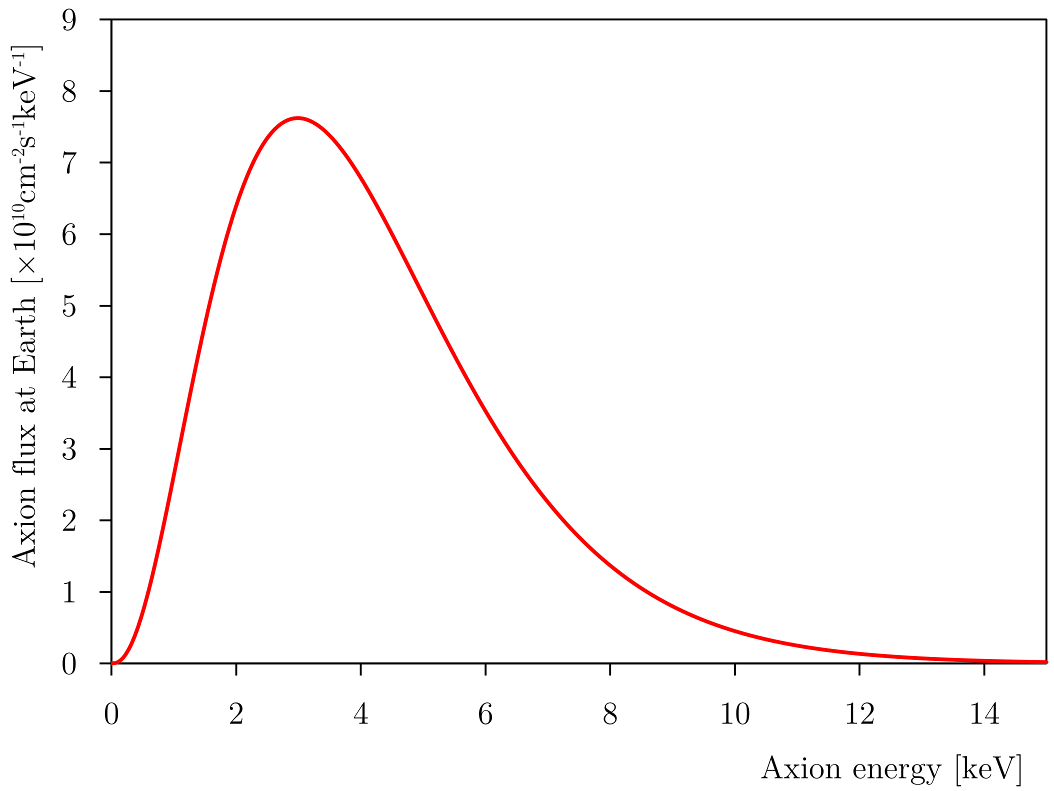

Figure 2.2: The axion flux at Earth, from the latest solar model [58]. The maximum axion intensity is at~3 keV and the average axion energy is $\langle E_a \rangle$=4.2 keV.

2.2 The detection principle of CAST

The solar axion search with a helioscope, such as CAST is based on the inverse coherent Primakoff effect. Solar axions will come from the Sun and convert in photons, in the presence of a strong transverse magnetic field, as seen in Figure 2.1 (right). The probability of conversion in the general case of a uniform optical medium inside a transverse and homogeneous magnetic field, which extends for length L, is [59]:

$$P_{a\to\gamma} = \left(\frac{B\, g_{a\gamma}}{2}\right)^2 \frac{1}{q^2 + \Gamma^2/4}\left[1 + e^{-\Gamma L} - 2e^{-\frac{\Gamma L}{2}}\cos(qL)\right] , \tag{2.2}$$

with Γ the inverse photon absorption length (damping factor) of the medium and q the momentum transfer, which for a photon of effective mass m_γ is:

$$q = \left|\frac{m_\gamma^2 - m_a^2}{2E_a}\right| , \tag{2.3}$$

with m_γ, being given by the plasma frequency of the medium:

$$m_\gamma \left[\frac{\mathrm{eV}}{\mathrm{c}^2}\right] = 28.77 \sqrt{\frac{Z}{A}\rho \left[\frac{\mathrm{g}}{\mathrm{cm}^3}\right]}\,, \tag{2.4}$$

as a function of the density ρ, the atomic number Z and atomic mass A of the medium.

If the medium inside the magnetic field is vacuum, then $\Gamma = 0,\ m_\gamma = 0$ and eq. (2.3) becomes:

$$q = \frac{m_a^2}{2E_a}\ . \tag{2.5}$$

The highest probability of conversion in eq. (2.2) comes when $qL < \pi$, which yields an axion mass limit of $m_a < \sqrt{2\pi E_a/L}$. For the CAST experimental setup, this condition brings a limit to the axion mass sensitivity in vacuum at m_a<0.02 eV.

In the case of an experiment with a buffer gas this condition can be fulfilled in a narrow mass range (Figure 2.3):

$$\sqrt{m_\gamma^2 - \frac{2\pi E_a}{L}} < m_a < \sqrt{m_\gamma^2 + \frac{2\pi E_a}{L}}\ . \tag{2.6}$$

The axions that are converted to photons in the presence of the strong magnetic field can be then detected by X-ray detectors, which reside outside the magnetic field area. The expected photon signal can be calculated as:

$$N_\gamma = \int \frac{d\Phi_a}{dE} P_{a\to\gamma}\, A\, t\, dE\ , \tag{2.7}$$

where $d\Phi_a/dE$ is the expected flux of solar axions, from eq. (2.1), A the axion sensitive area of the detector, and t the observation time.

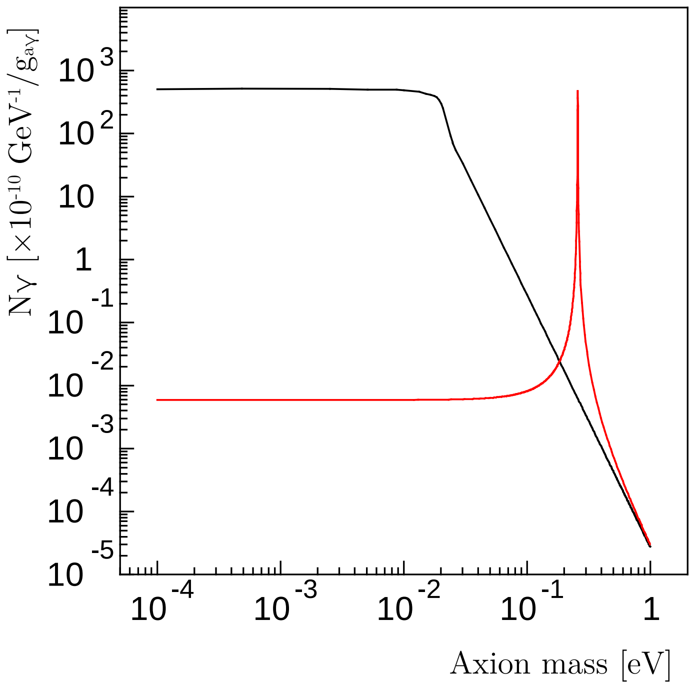

Figure 2.3 The difference in the expected number of photons N_γ, when the medium inside the transverse magnetic field region is vacuum (black line) and a buffer gas (in this case ^{4}He of 6.08 mbar). For a specific pressure of the buffer gas, the coherence is restored only for a small axion mass window.

2.3 The experimental setup of CAST

2.3.1 Introduction

The principle of detection of a solar axion telescope is the Primakoff effect. An incoming axion couples to a virtual photon from a transverse magnetic field of the telescope's magnet and it is converted to a real photon which carries the energy and momentum of the original axion. A schematic representation of the above principle, applied in the experimental layout of CAST, is shown in Figure 2.4.

The main component of the CERN Axion Solar Telescope (CAST) is the 10 m long, twin aperture decommissioned LHC prototype magnet, which can reach a field of 9 T [61]. The magnetic field configuration is shown in Figure 2.5. This prototype magnet was fabricated to be straight, thus it is not bent to cope with the LHC radius of curvature as the rest of the LHC magnets. It is comprised of two straight cold bores of 42 mm aperture. A cross-section of the CAST magnet is shown in Figure 2.6.

In the CAST experiment, the LHC prototype magnet is mounted on a moving platform which allows it to move from $-8°$ to $+8°$ in the vertical direction and from -40 degrees to +40 degrees in the horizontal, (Figure 2.4 and Figure 2.8), allowing it to follow the Sun for approximately 1.5 h during the sunrise and 1.5 h during the sunset, throughout the year.

Four low-background X-ray detectors (currently three Micromegas and one pn-CCD) are installed in each end of the cold bore tubes to identify the converted photons exclusively at times of alignment between the magnet and the core of the Sun (tracking), providing an axion signature. The remaining hours of the day the magnet stays idle in a horizontal parking position and reference background measurements are taken.

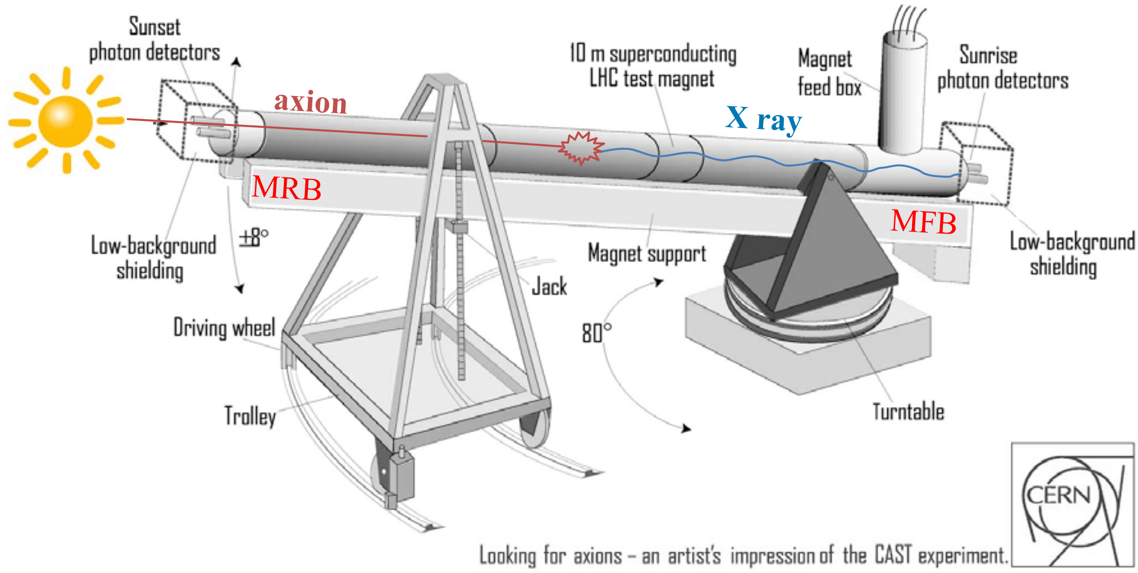

Figure 2.4 Schematic drawing of the principle of detection of axions in the CERN Axion Solar Telescope

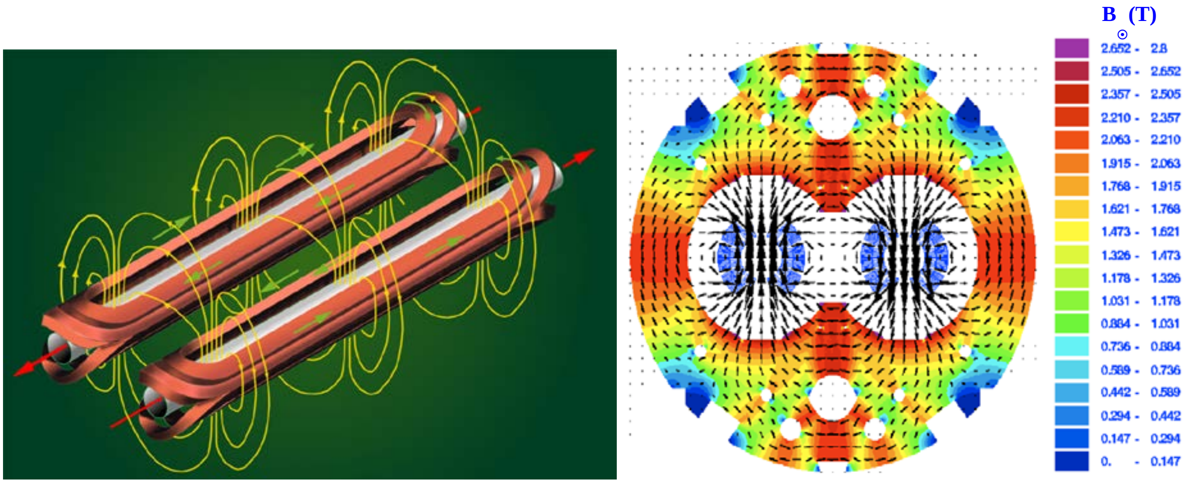

Figure 2.5: The magnetic field configuration of the CAST dipole magnet.

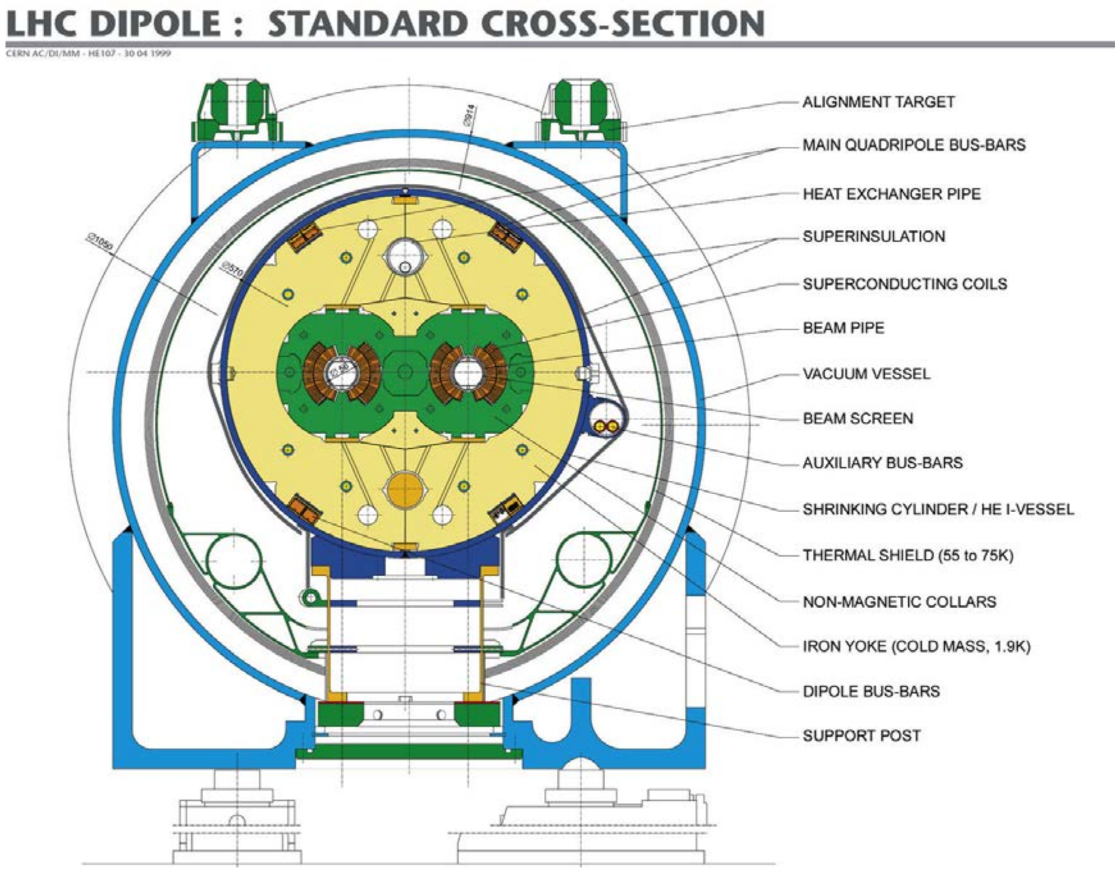

Figure 2.6 The cross section of the CAST magnet.

2.3.2 The cooling system

To obtain the maximum operating field of around 9 T the CAST magnet current has to rise to 13 kA. To avoid the enormous heat load it has to operate in the superconducting region. The use of superfluid ^{4}He as coolant ensures full liquid filling of the helium vessel and permits the cooling of the magnet to 1.8 K even when it is tilted.

The whole cryogenic infrastructure needed to cool down the magnet from ambient temperature and to supply it with liquid helium (at 4.5 K) has been recovered from the cryogenics of the LEP2 collider and the DELPHI experiment and adapted for use in CAST. To cool down and operate the magnet at 1.8 K a new ROOTS pumping group was installed. The cryogenic and electrical feed to the CAST magnet is done through the same magnet feed box (MFB) already used with the cryogenic LHC test benches adapted to the needs of CAST (Figure 2.4 and Figure 2.8). The MFB is connected to the liquid helium supply, the gaseous helium pumping group and the quench recovery system via seven transfer lines. The other side of the magnet, the Magnet Return Box (MRB), is closing the cooling circuit (Figure 2.4).

If a point of the superconducting coil enters the resistive state it will increase its temperature rapidly leading to the increase of the temperature of the surrounding area, in a chain-reaction manner, and eventually of the whole magnet, causing it to quench. In order to prevent damages to parts of the magnet, a quench protection system is deployed. When the system detects increase in the resistivity in a part of the magnet a controlled quench is provoked, with uniform heat dissipation along the coils. In the event of a quench the liquid helium starts boiling and is evacuated through exhaust pipes, as seen in Figure 2.7.

Figure 2.7 A quench in the CAST magnet. The liquid helium starts boiling and is evacuated through exhaust pipes in the atmosphere.

Figure 2.8 An actual picture of the CAST experimental setup, with its main components denoted.

2.3.3 The tracking system

The CAST magnet is supported by a large green metallic platform which is able to move by two structures, a green turn-table on the MFB side and a yellow girder on the MRB side, as seen in Figure 2.8. A green triangular structure, close to the MFB side, sits on the turn-table and allows the magnet to rotate vertically while the turn-table allows the magnet to pivot horizontally. The yellow girder on the MRB side is driving both movements with two motors. Horizontally the magnet moves by following two rails in the azimuth direction and the vertical movement is performed by two lifting jacks. Two encoders, one for the vertical and one for the horizontal motor, provide local integer measuring units (1 vertical encoder unit = 30 μm of magnet movement, 1 horizontal encoder unit = 35 μm of magnet movement). In order to protect the moving system from derailing or to abort erroneous manipulations of the 50 ton system, several emergency off buttons have been placed on the moving structure.

A local reference system (GRID) has been created, with precise measurements done in 2002, of 9 (zenith) × 10 (azimuth) points, with the help of the Survey group of CERN. The GRID correlates the horizontal and vertical position of the magnet to the encoder units, for easier reference and for the communication with the control software. A photo of the vertical encoder is shown in Figure 2.10, left.

The control of the magnet movement is done via a tracking program which was developed using the Labview system design software. A snapshot of its user interface is seen in Figure 2.11. For the position of the magnet and the projection of the Sun in the experimental area, it uses the reference GRID of 2002, with the Hardy's multiquadratic spline interpolation method for filling in the gaps between measurements. In order to achieve precise timing the pc's time is synchronised with the time servers at CERN. The complex calculations that it performs are done sequentially in steps.

Initially it calculates the relative position of the Sun in respect to the magnet, 1 minute in advance, using NOVAS (Naval Observatory Vector Astrometry Software) [62]. If the Sun is reachable and inside the safe band, which is the limits of the movement of the magnet $-7.2^o < V < 7.95^o$ and $46.8^o < H < 133.1^o$), it sets the speed of the motors to reach it. The speed is set successively with a difference of 1-2 s, first to the horizontal and then to the vertical motor.

This calculation is not done constantly and instantaneously for both motors, thus uncertainties are introduced. The precision achieved for tracking the Sun is calculated with the following formulas:

$$H_{\text{precis.}} = \left| \left(H_{\text{enc.measured}} - \frac{|a-b|}{\tau} \tau' \right) - H_{\text{goal end}} \right| \cdot 0.0026055 \text{ [degrees]} \qquad (2.8)$$

$$V_{\text{precis.}} = \left| \left(V_{\text{enc.measured}} - \frac{|a-b|}{\tau_1} {\tau_1}' \right) - V_{\text{goal end}} \right| \cdot 0.0003007 \text{[degrees]} \qquad (2.9)$$

with the parameters $a, b, \tau,\ \tau'$, for the case of the horizontal encoder, defined in Figure 2.9. The same definitions with $\tau,\ \tau'$ apply for τ_1 and ${\tau_1}'$, in the case of the vertical encoder.

The main sources of errors in the tracking of the Sun are summarised in Table 2.1. Overall, an accuracy better than 0.01° is achieved.

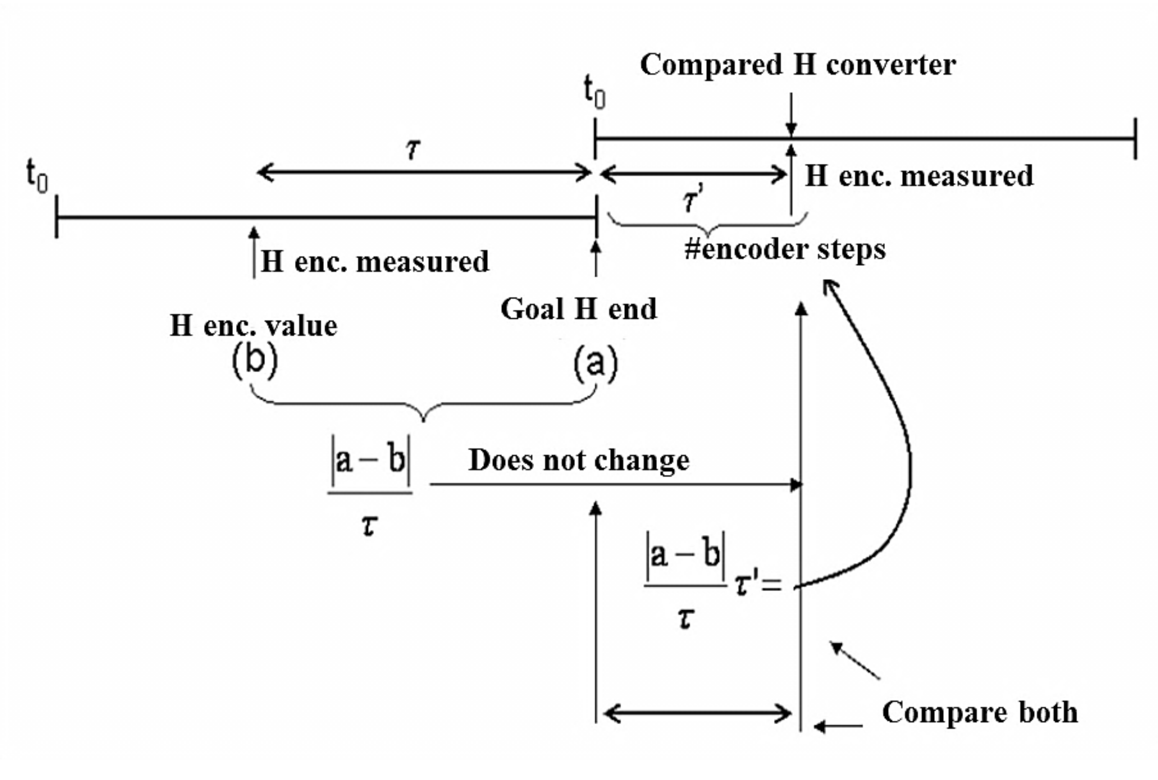

Figure 2.9: Scheme of the calculation of the precision during tracking from the horizontal encoder. Exactly the same principle is applied for the vertical encoder.

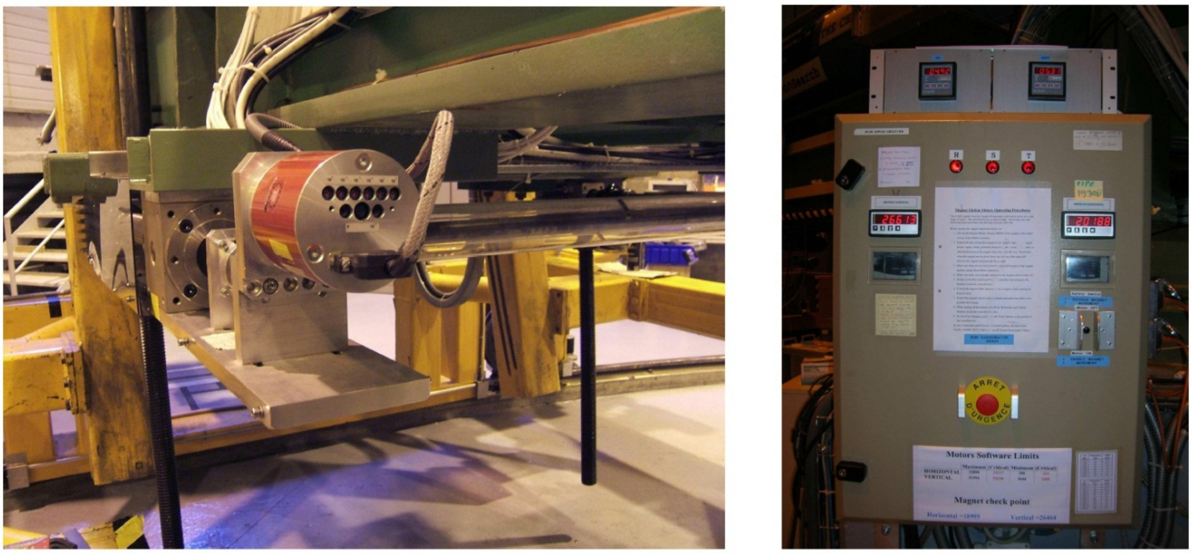

Figure 2.10 Left: The vertical encoder, converts the position of the magnet inside the experimental hall in encoder units. Right: The motors control box. It allows the manual/automatic manipulation and the communication with software

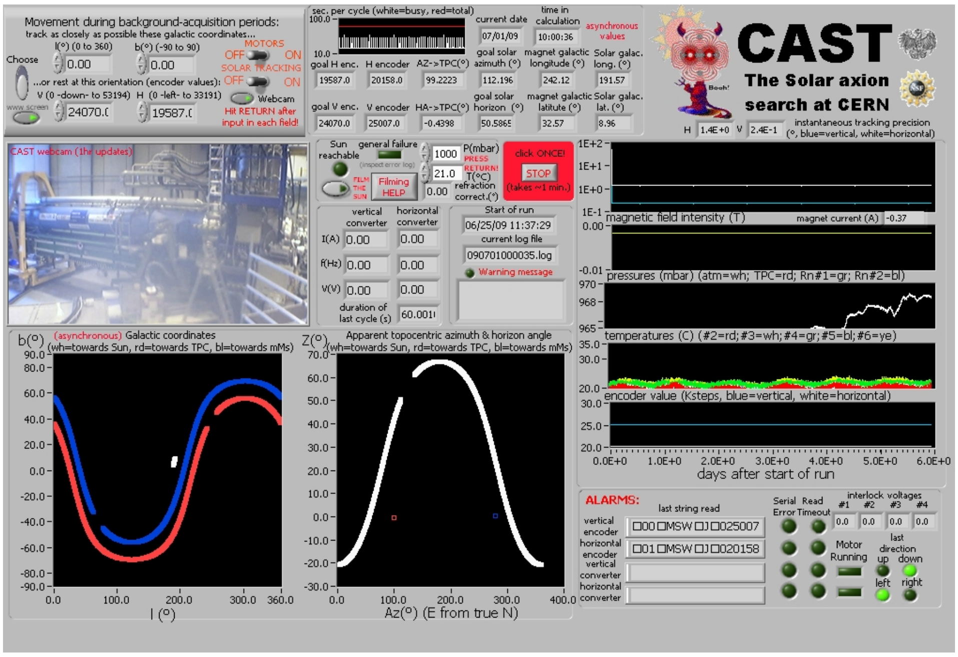

Figure 2.11 The user interface of the tracking program. The trajectory of the Sun, the position of the magnet, the precision of tracking and many other information are displayed.

2.3.4 Magnet position measurements

In order to verify that the required precision for tracking the Sun is maintained, two tests are performed. The systematic repetition of the GRID measurements and the Sun Filming.

2.3.4.1 GRID measurements

The calibration of the encoding of the motors has been done with the help of the Survey group of CERN in 2002. Since then, once or twice per year a subset of these points is selected (mini-GRID) and the measurements are reproduced. The objective is to detect any drift in the pointing accuracy of the system, with respect to the original calibration values of 2002. A second reference grid, completed much later, in September 2007 is also used for cross checking the results.

The latest measurements were performed in July 2011. The system was found substantially unchanged with respect to September 2007, and in good agreement with the reference values of the grid of 2002, the ones used from the tracking program, as seen in Figure 2.12.

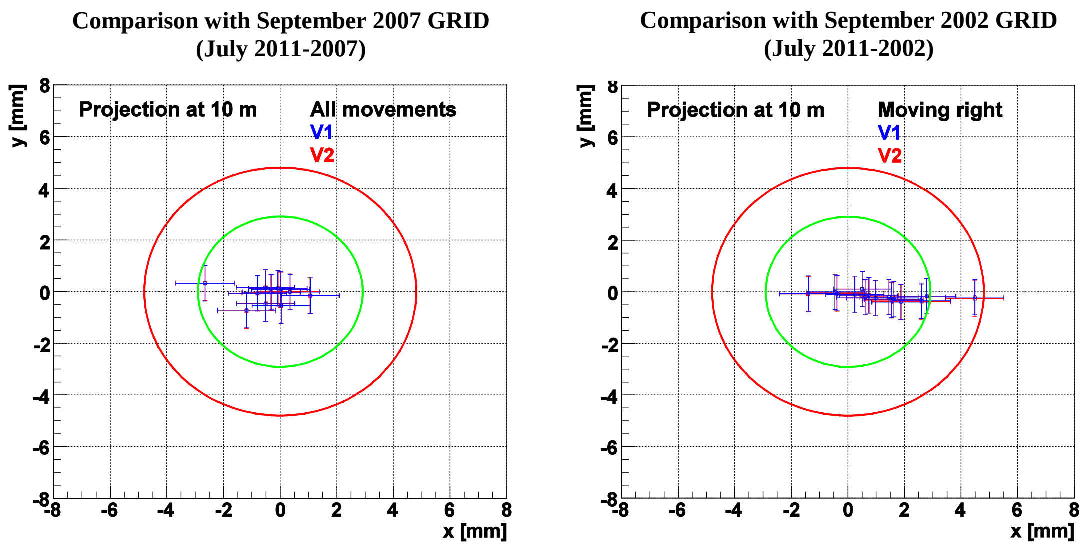

Figure 2.12: Comparison of the GRID measurements performed in July 2011 with the ones of September 2007 (left) and 2002 (right), for both magnetic bores, V1 and V2. The required precision of 1 arcmin is indicated by the green circle, while the red one represents the 10% of the Sun projected at 10 m. The rogue point in the comparison with 2002 (right) is of minimum importance because it refers to a position in the limit of the movement of the magnet, which is rarely visited.

2.3.4.2 Sun filming

Twice per year, in March and in September, it is possible to directly observe the Sun for some minutes, from the CAST experimental hall, through a small window in the east-facing wall (Figure 2.13).

The experimental setup consists of an SLR camera, with an ultra-zoom objective and special filters. The camera is aligned to the axis of the magnet with laser targets, as seen in Figure 2.14, and is controlled remotely by software. The tracking software, which drives the magnet to follow the Sun, is operating in a special mode, in which the refraction of light through the atmosphere is taken into account. This setup can measure the misalignment of the CAST magnet with the center of the Sun with a precision of 0.002°.

Figure 2.13 View of the window, through which the sun filming is possible twice per year.

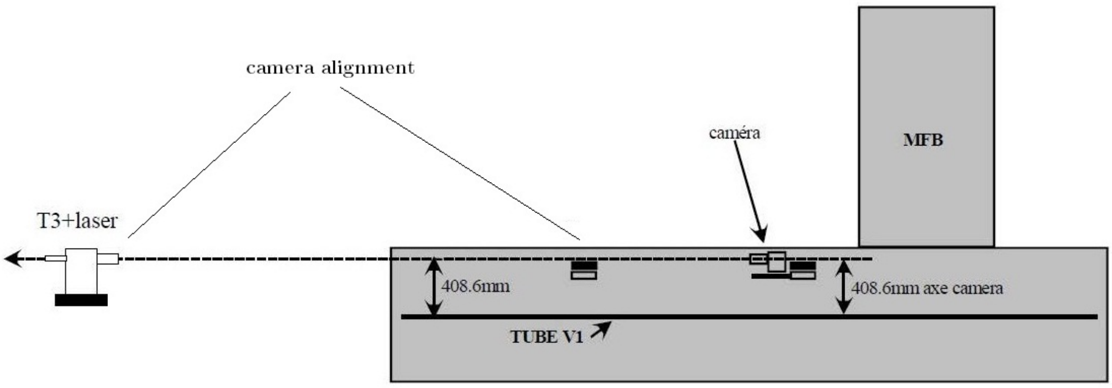

Figure 2.14 A sketch of the alignment setup used for the sun filming.

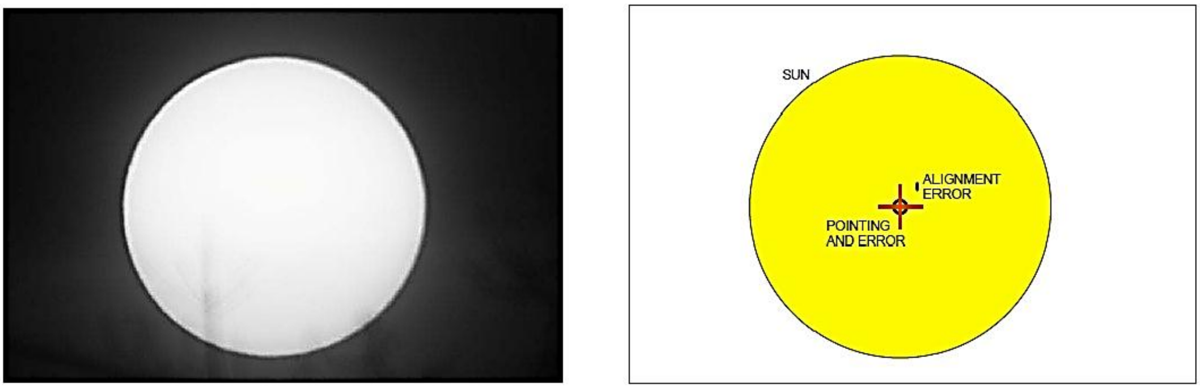

Figure 2.15 A photo of the sun (left) and the alignment of the camera with the center of the sun (right), during a sun filming.

Error in	Typical value (degrees)	Maximum value (degrees)
Astronomical calculations	0.002	0.006
Surveying measurements	0.001	
Mathematical error in interpolation of surveyor's measurements	0.002	<0.01
Horizontal encoder precision	~0.0014	
Vertical encoder precision	~0.0003	
Hysterisis	0.0034	0.02
Perfect linearity of motor speeds	<0.002	
TOTAL	0.01	

Table 2.1: The sources of error in the tracking of the Sun. Overall an accuracy better than 0.01^{o} is achieved.

2.3.5 Vacuum system

The vacuum system of the CAST experiment can be separated in three subsystems, as seen in Figure 2.16, each with its own pumping group. The cryostat vacuum provides thermal insulation of the cold magnet and cooling helium system against ambient temperature. The detector vacuum is the vacuum between each detector and the four gate valves (VT1 to VT4). These gate valves separate the detector vacuum and the third subsystem, the general CAST vacuum. They are normally open during data taking periods but they can be closed to isolate the detector subsystem in case of power failure, quench, degradation of vacuum or detector maintenance. The general CAST vacuum is between the gate valve of each detector and the cold bore area which contains the buffer gas. A series of interlocks and a Programmable Logic Controller (PLC) for the pn-CCD detector, provide automated protection of each subsystem from problems to the others, such as leaks or erroneous manipulations.

In order to monitor any possible contamination in the cryostat and general CAST vacuum two residual gas analysers (RGA) have been installed one for each subsystem. They are essentially mass spectrometers, which allow a real time identification of the constituent gasses of the vacuum.

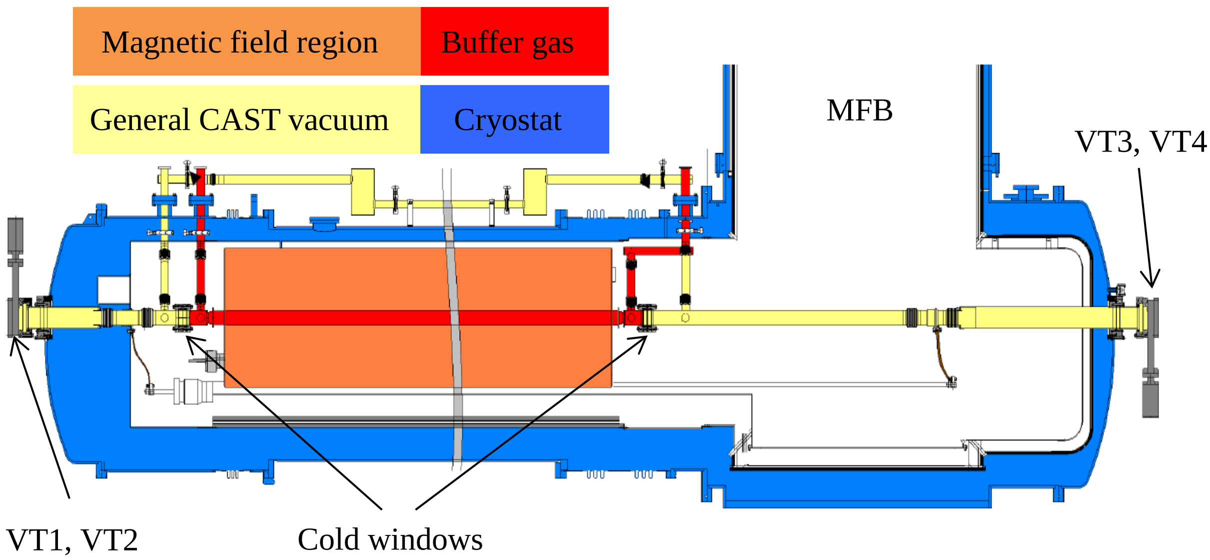

Figure 2.16: The different subsystems of the CAST magnet. The cold windows separate the buffer gas region and the general CAST vacuum system.

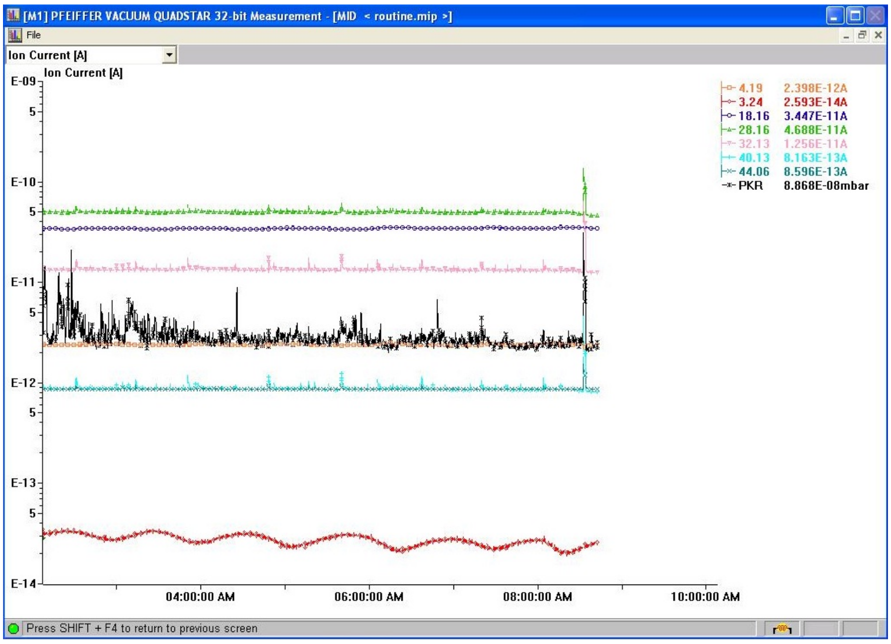

Figure 2.17 Snapshot of one of the two RGA programs used in CAST. It displays in real time the contribution of each constituent gas to the overall vacuum (i.e. a.m.u 2 corresponds to H_2, 3 to ^3He, 28 to N_2 etc).

2.3.6 Slow Control system

The Slow Control system of the CAST experiment is a dedicated program, based on the Labview system design software, to monitor and log all the important variables for the stability of the experiment. It has been operating since the beginning of the experiment in 2003, and has been upgraded and expanded continuously with more signals and variables. It monitors vacuum pressures, pressure in the cold bores, temperatures in different parts of the magnet, ambient temperatures, magnet movement, detector parameters, valve statuses and many other variables through multiple National Instruments data acquisition cards.

One of the main functionalities of the Slow Control is that it is programmed to detect abnormal variations in key parameters of the experiment. In case one parameter changes with a higher rate than normal or reaches a certain predefined value, it triggers the fast acquisition and logging mode, in order to monitor in the highest possible detail the potentially crucial event. It also sends warning SMS messages and e-mails, to the people responsible for the system, so that they can react immediately.

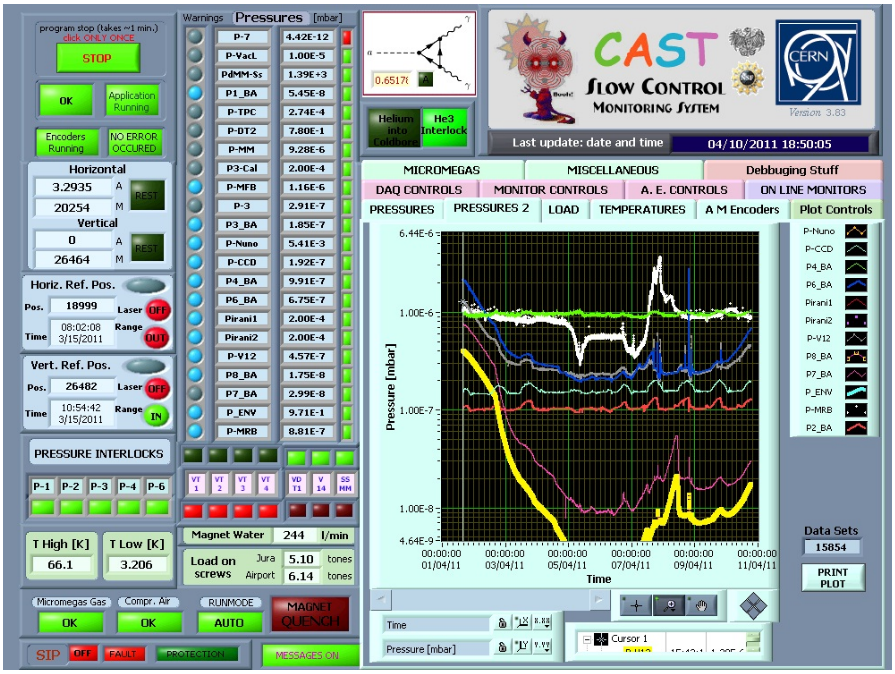

Figure 2.18 Snapshot of the last revision of the Slow Control system of the CAST experiment.

2.3.7 ^{3}He buffer gas system

During its first data taking phase, which started in 2003, the CAST experiment was operating with vacuum in the magnet bores and it was sensitive to axion masses up to 0.02 eV. In the first part of its second phase (2005-2006), ^{4}He was used as buffer gas, thus restoring the coherence for axion masses up to 0.39 eV. Due to the saturation vapour pressure of ^{4}He, of 16.405 mbar at 1.8 K, in order to scan for higher axion masses, ^{3}He was introduced as a buffer gas, for the second part of Phase II which started in 2008. The ^{3}He, having a saturation vapour pressure of 135.8 mbar at 1.8 K, allowed the restoring of the coherence for axion masses up to 1.16 eV. The existing system had to be upgraded to perform safely up to the saturation vapour pressure of the ^{3}He.

2.3.7.1 Thin cryogenic cold windows

Introducing a buffer gas in the magnet bores, required an object to confine it. Therefore the cold bore tubes had to be closed with four “Thin Cryogenic Cold Windows”. Their position is shown in Figure 2.16. The characteristics of these cold windows had to be: operation at low temperatures (1-120 K), mechanical robustness, to withstand the differential pressure of the buffer gas normally below 130 mbar (but could reach 1.2 bar in case of a magnet quench), low permeability to helium, highly transparent to X-rays of 1-7 keV and transparency to visible light (for visual inspection of contaminations and detector alignment purposes).

After extensive research and development, performed at CERN [63], following the original design by CEA-Saclay, the cold windows developed, consisted of 15 µm thick polypropylene foil, glued to a stainless steel strongback, forming a grid of square cells, for mechanical robustness, as seen in Figure 2.19.

The cold window temperature can be modified, by heaters, on the window flanges. If no heating is applied, the windows become the coldest part of the general CAST vacuum, cryo-pumping gases. This reduces their X-ray transmission. In this case it is necessary to occasionally “bake out” the windows, heating them to 200 K, so that the frozen gases which are stuck in the foil evaporate.

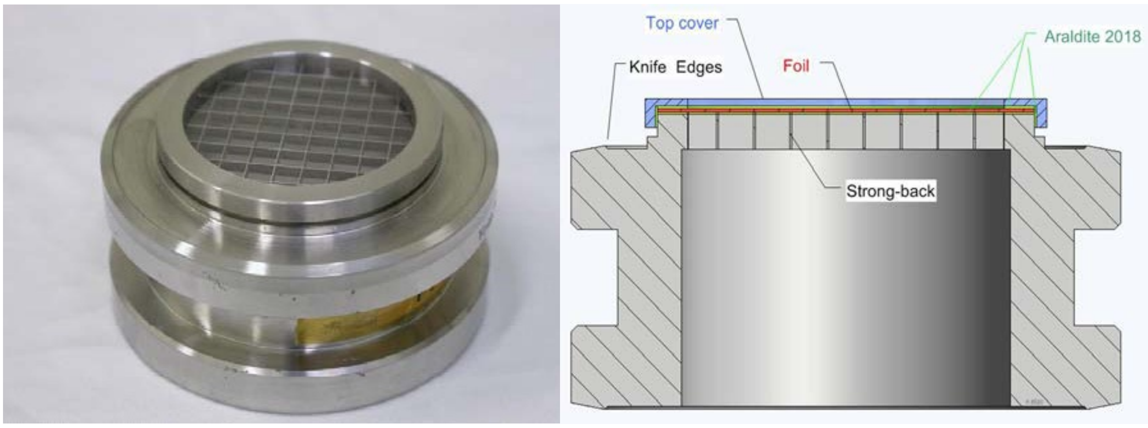

Figure 2.19 A picture of one of the cold windows, mounted on a CF63 flange (left) and the cross section of the configuration where the different components are shown (right).

2.3.7.2 Main functions and principles

The buffer gas system is kept in a pressure lower than atmospheric, so that in the unlikely event of a leak, the smallest amount of gas possible will escape, due to the pressure difference [64].

The most important functionalities of the system are:

- The metered transfer of ^{3}He gas into the cold bores.
- The recovery of the ^{3}He in the case of a quench.
- The purification of the gas.
- The safe storage.

Metering of the gas

CAST is scanning a wide range of axion masses. To ensure reproducibility and precision in the calculation of the axion mass scanned, the exact amount of gas that is injected in the cold bores has to be known. For this reason the gas is injected in the cold bores through one of the two existing metering volumes.

The one volume, called Metering Volume 2, has a volume of 1.63 litres and is serving mainly for a step increase in the density of the gas in the cold bores, in the middle of a tracking of the Sun, in order to scan for higher axion masses. The evolution of the metering volume's pressure together with the one in the cold bores during this procedure is shown in Figure 2.20. In Figure 2.21, in green colour, the path of the gas through the system is denoted, for the same procedure.

The second volume, Metering Volume 10, has a volume of 8.53 litres and is used primarily for injecting large amounts of ^{3}He in the cold bores to reach a specific density accurately and in a short period of time.

The measurement of the amount of gas injected is done by accurately measuring the pressure difference on the metering volume used, before and after the injection of gas in the cold bores. Both volumes are maintained at a constant temperature of 309 K inside a thermostatic bath, with temperature stability of $\pm$0.01 K. In Figure 2.22 one can see the thermostatic bath, with the screen of its controller, on the left, and on the right the Labview-based software that was developed to record its temperature and send alarms in case it exceeds the predefined levels.

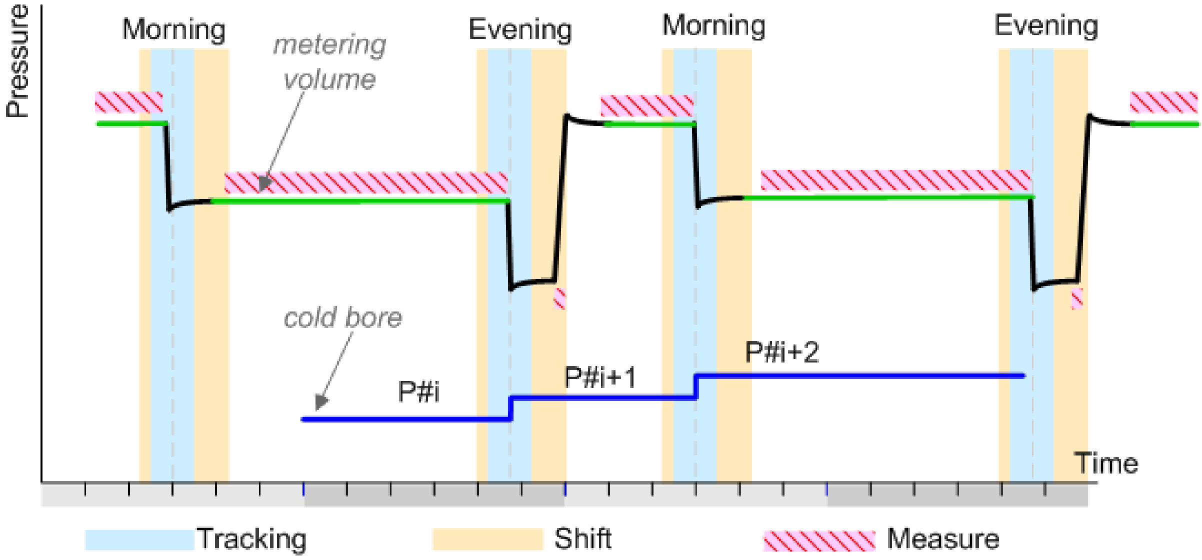

Figure 2.20 The standard filling scheme, followed in the ^{3}He phase. A precise amount of gas is injected to the cold bores, during each tracking [64].

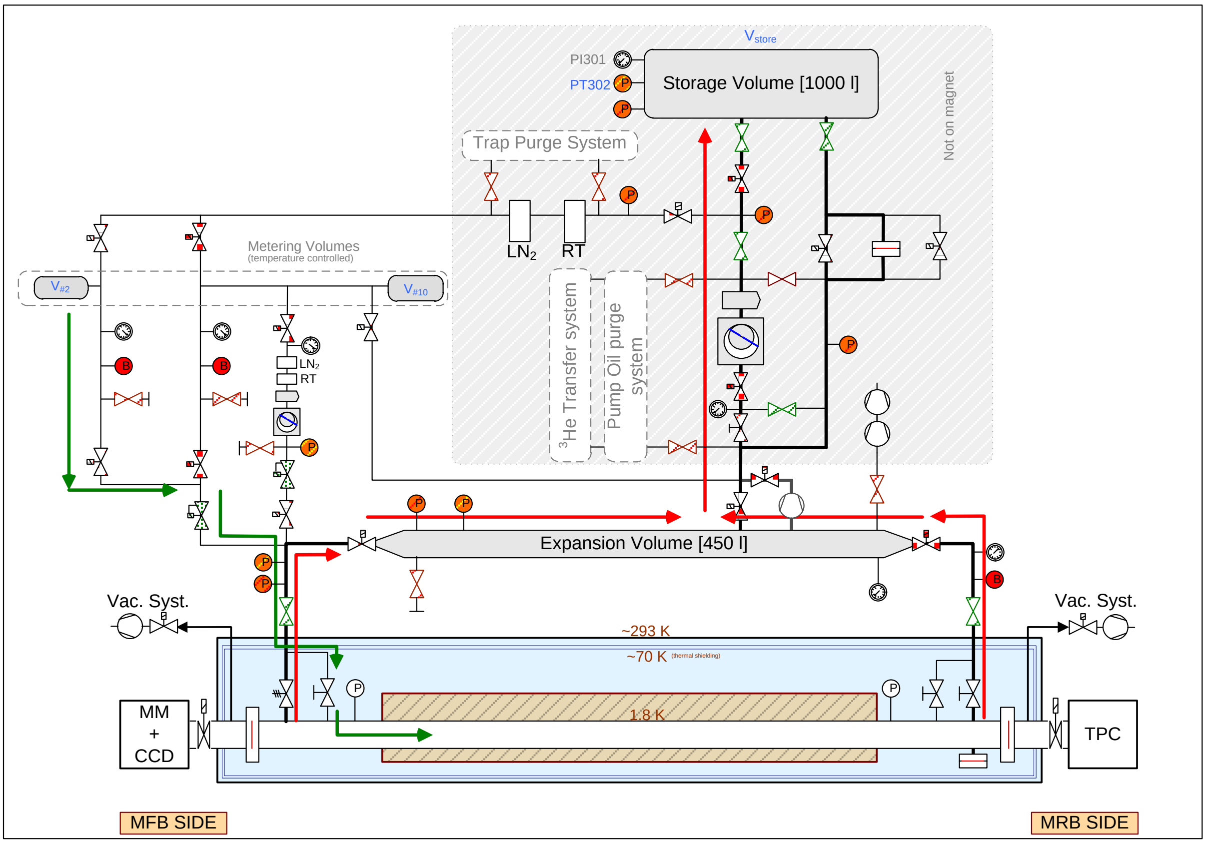

Figure 2.21 The ^{3}He system of CAST. Green arrows: The standard filling procedure during data taking. Red arrows: The recovery procedure and safe storage of the gas.

Figure 2.22 The thermostatic bath (left) keeps the Metering Volumes at a constant temperature to ensure reproducibility and high precision. Since the constant temperature of the bath is of high importance, control software was developed (right) to monitor and alarm for possible malfunctions of the device.

Recovery and storage of ^{3}He

In the event of a natural quench or a quench provoked by interlocks, the temperature of the magnet rises rapidly. To avoid breaking the cold windows, two electro-pneumatic valves, one on each side of the magnet, open and connect the cold bore with a 10 m long, 450 l volume at room temperature (Expansion Volume). Afterwards the ^{3}He is recovered from the cold bores and the Expansion Volume, through a hermetic ^{3}He pump and is stored in the Storage Volume. The Storage Volume is a container of 963 l and it is designed to contain the entire supply of ^{3}He at a pressure below atmospheric pressure. The whole procedure is presented in Figure 2.21.

Purification of the ^{3}He gas

To remove any impurities from the ^{3}He gas, a system of two charcoal traps is used. The first one is at room temperature and traps water vapour and oil from the pumps and the second one is immersed in a liquid Nitrogen bath and removes the rest of the impurities. For an efficient purification the charcoal traps have to be regenerated systematically.

The Programmable Logic Controller (PLC)

Due to the complexity of the system, and the rarity of the gas used, a Programmable Logic Controller was installed, based on the UNICOS framework and developed for the cryogenic systems of LHC.

The PLC allows the transfer of the gas to the different volumes, either by automatized routines, or manually, by controlling the valves and pumps of the system. It also handles the interlocks and can initiate a recovery procedure automatically.

A Supervisory Control and Data Acquisition system (SCADA) was set up, based on PVSS II in order to provide a graphics user interface for the PLC. It is used to connect the hardware devices of the system, such as valves, pumps and pressure sensors, acquire and log their data and use it for their supervision. The data of all the devices are logged in an online data base of CERN, called “TIMBER”. In Figure 2.23 the graphics interface of the PVSS II program is shown, through which the user is allowed to interact with the hardware of the system.

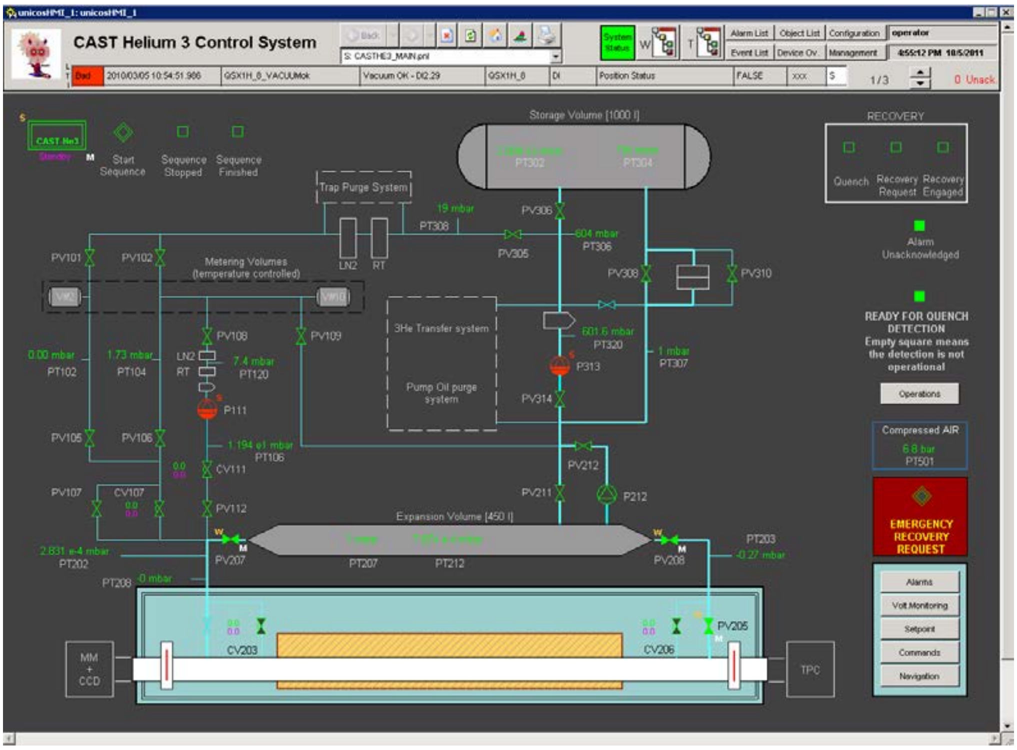

Figure 2.23 The computer interface of the PLC. It is a wire diagram of the actual ^{3}He system, with active elements that can be controlled.

2.3.8 X-ray detectors

The X-rays from the conversion of axions inside the magnet cold bores can either be observed directly, with a detector covering the full aperture of the bore or they can be focused, using X-ray optics, to a focal plane detector.

Four low background X-ray detectors are operating in the CAST experiment, one in each end of the two cold bores of the magnet, sensitive to X-ray signal in the range from 1 to 10 keV. The two ends of the cold bores in the sunset side are occupied by two microbulk Micromegas detectors, while in the sunrise side there is one microbulk Micromegas detector on one bore and on the other an X-ray mirror telescope focusing the photons to a pn-CCD detector. The Micromegas detectors will be reviewed extensively in Chapter 3.

2.3.8.1 pn-CCD detector system

X-ray telescope

The X-ray telescope of the CAST experiment [65, 66], seen in Figure 2.24, was originally created as a spare module, for the satellite mission ABRIXAS [67]. It has a focal length of 1600 mm and consists of 27 gold coated nickel parabolic and hyperbolic mirror shells nested in a spoke structure subdividing the mirror aperture into 6 azimuthal sectors (Figure 2.25), one of which is illuminated by the cold bore. Its purpose is to focus X-rays from the conversion of solar axions inside the magnet bore. The aperture of 14.5 cm^2 is focused to a spot of 6 mm^2 in the pn-CCD detector, enhancing the signal to background ratio. Moreover it allows for the remaining part of the detector to be taking background measurements simultaneously. In Figure 2.26, a schematic view of the principle of operation of the X-ray telescope is shown.

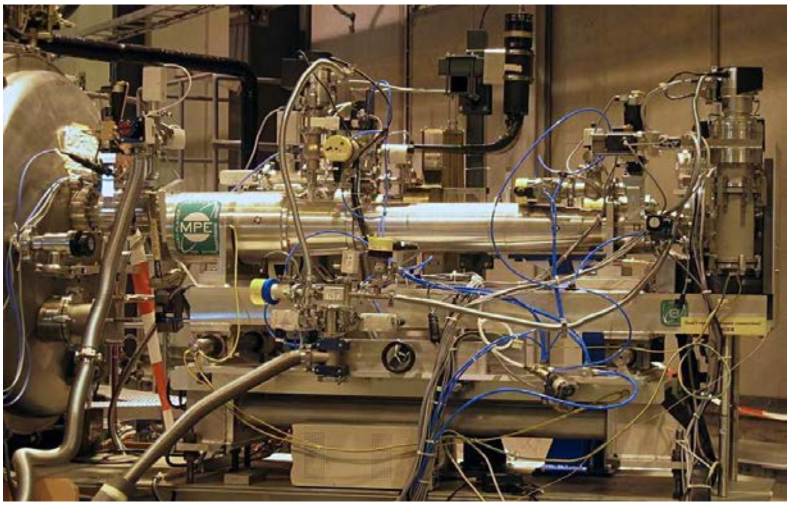

Figure 2.24 The X-ray telescope mounted on the CAST magnet

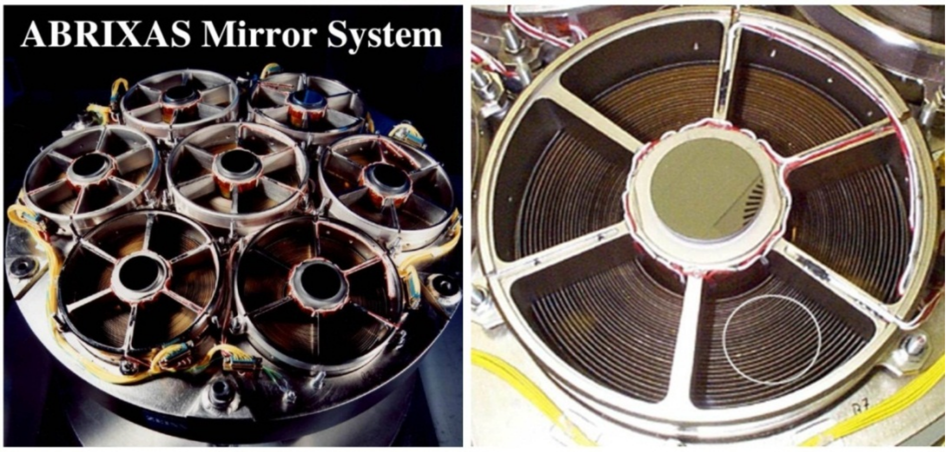

Figure 2.25 Front view of (left) the ABRIXAS X ray focusing system and (right) the CAST mirror system. One of the six sectors is illuminated through the magnet bore. Its size is indicated by the white circle.

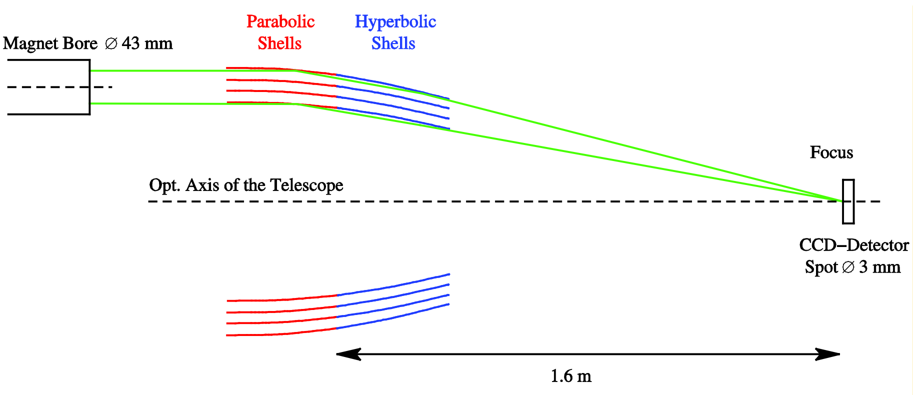

Figure 2.26 Schematic view of the principle of operation of the CAST X-ray telescope

pn-CCD detector

The detector that is placed in the focal plane of the CAST telescope is a fully depleted pn-CCD detector, [68]. It has a sensitive area of 2.88 cm^2 divided into 200 × 64 pixels with a size of 150 × 150 μm^2 each. The axion signal from the core of the Sun has a diameter of 19 pixels or 2.83 mm^2. The 64 columns of 200 pixels are read out in parallel in 6.1 ms followed by an integration period of 65.7 ms, resulting in a total cycle time of 71.8 ms. Since the detector is operating continuously, it has no dead time.

The main advantage of this detector is its high quantum efficiency (Figure 2.27) in the entire range of interest for the search of solar axions, due to the very thin (20 nm) and uniform, radiation entrance window. Daily calibrations with an ^{55}Fe source, monitor its stability.

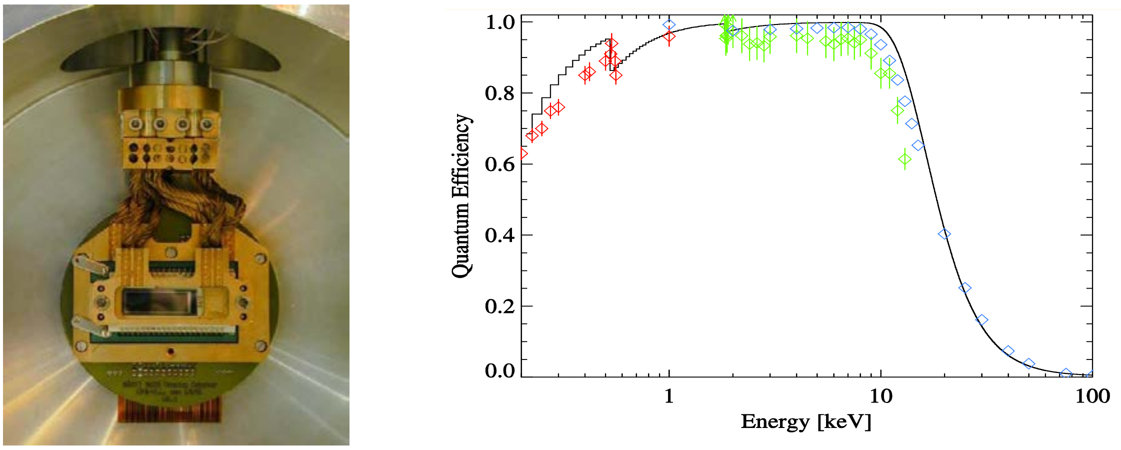

Figure 2.27: Left: The pn-CCD detector. The rectangular pn-CCD chip is visible in the centre, surrounded by the gold plated cooling mask. Right: The Quantum Efficiency of this type of detector is close to 90% for the region of interest of 1-7 keV.

2.4 The CAST scientific program

The CAST experiment has been searching for solar axions since 2003. During 2003, and 2004 (with improved conditions), it has operated with vacuum in the cold bores (Phase I). From the absence of excess in the X-ray signal, while pointing to the Sun, it set the best experimental limit for the axion-photon coupling constant for axion masses up to 0.02 eV/c^2 [69]:

$$g_{a\gamma} < 8.8\times10^{-11}\ \text{GeV}^{-1} \text{ at } 95\%\ \text{CL} \tag{2.10}$$

To extend its sensitivity to higher axion masses, the experiment underwent a large upgrade in 2005 in order to operate with a buffer gas of variable density in the magnet bores (Phase II). The first part of Phase II was completed with ^{4}He as buffer gas. With 160 different pressure settings, CAST scanned the region of axion masses up to 0.39 eV/c^2, setting for the first time restrictive limits for the axion to photon coupling constant that were inside the theoretically favoured region [70]:

$$g_{a\gamma} \leq 2.2\times10^{-10}\ \text{GeV}^{-1} \text{ at } 95\%\ \text{CL} \tag{2.11}$$

In 2007 CAST upgraded again the buffer gas system, to accommodate ^{3}He as a buffer gas. The second part of Phase II started in 2008 and finished on the 22nd of July 2011, scanning axion masses up to 1.18 eV/c^2. The latest limit in the range 0.39 eV/c^2 $\leq m_a \leq$ 0.64 eV/c^2, was provided in [71]:

$$g_{a\gamma} \leq 2.27\times10^{-10}\ \text{GeV}^{-1} \text{ at } 95\%\ \text{CL} \tag{2.12}$$

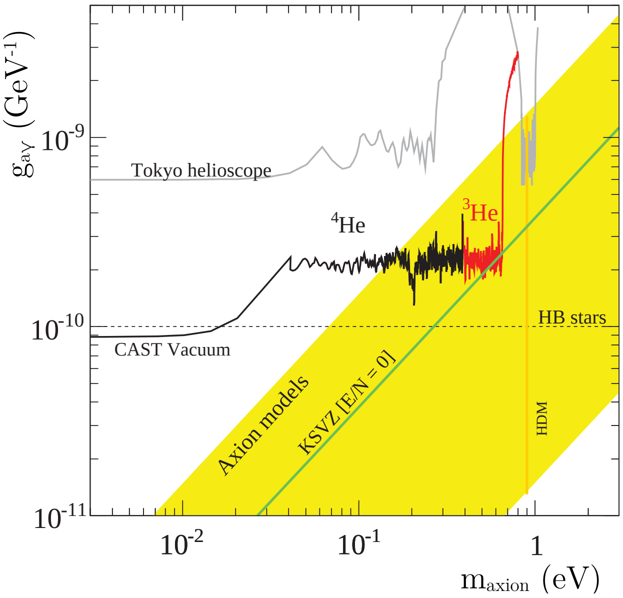

Figure 2.28 The exclusion plot for the axion to photon coupling constant versus the axion mass, achieved in the vacuum [69], ^{4}He [70] and ^{3}He [71] phase. The constraints set by the Tokyo helioscope [55], the horizontal branch (HB) stars [22] and the hot dark matter bound [72] are also shown. The yellow region represents the typical theoretical models with |E/N-1.95| in the range 0.07-7. The green line corresponds to E/N=0 (KSVZ model).

3. Micro Pattern Gas Detectors – Micromegas

Contents

3.1 Historical overview of the Micro Pattern Gas Detectors (MPGDs)

All MPGDs originate from the concept of E. Rutherford and H. Geiger, who in 1908 described the implementation of gas amplification near a wire [73]. Throughout the century many studies and improvements have been made, making the gaseous detectors more and more attractive. In 1968, G. Charpak *et al* took the idea a step further by introducing the Multi Wire Proportional Chambers (MWPCs) [74]. A. Oed, in 1986, made the first attempt to replace the wires with micro pattern plates, developing the Micro Strip Gas Chamber (MSGC) [75] and paving the way for the MPGDs. A new idea of gas amplification, using a very asymmetric parallel plate chamber, the MICROMEGAS detector was invented by G. Charpak and Y. Giomataris [76] and soon after, in 1996, F. Sauli, announced a different approach to the same principle, the Gas Electron Multiplier (GEM) [77].

3.2 Phenomenology of MPGDs

3.2.1 Gas ionization

The basic configuration of the Micro Pattern Gas Detectors (MPGDs) consists of a container (usually cylindrical) with a thin, conductive cap window on top and a readout plane on the bottom. A third contacting plane is placed in between, dividing the MPGD in two regions, the drift region and the amplification region. The container is filled with a suitable gas, usually a noble gas like argon.

If photons or charged particles penetrate a gaseous detector, a number of electron-ion pairs will be created. The mean number of pairs created is proportional to the energy deposited in the container. The ionization electrons are drifted through the gas (drift region) and multiplied (amplification region) creating an avalanche, which is the detected electrical signal.

Ionization electrons are generated through two mechanisms. The first one is the typical primary ionization, of the noble gas X:

$$X + p \rightarrow X^{+} + p + e^{-} \ , \tag{3.1}$$

where p is a charged particle. The second mechanism is a secondary effect, which occurs after the de-excitation of the gas X via photons, in the presence of a second gas, usually polyatomic, called “quench gas” or “quencher”. The polyatomic molecules of the quencher have many degrees of freedom, thus large photoabsorption coefficients and can dissipate the energy of the photons through dissociation or elastic collisions (Penning effect).

The average number of ion-electron pairs produced in a gas for a given initial energy E_0 is:

$$n_e = \frac{E_0}{W} \ , \tag{3.2}$$

where W is the mean energy needed for the ion-electron pair creation which is the sum of the ionization potential and the amount that is spent for excitation. In Table 3.1, the excitation, ionization and ion-electron pair production energies for various gases are shown.

Although the number of ion-electron pairs produced is an indication of the efficiency of the detector, it is not certain that they will reach the electrodes and be measured. The two main mechanisms which are competitive to the ion-electron pair production are the recombination of the atoms and the electron attachment. In the absence of an electric field, ion-electron pairs will recombine, under the force of their electric attraction. Electron attachment involves the capture of free electrons by electronegative atoms, which results to the formation of negative ions. The presence of electronegative gases such as O_2, CO_2 or H_20 in the gas, could result in the capture of the electrons before they reach the electrodes, affecting the efficiency of the ion-electron collection of the detector. The noble gases are not electronegative; therefore they are the most commonly used in the gaseous detectors [78].

	E_{exc} [eV]	E_{ion} [eV]	W [eV]
H_2	10.8	15.4	37
He	19.8	24.6	41
N_2	8.1	15.5	35
O_2	7.9	12.2	31
Ne	16.6	21.6	36
Ar	11.6	15.8	26
Kr	10.0	14.0	24
Xe	8.4	12.1	22
CO_2	10.0	13.7	33
CH_4		13.1	28
C_4H_{10}		10.8	23

Table 3.1: The excitation, ionization and ion-electron pair production energies for various gases [78].

3.2.2 The Fano factor

The outcome of the collision of an electron with a gas molecule is of statistical nature, thus the number of primary electrons created from an initial energy E_0 is subject to statistical variations. The knowledge of these statistical variations is of interest, especially when the ionization produced by particles serves as a measure for their initial energy. The standard deviation is accounted by the Fano factor [79]:

$$\sigma_{n_e}^2 = F \cdot n_e \tag{3.3}$$

The Fano factor F indicates the magnitude of the fluctuations in the number of primary electrons n_e produced from a particle of initial energy E_0 and its value ranges between 0 and 1. Higher values of the Fano factor thus indicate a broader distribution of the number of n_e than that described by lower values of F. The theoretical limit F =0, would describe the electron degradation process in which only ionization processes occur. Both the W and the F values are characteristics of the gas. They only slightly depend on the kind of the incident particle, and both increase (W towards infinity, F towards 1) as the initial electron energy decreases approaching the ionization potential of the gas. For high-energy electrons they acquire almost constant values.

3.2.3 Energy resolution

The most important characteristic of detectors designed to measure the energy of an incident particle or radiation, is the energy resolution. This is the ability of the detector to distinguish between two energies with close lying values. The resolution is measured by irradiating the detector with a monoenergetic beam and evaluating the spectrum. The ideal case would be a delta-function peak, but in reality what one measures is a Gaussian-like peak.

The resolution is usually given in terms of full width at half maximum. Energies that are within this width can hardly be distinguished by the detector. A general formula for the resolution can be expressed as:

$$R\ (\%\ \mathrm{FWHM}) = \frac{\Delta E}{E}\ . \tag{3.4}$$

From the above formula it is evident that the resolution of a detector depends on the deposited energy. The higher the energy of the incident particle the better the resolution of the detector.

The fluctuation in the number of primary electrons n_e, in eq. (3.3), constitutes the first limiting factor of the resolution of a gaseous detector. It gives a limit to the energy resolution of detection of an incident particle with energy E, given by the expression:

$$R\ (\%\ \mathrm{FWHM}) = 2.35\sqrt{\frac{F \cdot W}{E}}\ , \tag{3.5}$$

where the factor 2.35 relates the standard deviation of a Gaussian distribution to its FWHM.

3.2.4 Transport of electrons and ions in gases

Microscopically, the ions and electrons, in the presence of the electric field, drift through the gas colliding with gas molecules. As a result their direction is randomized after each collision. On average they assume a speed u, in the direction of the electric field $\boldsymbol{E}$ which is much smaller than the instantaneous speed c that they acquire between collisions. The gases that are used in the gaseous detectors are sufficiently dilute, so that the distance that corresponds to the mean free path of electrons is much greater than their Compton wavelength. Thus their motion can be described with classical considerations.

3.2.4.1 Diffusion

In the absence of an electric field, electrons and ions start spreading uniformly due to the multiple collisions with the gas molecules. Assuming a thermal equilibrium, their mean speed can be given by the Maxwell distribution:

$$v = \sqrt{\frac{8kT}{\pi m}} \,, \tag{3.6}$$

with k the Boltzmann constant, T the temperature and m the mass of the particle. From eq. (3.6) it is evident that the mean speed of the electrons is much higher than the one of the ions, due to their much smaller mass. The distribution of charges in one dimension can be described by a Gaussian distribution:

$$\frac{dN}{dx} = \frac{N_0}{\sqrt{4\pi Dt}} e^{-\frac{x^2}{4Dt}} \,, \tag{3.7}$$

where t is the elapsed time, x the distance from the point of creation and D the diffusion coefficient. The standard deviation of the above distribution can be expressed as:

$$\sigma(x) = \sqrt{2Dt} \,. \tag{3.8}$$

With similar considerations, one can extract the same formula for three dimensions:

$$\sigma(r) = \sqrt{6Dt} \,. \tag{3.9}$$

The diffusion coefficient D can be described from the classic kinetic theory:

$$D = \frac{1}{3}\upsilon\lambda \ , \tag{3.10}$$

where λ is the mean free path of the electrons or ions in the gas, which can be classically described:

$$\lambda = \frac{1}{\sqrt{2}}\frac{kT}{\sigma_0 P} \ , \tag{3.11}$$

with σ_0 the total cross section of collision with a gas molecule and P the pressure of the gas.

Substituting eq. (3.11) to (3.10), one can see the dependence of the diffusion coefficient with the parameters of the gas:

$$D = \frac{2}{3\sqrt{\pi}}\frac{1}{\sigma_0 P}\sqrt{\frac{(kT)^3}{m}} \ . \tag{3.12}$$

3.2.4.2 Drift

The ions and electrons, in the presence of the electric field drift through the gas, colliding with gas molecules. The collision causes a reduction in their speed and a scatter, around their mean trajectory. The average velocity that they gain is defined as the drift velocity and it is dependent on the mean time between two collisions τ, the electric field E and their mass m. In addition, for the ions the drift velocity is inversely proportional to the pressure of the gas.

The mobility of the electrons and ions can be defined as:

$$\mu = \frac{u}{E} \ , \tag{3.13}$$

where u is the drift velocity. For ideal gases, in which the ions and electrons remain constantly in thermal equilibrium, the mobility and the diffusion coefficient can be connected with the expression:

$$\frac{D}{\mu} = \frac{kT}{e} \ . \tag{3.14}$$

From the above equation, it is evident that the diffusion of electrons is much higher than the one of the positive ions, due to their higher mobility.

3.2.5 Multiplication

When the electric field is big enough that the electrons, between two collisions, pick up enough energy to produce ionization, another electron is created and the avalanche begins. As the number of electrons multiplies in successive generations, the avalanche continues to grow, until all the electrons are collected at the anode. Because of the higher mobility of the electrons, they are gathered in the front of a water drop-like shape and the ions, drifting slowly, are left in the tail, as seen in Figure 3.1.

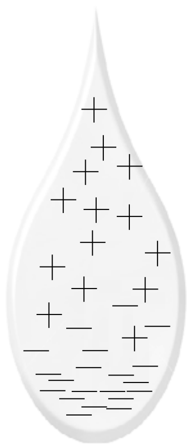

Figure 3.1: The more agile electrons move faster, gathering at the bottom of the avalanche, while the positive ions are slowly moving towards the opposite direction.

The distance that the electron will travel among two ionizations, is defined as the mean free path of ionization. The first Townsend coefficient, a, is the inverse of this quantity. It represents the number of ion-electron pairs, created per unit length. If originally there are n electrons, then after a path dx the amount of electrons created will be:

$$dn = n\, a\, dx\ . \tag{3.15}$$

Integrating the above formula, one gets an expression of the total number of electrons created in a path x, in the case of a homogenous electric field:

$$n = n_0\, e^{ax}\ , \tag{3.16}$$

with n_0 being the original number of electrons.

The multiplication factor, or gas gain G, is then given by

$$G = \frac{n}{n_0} = e^{ax} \ . \tag{3.17}$$

The gas gain cannot increase without a limit, because after a certain value a breakdown occurs. The most demanding task in gaseous detectors is to achieve stable operation, with the maximum possible gain. The limit of the gas gain is called Raether limit and it is defined as:

$$G < 10^8 \ . \tag{3.18}$$

3.2.6 The choice of gas

The choice of gas in gaseous detectors can be biased by several requirements: low operating voltage, high gain, high rate capability, low cost and inflammability. A suitable combination of the above characteristics can only be met by using a gas mixture. Usually, for gaseous detectors noble gases are used as the base of the mixture, because they require the lowest electric fields for multiplication, they are not electronegative and don't react chemically with the detector components. From the noble gases, argon is the most widely used because of its low cost. Other noble gases with higher atomic numbers (i.e., krypton and xenon) may be used if increased sensitivity to X-rays or gamma rays is required. Hydrocarbon gases (i.e., methane, propane and ethylene) can also serve as a fill gas, but they have the disadvantage of being flammable.

With pure argon, gains higher than 10^3 - 10^4 cannot be achieved due to the discharge of the detector. The reason is argon's high excitation energy (11.6 eV). When the argon atoms in the avalanche de-excite, they emit photons of visible light or UV. These photons can interact with the gas and causing the avalanche to spread along the anode with further ionizations. This can result in a non-linear relationship between the energy deposited in the detector gas and the size of the resulting pulse. These photons, particularly if they interact with the cathode, can also lead to discharges. The solution is to add a small amount of a polyatomic gas known as "quench gas" or "quencher". The quench gas preferentially absorbs the photons, but unlike the fill gas, it does not get ionized. The molecules of the quencher absorb the energy of the photons and dissipate it through dissociation or elastic collisions. A small amount of polyatomic gas could result to dramatic enhancement to the gain performance of the gas.

Quenchers can be inorganic, such as CO_2 and BF_3, or organic like methane (CH_4) and isobutane (iC_4H_{10}). The use of an organic quencher in conditions of high rates of irradiation can result in the creation of liquid or solid polymers from the recombination of the dissociated organic molecules, which accumulate in the anode and cathode of the detector. This could lead to a deterioration in the efficiency of the detector or even, in very high irradiation conditions, to the formation of a continuous discharge. In these conditions the use of an inorganic quencher is necessary.

In general, the proportional gas should not contain electronegative components such as oxygen, CO_2 or H_2O. Otherwise, electrons heading towards the anode will combine with the electronegative gas. In this case a negative ion goes to the anode rather than an electron and unlike the electron, the negative ion will fail to produce an avalanche. The resulting pulse will probably be too small to exceed the threshold setting and will not be counted.

3.3 The Micro Strip Gas Chamber (MSGC)

The MSGCs consist of alternating thin wire cathode and thinner anode strips, with a pitch of the order of 100 μm, printed with photolithographic methods on an insulating substrate – usually glass, as seen in Figure 3.2(a).

In Figure 3.2(b) the form of the electric field is shown. The electric field is of the order of a few hundred V/cm and it is uniform in the vicinity of the drift plane. Applying the proper voltages between the anode and cathode strips, a strong dipole field is created, which amplifies the electrons due to avalanche processes. The electrons are focused on the anode strips and the ions created in the avalanche process are collected on the cathode.

The main problem of the MSGCs was that they were prone to ageing, especially by high trigger rates or long irradiation. The gain could not exceed 10^4, because the charge accumulated in the strips changed the electric field, resulting in lower gain. Moreover the anode strips were very sensitive and could be damaged by discharges. Several new layouts were proposed to overcome these disadvantages. The most commonly used ones are the Micromegas and the Gas Electron Multiplier (GEM).

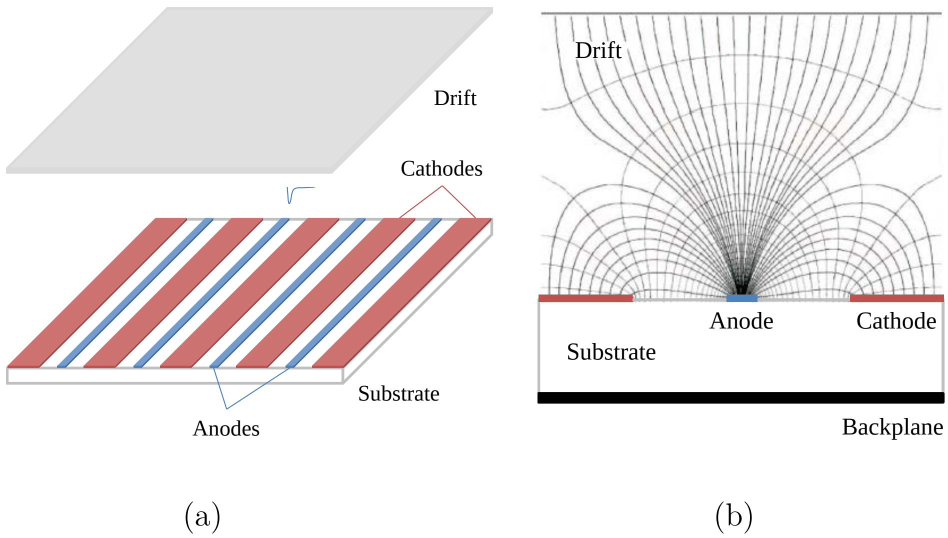

Figure 3.2 : (a) Schematic representation of the main components and (b) Electric field configuration of the MSGC.

3.4 The Gas Electron Multiplier

The new approach to the gaseous detectors that was introduced by F. Sauli [77], the Gas Electron Multiplier, was built at CERN, by standard chemical etching processes, as shown in Figure 3.3. The 50 μm kapton foil is clad in both sides with 5 μm of copper.

The resulting GEM has double-conical holes with a pitch of 140 μm and a diameter of 60 – 70 μm. It divides the detector in three regions, one with intense field, inside the holes of the GEM and one above and below it, with less intense field, for the primary conversion (drift region) and the transfer of the electrons (transfer region), respectively. Typically a voltage difference of 400 - 500 V is applied to the two electrodes, resulting in a very intense field of ~100 kV/cm inside the holes.

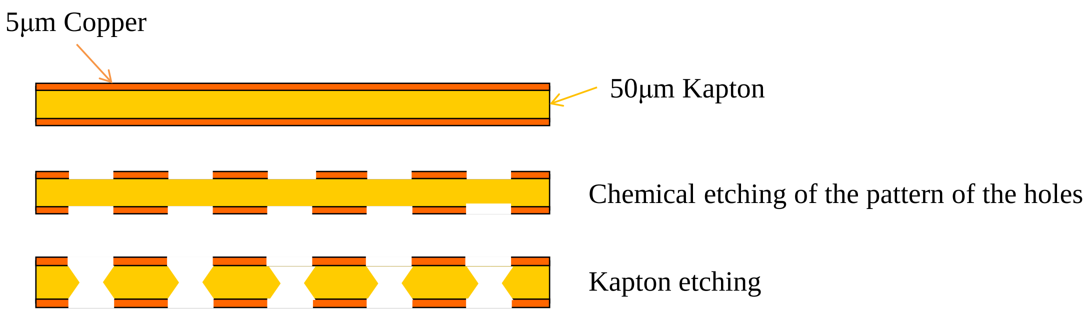

Figure 3.3 The chemical process of the GEM detectors.

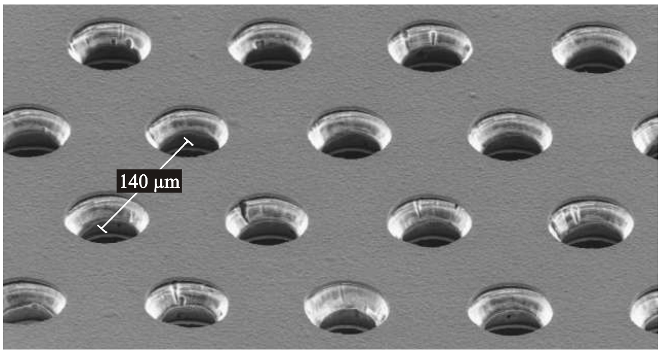

(a)

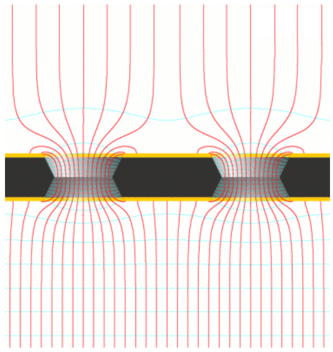

(b)

Figure 3.4 (a) A microscope picture of a GEM plane with 140 µm pitch and 70 µm of hole diameter (b) the electric field in a GEM detector.

Electrons from the drift region pass through the holes guided by the dynamic lines of the field, seen in Figure 3.4(b), and they are multiplied inside the holes. Due to retrodifussion only 60% of the electrons from the avalanche in the holes exit to the transfer region, where they drift to the readout plane.

GEM detectors do not have sparking problems, due to the fact that the multiplication and readout planes are different. On the other hand they have low gain, therefore GEMs are commonly used to multiple stage amplification detectors, in which two or three of them are stacked (double or triple GEM respectively) applying a lower voltage to each one but achieving an overall higher gain in the readout plane. The disadvantage of these arrays is that the electron charge distribution in the read out plane is wide.

GEMs have been used in a number of experiments like HERA-B, COMPASS, TOTEM and LHCb. The GEM community is developing detectors, to expand to other applications as well, such as X-ray Astronomy, Medical Imaging and X-ray polarimetry.

3.5 The Micromegas detector

In 1996 G. Charpak and Y. Giomataris [76] presented a new approach to the MSGC concept. They replaced the wire plane with a thin electroformed nickel mesh. The mesh was stretched and glued on an insulating frame and placed above the anode plane. It was kept in position with precise spacers (pillars) at a distance of 50 – 100 μm from the readout. The pillars were fixed to the anode strips by a standard printed circuit technique. They called the new detector MICROMEGAS (MICRO-Mesh Gaseous Structure).

The micromesh separates the two regions of the detector, the drift region (with a typical electric field of $10^2 - 10^3$ V/cm) and the amplification region (with a typical field of $10^4 - 10^5$ V/cm), as seen in Figure 3.5. The electric field of the drift region is achieved by applying a positive high voltage (HV2) to the micromesh and a higher positive voltage (HV1) to an electrode plane, the drift electrode, placed a few cm above the micromesh thus defining the drift region (Figure 3.5). The readout plane is kept grounded. The whole structure is placed in a leak tight chamber and operates, typically, with a gas mixture of argon and a small amount of a polyatomic gas.

With sufficiently thin micromesh, the amplification inside its holes is negligible. The shape of the field close to the micromesh is crucial for the transparency to electrons and the fast evacuation of the positive ions. The voltages are applied in a way that the amplification field is one order of magnitude higher than the drift field, so that the field lines coming from the drift region do not end to the bottom of the micromesh. As a result the ions are quickly collected in the micromesh and only a small fraction, inversely proportional to the electric field ratio defuses to the drift region and the transparency to the drift electrons is ensured. The electric field of the Micromegas has the form shown in Figure 3.6.

The signal, finally collected in the anode strips, consists of the electrons of the avalanche in the amplification region. The signal collected in the micromesh, derives from the positive ions. The collection of the signal in the micromesh takes place within 100 ns, depending on the width of the amplification gap and the gas mixture used.

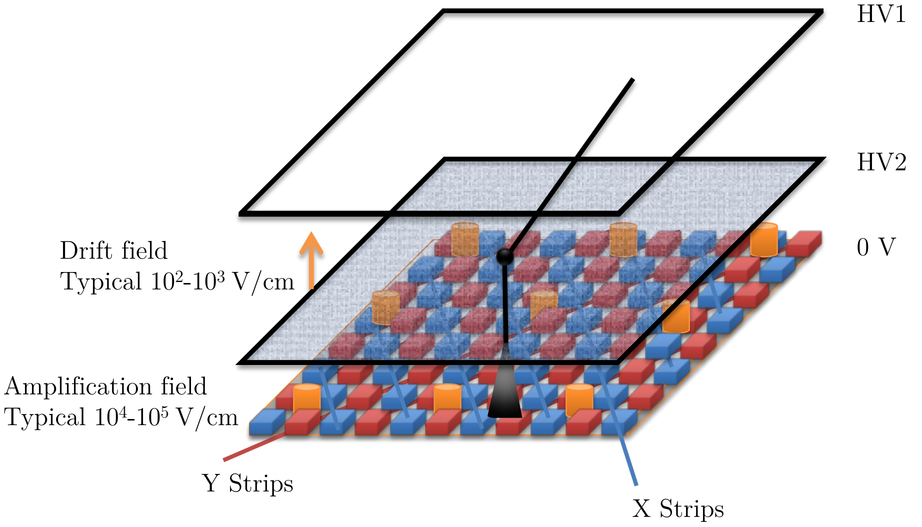

Figure 3.5: Schematic representation of the MICROMEGAS detector

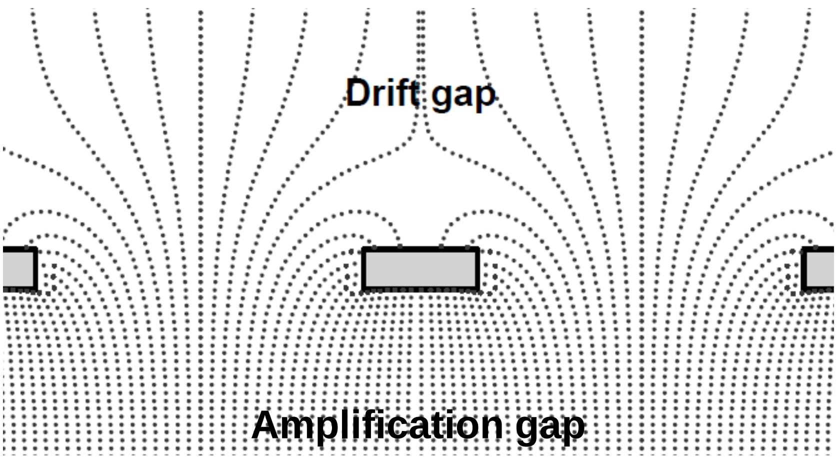

Figure 3.6: The electric field configuration of a Micromegas. The micromesh is almost transparent to the drifting electrons.

3.5.1 Micromegas performance

3.5.1.1 Gain

The Micromegas performance, in terms of electron gain, is not affected by small variations of the length of the amplification region [80], like mechanical defects in the construction of the micromesh, due to its narrow gap. The electron multiplication in the amplification region is given by:

$$G = e^{al} \ , \tag{3.19}$$

where a is the Townsend coefficient (mean free path of an electron between two ionizations) and l is the length of the amplification region.

The Townsend coefficient can be expressed by the Rose and Kroff formula:

$$a = PAe^{-BP/E} \ , \tag{3.20}$$

where P is the pressure and A and B parameters of the gas mixture.

E is the electric field of the amplification region:

$$E = \frac{V}{l} \ . \tag{3.21}$$

Substituting eq. (3.20) and (3.21) to (3.19), results to:

$$G = e^{APle^{-BPl/V}} \ . \tag{3.22}$$

From eq. (3.22) it is evident that the gain, G, is dependent on the term Pl. For a constant pressure P, G increases when l is increasing, reaches a maximum and then decreases again, for higher values of l, as seen in Figure 3.7. The maximum value can be obtained by differentiation of eq. (3.22) and it is for $l = V/B$. The dependence of the gain from the mesh voltage for different gas mixtures in a microbulk Micromegas is shown in Figure 3.8 [81].

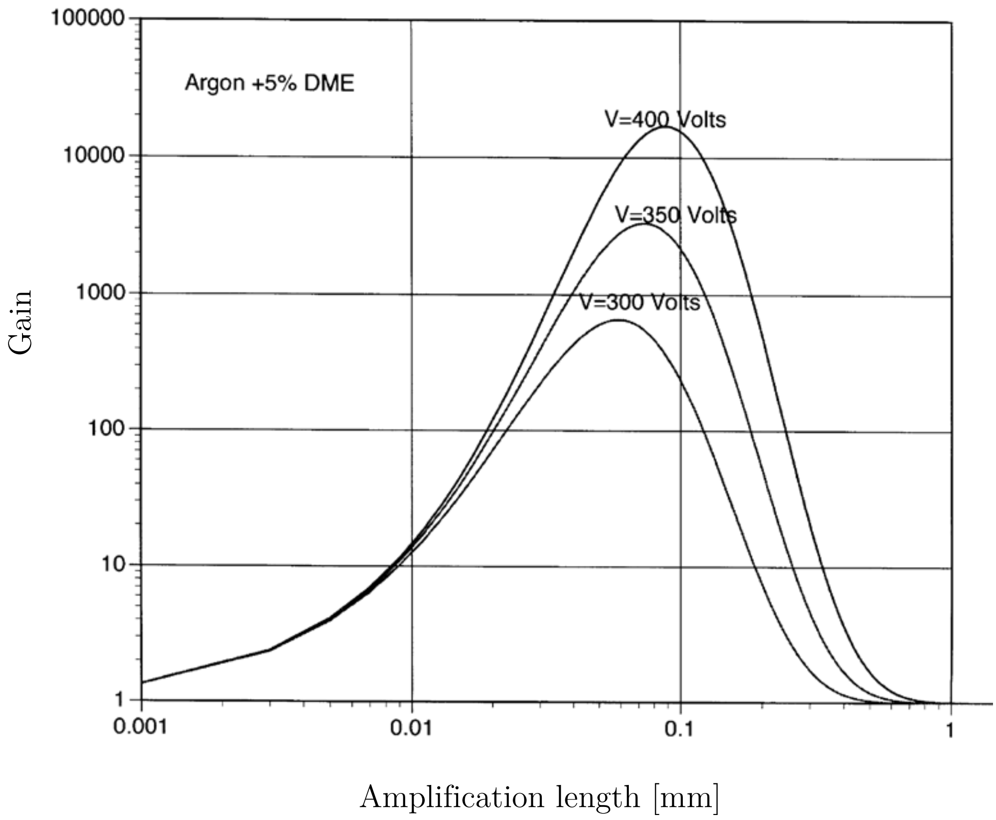

Figure 3.7: The gain as a function of the amplification length for a given gas mixture of argon+5%DME, at a pressure of 1 bar. Extracted from [80].

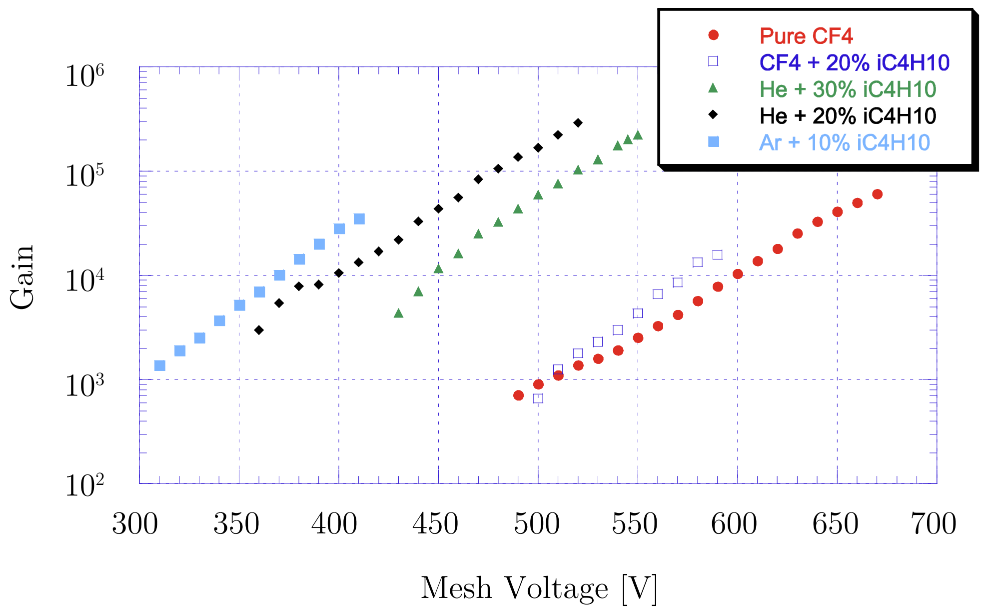

Figure 3.8: The measured gain as a function of the mesh voltage (HV2), for various gas mixtures.

3.5.1.2 Energy resolution

In the ideal case the energy resolution of a gaseous detector depends only on the fluctuations of the number of the primary and avalanche electrons. In reality a number of other parameters can contribute to the shape and resolution of the pulse. Such parameters in a Micromegas detector are impurities in the gas, non-uniformity of the amplification field due to considerable distortions in the mesh foil, the electric field ratio $\rho = E_\alpha / E_d$, which influences the mesh transparency to electrons, and the gain (because of statistical fluctuations in the multiplication process, the energy resolution is degrading with the increase of gain).

In Figure 3.9 [81] a typical dependency of the energy resolution with the field ratio ρ is shown. The result was obtained with a gas mixture of argon with 10% isobutane, using an ^{55}Fe source that emits two photons of energies 5.9 keV and 6.5 keV in a ratio of 8.5:1. The dependency has the same behavior for all gas mixtures, with the resolution rapidly decreasing to a minimum and then slowly increasing for higher values of ρ. Of course the minimum resolution achieved and the field ratio ρ for different detector configurations may differ considerably.

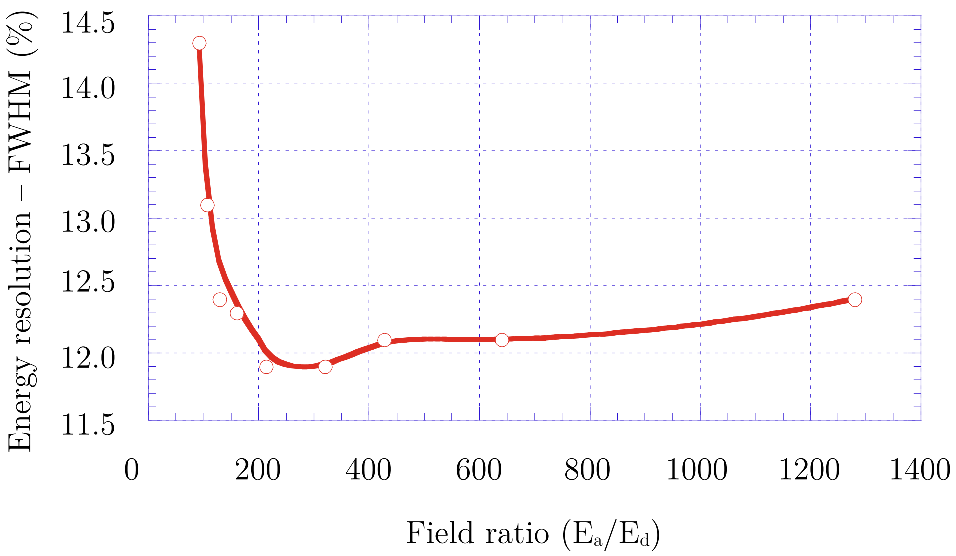

Figure 3.9: Energy resolution as a function of the field ratio ρ. The optimum resolution is obtained for 200< ρ <300.

3.5.1.3 Spatial resolution

The spatial resolution is independent of the gain of the chamber but the spread of the electrons is observed mainly due to the transverse diffusion, which depends also on the amplification gap and the diffusion coefficient of the gas mixture used. Several tests with different detector configurations have been performed. Their results are summarized in Table 3.2. The best value achieved was a spatial resolution of 11 μm, for a detector with a strip pitch of 100 μm, and a gas mixture of CF_4 with 20% isobutane [82].

Gas Mixture	Resolution [μm]	Pitch [μm]	Drift field [kV/cm]
Ar+10% iC_4H_{10}	42.5	100	1.0
He+6% iC_4H_{10}+5% CF_4	35	100	1.8
He+10% iC_4H_{10}+5% CF_4	30	100	1.8
He+20%DME	25	50	1.0
CF_4+20% iC_4H_{10}	18	100	0.4
CF_4+20% iC_4H_{10}	11	100	2.7

Table 3.2: Summary of spatial resolution tests performed with different configurations of the Micromegas detector.

3.5.1.4 Rate capability with X-rays

The small amplification gap of the Micromegas, results in a fast evacuation of the slow moving ions, in less than 100 ns. Therefore the Micromegas detectors have a very high rate capability. A detailed study for various mixtures and varius fluxes is presented in [83]. The highest rate observed without saturation of the gain was 10^5 Hz mm^{-2}. Systematic studies have shown though that the maximum achievable gain decreases with the flux. For fluxes of X-rays of 8 keV of the order of 10^7 Hz mm^{-2}, the maximum gas gain achieved is higher than 10^3, which still allows a full detection efficiency.

3.5.1.5 Radiation Resistance

The Micromegas detector as a parallel plate detector, exhibits a high radiation resistance. The creation of organic polymers in the anode, in high irradiation evironments, has little effect on the performance of the detector. The radiation resistance of the detector has been measured in [83]. With a gas mixture of argon and 6% isobutane, the gain of the detector remained stable for a total accumulated charge up to 18.3 mC/mm^2.

3.5.2 Fabrication and evolution

The Micromegas technology has many applications in particle and X-ray physics. An extensive review will be presented for the use of the Micromegas detectors in the CAST experiment, for detecting X-rays.

Since the start of data taking, in 2002, the COMPASS experiment makes use of large 40×40 cm^2 Micromegas detectors for tracking close to the beam line with particle rates of 25 kHz/mm^2. In T2K, Micromegas detectors of bulk technology are used as amplification devices in time projection chambers. The NA48 experiment at CERN is using Micromegas detectors for the charged kaon upstream spectrometer consisting of three stations of Micromegas coupled to a time projection chamber.

The request for better performing, more stable detectors that are simple to manufacture in big surfaces, resulted in the development of two advanced techniques. The new detector types were called bulk-Micromegas [84] and microbulk-Micromegas [85].

3.5.2.1 Bulk Micromegas

In the development of the bulk Micromegas, a woven wire mesh of 30 μm was used, instead of the electroformed micromesh of the conventional technology Micromegas. The manufacturing procedure developed was simple, relying in well-known technology and techniques.

The base material consists of an insulating material (i.e. FR4), which carries a Copper plane – the strips. A photoresistive film (Vacrel) of 128 μm thickness, and the woven wire mesh are all laminated together, at high temperatures, becoming a single unit. With a photolithographic process, the photoresistive material is etched, leaving the pillars. The whole process is shown in Figure 3.10.

The bulk Micromegas detector has an easily achievable, good resolution (~14% FWHM for the 5.9 keV peak of ^{55}Fe), which is limited by the thickness of the mesh. It is also uniform and robust, with easy manufacturing process and it has low noise due to its lower capacitance with respect to the conventional technology Micromegas.

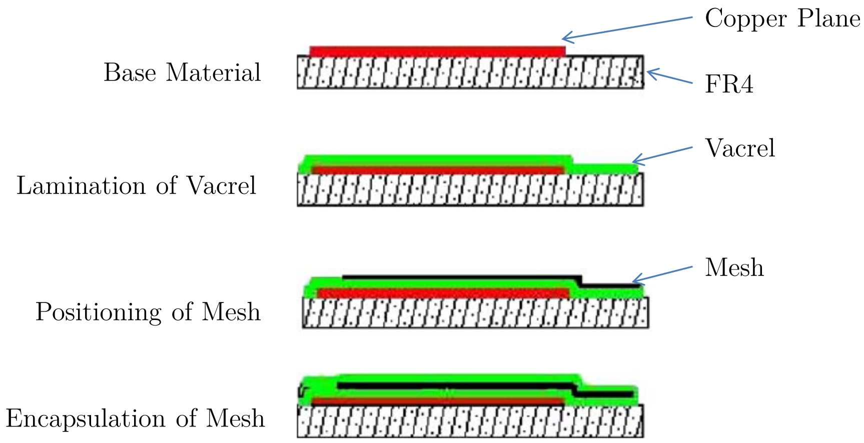

Figure 3.10 : The fabrication process of a bulk Micromegas detector.

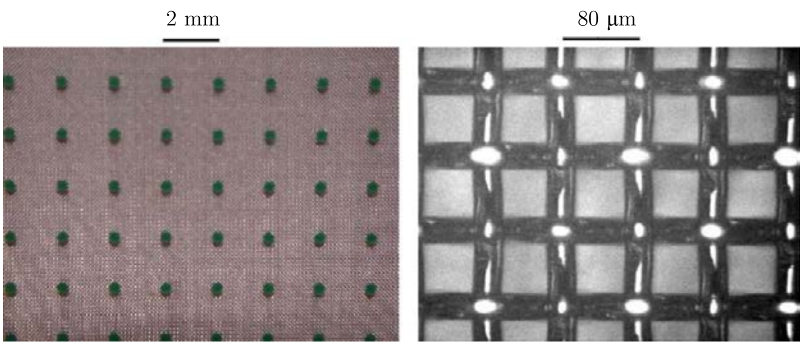

Figure 3.11: The cylindrical pillars have a diameter of 300 µm and a distance of 2 mm with each other (left). A detail of the woven mesh (right).

3.5.2.2 *Microbulk Micromegas*

The new process developed involves high accuracy photo-chemical and photo-lithography techniques on copper-clad kapton foils. It was inspired by the GEM detector fabrication process [77].

In this process a mask is created using a thin photoresistive film. This mask is put on top of the copper clad kapton foil, and the copper is then removed by a standard lithographic process, producing the pattern of the thin mesh.

The microstructure is usually glued to a substrate, providing support and rigidity and the read out plane of the strips. The kapton is then etched and partially removed in order to create tiny pillars in the shadow part below the copper mesh. The result is shown in Figure 3.12.

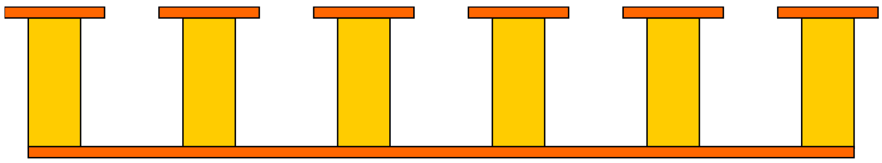

Figure 3.12: The pillars are created in the shadow of the mesh with standard etching technology.

3.6 Background and shielding

3.6.1 Sources of background

Since the magnitude of the background determines the minimum detectable radiation level, the knowledge of its origin is crucial. The sources of background can be grouped in five categories:

- *Radiation of construction materials and the activity of the earth's surface,*
- *radioactivity of the detector materials,*
- *radioactivity from the air surrounding the detector and the ventilation of the facility,*
- *cosmic radiation,*
- *radioactivity of the surrounding materials, in the vicinity of the detector, such as pipes, shielding etc.*

The radioactivity of the Earth and the construction materials is due to low concentrations of naturally radioactive elements. The most important components are potassium, thorium, uranium and the products of their decay chains. Potassium contains 0.012% ^{40}K which decays in ^{40}Ca by β-emission with 1.31 MeV energy (89 % yield) and in ^{40}Ar by emitting a γ-ray of 1.46 MeV (11%). This process has a half-life of 1.26×10^{9} yr. Thorium uranium and radium are members of a long decay chain that emits a spectrum of α, β, and γ rays. These materials can be found as impurities in the construction materials of the detector as well. Electrolytically prepared copper, magnesium and stainless steel show low levels of background. The electrical soldering in the electronics and some circuit board materials can be high in radioactivity, so attention has to be given either to minimize the use of these materials or that they are outside the shielding of the detector.

A measurable amount of radiation can be found in the ambient air surrounding the detector either in the form of radioactive gases or from the airborne dust. ^{222}Rn (with half-life 3.825 yr) and ^{220}Rn (with half-life 55.6 s) are short lived radioactive gas products of the decay chains of uranium and thorium. In order to reduce the effect of the airborne radioactivity the area surrounding the detector has to be air tight and flushed with a clean gas such as nitrogen.

Another source of background comes from the secondary cosmic radiation, like pions, muons, electrons, protons, neutrons and photons with a large band of energies. At sea level, muons constitute 80% of the flux of cosmic radiation with a rate of 1 muon/cm^2/min.

The secondary particles from the cosmic radiation can interact with the materials surrounding the detector, such as metallic pipes and shielding that have high atomic number materials and produce high energy electrons and γ-rays. Neutrons can also create γ-rays when absorbed by high atomic number materials.

3.6.2 Passive shielding of detectors for low energy X-ray detection

The most common material used for detector shielding is lead, because of its high density and atomic number. It can absorb high energy gammas from the cosmic background. There is an optimum thickness that has to be used, depending on the application, to avoid the secondary radiation from the interaction of the cosmic radiation with the lead itself. It can generate 77 keV and 170 keV fluorescent X-rays generated by photoelectric absorption of γ-rays. Furthermore ordinary lead has natural radioactivity from contaminants. A recently produced lead can contain significant amounts of ^{210}Pb, a product of the decay chain of ^{226}Ra with a half-life of 22.2 yr. For low background applications lead that is recovered from very old sources should be used. In some cases where the use of lead has to be limited due to restrictions in cost or weight, steel is a good compromise. Tungsten can also be a good candidate with its high atomic number and density. Although it is difficult to machine, special techniques or alloys of tungsten with nickel and iron or copper can be used.

To reduce the effect of the production of X-rays from the interaction of cosmic rays with the high atomic number materials of the shielding they have to be used with an inner low atomic number material to absorb the secondary radiation. Few mm of copper or cadmium are usually enough.

A measurable neutron component can be found in the cosmic radiation at sea level and low background X-ray detectors can be influenced by a fast neutron background. The principle of neutron shielding is to quickly reduce their energy and then absorb the thermalized neutrons with materials with high absorption cross sections. The most effective materials for reducing the energy of the neutrons are the ones with low atomic numbers, containing hydrogen, like water paraffin and polyethylene. The second material that will absorb the thermal neutrons can be either mixed with the above materials or placed below them as an absorbing layer. Cadmium is the most commonly used material, because a thin layer of 0.5 mm is enough due to its very high absorption cross section.

3.7 Micromegas detectors in CAST

3.7.1 Evolution

Throughout the running periods of CAST all Micromegas technologies have been used. In the start of the data taking of CAST Phase I in 2003 and in the CAST Phase II ^{4}He run in 2005, 2006, a conventional technology Micromegas was used in the sunrise side.

In the shutdown of 2007, for the CAST Phase II ^{3}He phase, a complete redesign of the detector lines of the experiment was performed, which brought bulk and microbulk Micromegas detectors in three out of four ends of the cold bores.

The Microbulk detectors are the best choice for the CAST experimental conditions. Their low material, high radiopurity and better energy resolution makes them suitable for rare event detection experiments such as CAST. They combine all the advantages of the bulk detectors with enhanced performance, uniformity and stability. CAST Microbulk detectors have reached energy resolution of less than 12% FWHM, whereas bulk detectors cannot reach values better than 14% FWHM. Since 2008 three out of four detector lines of the experiment are occupied with microbulk detectors.

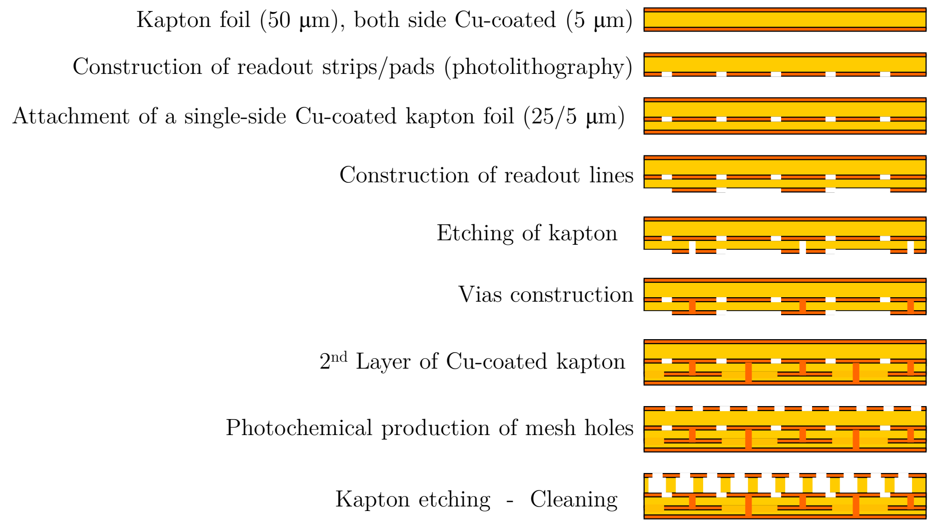

Figure 3.13: Construction process of a CAST Microbulk detector

3.7.2 Microbulk detectors in CAST

The Microbulk detectors for CAST have a construction process which is shown in Figure 3.13 [85]. The anode has a 2D readout scheme, with the strips interconnected diagonally through vias, in one or two extra layers, as seen in Figure 3.14. The strip pitch is 350 μm and the spatial resolution, due to diffusion, is better than 100 μm. Each detector has 192 X and 192 Y strips, making up an active area of about 45 cm^2.

Special care has been taken in the materials used in the construction of the detector, in order to minimize its internal radioactivity. The drift chamber, which defines the drift region of 2.5 to 3 cm and the supporting plane of the detector are made out of plexiglas, the weldings inside the detector are made with low radioactive soldering and the readout plane is made out of kapton. The detector is coupled with the vacuum line of the magnet with an aluminised mylar ($C_{10}H_8O_4$) window of 5 μm with an aluminium strong back, seen in Figure 3.15.

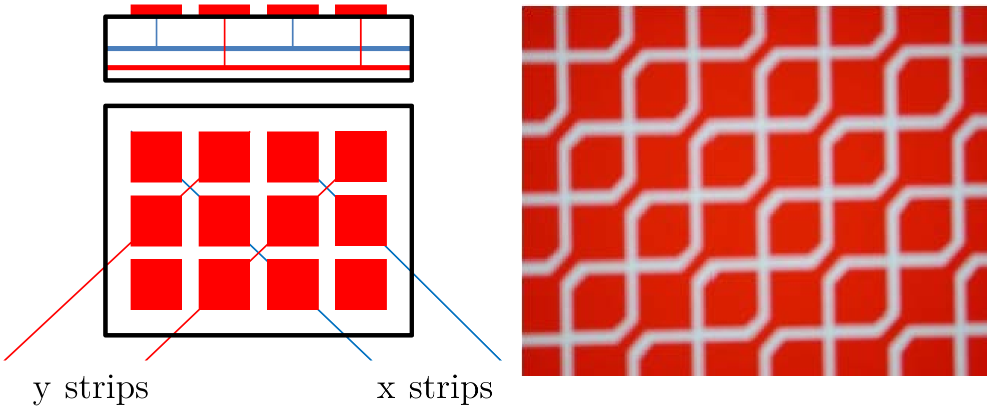

Figure 3.14 Schematic drawing of the connection of the strips with two layers of vias (left), and with one direction connected already on the strip plane (right).

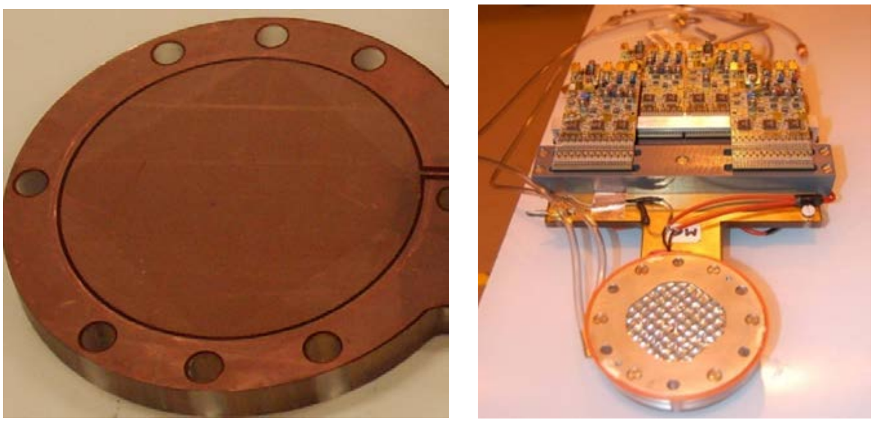

Figure 3.15: Left: A zoomed picture of the mesh of the CAST Micromegas detector. Right: A picture of the detector with its front end cards. The aluminised mylar drift window is covering the active area of the detector.

3.7.3 Sunrise Micromegas line

During the shutdown of 2007, the Micromegas line of the sunrise side was completely redesigned [86]. The new line was previewed to integrate X-ray optics (which was finally not implemented). The key novelties were better vacuum performance, the addition of control systems to monitor key parameters of the detector (such as vacuum pressure, detector pressure and gas flow), enough space for passive shielding and an in-line automated calibration system. A design of the sunrise line is displayed in Figure 3.16.

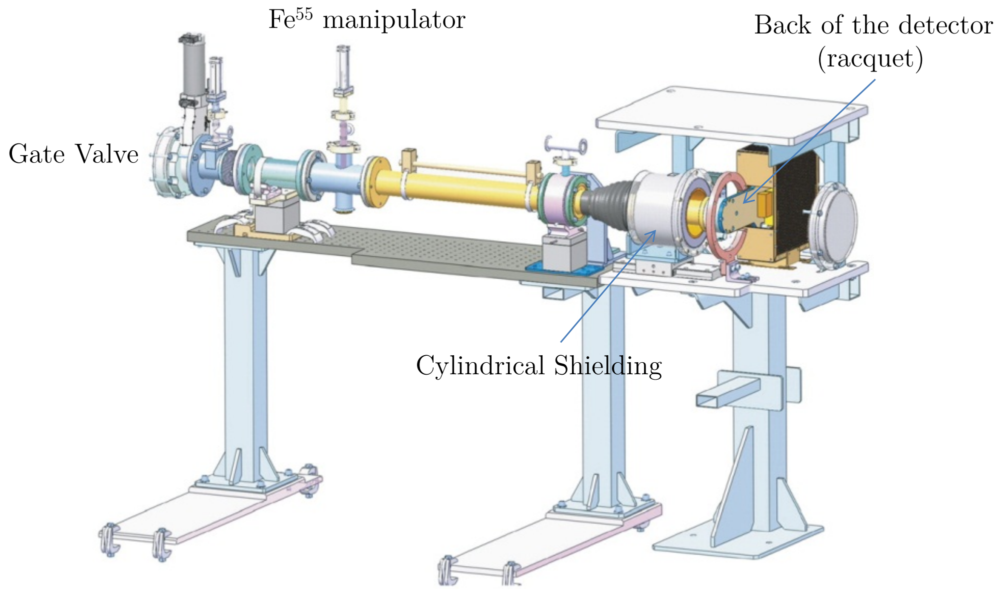

Figure 3.16: Illustration of the sunrise Micromegas line.

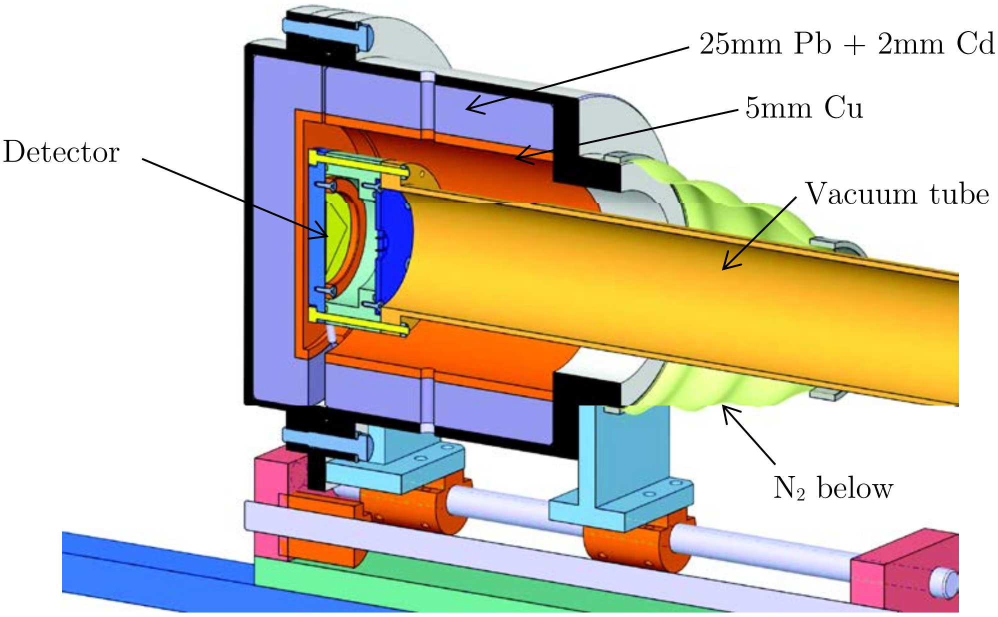

Figure 3.17: A section of the multi-layer passive shielding of the sunrise detector.

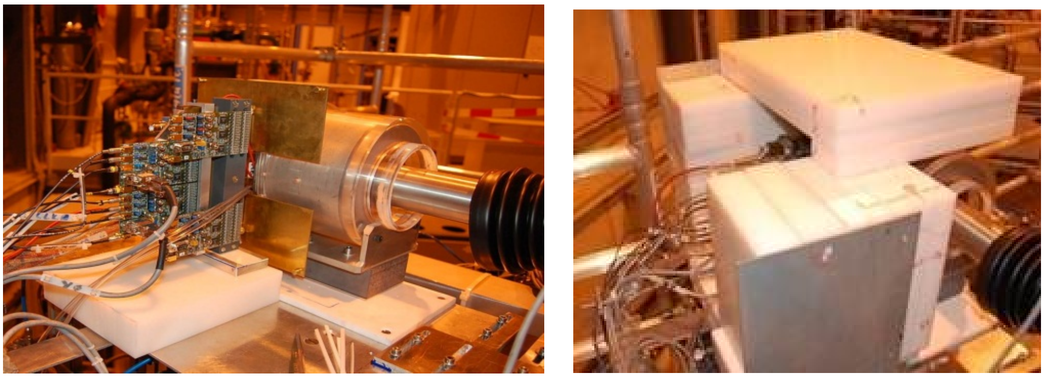

Figure 3.18: The sunrise Micromegas detector placed in line. On the left the cylindrical shielding is visible, surrounding the detector. On the right the polyethylene blocks are in place, covering the maximum solid angle possible, taking into account the space limitations.

3.7.3.1 Passive shielding

The passive shielding implemented in the sunrise Micromegas line is attempting to reduce environmental radiation, like gammas and neutrons. It is a multilayer cylinder which surrounds the detector and consists (from outer to inner radius) of 2 mm cadmium foil, to absorb thermal neutrons, 25 mm archaeological lead and 5 mm copper, which also acts as a Faraday cage. The cylinder is covered with polyethylene blocks of thickness up to 25 cm, to thermalize neutrons, with dimensions limited by space constraints.The space between the detector and the shielding is flushed with Nitrogen, to reduce the concentration of air, thus reducing Radon radioactivity. The front-end electronics are placed outside the shielding in a Faraday cage.

A section of the multilayer passive shielding is shown in Figure 3.17 and two pictures of it, with and without the polyethylene blocks installed is shown in Figure 3.18.

3.7.3.2 Calibration source and source manipulator

The daily calibrations of the detector are performed using an ^{55}Fe source. The isotope decays to ^{55}Mn (Manganese-55) by electron capture. The ^{55}Mn then emits fluorescence photons of 5.9 keV (K_α) and 6.49 keV (K_β) with a ratio of 8.5:1. This decay has a half-life of 2.73 years.

The ^{55}Fe source resides in a mechanical manipulator which is placed in the CAST vacuum line, in front of the detector at a distance of 1.1 m, to ensure uniform illumination of its full area. The manipulator can be operated manually or automatically by the acquisition software.

The position of the source is monitored by using two position sensors integrated in the Micromegas acquisition system. The two possible positions of the source are the "garage" and "calibration". When the source position is set to "garage" the manipulator moves the source upwards, outside the field of view of the detector. When the source is set to "calibration" position the manipulator moves the source approximately 10 cm down placing it in front of the detector and illuminating it. A picture of the source manipulator is shown in Figure 3.19 [87].

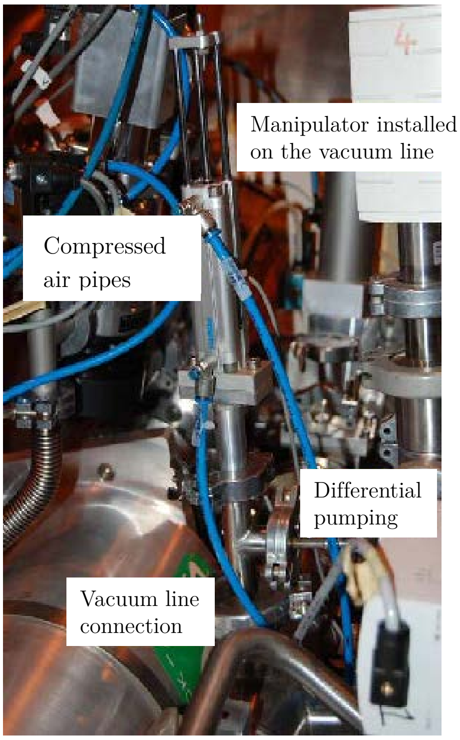

Figure 3.19: The ^{55}Fe source manipulator in the sunrise Micromegas line

3.7.3.3 Gas system

The choice of gas

The gas mixture of choice for the sunrise Micromegas detector is argon with 2.3% isobutane as a quencher. X-rays, in the energy range of 2 to 7 keV will interact with argon mainly with the photo-electric effect. Argon and argon based mixtures have the highest conversion probability amongst the noble gases having a mean free path of 2.7 cm for X-rays of 7 keV and pressure of 1.4 bar. This makes it ideal for use in the Micromegas detectors of CAST which have a drift region of 3 cm. The specific gas mixture also fulfils the requirements for low working voltage, high gain, good proportionality, low cost and non-flammability.

^{55}Fe energy spectrum

X-rays coming from an ^{55}Fe source into the argon filled chamber will interact with electrons in the K_α shell via the photo-electric effect. In about 15% of the cases the photoelectric absorption is followed by the emission of a secondary photon. This photon, having energy slightly lower than the K-edge, has a very long mean free path, thus a high probability of escaping the chamber. The total energy deposited is about 2.9 keV and corresponds to the characteristic escape peak of argon. In the rest of the cases the photoelectron emission is followed by Auger cascades with total energy deposits of about 5.9 keV. This line is the photo-peak of argon. Figure 3.20 shows the typical form of an ^{55}Fe energy spectrum recorded with a microbulk Micromegas, filled with a mixture of argon-2.3% isobutane.

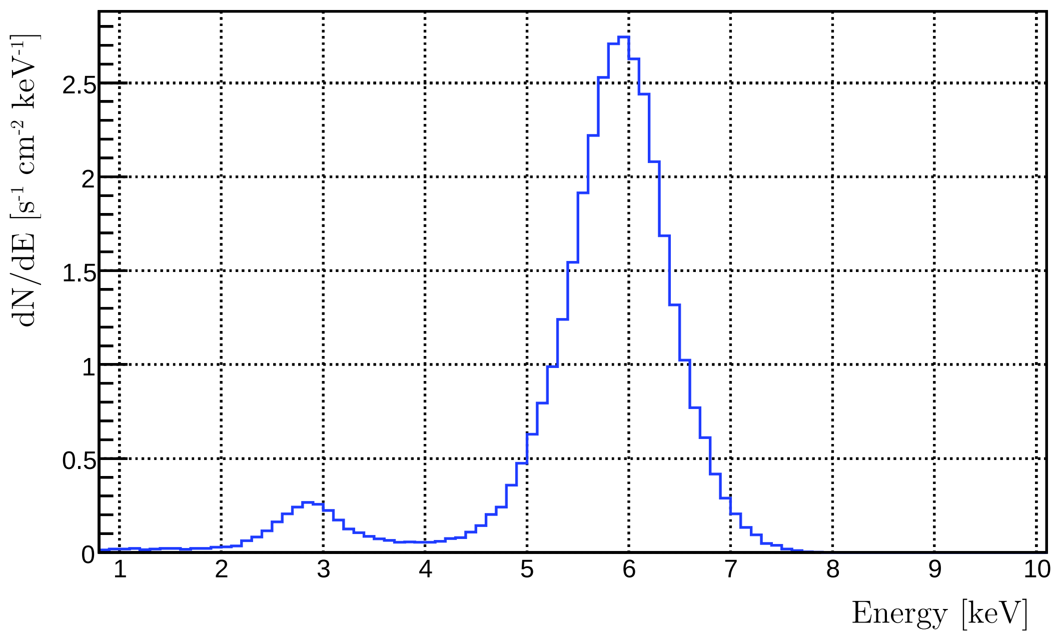

Figure 3.20: Energy spectrum of a calibration run with an ^{55}Fe source. The various emission lines are merged to two main distributions at 2.9 and 5.9 keV.

Setup

The gas system of the sunrise Micromegas was designed to keep a constant pressure of the gas inside the detector chamber. For this reason an MKS mass flow controller was installed in order to maintain the pressure constant at 1.43 bar. The over pressure diminishes the possibility of contamination of the gas and helps achieve higher multiplication values and lower mean free path in comparison with operation in atmospheric pressure.

3.7.3.4 Pumping system

To minimize the danger of a leak from the Micromegas detector to the CAST vacuum, a differential pumping system was realised. A simplified diagram is shown in Figure 3.21. An intermediate volume (detector vacuum) is created, with the use of a 4 µm polypropylene $(C_3H_6)_x$ window, which is constantly pumped and separates the two systems.

The pumping group consists of one primary pump, assisted by two turbo molecular pumps. These pumps, together with the sunrise line vacuum can be isolated through two manual valves for long periods of shut down. A normally open electro-valve is connecting the detector vacuum with the CAST general vacuum. The electro valve is connected to an interlock; when the pressure difference between the two vacuums (detector and CAST general) becomes higher than a predefined value (0.1 mbar), the electro-valve opens, to avoid breaking the differential window. In this case the gate valve VT3 closes, to protect the rest of the vacuum systems from potential contamination.

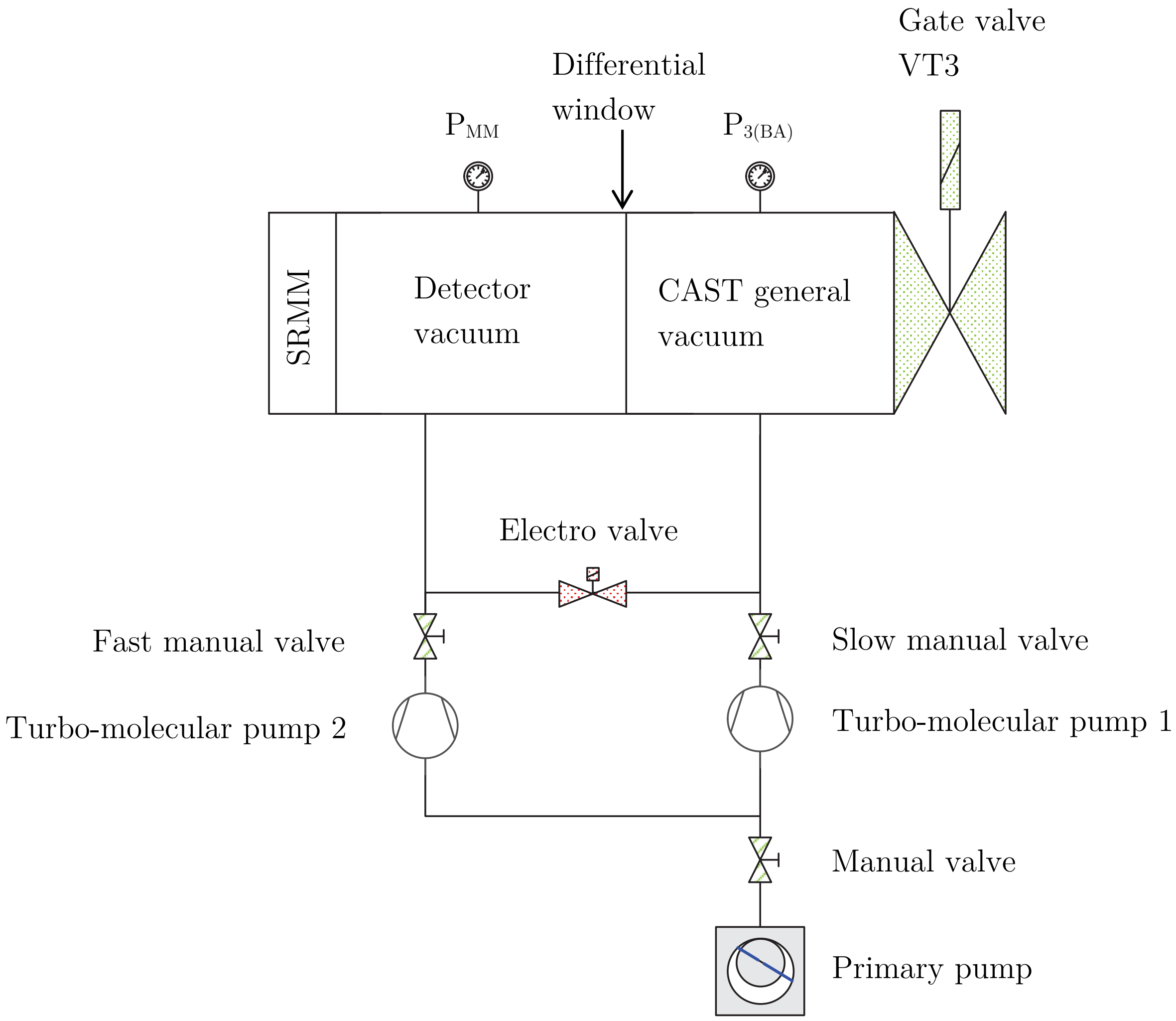

Figure 3.21: A simplified sketch of the sunrise Micromegas vacuum system. The valves denoted with green are open during data taking and the ones with red, closed. The detector vacuum is monitored by the P_{MM} sensor and the CAST general vacuum, by $P_{3(BA)}$.

3.7.4 Sunset Micromegas line

The sunset line incorporates two Micromegas detectors. The detector system, seen in Figure 3.22, includes two Faraday cages that completely cover the detectors and their electronics. The calibration of the detectors is done with an automated calibration system with an ^{55}Fe source, from the back of the detectors, in an area were the thickness of the supporting material (plexiglass) is reduced to allow the X-rays to reach the volume of the detectors.

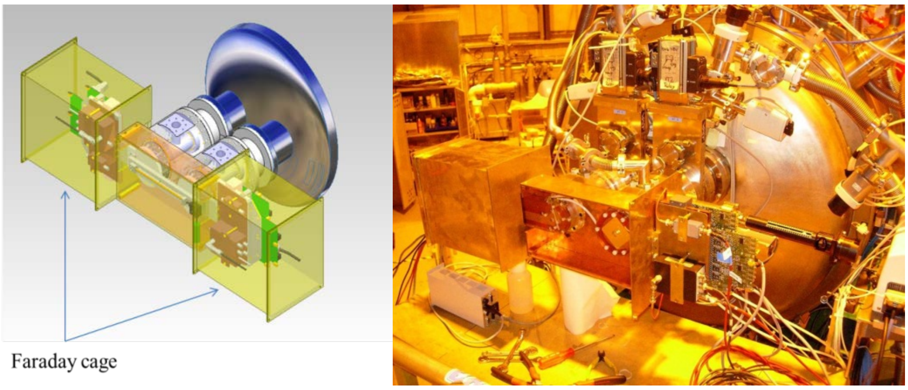

Figure 3.22 (Left) A schematic view of the sunset detector lines. (Right) a picture of the Sunset detector line. The one detector is seen without the Faraday cage installed.

3.7.5 Efficiency of the CAST Micromegas line in X-rays

The Micromegas detectors and the detector lines in CAST have been designed and optimized for the efficient detection of X-rays, in the range from 2 to 7 keV. In order to couple a gaseous detector with the vacuum of the magnet side, the solution of two differential windows was adopted [88].

These two windows separate the line in three zones, as seen in Figure 3.23. Zone A corresponds to the detector, with pressure 1 to 1.4 bar, zone B is a closed volume with a pumping system and has a pressure of the order of 10^{-4} mbar and zone C is the vacuum tube of the detector line, with typical pressure of 10^{-7} mbar. The pressure difference of Zone A and B, imposes the use of a strong back to strengthen the detector window. Therefore an aluminised mylar window is used (5 μm), with an aluminium strongback. The strongback has 94.6% transparency in X-rays with energies between 2 and 10 keV.

The total efficiency of the detector, the contributions of the materials of all the windows, the gas mixture absorption and the dimensions of the detector, have been simulated using GEANT4 [89]. The results are summarized in Table 3.3, for the energy range of interest.

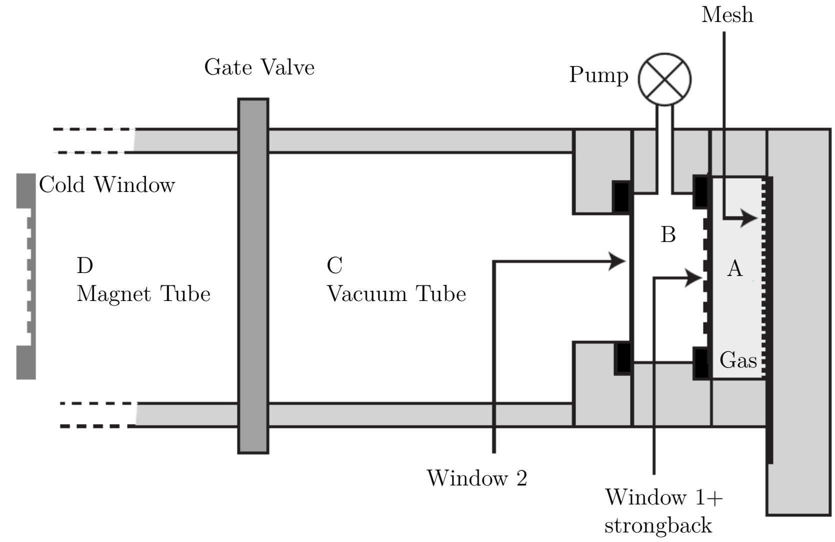

Figure 3.23: Schematic view of the Micromegas line in CAST

Detector efficiency (gas absorption+ drift window)	75 %
+ differential window (4 µm polypropylene)	74 %
+ cold window (15 µm polypropylene)	60 %

Table 3.3 The overall efficiency in the detection of X-rays in the range of 2-7 keV for 1.4 bar, in the Micromegas line of CAST, for gas mixture of argon-isobutane 2.3 of 1.4 bar.

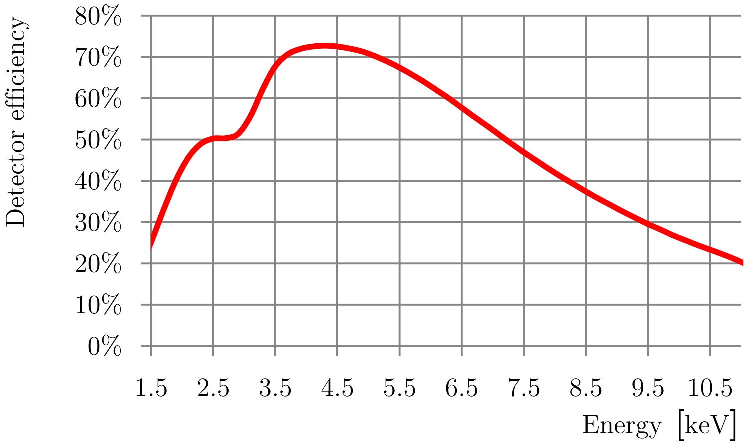

Figure 3.24: The simulated efficiency of the Micromegas detector, taking into account the contributions of all the elements across the CAST line.

3.7.6 Read out electronics

3.7.6.1 Strips signal

The signal collected from the strips, consists of the electrons of the avalanche in the amplification region. It is integrated and stored by four front-end electronics cards, based on the Gassiplex chip [90]. Each card has 6 Gassiplex chips, with 16 channels each. The total of 96 channels, are connected to 96 strips, each channel corresponding to a single strip, and can be read with a maximum clock speed of 1 MHz. The cards are powered by a standard 6 V power supply (positive and negative). The Gassiplex card is shown in Figure 3.25.

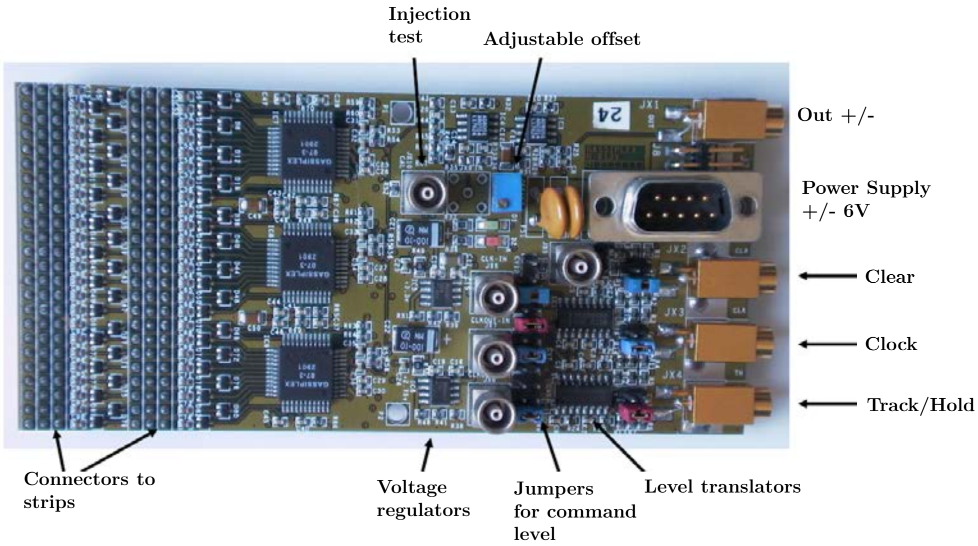

Figure 3.25: The Gassiplex card used in the Micromegas detectors of CAST.

All four Gassiplex cards are controlled by a sequencer (CAEN V551B) with two CRAMs (CAEN V550) housed in a VME crate. The sequencer provides the timing signals (Track/Hold, Clock and Clear). The Track/Hold pauses the acquisition of the card, latching in its memory the signal from the strip charge. Each time a Clock signal is sent one channel of the card is read.

The output of the Gassiplex is a multiplexed, multilevel voltage signal, and each level corresponds to a signal from a particular strip. The signal can be positive or negative, depending on which output of the card is connected. When all 96 Clock signals have been read by the CRAMs, the Sequencer sends the Clear signal, which resets the memory of the Gassiplex card. The sequence of the readout signals is shown in Figure 3.26:. The CRAMs digitise and store the acquired signal from each Gassiplex card (two Gassiplex cards are read from one CRAM module), until the VME crate reads it and sends it to the PC. The trigger for the Track/Hold signal of the Sequencer comes from the Mesh signal, after it is shaped and amplified, so as to produce an appropriate trigger.

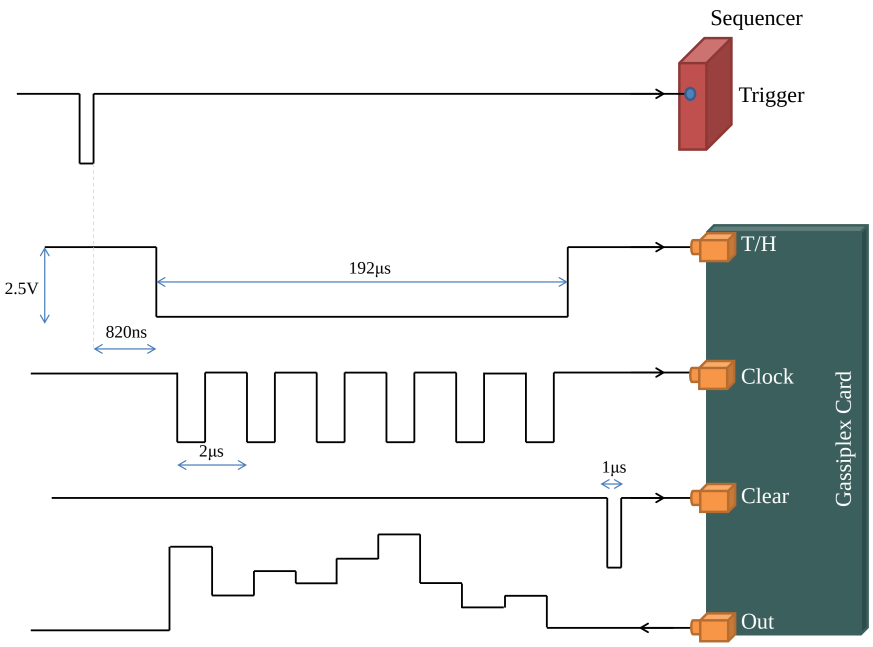

Figure 3.26: The sequence of signals that trigger the acquisition of the Gassiplex card.

3.7.6.2 Mesh signal

The signal from the Mesh is produced by positive ions, created in the amplification region. It is preamplified via a Camberra 2004 preamplifier and then it is amplified and shaped from an Ortec 474 Timing Filter Amplifier – Shaper. With a Linear Fan In/Out, the signal is split in two. One passes through a discriminator (LeCroy Model 821C), to provide a digital trigger. If the pulse exceeds a previously set threshold (set to be above the electronic noise), a trigger pulse is created and sent to the Gassiplex cards. The other is recorded through a high rate sampling VME digitizing board, the MATACQ (Matrix for ACQuisition) [91], which stores the timing information of the mesh pulse. A flow diagram of the signal propagation in the sunrise Micromegas detector is shown in Figure 3.27.

Both signals from the mesh and the strips are acquired and stored in less than 20 ms. During the acquisition process the system cannot detect any signal because all the modules are receiving a veto. This is the dead time of the particular configuration. Due to the fact that the normal trigger rate of a background run is of the order of 1 Hz, it is evident that the total loss of signal is less than 2%.

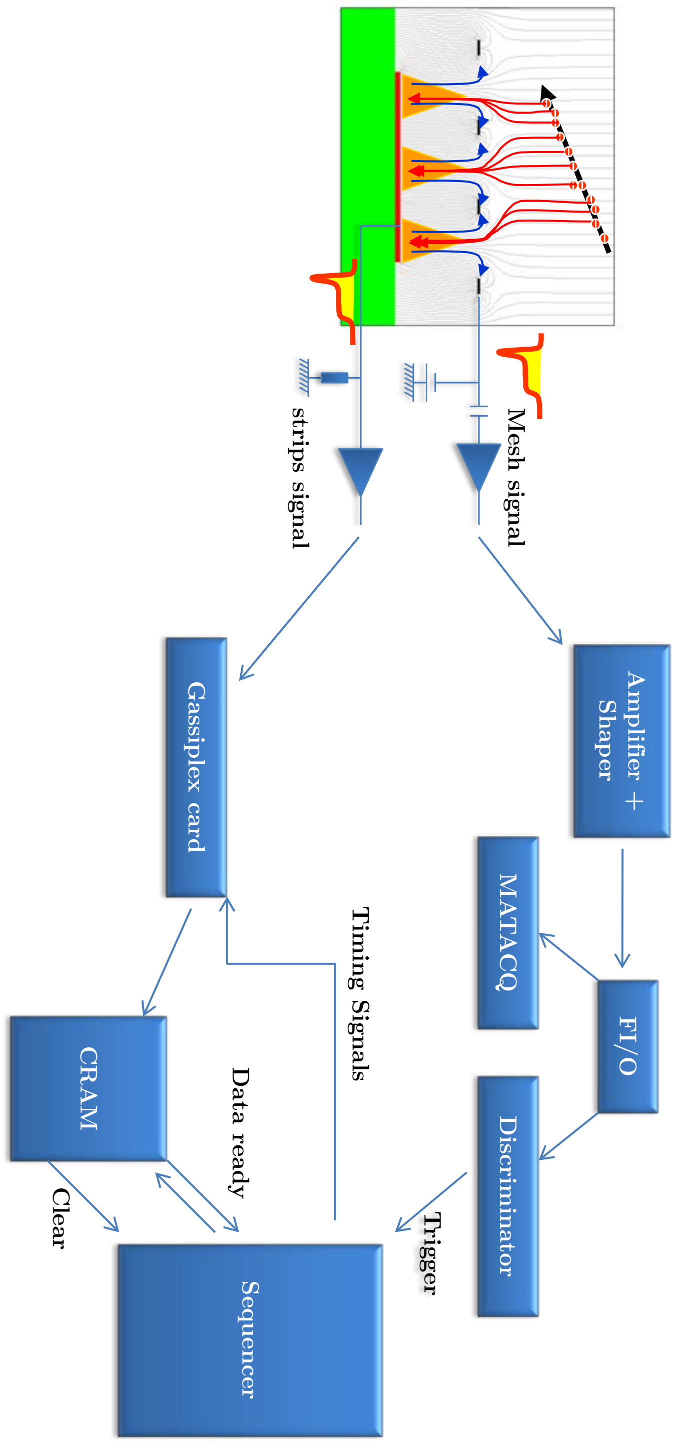

Figure 3.27: The trigger and readout layout of the Micromegas detectors in CAST.

3.7.7 Data acquisition

The connection of the modules with the data acquisition PC is done via a VME controller (NI VME-MXI2) and a bus card to the PC (NI PCI-MXI2). The data acquisition software running on the PC is based on the Labview system design software, by National Instruments. The operating system of choice is Scientific Linux (CERN distribution), with large capabilities of communication protocols, timing and synchronization. The data acquired, are uploaded in a daily basis to CASTOR (CERN Advanced STORage manager) in form of binary files, for safety and backup via a routine program (mMmonitord) which is constantly running in the background. The maximum acquisition rate of the sunrise data acquisition setup is 60 Hz. The whole configuration was originally installed in 2002 [92].

A friendly graphic environment allows the operator to control the data acquisition and view the mesh and strip pulses in real time. Its main virtual instruments (VIs) are:

RunControlAll.vi
It enables the user to start and stop the application, define the type of run (Pedestal, Calibration or Background) and select to display or not the real time monitoring VIs, RunMon.vi and RunEvd.vi (Figure 3.28, left).

RunControlMonitor.vi
In this VI the user can view crucial parameters of the current run like the number of events recorded, the trigger rate of the data acquisition system (number of signals above a set threshold) and the counter rate (the number of total events detected). The user can also get information such as the name and the start date of the run, (Figure 3.28, right).

RunEvD.vi
It displays one out of ten events that have triggered the DAQ. Valuable information can be extracted regarding the performance of the strips or the gassiplex cards, electronic noise in the data acquisition modules or even sparks that occur in the detector, (Figure 3.29).

RunMon.vi
It provides a quick spectroscopy outlook of the current run. It displays the FADC energy spectrum of the current run, a history of the trigger rate and real time plots of the Multiplicities and X-Y distributions of the actual run, (Figure 3.30).

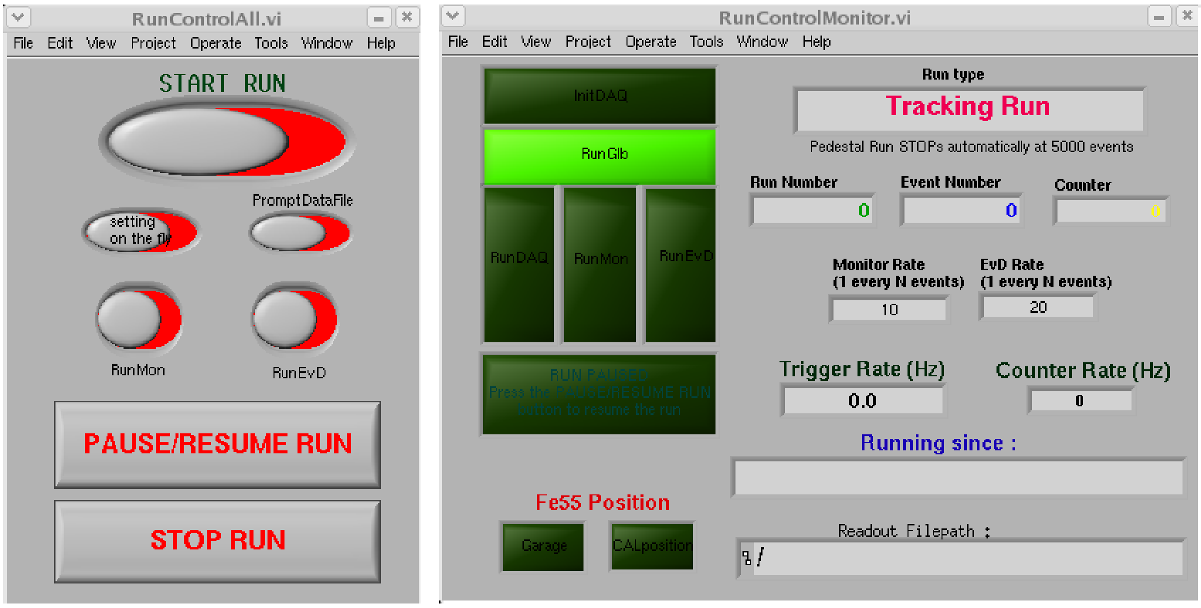

Figure 3.28: The main graphics interface of the sunrise DAQ system constitutes from the RunControlAll.vi (left) and the RunControlMonitor.vi (right). They provide full control and information for the current run.

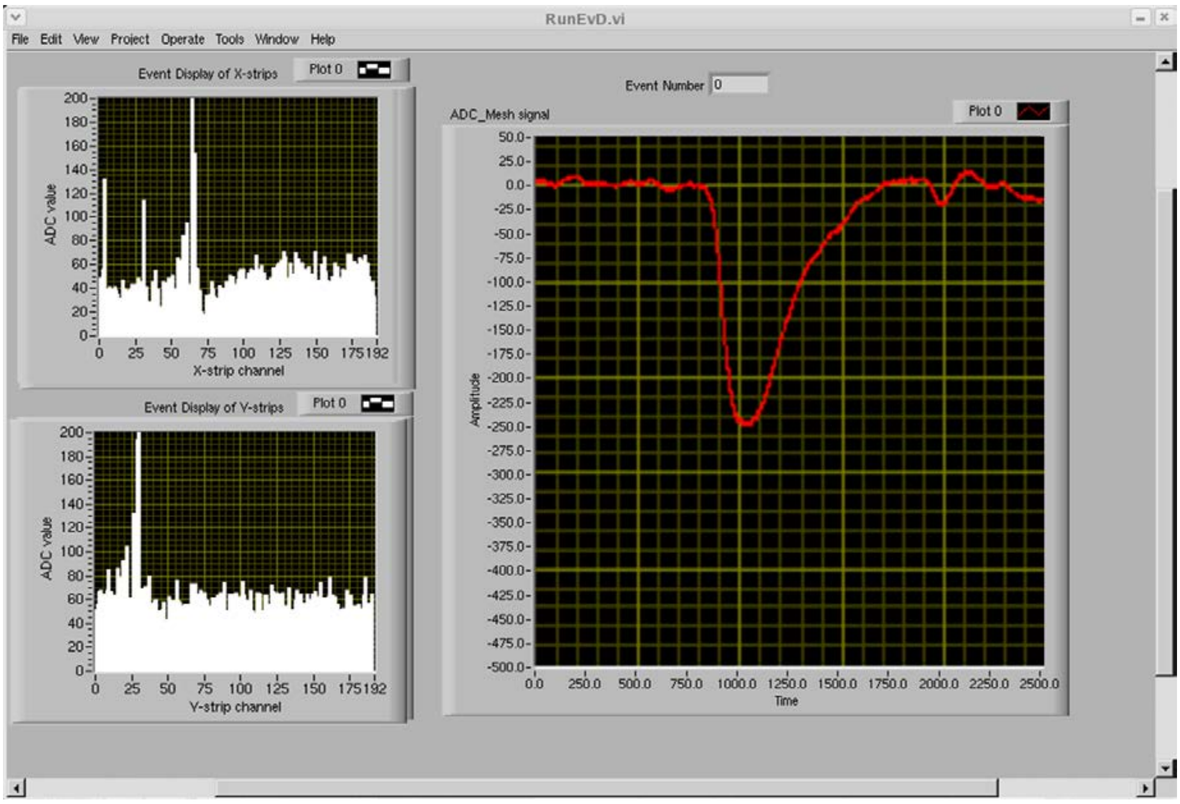

Figure 3.29: The RunEvD.vi displays the charge of the X and Y strips and the Mesh signal in real time, refreshing every 10 events.

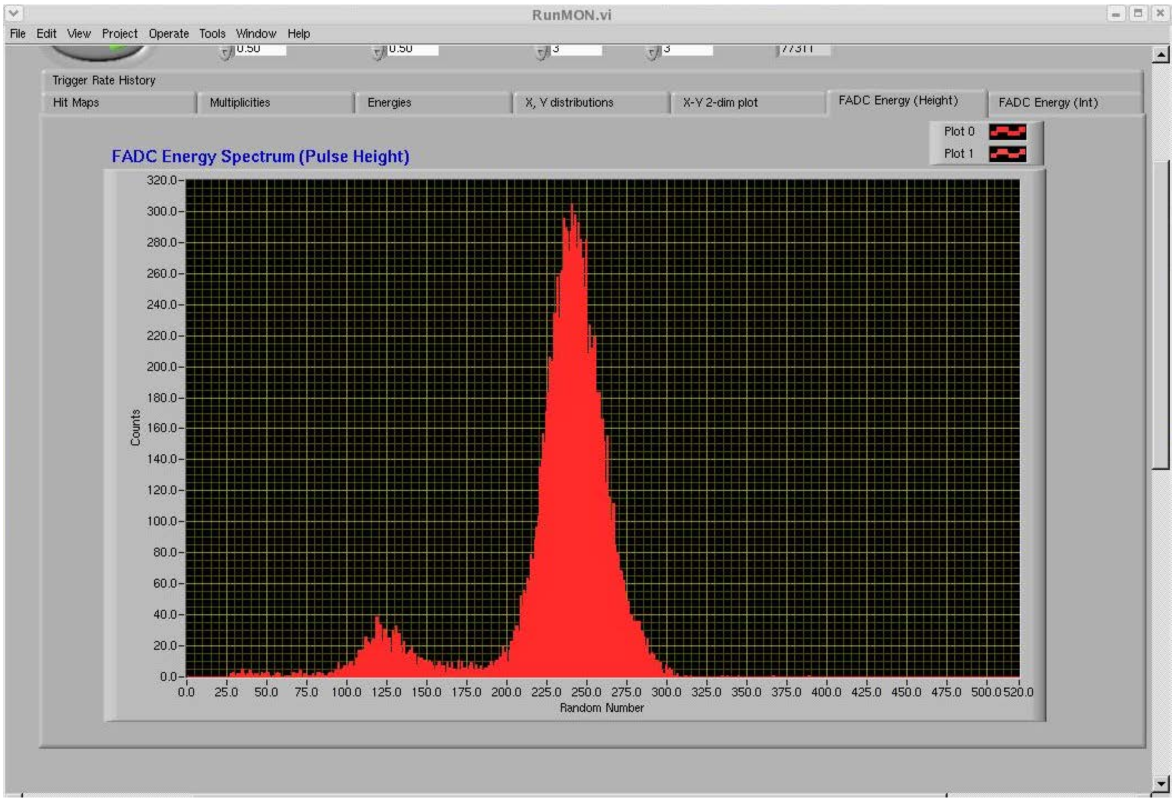

Figure 3.30: The RunMon.vi displays a number of plots for an overview of the performance of the detector. In this plot the FADC spectrum of a Calibration run is shown.

4. Raw data analysis and background discrimination

Contents

4.1 Introduction

During the data taking period three types of runs are being acquired (pedestal, calibration and background). The binary files produced by the data acquisition program of the sunrise Micromegas have to be decoded and all the necessary information for the events to be extracted. An event recorded in the raw data files is constituted by the signal read from the strips and 2500 samples of the mesh pulse that triggered the Gassiplex. The two basic sets of information are the X and Y spatial information that come from the signal collected from the strips and the pulse timing information that come from the signal that is collected from the mesh.

After the information is extracted, a pattern recognition algorithm is applied, to distinguish the X-ray events from the rest, i.e. cosmic muons and high energy gammas, which are the main source of background in the Micromegas detectors in the CAST experimental conditions, with a rate of approximately 1 Hz. The X-rays with energy less than 10 keV produce a primary ionization localised in less than 1 mm. After traversing the amplification area, the charge produced will have a short risetime and a maximum dispersion of 5 mm. The muons and high energy gammas have a broader ionization which causes wider pulses. Therefore their charge signature is completely different from the one of X-rays in the energy range of interest (2-7 keV), making them easily identified and further suppressing the background.

4.2 Raw data acquisition and file format

The sunrise Micromegas data acquisition software stores all the information of each run to one single binary file with name mmRXXXXX.dat, with XXXXX a unique, increasing number for each run. The maximum number of events that can be stored in each file is set to 250.000. It consists of words of 4 bytes (32-bit) and its format is shown in Table 4.1.

During data taking periods, three types of runs are acquired each day:

Pedestal run (type 2)

This run consists of 5000 events. The events that are recorded are the ones that occur with the absence of external trigger. These files are not used, since another way of extracting the pedestals is implemented, from the background runs (explained below).

Calibration run (type 1)

Once every day an ^{55}Fe source is placed in front of the detector, for calibration purposes. A total of 60000-80000 events are taken with a rate of 55-60 Hz, limited by the capabilities of the DAQ system. The daily calibrations ensure that any environmental effects, do not affect the response of the detector.

Background run (type 0)

The detector is recording data during the day, for approximately 23 hours. During this time the morning (sunrise) tracking may take place. All the events of the background run, except the ones during the morning tracking, are considered as background events. The ones that are recorded during the morning tracking interval are the tracking events.

Run Header	Run Header start flag 0x90000000	
	Run Number	
	Date	
	Date Offset	
	Start time	
	Run Type (0, 1, 2)	
	Magnetic field	
	Detector Number	
	HV1 (drift)	
	HV2 (mesh)	
	Gas composition (% Isobutane)	
	Run Header end flag 0x9FFFF000	
Event Header	Event start flag 0x80000000	
	Event ID	
	Event timestamp	
	Trigger Counter	
ADC Data(32 bits)	Number of ADC data	
	Event 2n : Bits 0-15	
	Event 2n+1 : Bits 16-31	
Strip Data (32bits)-decoding applied	Number of strips (Gassiplex 0)	x 4 (Gassiplex 0-3)
	Strip charge : Bits 0-11 Strip ID : Bits 12-22 Valid flag : Bit 30 Overflow flag : Bit 31 Reserved : Bits 23-29	
Event Footer	Event end flag 0x8FFFF000	
	N events follow…	
Run Footer	Run Footer start flag 0xA0000000	
	Total Number of Events	
	Run Footer end flag 0xAFFFF000	

Table 4.1: The format of the binary raw file that is produced from the data acquisition program.

4.3 Raw data analysis

After the raw data are stored and their information is extracted, the first order analysis is performed. For the strip signal, this involves the pedestal extraction, the definition of charge clusters and the storage of their characteristics in an easily accessed data base (ROOT trees). For the mesh pulse, a pulse shape analysis is performed to extract the timing information of each event.

4.3.1 Strip signal

4.3.1.1 Pedestal subtraction

The strips have an intrinsic electronic noise which occurs when there is no trigger from the Matacq to the Gassiplex card. This leads to the constant record of a charge with a well-defined mean level. The pedestal of a strip is defined as the level of this charge and it has to be subtracted from the recorded charge of a real event, to find the real charge deposition. Figure 4.1 shows the level of the pedestal for every strip of one Gassilpex card, with the corresponding sigmas, for a random data file, taken in 2010.

The mean value of the pedestal of each strip is extracted from the background files (type 0). In each event that triggered the acquisition of the Gassiplex, only a certain number of strips have recorded the charge deposition coming from the particle. The rest will just record their pedestal level. The condition that is used for discriminating a real event recorded in a strip is that the charge collected is 3 sigma higher than its pedestal level. The procedure involves three iterations to find the pedestal levels of each strip and one to calculate their mean value and its sigma.

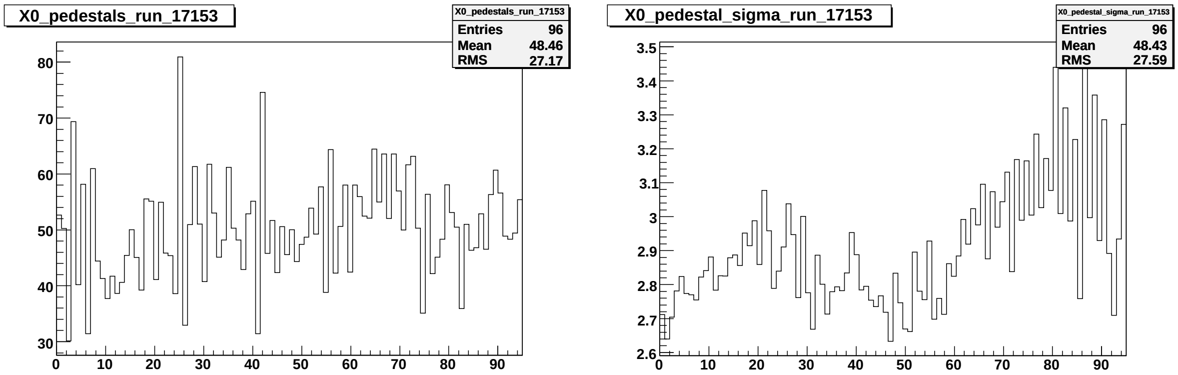

Figure 4.1: The mean pedestal levels (left) and sigmas (right) of the X0 strips of background run 17153, during 2010 data taking. The pictures correspond to strips number 0-95 (Gassiplex 0).

4.3.1.2 Cluster identification and characteristics

A cluster is defined as two or more consecutive strips that recorded a charge. The cluster identification is done separately in the X and Y strips. In order to account for some dead or missing strips, the condition for the end of the cluster allows up to two strips with no charge inside the cluster. When three consecutive strips are found with no charge, the condition for the end of the cluster is met. In some cases more than one cluster is recorded in each direction. The information extracted from the cluster of each event is:

Strip Multiplicity in each axis
The total number of strips that are included in the cluster of each axis.

Cluster Charge
The sum of the charge recorded in each strip of the cluster.

Cluster Sigma
The sigma of the charge distribution of each cluster.

Cluster Position
The position of the strip of the cluster with the highest charge.

Total Charge of event
The sum of the charge of all the X and Y strips in a single event.

Cluster Multiplicity of each event
The number of clusters in X and Y axis that are recorded in a single event.

4.3.2 Mesh signal

The mesh signal is recorded by the Matacq as 2500 consecutive samples, of 1 ns each. A pulse shape analysis of the mesh signal, shown in Figure 4.2, can provide information regarding the energy deposited and the characteristics of the signals deriving from X-rays for the background discrimination.

The pulse characteristics of the mesh signals which are being studied are:

Baseline
It is calculated as the average value of the first 100 samples (100 ns) of the recorded signal by the Matacq, composed by 2500 samples of 1 ns. The actual peak starts more than 400 ns later.

Baseline fluctuation
The standard deviation of the baseline.

Peak Time
The point when the pulse reaches its maximum height.

Peak Amplitude
The height of the peak (in mV) after correcting for the baseline fluctuation.

Start of the peak
The time when the pulse has reached the 15% of the peak height, before the peak.

End of the peak
The time when the pulse has reached the 15% of the peak height, after the peak.

Peak Risetime
The time from the Start of the peak until the Peak Time.

Peak Integral
The integral between the Start and End of the peak.

Default Integral

The integral between the Start time and 500 ns after.

Rise Integral

The integral between the Start of the peak and the Peak Time.

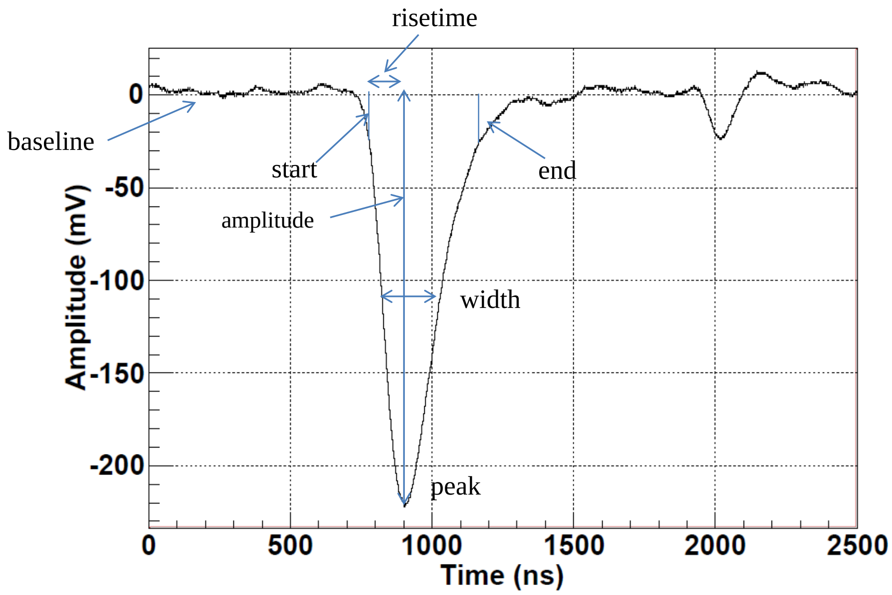

Figure 4.2: A typical mesh pulse of an X-ray event with its characteristics.

4.4 Detector calibration

During the data taking periods the Sunrise Micromegas detector is calibrated with an ^{55}Fe source. The intensity of this source was measured in November 2010 to be 48.45 MBq. It is placed in front of the detector, at a distance of 1.1 m by an automatized manipulator which is controlled by the data acquisition software. This setup allows a uniform illumination of the detector with a high rate of X-rays of 5.9 keV, as shown in Figure 4.3.

The daily calibration runs determine the energy calibration of the detector, showing day to day variations, problems of stability or uniformity. They also provide a valuable set of observables from all the timing and spacial information extracted from the raw data file analysis, which composes an X-ray profile.

The X-ray profile is then used to form the selection criteria (cuts), with which all the background events are compared in order to distinguish the X-ray like events from the rest. More specifically, projections to multiple parameter spaces are created, in which the X-ray events from the calibrations have a very stable and well defined distribution. These are compared sequentially with the distributions of the background events. The background events that fall inside all these distributions pass the criteria and are considered as X-ray events.

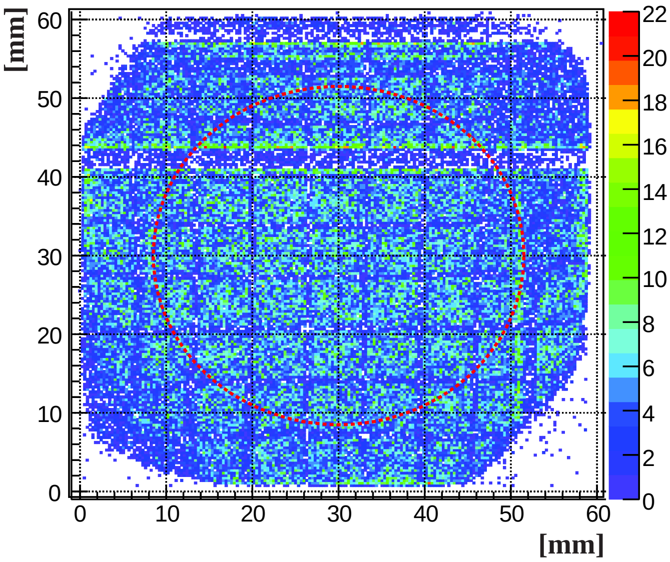

Figure 4.3: The X-Y distribution of events in the strips of the detector in a calibration run. The illumination of the detector is quite uniform. The area of the cold bore is denoted with the orange circle. The horizontal and vertical lines of the strong back of the aluminized drift window and two areas were the strips are damaged are visible.

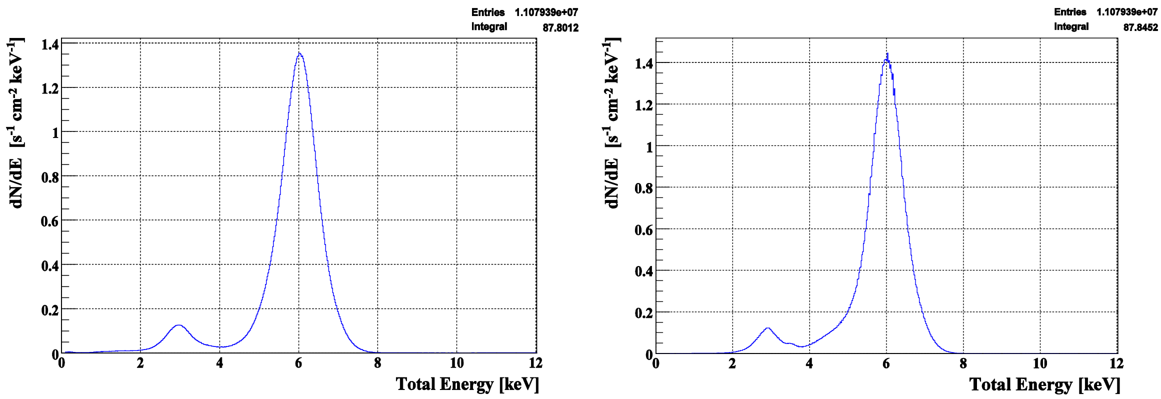

Figure 4.4: The calibration energy spectra for the strips (right) and for the mesh (left) in CAST detector units for the whole of 2010. The 5.9 keV peak of the ^{55}Fe is the dominant one, with the 6.49 keV being shadowed by the resolution of the detector. Their relative intensity is 150 and 17 respectively and they are visible as one peak with maximum at around 6 keV. The escape peak of 3 keV of Argon is also visible.

4.5 Background selection

In order to distinguish the X-ray events of the background run, a calibration run is taken, usually right after the morning shifts. This calibration run offers the necessary information that will compose the selection criteria for the X-rays of the background run.

A background event has to pass sequentially all the selection criteria in order to be identified as an X-ray. These selection criteria are formed both from the mesh and the strips information and they are separated in two categories. The “manual” criteria, which are extreme values of some parameters that are manually fixed and the “automatic” criteria, which are projections to a parameter space, in which a selection area that includes 95% of the events is created.

4.5.1 Manual selection criteria

The manual selection criteria that are applied are:

Fiducial selection:
The X and Y strips should be inside a circle which corresponds to the aperture of the cold bore.

$$\sqrt{X^2 + Y^2} \leq 21.5 \text{ mm} \quad . \tag{4.1}$$

Number of clusters per strip axis:

$$N_{\text{Clusters X}}=1 \ \& \ N_{\text{Clusters Y}}=1 \quad . \tag{4.2}$$

The collected charge in each axis:

$$\left|\frac{Q_X - Q_Y}{Q_X + Q_Y}\right| < 0.3 \quad . \tag{4.3}$$

4.5.2 Automatic selection criteria

The automatic selection criteria have one or two dimensional distributions of parameters that, for X-rays, have very well defined distributions, meaning that most of the events are confined within a well-defined shape. The selection is based in the contour plotting abilities of ROOT, a powerful analysis tool, developed at CERN.

The parameters used are a subset of the ones defined in Chapters 4.3.1 and 4.3.2.

4.5.2.1 Two dimensional multiplicity cut

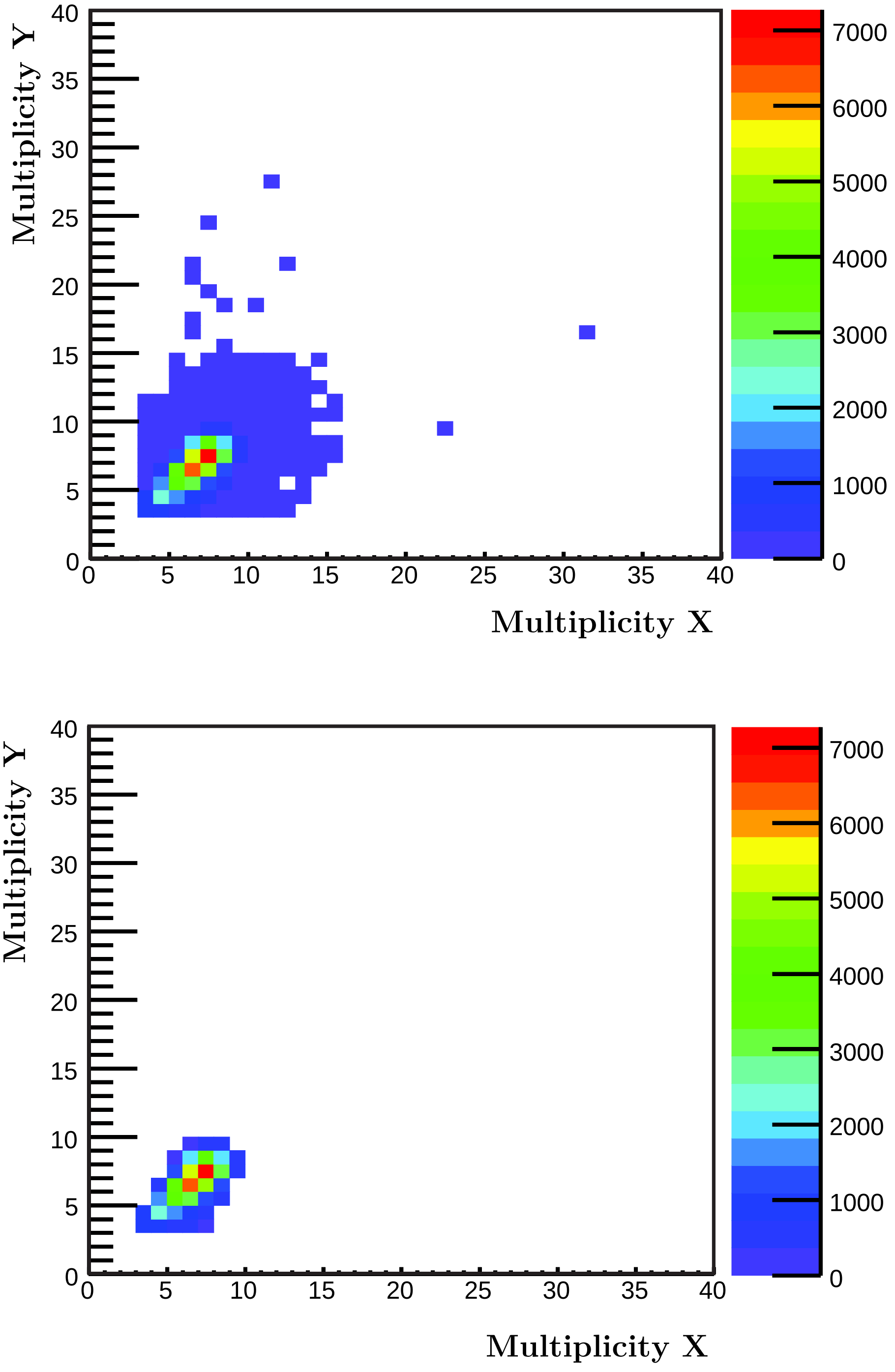

Figure 4.5: The original (top) and the selected (bottom) two dimensional distributions of calibration events.

4.5.2.2 X sigma vs Y sigma cut

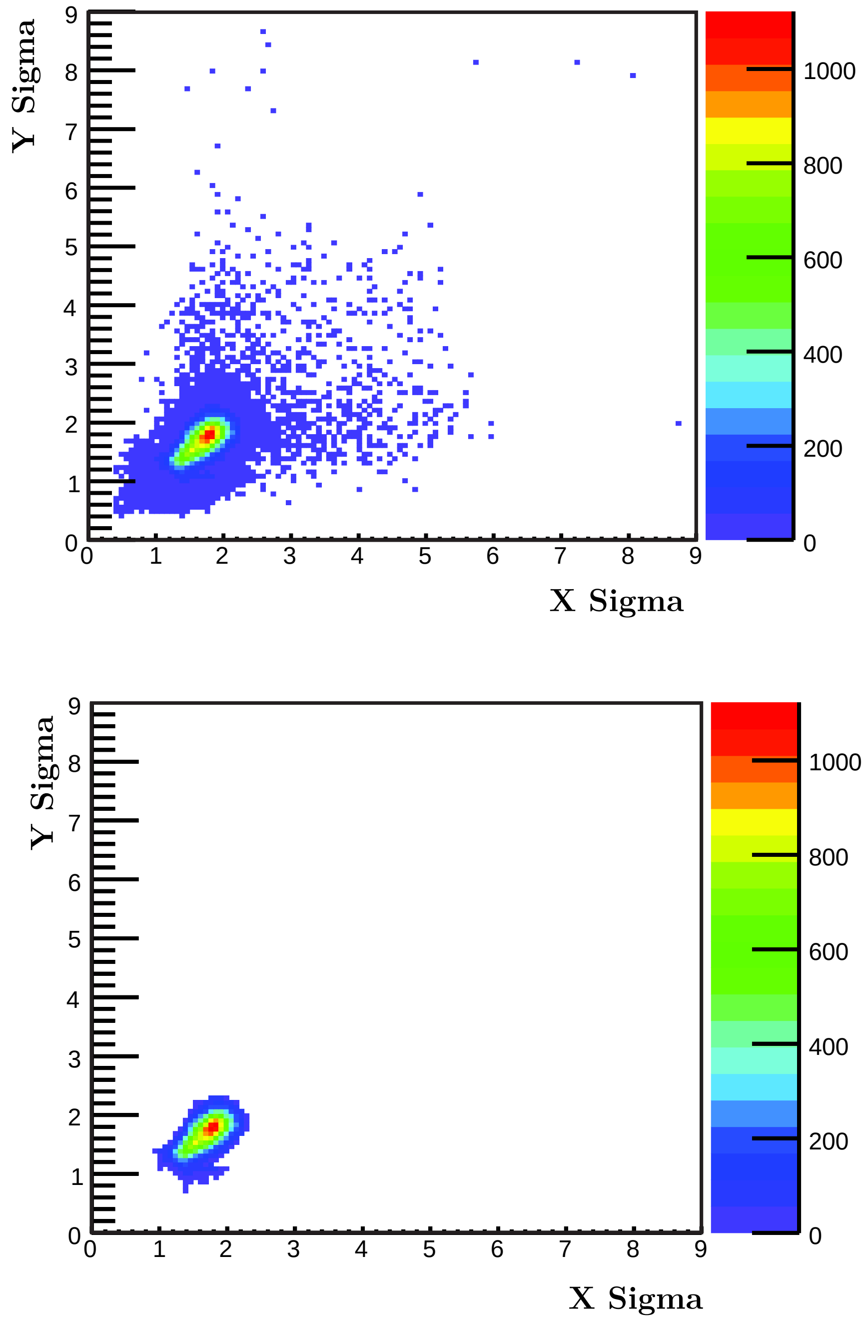

Figure 4.6: The original (top) and the selected (bottom) two dimensional sigma distributions of the strips of calibration events.

4.5.2.3 Pulse width versus risetime

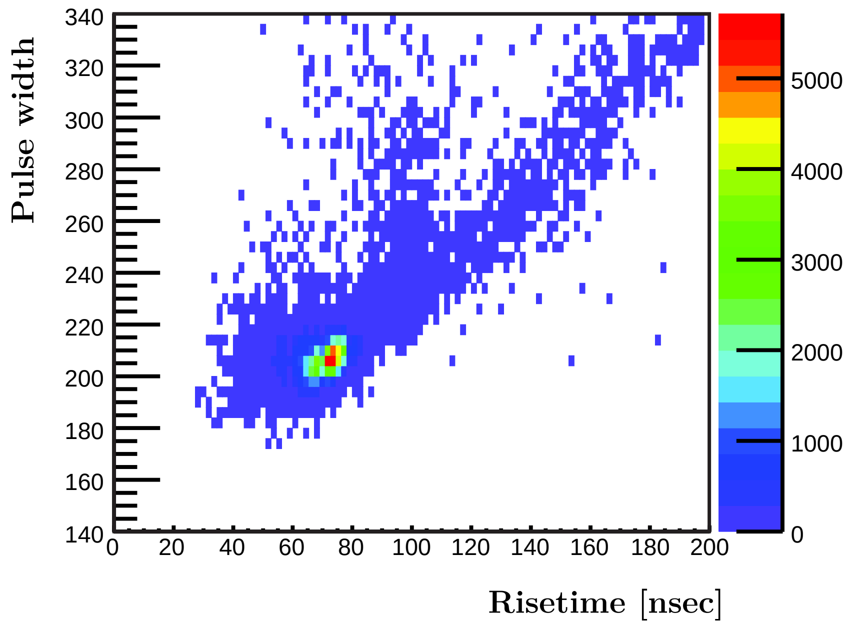

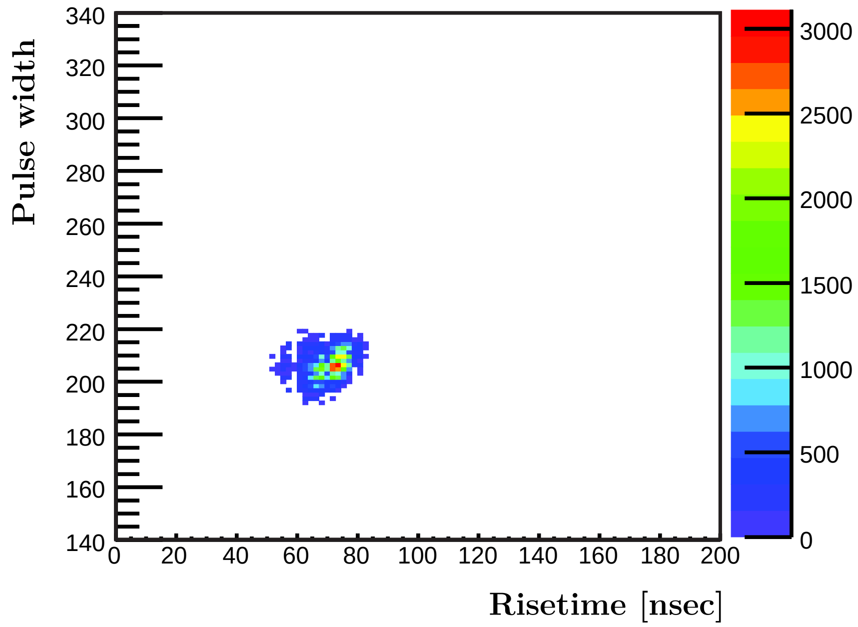

Figure 4.7: The original (top) and the selected (bottom) two dimensional distribution of the amplitude over charge of the pulse, versus its rise time, in calibration events.

4.5.2.4 Pulse Width over Pulse mean versus Pulse Amplitude over Pulse Charge

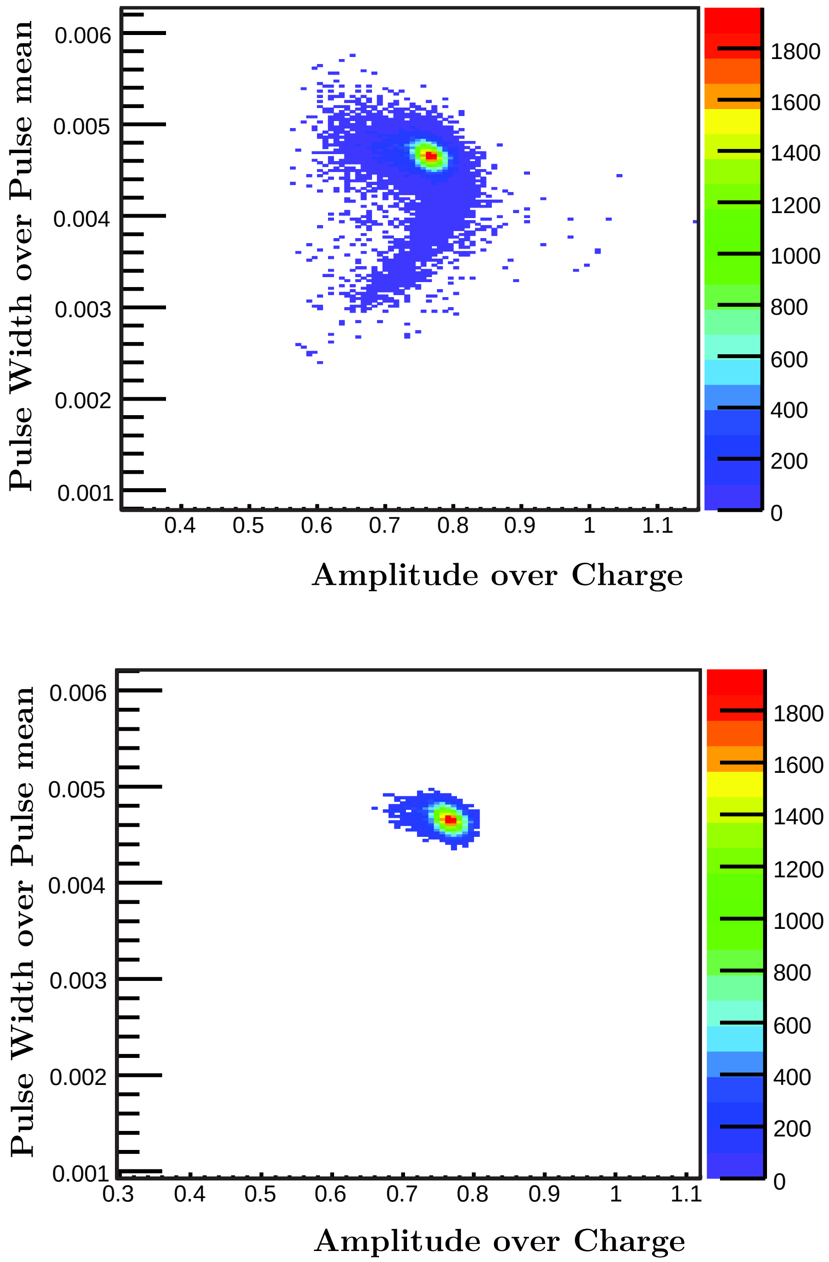

Figure 4.8: The original (top) and the selected (bottom) two dimensional distribution of the width over the mean of the pulse, versus the amplitude over the charge of the pulse, in calibration events.

4.5.2.5 Baseline fluctuation

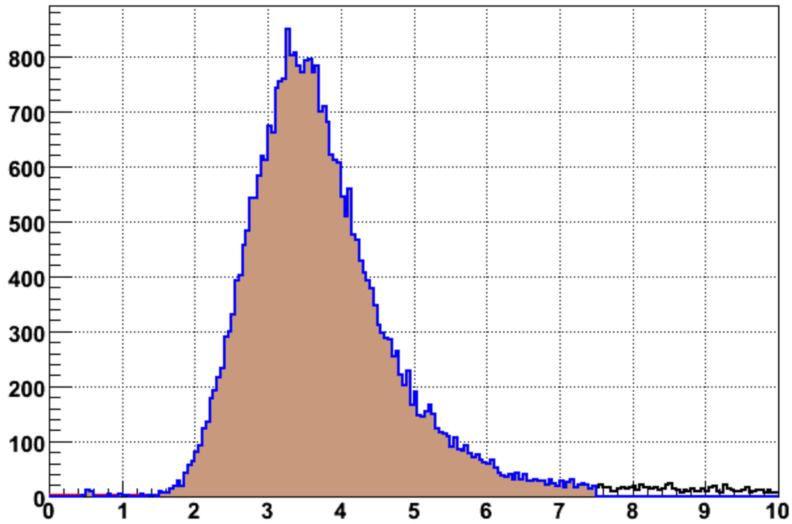

Figure 4.9: The 98% of the distribution of the baseline fluctuation for calibration events is selected. Background events that have a fluctuation of baseline within this limit are X-ray candidates.

5. The CAST detector lab

Contents

5.1 Introduction

A new detector lab has been realized at CERN, at building 162 S-065. It incorporates a variable energy calibration system based on an X-ray beam line which was built at the Max-Planck-Institut für extraterrestrische Physik/Garching (MPE). The purpose of the project is to be able to calibrate for the first time the present and future CAST detectors, in a number of energies between 2 and 10 keV. This study is necessary for the data analysis because it is the only way to define the efficiency of the software data selection in the energy range of interest and the linearity of the detectors. Furthermore since an X-ray beam line of variable energy is difficult to find, having one at CERN is a unique opportunity to enhance the performance of the software data selection.

5.1.1 General information

X-rays are electromagnetic radiation with a wavelength in the range of 0.01 to 10 nm which corresponds to energies from ~100 eV to ~100 keV, Figure 5.1. The electromagnetic radiation from nuclear reactions, called γ-rays can also be produced in the same energies as X-rays but they are differentiated because they have a different production mechanism. X-rays are produced outside the nucleus, while γ-rays are produced inside the nucleus. X-rays are sometimes called Röntgen rays after their discoverer, Wilhelm Conrad Röntgen.

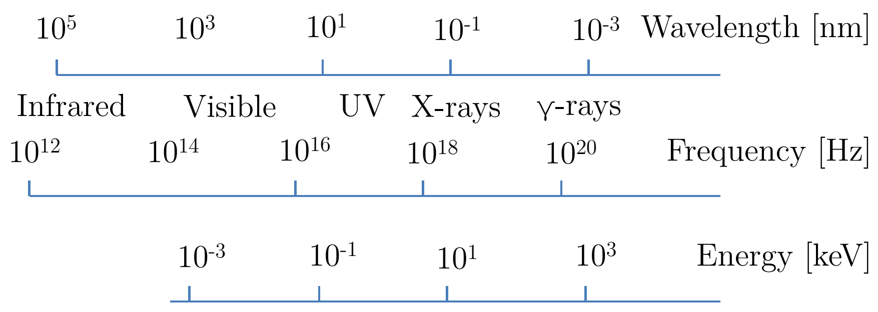

Figure 5.1: The X-rays are shorter in wavelength than UV and longer than γ-rays.

5.1.2 X-ray generation

X-rays can generally be produced by directing a beam of energetic particles to a material. The most common practice in a lab is to use X-ray tubes in which electrons are the energetic particles. The electrons are produced in vacuum by a heated filament, they are accelerated by an intense electric field and bombard the anode (target), as seen in Figure 5.2. When the energetic electrons hit the target they produce X-rays but also photoelectrons, Auger electrons and heat.

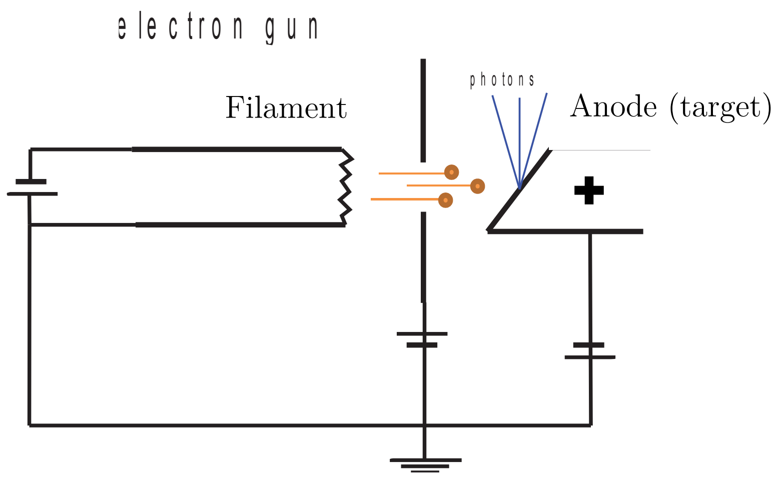

Figure 5.2: Schematic view of the principle of operation of an X-ray tube.

5.1.3 X-ray spectrum

When a highly energetic electron hits the target it might ionize an atom or not. In the latter case, it is slowed down or completely stopped by the interaction with the negative electric field from the electrons of any atom it encounters. If the electron is slowed down, it will exit the material with less energy. The energy that the electron loses is radiated as X-rays of equal energy. These X-rays and the electron will interact with matter in a similar fashion to produce more radiation at lower and lower energy levels. The X-rays produced by this mechanism form a continuous band in the X-ray spectrum, called Bremsstrahlung, which in German means “braking rays”. The maximum of this spectrum occurs when an accelerated electron loses all of its energy in one interaction and it is equal to the acceleration voltage.

When the energy of the accelerated electron is higher than a certain threshold value, which depends on the material of the target, a second type of spectrum is obtained and it is superimposed to the continuous Bremsstrahlung spectrum. This spectrum is called the characteristic radiation of the material and consists of discrete peaks. When an accelerated electron has enough energy to eject one of the atom-bound electrons of the inner shells, an electron of a higher shell will drop to the empty hole of the inner shell, emitting an X-ray with energy which is approximately equal to the energy difference of the two shells. (Due to the need to conserve energy and momentum, a small amount of energy must be transferred to the atom which then recoils). Hence the energy and intensity of the peaks in this secondary process depends only on the material of the target. In Figure 5.3, the X-ray spectrum of copper is shown.

The characteristic lines of an X-ray spectrum are named after the shell that the vacancy was created, i.e. K, L, M etc. When an electron drops from the next shell then the transition is described as α and when it occurs between shells that are separated by one more, it is described as β. If the shell has subshells, then to distinguish the transitions a number is put after the Greek letter, i.e. 1,2, as seen in Figure 5.4.

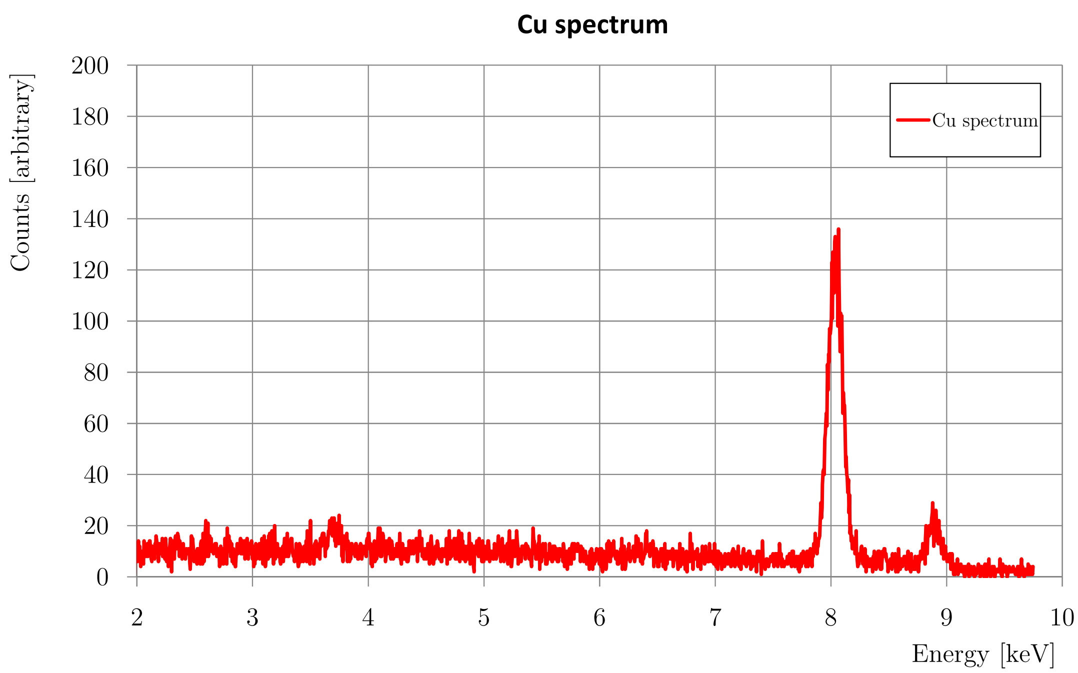

Figure 5.3: X-ray spectrum of a copper target. The characteristic peaks and the Bremsstrahlung spectrum can be seen.

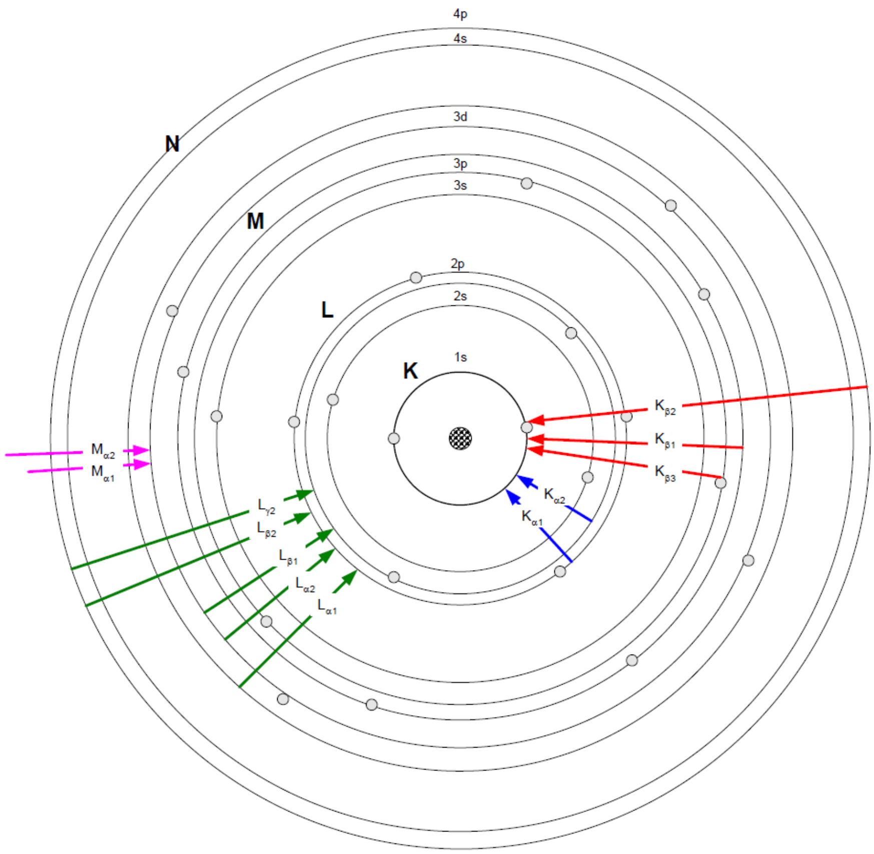

Figure 5.4: Graphical representation of the various transitions in an atom, extracted from [93].

5.1.4 X-ray absorption

The main absorption mechanism in a solid material is ionisation. An incoming photon will lose its whole energy when exciting or ionizing an atomic shell. Absorption increases rapidly with increasing atomic number and decreases with the energy of the X-rays. However this variation shows discontinuities. For a given material, these discontinuities, called absorption edges, correspond to the energies of the X-rays that are associated with the energy levels of the shells. When the incident energy increases, it reaches the shell energy level and the transmission is reduced rapidly, as one can see in Figure 5.5.

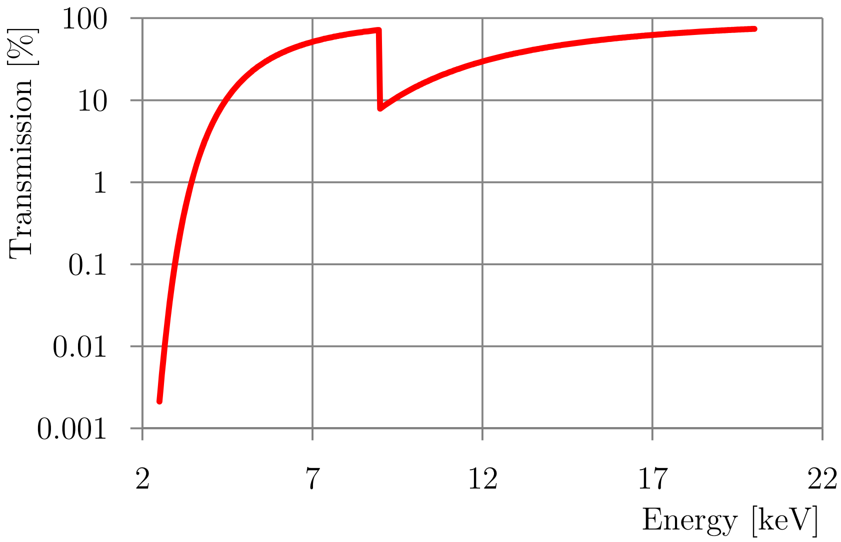

Figure 5.5: The transmission of 10 μm of copper versus the energy of the incident X-ray beam. One can distinguish the absorption edge at 8.9789 keV.

5.1.5 Filters

The great variation of the X-ray transmission on both sides of an absorption edge can be exploited with the use of filters. When the energy of a photon is just above the energy level of a shell of a material, then it strongly absorbs the photon beam. If a material can be found that has an absorption edge between the K_α and K_β lines of the target material that produced the X-ray beam, it can strongly absorb the K_β line, since the photons with this energy will be able to excite the filter material K level, but not the K_α photons. This kind of filter is called β-filter. For a target material with mass number Z, the corresponding β-filter has generally Z-1. For heavy elements, it can also be Z-2. The thickness of the β-filter can be chosen so that it can reduce the intensity of the K_β line by a factor of 100, while reducing the intensity of the K_α line only by a factor of 10. In Figure 5.6, an example of a β-filter application is shown. The β-filter used is 0.1 mm of nickel and the target is copper.

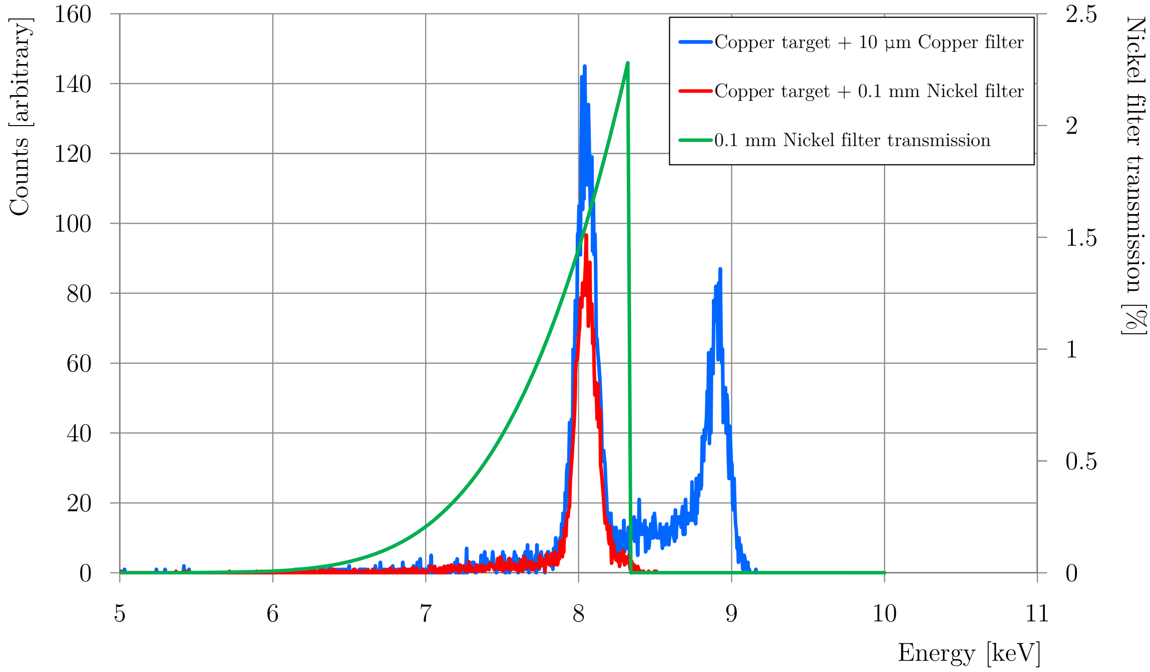

Figure 5.6: An example of a β-filter application. In this case the target is copper with a nickel filter of 0.1 mm. The spectrum with the filter was normalized so that it can be easily displayed; therefore the ratio of the peaks with and without the filter is not the real one.

5.2 The MPE X-ray beam line

5.2.1 X-ray source

The MPE X-ray beam line has a variable energy calibration system which was built at the Max-Planck-Institut für extraterrestrische Physik/Garching (MPE). In Figure 5.7, the X-ray generator is shown from the side, while in Figure 5.8, the system of the variable targets is shown. There are 18 slots for the various targets but in the first set of measurements only 5 will be used. In Table 5.1 and Table 5.2, the available anode targets and filters are shown.

The principle of the X-ray generation is the one described in section 4.1.2, with the voltages supplied by three power supply modules from FUG, shown in Figure 5.9. The anode power supply can reach 35 kV, but for the purposes of the lab and for safety it operates up to 18 kV. The Wehnelt power supply provides a focusing field in the path of the accelerated electrons from the filament but since a focused X-ray beam is not needed, it is not used.

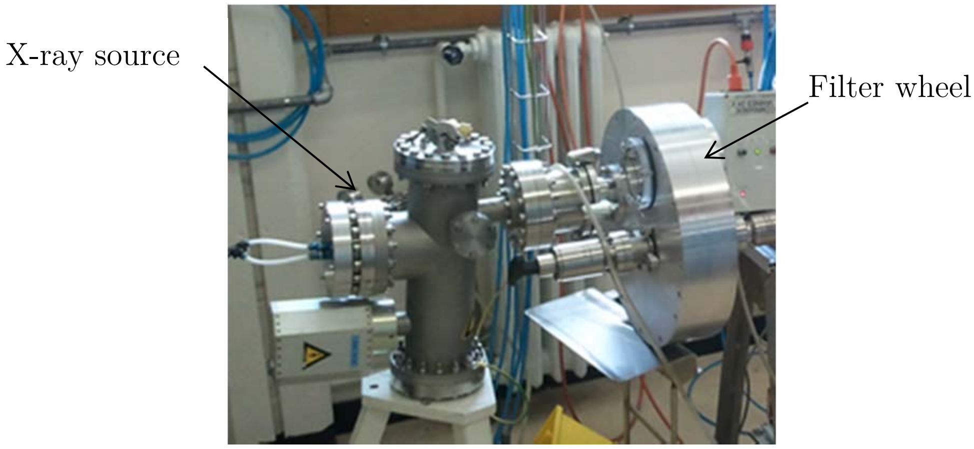

Figure 5.7: Side view of the X-ray generator system.

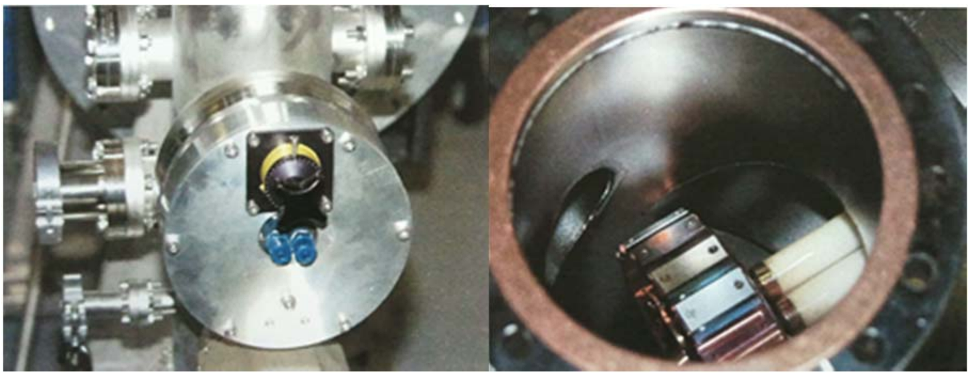

Figure 5.8: The variable target X-ray source (left) and the anode wheel with the different materials (right).

Figure 5.9: The power supply units for the X-ray beam line.

Position	**Target**	**Peak(s) of interest [keV]**
1	Ti	4.51
5	Mo	2.29
6	Au	2.12
11	Al	1.49
12	Cu	8.05, 8.9

Table 5.1: The available targets and the energy of the peak of interest for the CAST detectors.

Filter	Thickness
Ni	0.1 mm
Al	5 µm
EPIC	200 nm Al + 0.5 µm PP
Cu	10 µm

Table 5.2: The filters in the filter wheel of the X-ray line.

5.2.2 Vacuum system

The X-ray source as well as the detectors must be operated under vacuum. The line is divided in two sides, the generator and the detector side, left and right from the V_2 gate valve respectively, Figure 5.10. Each side has its own pumping system. The generator side including the X-ray generator, the filter wheel, and the residual gas analyser is pumped by the turbo molecular group "main pump" and by the sputter ion pump. The detector side is pumped by two turbo molecular groups the "detector pump" and the "guard pump".

The gate valve V_2, the "detector valve", when closed keeps the generator side under vacuum in case work is needed to install or exchange the detector. As the gate valves must not be operated with a pressure difference, the detector side must be under vacuum before opening the valve V_2. In the detector side, the guard vacuum is separated from the detector vacuum, Figure 5.10, with a thin differential window made of 4 µm polypropylene. The two volumes can be linked with the bypass valve, V_3. This setup protects the generator side from the risk of a potential minor leak in the detector vacuum.

After the installation of a Micromegas detector the detector side is first pumped by slowly opening the inlet valve Vs of the "Guard pump" with the bypass valve V_3 open and at a reduced pump speed in order to keep both sides of the differential window at the same pressure. When they are under vacuum the valve can be fully opened, the pump run at nominal speed, the detector pumping group started and the bypass valve can be closed.

In operation with a Micromegas detector the generator side is pumped by the sputter ion pump in order to keep a clean vacuum, the gate valve V_1 is locked in closed position and the main pumping group can be stopped. If this valve has to be opened when not under vacuum on each side, a special procedure must be followed with extreme caution. If the sputter ion pump is not sufficient to maintain a good vacuum, or if this pump produces parasitic X-rays, the main pumping group must be used, and the valve V_1 should be open [94].

5.2.3 Residual gas analyser (RGA)

A residual gas analyser (prisma quadropole) is placed in the system for leak detection monitoring of the outgasing of the components close to the generator, Figure 5.10. The RGA is controlled via an RS-232 port from a computer. It controls a pressure gauge, named P_4 and uses it as interlock. P_4 is recorded by the dedicated software for the RGA, made by Balzers.

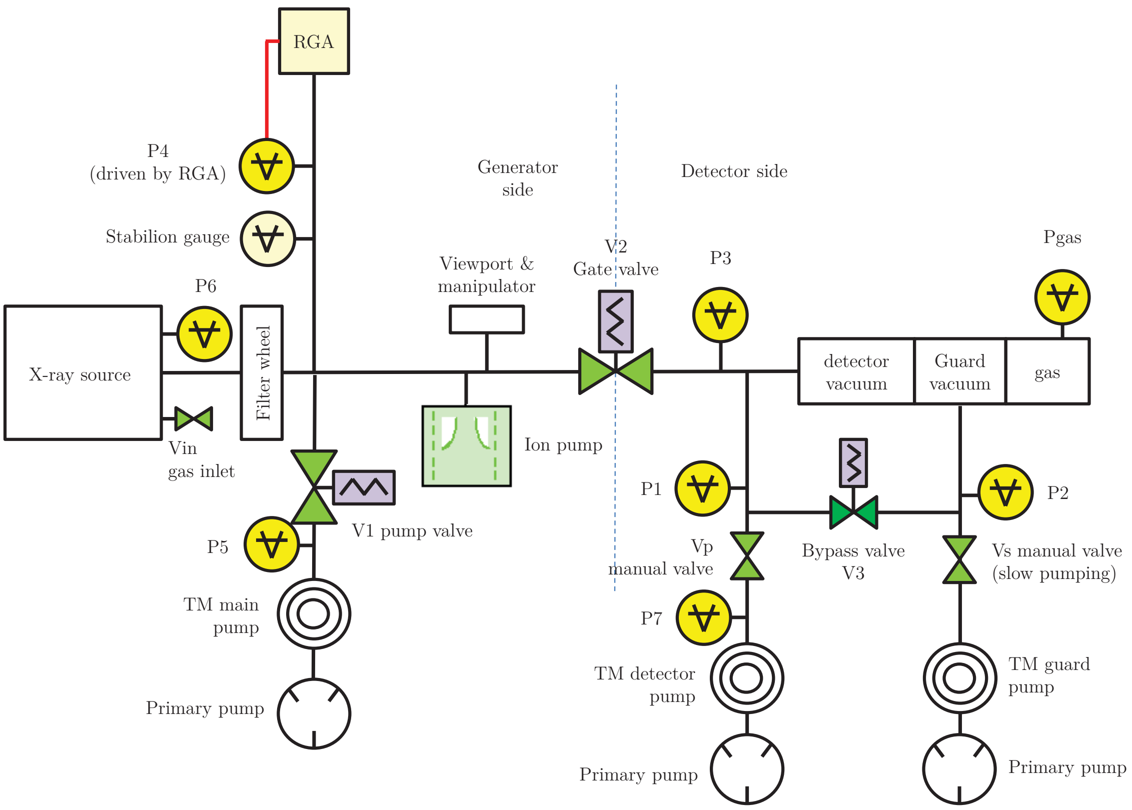

Figure 5.10: The vacuum system of the X-ray beam line

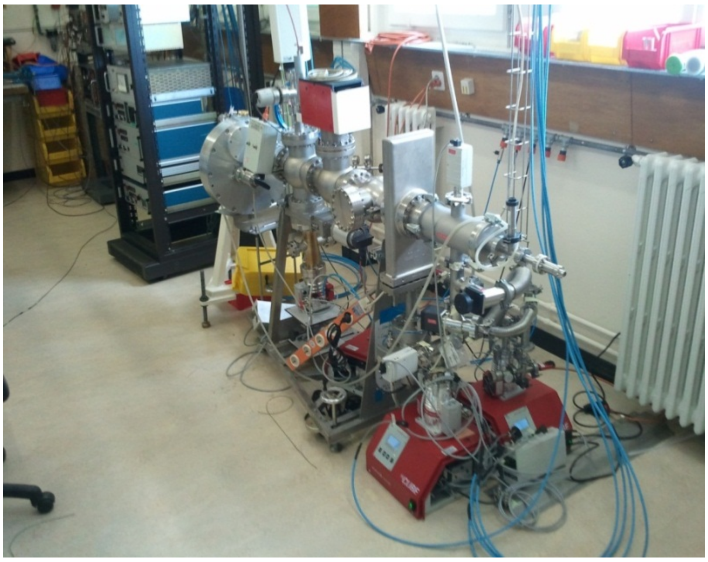

Figure 5.11: An actual image of the X-ray beam line.

5.2.4 Control and interlocks

5.2.4.1 Pressure gauges

For monitoring the pressure in the various systems of the X-ray beam line a series of pressure gauges has been installed. In Table 5.3, the list of the names given to the pressure gauges is shown together with their function. Their actual position in the line is shown in Figure 5.10.

The values of all pressures are continuously monitored in a dual gauge display and a Maxigauge display, Figure 5.12.

Name	Type	Code	Measures
P_1	Pirani	TPR	detector vacuum
P_2	Pirani	TPR	differential vacuum
P_3	B.A.	PBR	detector vacuum
P_4	Penning	PKR	generator
P_5	Penning	PKR	main pump
P_6	Process	PKR	generator
P_7	Process	IMR	detector pump
P_{gas}	Linear	APR	detector gas

Table 5.3: List of pressure gauges in the X-ray beam line.

5.2.4.2 Interlocks

To ensure the safe operation of the user and the components of the X-ray beam line, a series of interlocks has been introduced related with the operation of the three valves V_1, V_2 and V_3, as well as the operation of the high voltage power supply for the target of the X-ray generator.

The interlocks are enforced to the system through the logic of the interlock box, Figure 5.12. They are based on the pressures that are monitored from the Maxigauge. When one or more pressures related to an interlock is above or below a value, the signal of the corresponding relay switch contact is sent to the interlock box which sends the appropriate signal to the valve or power supply. More specifically the interlocks that are implemented are:

Bypass valve V3

This valve links the “guard” with the “detector” vacuum. It is normally open (meaning that in case of a power loss it opens, for safety and it is programmed to stay open when the power is back). It can be closed only if both P_1 and P_2 are lower than 9×10^{-3} mbar. It opens automatically when one of the above pressures increases higher than 1×10^{-2} mbar.

Gate valve V_1

It is the gate valve, through which the "main" pump is pumping the system in the generator side. V_1 can be opened if both sides of it are under vacuum. The interlock is OK when P_5 is below 1×10^{-5} mbar and P_6 below 5×10^{-5} mbar. It will close automatically if P_5 goes above 2×10^{-4} mbar and P_6 above 8.4×10^{-5} mbar.

Gate valve V_2

It is normally closed, to isolate the two systems and must close in case of power loss. V_2 can be opened only if both sides are under vacuum. The interlock is OK when P_2 is below 8×10^{-3} mbar and P_6 below 5×10^{-5} mbar.

X-ray generator

The high voltage power supply for the target of the X-ray generator is interlocked with the pressure P_6. This pressure has to be better than 5×10^{-5} mbar so that the power supply can operate and it will stop working if the pressure goes above 8.4×10^{-5} mbar.

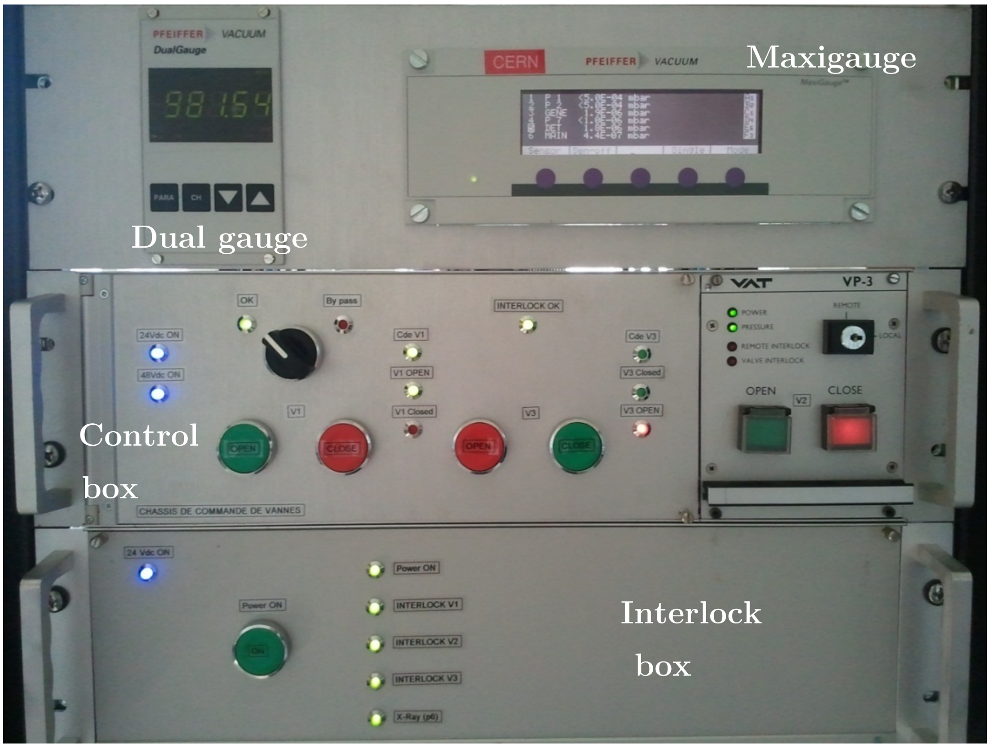

Figure 5.12: From top to bottom: The Pfeiffer displays (Dual gauge on the left and Maxigauge on the right) show the pressures recorded from the gauges, the control box can operate the electrovalves, provided that the corresponding interlocks are OK, and the interlock box shows the status of the interlocks.

5.2.4.3 Slow control

A new slow control system has been developed for the needs of the lab, based on the Labview system design software. Its user interface is shown in Figure 5.13. It is used for monitoring and logging the evolution of all the key parameters in the lab like vacuum pressures, detector parameters, and valves' status and also sending an inhibit signal to the power supply of the detector if necessary. All the signals are acquired and sent through a National Instruments data acquisition card (NI-USB 6341).

One of the main functionalities of the slow control is that it is programmed to detect abnormal variations in key parameters of the lab. In case one parameter reaches a certain predefined value (i.e. in the event of a power cut), it sends warning SMS messages and e-mails, to the people responsible for the system, so that they can react immediately.

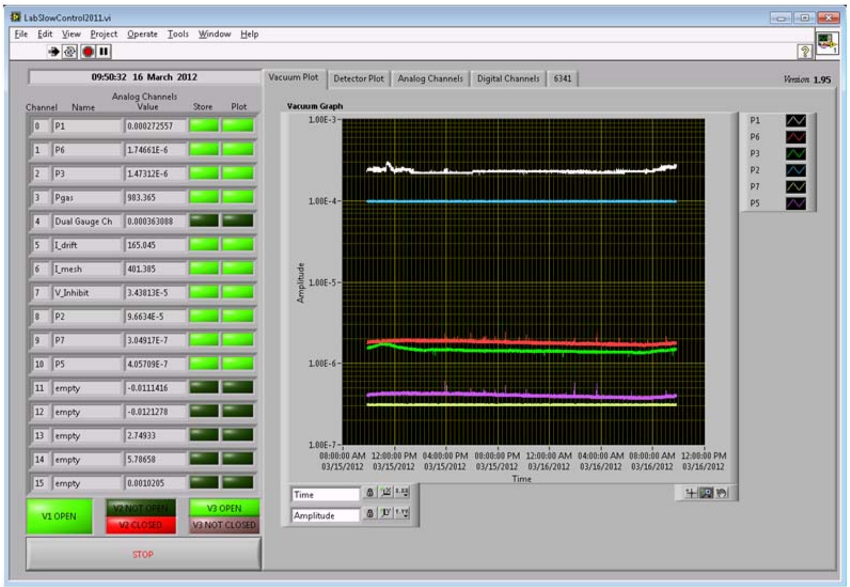

Figure 5.13: The Slow control system of the CAST detector lab

5.3 Detectors

Apart from the Micromegas detectors currently used in CAST, a new plug and play Silicon Drift Detector has been purchased for the lab, mainly to monitor the first commissioning of the X-ray beam line and acquire the first spectra from the energy range of interest for CAST. In the future this detector will serve as an R & D test bench for possible future use in CAST.

5.3.1 The Silicon Drift Detector (SDD)

5.3.1.1 Introduction

In 1983, Gatti and Rehak [95], proposed a new detector scheme based on sideward depletion. The idea was that a semiconductor volume of high resistivity, like n-type silicon, can be fully depleted by a small n^+ ohmic contact positively biased with respect to the p^+ contacts covering both sides of the silicon volume. An electric field with a strong component parallel to the surface drives signal electrons towards a small sized circular collecting anode, Figure 5.14. The drift electrodes that surround the anode are annular. These electrodes are biased so as to create an electric field which guides the electrons through the detector, to the anode. The SDD was seen as the solid state equivalent of gas drift chambers then in use and was initially proposed to measure the spatial location of interaction (derived from the drift time).

The small area of the anode keeps the capacitance very small. The active volume of the detector can be enlarged by adding more electrodes, but keeping the same anode area, therefore keeping the input capacitance constant. This results in low noise particularly in short shaping times.

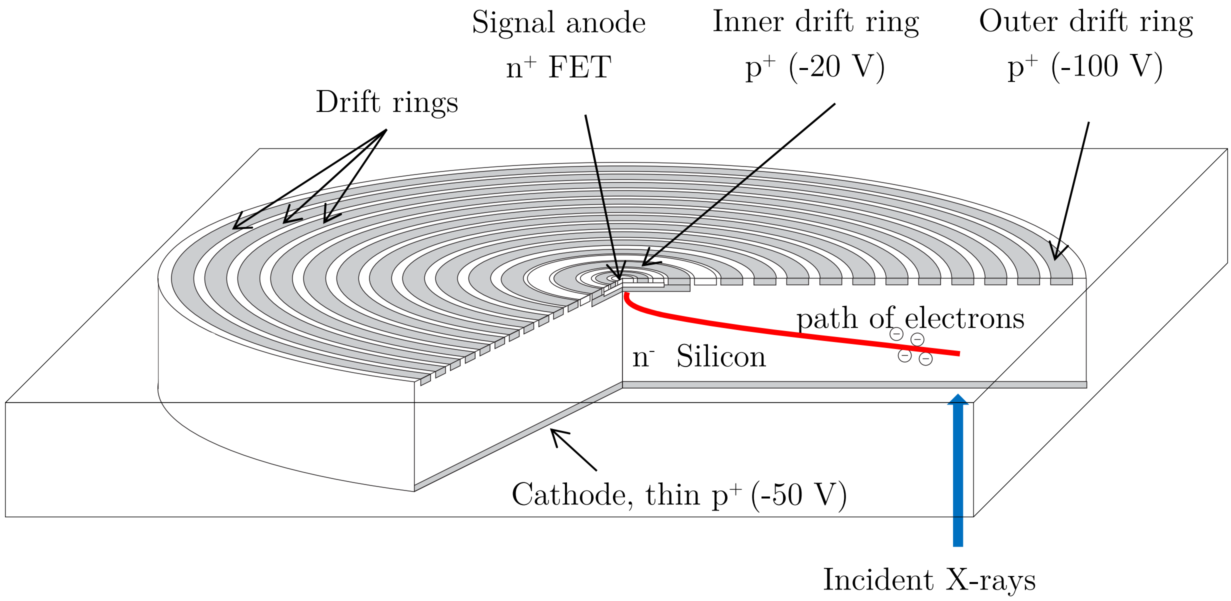

Figure 5.14: A schematic drawing of the Silicon Drift Detector.

5.3.1.2 Amptek XR-100SDD

The XR-100SDD from Amptek is a high performance silicon drift X-ray detector which incorporates a preamplifier, and cooler system in a compact and hermetic case with a thin Si_3N_4 window with aluminium coating (C2 series). The temperature of operation of the components is approximately -55 °C. The detector size is 25 mm^2 and the silicon thickness is 500 µm. The resolution of the detector is 125 - 140 eV FWHM at 11.2 µm peaking time for the 5.9 keV peak of the ^{55}Fe source.

The detector is combined with a high performance pulse processor and power supply module, the Amptek PX5. This device also includes a digital pulse processor (DPP). The DPP digitizes the preamplifier output, applies real-time digital processing to the signal, detects the peak amplitude, and bins this in its histogram memory. The spectrum is then transmitted to Amptek's own MCA software via USB. The PX5 includes all power supplies necessary to operate the detector detectors. In Figure 5.15, the detector and its internal components are shown together with the PX5 [96].

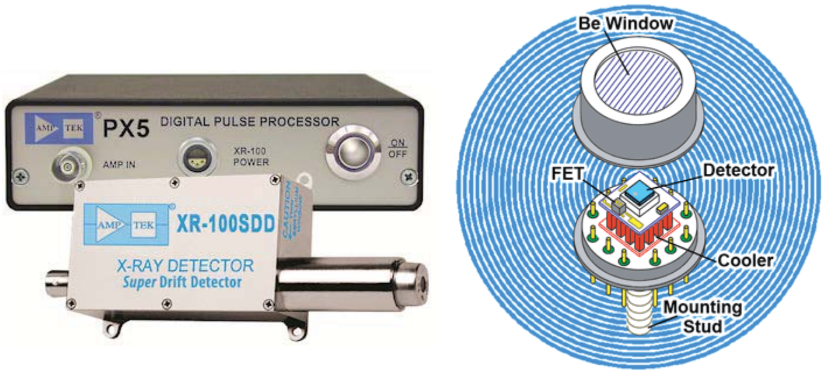

Figure 5.15: The XR-100SDD detector and PX-5 digital pulse processor from Amptek (left) and the inner components of the XR-100SDD detector (right).

5.3.2 Micromegas detectors

The Micromegas detectors used in the CAST experiment have been extensively covered in Chapter 3. The purpose was to keep, as much as possible, the same configuration and operation conditions with CAST so that there can be a direct comparison of the results.

5.3.2.1 Data acquisition

The signal propagation follows the same scheme as the one presented in Figure 3.27. The connection of the modules with the data acquisition PC is done with optical fibers via a VME controller (CAEN V2718) and a bus card to the PC (CAEN V2818 PCI optical link) or alternatively with a lemo cable from the amplifier directly to an Amptek MCA-8000A Pocket multichannel analyzer.

There are two data acquisition software running on the data acquisition PC. The one based on the Labview system design software, by National Instruments, is an adapted version of the software running in the sunset Micromegas PC. The other is a plug and play multichannel analyzer software by Amptek. The operating system of choice is Windows 7. The data acquired, are uploaded in a daily basis to lxplus in form of binary files, for safety and backup via a routine program, written in Labview, which is constantly running in the background.

5.3.2.2 On bench calibration system

For testing the detectors before installing them in the beam line, an on bench calibration system has been setup, shown in Figure 5.16 and Figure 5.17. The detector is housed in a Faraday cage, facing downwards and supported by an insulating material. All the signals and power supplies pass via feedthroughs to the Micromegas rack and from there to the PC. For the calibration an ^{55}Fe source (n° 3600RP) of 2.92 MBq on 15.07.2011) is used. It is placed in a socket that screws directly to the bottom of the Faraday cage (Figure 5.17 – left).

Figure 5.16: The Faraday cage and the position of the detector on the test bench (left) and the complete calibration system (right).

Figure 5.17: The Faraday cage is closed during a calibration for minimizing the noise (right). The socket in which the radioactive source is placed, on the bottom side of the Faraday cage (left).

5.3.2.3 Gas system

The gas mixture used in the lab for the Micromegas detectors (premixed) is argon with 2.3% iC_4H_{10} as a quencher, the same as the one used in the sunrise Micromegas detector in CAST. The gas arrives to the chamber of the detector through the gas lines sketched in Figure 5.18. There are three lines for the gas mixture of Ar/iC_4H_{10}. Two of them, used for the second beam line and the on bench calibration system, operate in atmospheric pressure and the third has a pressure regulation system with a buffer volume of 1 l that can operate in higher pressures. All of the lines are subject to the daily and seasonal variations of atmospheric pressure but for the purposes of the lab an absolute pressure regulating system was not needed.

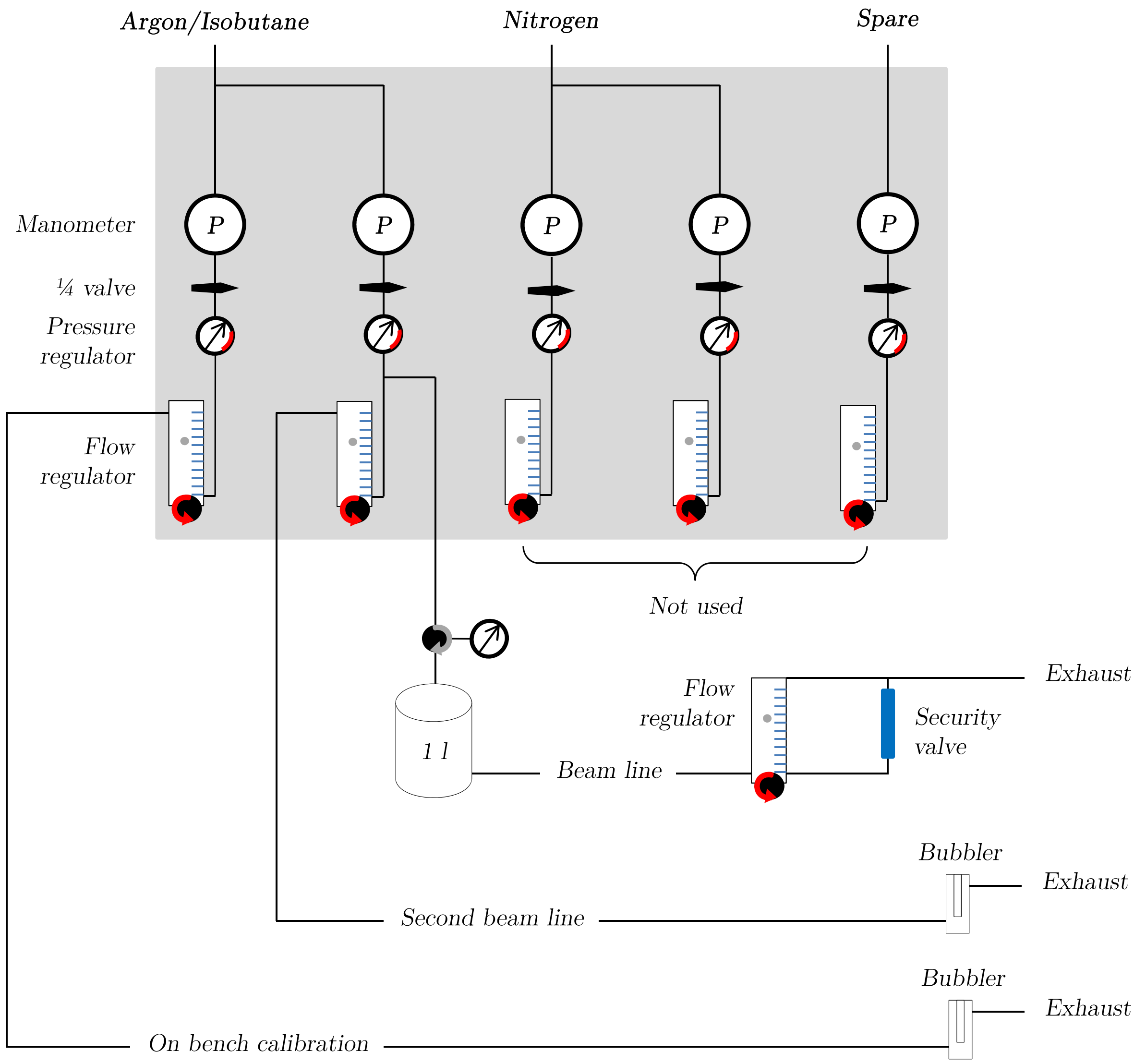

Figure 5.18: The gas system of the CAST detector lab.

5.4 Measurements

5.4.1 XR-100SDD spectra

The commissioning of the X-ray generator was done with the Silicon Drift Detector. A series of measurements took place with all the targets and combinations of filters. The gain of the detector was set to 140× and the low energy threshold to 0.13 keV. The measurements are summarised in Table 5.4 and the spectra acquired are shown in Figure 5.19 to Figure 5.26.

Target	**Filter**	**HV [kV]**	$\mathbf{V_{filament}}$ **[V]**	$\mathbf{T_{acq}}$ **[min]**	$\mathbf{N_{events}}$
Al	EPIC	7	3.1	14.16	33095
Al	Al	7	3.4	18.28	41559
Mo	EPIC	7	3.2	17.73	37206
Au	EPIC	7	3.1	14.48	38347
Ti	EPIC	9	3.1	25.21	37662
Cu	EPIC	13	3.1	14.14	39468
Cu	Cu	13	4.5	25.99	36432
Cu	Ni	12	4.5	15.00	24022

Table 5.4: Summary of the spectra taken with the SDD.

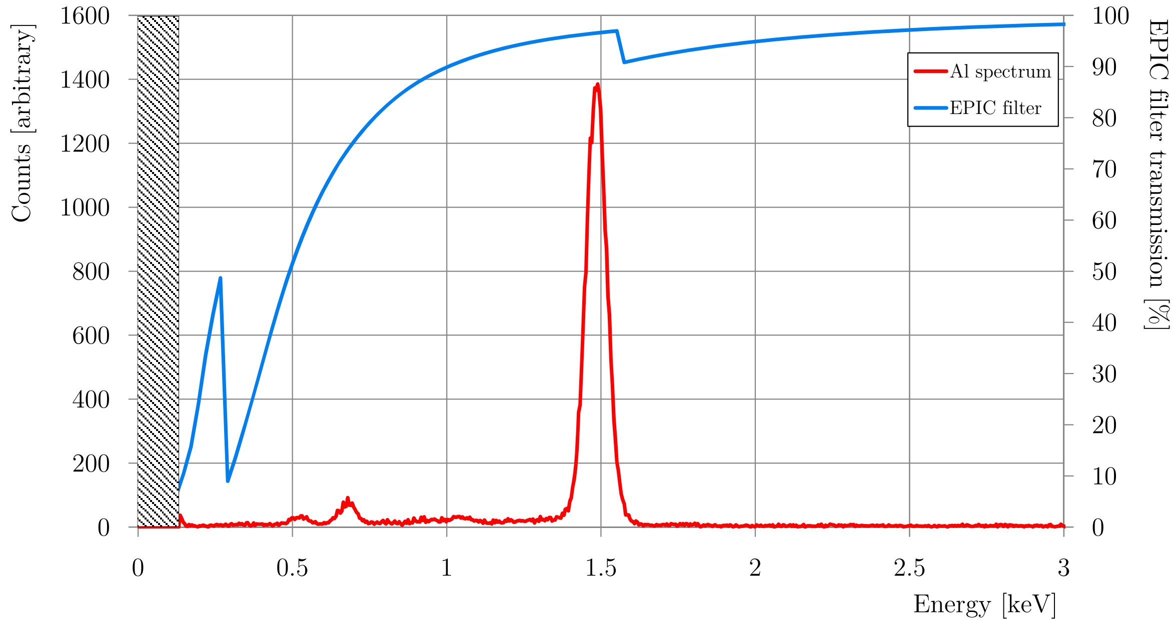

Figure 5.19: Spectrum of aluminium target with EPIC filter. The Kα1 Al peak is at 1.49 keV. In the same spectrum one can see the O Kα1 line of 0.525 keV and another peak at 0.68 keV possibly from F (Kα1,2) coming from the Viton of o-rings.

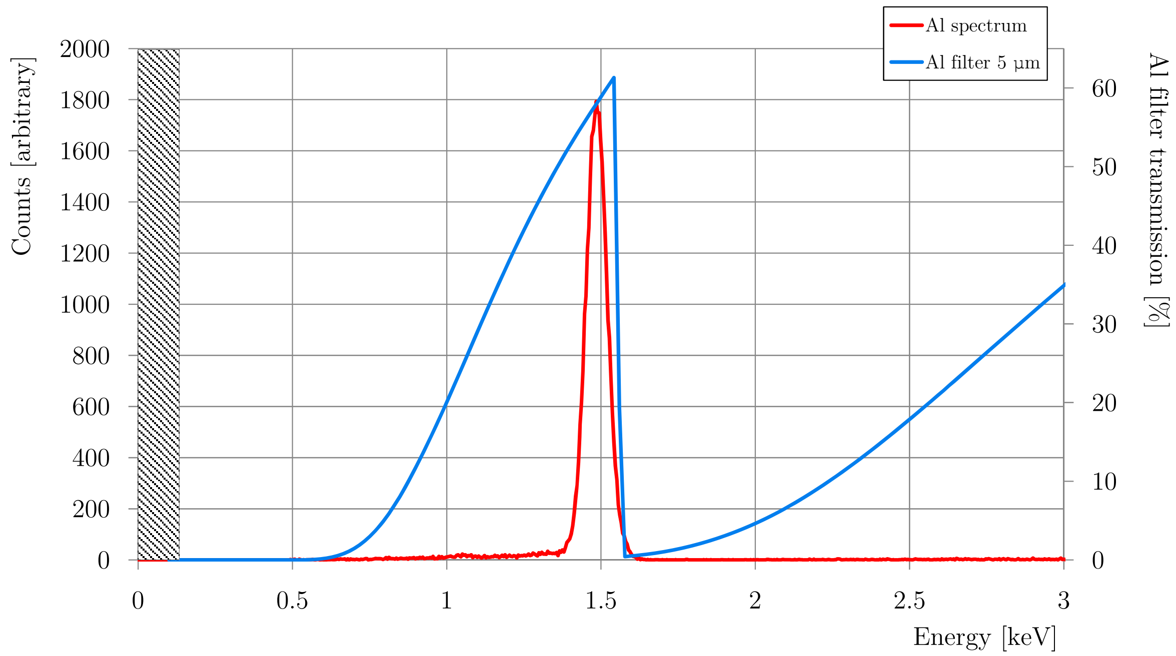

Figure 5.20: Spectrum of aluminium target with aluminium filter. Only the Kα1 Al peak can be seen at 1.49 keV.

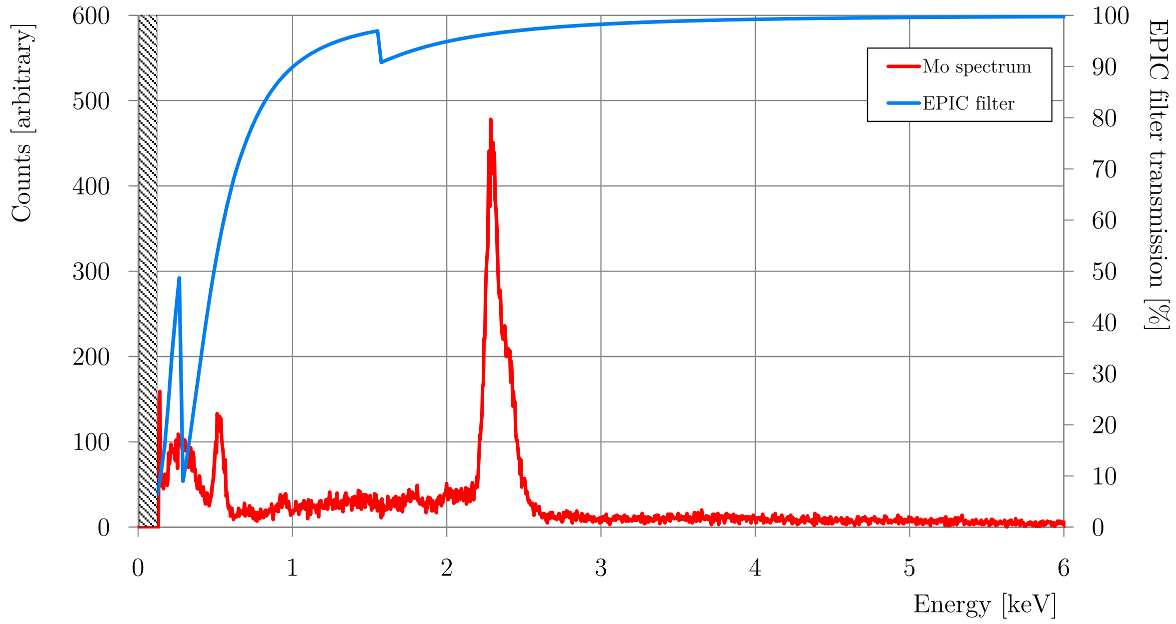

Figure 5.21: Spectrum of molybdenium target with EPIC filter. The most prominent peak of Mo is at 2.2932 keV (Lα1), with relative intensity 100, but one can also see the Lβ1 peak at 2.3948 keV (relative intensity 53). The Kα1,2 peak of O at 0.525 keV is also visible.

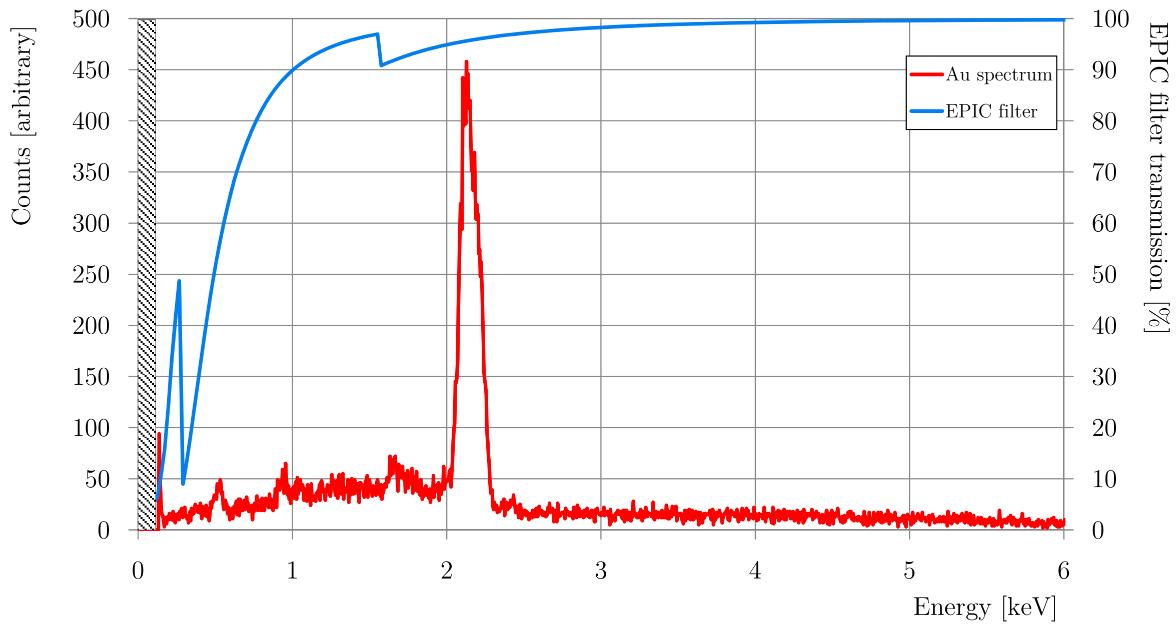

Figure 5.22: Spectrum of gold target with EPIC filter. The Mα1 peak of Au is at 2.123 keV.

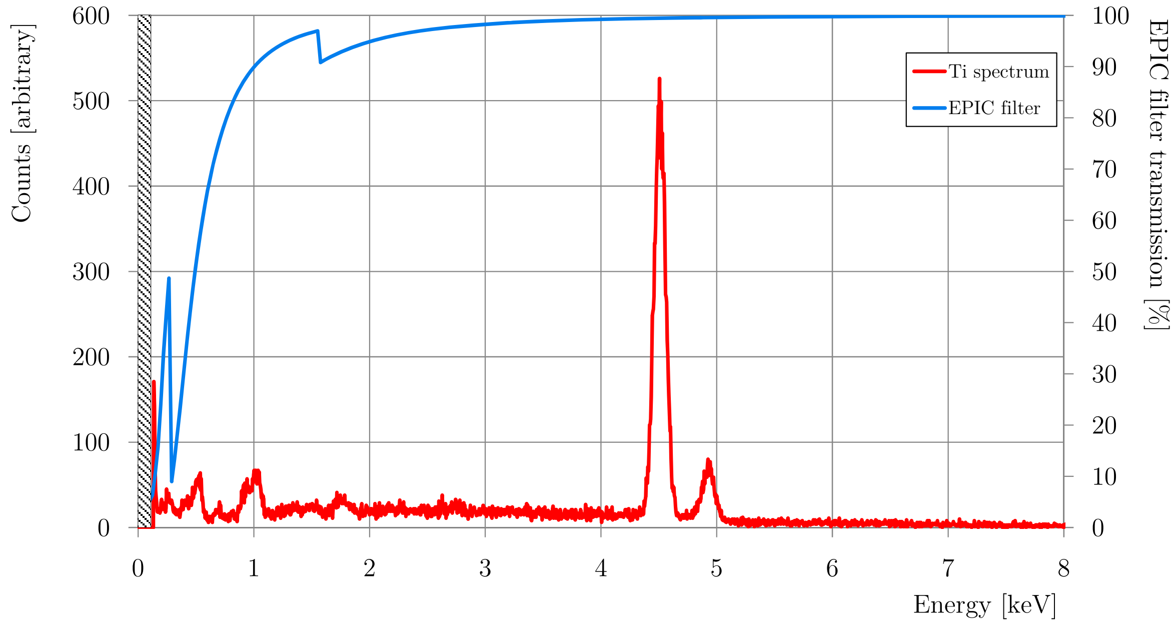

Figure 5.23: Spectrum of titanium target with EPIC filter. The Ti peaks of Kα1 and Kβ1,3 are at 4.51 and 4.93 keV with relative intensities 100 and 15 respectively. One can also see the O Kα1 peak at 0.525 keV and some Cu L peaks (Lα1,2 and Lβ1 with energies 0.93 and 0.95 keV and relative intensities 111 and 65 respectively).

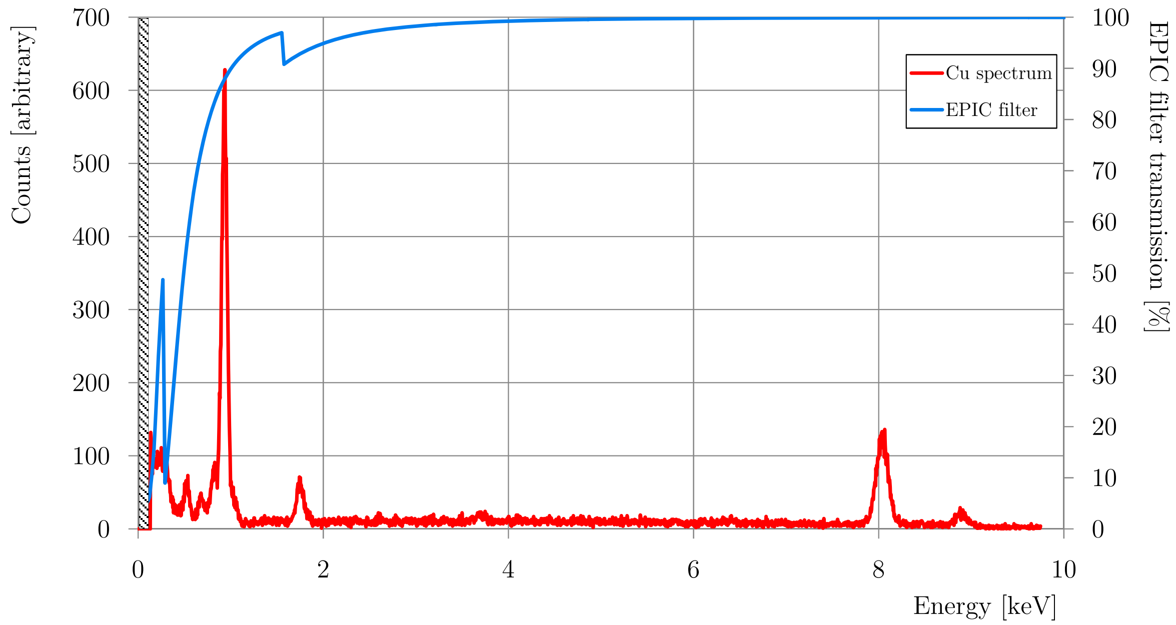

Figure 5.24: Spectrum of copper target with EPIC filter. The most prominent peak is the combination of the Cu Lα1,2 and Lβ1 peaks with energies 0.93 and 0.95 keV and relative intensities 111 and 65 respectively). The Kα1, Kα2 (seen as one peak) and Kβ1,3 peaks of Cu can be seen at the right side of the spectrum with energies 8.05, 8.03 and 8.9 keV and relative intensities 100, 51 and 17 respectively. Other peaks are the O Kα1,2 peak at 0.525 keV and the Si Kα1 peak at 1.74 keV.

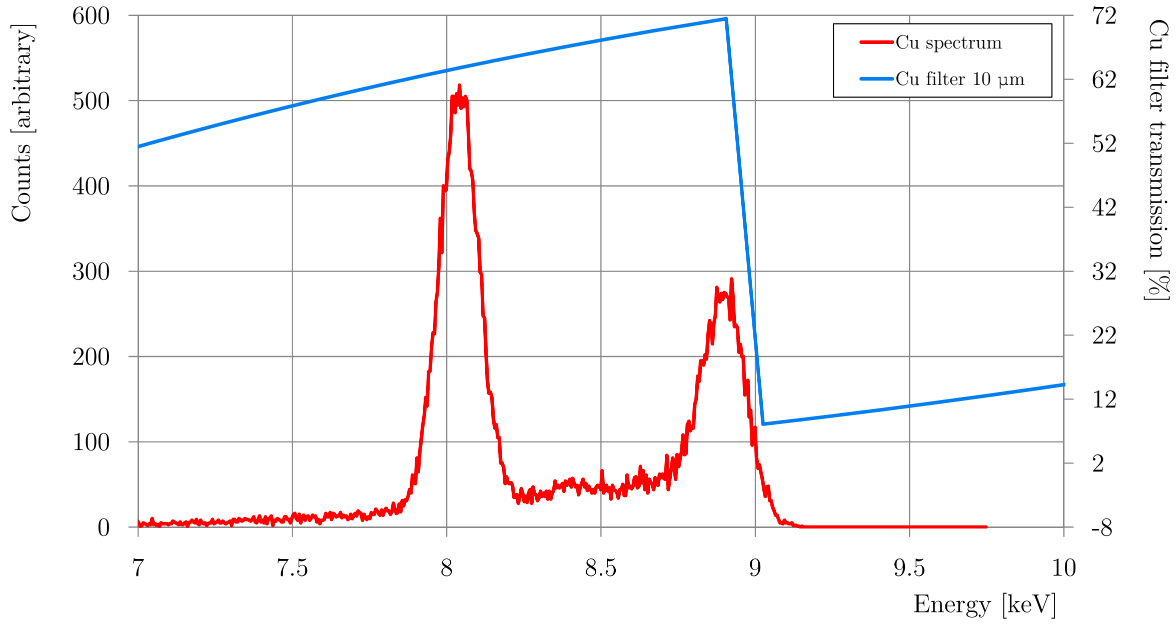

Figure 5.25: Spectrum of copper target with copper filter. The Kα1 and Kα2 (seen as one peak) and Kβ1,3 peaks of Cu can be seen with energies 8.05, 8.03 and 8.9 keV and relative intensities 100, 51 and 17 respectively.

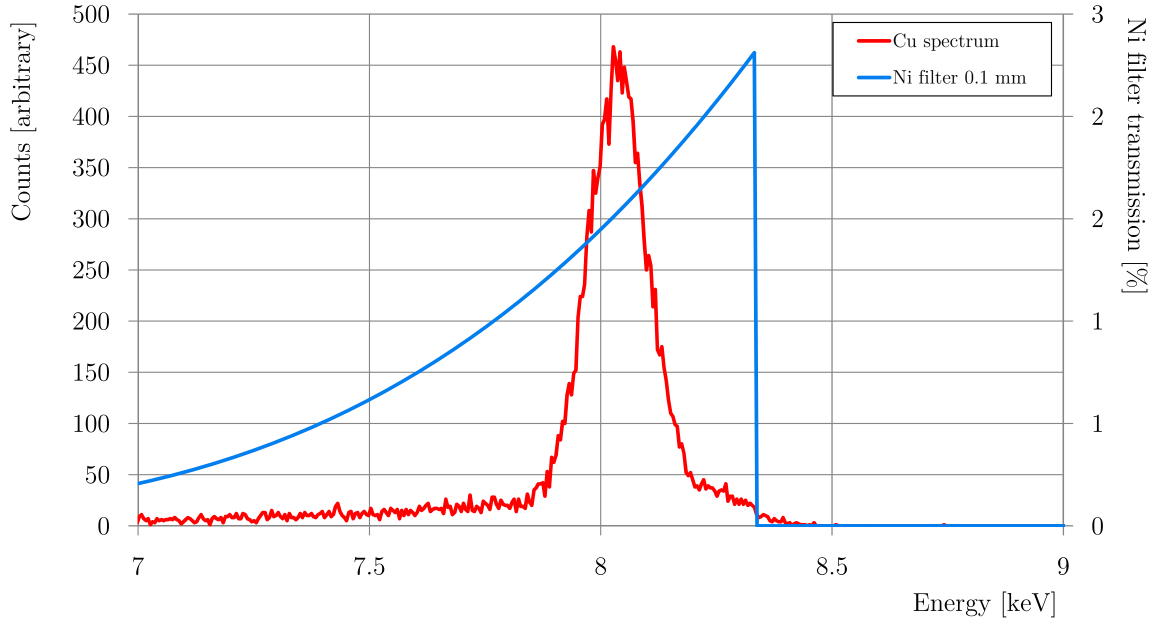

Figure 5.26: Spectrum of copper target with nickel filter. Only one peak is visible, which is a superposition of the Kα1 and Kα2 peaks of Cu with energies 8.05, 8.03. The Kβ1 line is cut off due to the fact that nickel is a β-filter.

5.4.2 Micromegas detectors

After the commissioning of the X-ray beam line and the first measurements taken with the SDD, four Micromegas detectors were installed in line. The detectors were housed inside a Faraday cage, as seen in Figure 5.1. The connections of the gas lines and the signals were made via feedthroughs.

The calibration of the detectors was made from the back of the detector with an ^{55}Fe source that was placed in a socket machined in the back cover of the Faraday cage (Figure 5.1 (b)). The calibration from the back is possible because all of the detectors have an area of 10 mm in diameter in their centre, where the plexiglass of the racquet has a thickness of 2 mm (instead of 10 mm), in order to allow the X-rays to pass through to the detector.

In the CAST detector lab four Micromegas detectors were tested, M14, M16, M18 and M19. The M14, together with M9 (that was not tested) are the two detectors that were mounted in the sunset side of the CAST experiment and the M18 and M19 are the ones that are replacing them. M16 is a spare detector that was offered from CEA-Saclay for testing.

Prior to each set of measurements a thorough leak test was done in each detector. An inherant leak rate of 1-3 mbar $\cdot$ l/s was found in all the detectors, when installed in the line under vacuum, with the most leak tight being the M18 (1.3 mbar $\cdot$ l/s and the rest around 3 mbar $\cdot$ l/s).

The results of the analysis of all the detectors were similar, except M14 whose performance was very bad. In this chapter the results that are going to be presented are based on the analysis of the data taken with M19.

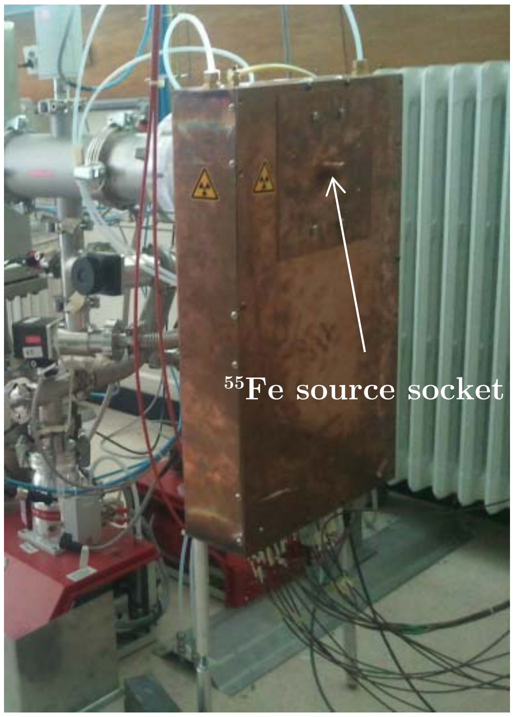

(a) (b)

Figure 5.27: (a) The connection of the Micromegas detector in the X-ray beam line and (b) a view of the setup with the Faraday cage closed. The socket of the ^{55}Fe source is visible in the back cover of the Faraday cage.

5.4.2.1 M19

The measurements that were carried out with M19 are summarised in Table 5.5 and Table 5.6 together with all the settings and significant parameters that were recorded.

^{55}Fe Calibrations			
V_{mesh} [+V]	325	325	325
V_{drift} [+V]	611	611	611
P_3 [mbar]	5.9×10^{-7}	5.5×10^{-7}	4.9×10^{-7}
P_6 [mbar]	1.4×10^{-6}	1.4×10^{-6}	1.4×10^{-6}
P_{gas} [mbar]	1402.5	1395.0	1423.54
HV [kV]	-	-	-
$V_{filament}$ [V]	-	-	-
$I_{filament}$ [V]	-	-	-
Rate [Hz]	26.7	25.3	25.2
Raw event N	50000	50000	40000
Run number	825	832	837

Table 5.5: Summary of the ^{55}Fe calibrations taken with the M19 detector and the corresponding settings and parameters.

Target:	**Al**	**Au**	**Mo**	**Ti**	**Cu**
Filter:	**Al**	**EPIC**	**EPIC**	**EPIC**	**Ni**
V_{mesh} [+V]	325	325	325	325	325
V_{drift} [+V]	611	611	611	611	611
P_3 [mbar]	5.4×10^{-7}	5.7×10^{-7}	5.4×10^{-7}	5.8×10^{-7}	5.6×10^{-7}
P_6 [mbar]	1.4×10^{-6}	1.4×10^{-6}	1.4×10^{-6}	1.4×10^{-6}	1.4×10^{-6}
P_{gas} [mbar]	1404.7	1405.0	1416	1401.18	1396.8
HV [kV]	5	7	7	9	13
$V_{filament}$ [V]	2.8	2.5	2.6	2.58	3.65
$I_{filament}$ [V]	0.71	0.67	0.68	0.66	0.82
Rate [Hz]	63.3	63.4	61.9	54.2	48.8
Raw event N	80000	110000	80000	120000	110000
Run number	834	829	836	827	831

Table 5.6: Summary of the measurements with the X-ray target, taken with the M19 detector and the corresponding settings and parameters.

The superposition of the X-Y distribution of all the runs with the X-ray beam and the ^{55}Fe calibration events are shown in Figure 5.28 and 5.29 respectively. In Figure 5.28 one can observe what seems to be a dead X strip in the left side of the detector. This exact same pattern has been observed in all the detectors tested, with different gassiplexs, so it is not a faulty gassiplex. The reason is a CRAM with one faulty channel, which has already been changed.

In Figure 5.30, the raw images of the energy recorded from the mesh versus the energy recorded from the strips are shown for all the runs, including the calibration. The recorded events that do not follow the band E_{mesh}=E_{strips} are uncorrelated events, meaning that in these cases the pulse that was recorded from the Matacq was different from the one that the gassiplexs recorded. The cause has been identified as a fine tune of the timing settings of the sequencer (delay between the trigger and the track and hold signals). Nevertheless the number of these events is very small.

In order to clear the data from the uncorrelated events, before the calculation of the software efficiency, a manual cut was implemented:

$$E_{\text{mesh}} > 1.1 \cdot (E_{\text{strips}} - 2) + 2.4 \tag{5.1}$$

and

$$E_{\text{strips}} > 1.1 \cdot (E_{\text{mesh}} - 2) + 2.4 \quad . \tag{5.2}$$

The results of this selection are seen in Figure 5.32, Figure 5.34, Figure 5.36, Figure 5.38 and Figure 5.40.

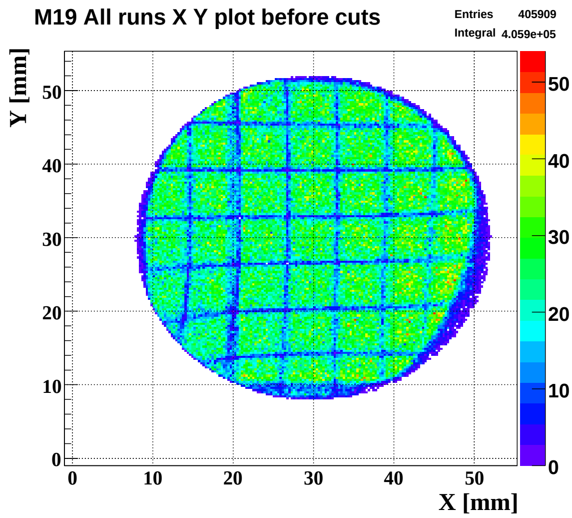

Figure 5.28: The X-Y hit map of all the runs with the X-ray beam.

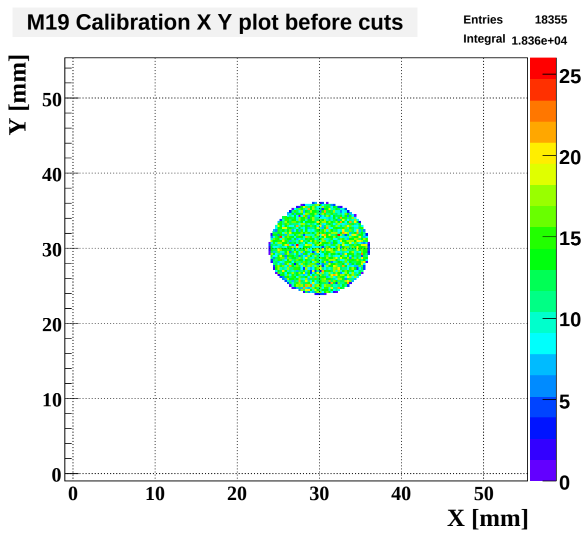

Figure 5.29: The X-Y hit map of a calibration with the ^{55}Fe source from the back.

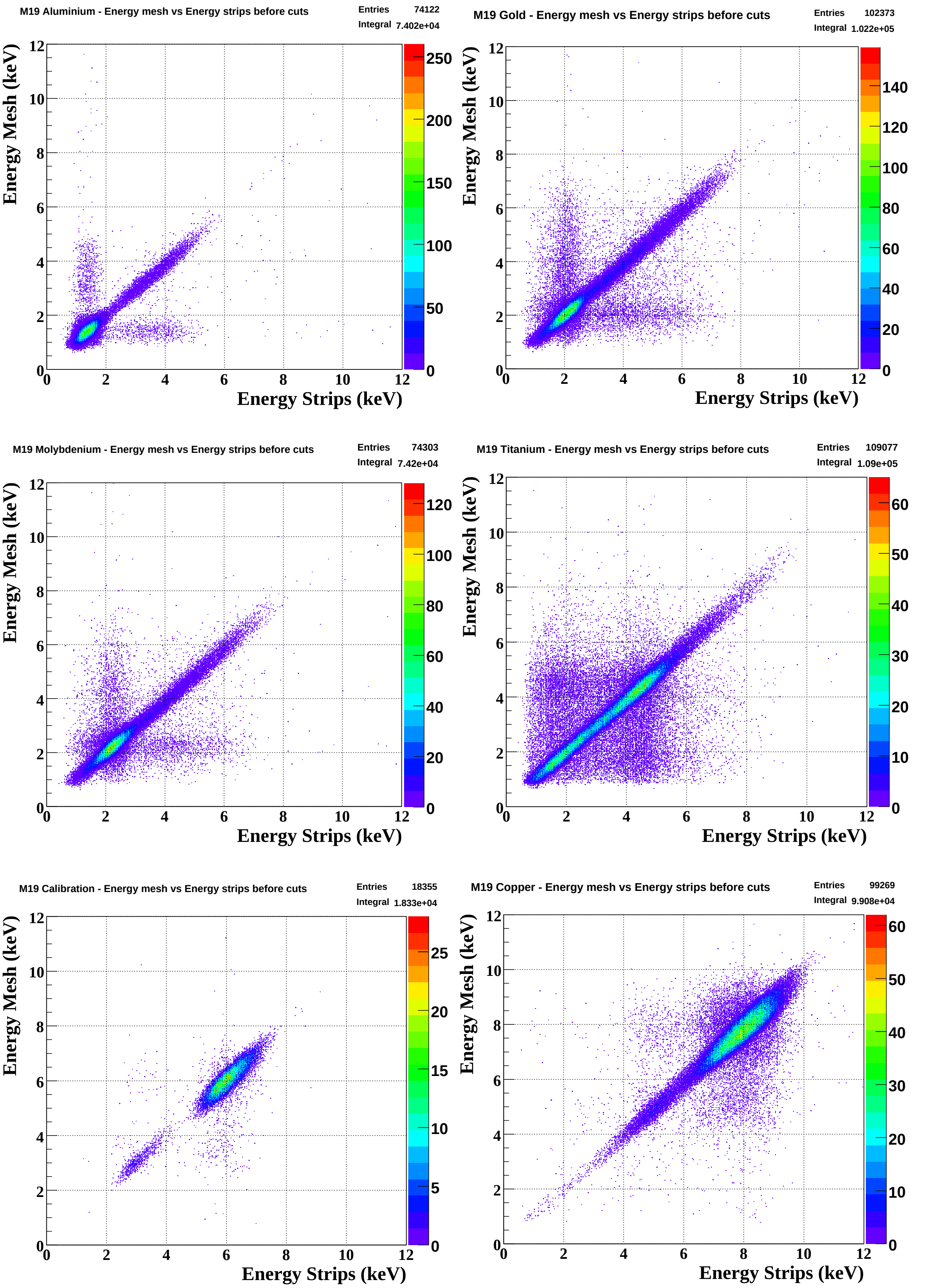

Figure 5.30: The raw images of the energy recorded from the mesh versus the energy recorded from the strips for all the runs.

Calculation of the software efficiency in the emission energies of the targets

The main goal of the CAST detector lab was to evaluate the efficiency of the selection criteria used in the analysis of the Micromegas detectors in CAST. In each measurement with the X-ray beam line, the energy calibration was done with an adjacent ^{55}Fe run. The mean energy of each peak was calculated with the best Gaussian fit. In Table 5.7 the energies of the peaks of each target are shown, together with the expected ones [96].In Figure 5.31 the deviation of the calculated and the expected peak energy versus the energy of the peak is shown.

Target/source	**Measured peak[keV]**		**Real peak [keV]**
	Strips	**Mesh**	
Al	$1.38 \pm 4.8 \times 10^{-2}$	$1.40 \pm 4.8 \times 10^{-3}$	1.487
Au	$2.09 \pm 1.0 \times 10^{-1}$	$2.07 \pm 1.0 \times 10^{-1}$	2.123
Mo	$2.25 \pm 1.1 \times 10^{-1}$	$2.22 \pm 1.1 \times 10^{-1}$	2.327
Ti	$4.40 \pm 2.6 \times 10^{-1}$	$4.29 \pm 3.8 \times 10^{-2}$	4.547
^{55}Fe	$6.00 \pm 2.7 \times 10^{-1}$	$6.03 \pm 2.65 \times 10^{-1}$	5.96
Cu	$7.98 \pm 2.64 \times 10^{-1}$	$7.78 \pm 2.48 \times 10^{-1}$	8.041

Table 5.7: The calculated energies of the peaks of each target or source and the expected ones [97].

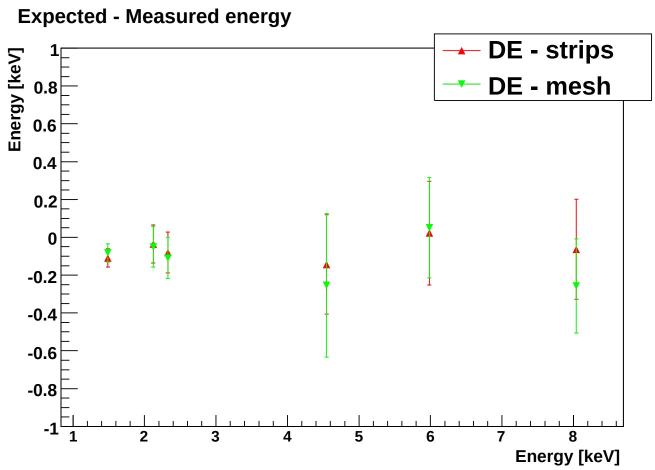

Figure 5.31: Difference of the expected energy of the peak of each target and the measured one from the mesh and the strips.

After the calculation of the energy of each peak an integration is performed at ±0.25 keV around the peak. The efficiency is then calculated as:

$$Efficiency = \frac{\int_{m-0.25}^{m+0.25} dN \text{ (after cuts)}}{\int_{m-0.25}^{m+0.25} dN \text{ (before cuts)}}, \tag{5.3}$$

where m is the mean of the Gaussian fit to the peak. The efficiency is calculated for the mesh cuts, the strip cuts and all the cuts separately. Mesh cuts are the selection criteria that are based on information from the mesh pulses such as the pulse width and amplitude and strip cuts are the ones that are defined by the information from the strips, like multiplicity, sigma etc. (see Chapter 4).

Figure 5.32 to Figure 5.43 show the spectra acquired from all the targets and the effect of the different cuts. Figure 5.44 is a superposition of all the counts acquired from all the targets and the ^{55}Fe source. It shows generally linear behaviour between the mesh and the strips, although in high energies (above 7 keV) the mesh energy seems not to increase linearly, probably due to the fact that the pulse duration is longer than the integration time of the amplifier and as a result a fraction of the energy is lost. Table 5.8 summarises the software efficiency acquired with each target and the ^{55}Fe source and the graphical representation is shown in Figure 5.45 and Figure 5.46.

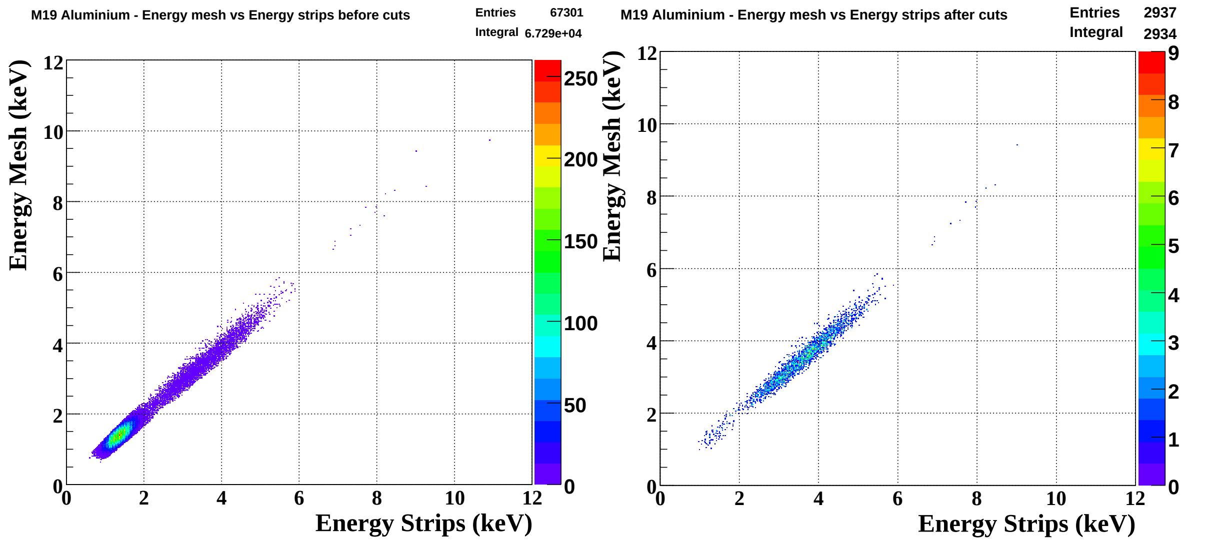

Figure 5.32: Energy from the mesh versus energy from the strips from aluminium before (left) and after (right) the application of cuts.

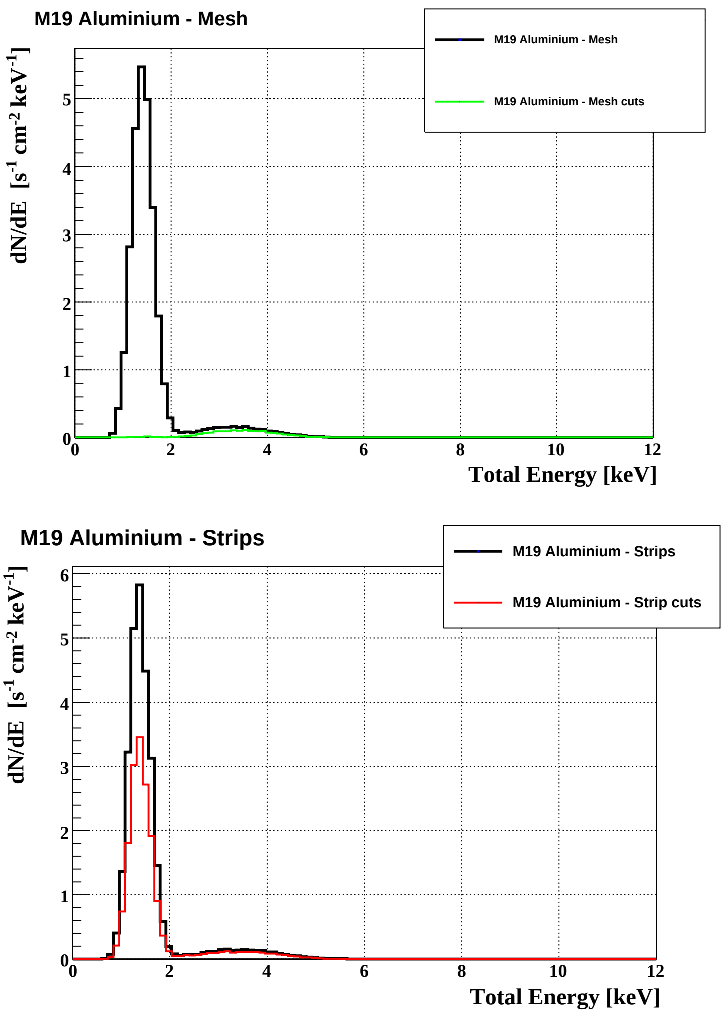

Figure 5.33: Energy spectrum of aluminium acquired from the mesh (top) and the strips (bottom) before and after the cuts.

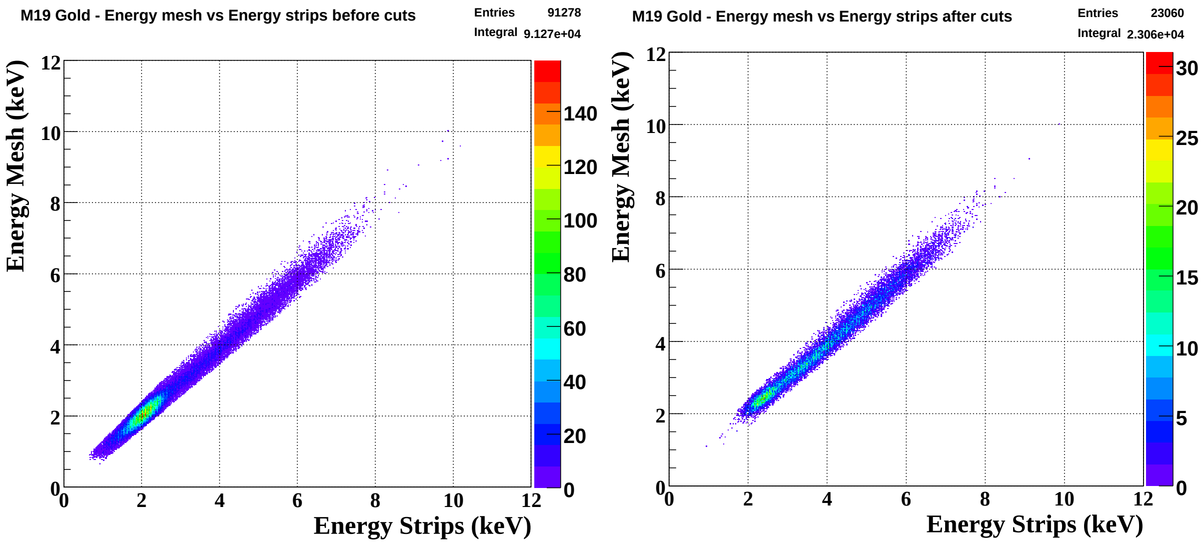

Figure 5.34: Energy from the mesh versus energy from the strips from gold before (left) and after (right) the application of cuts.

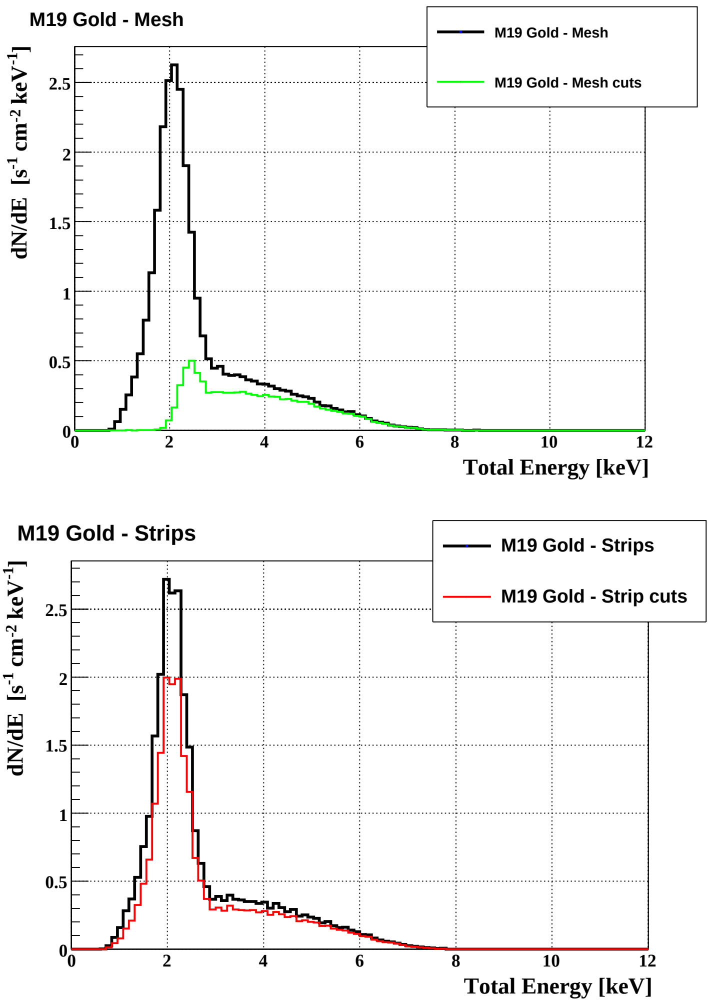

Figure 5.35 Energy spectrum of gold acquired from the mesh (top) and the strips (bottom) before and after the cuts.

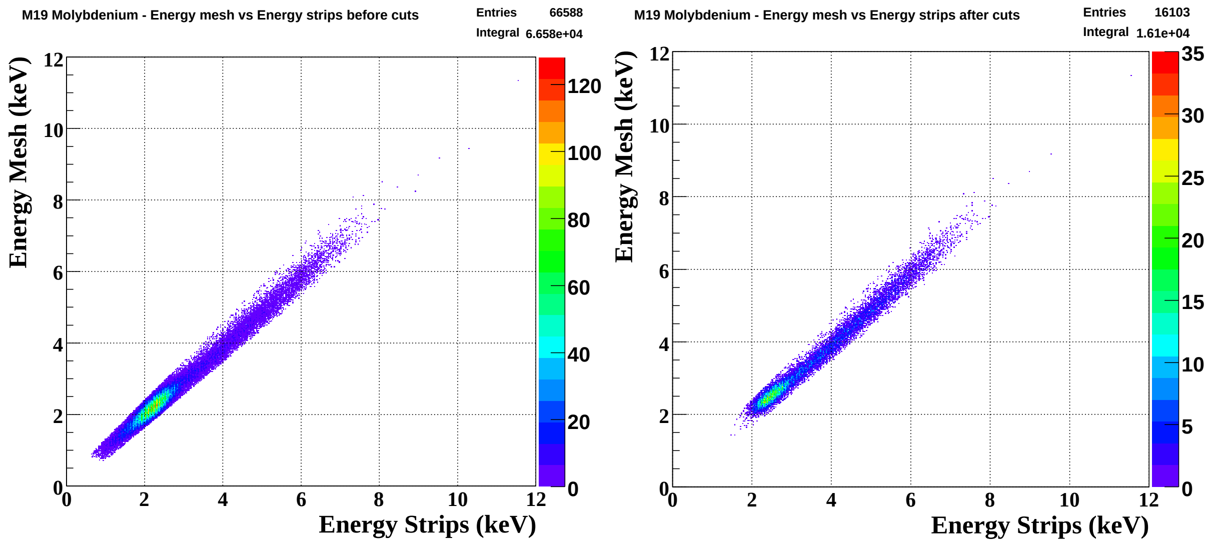

Figure 5.36: Energy from the mesh versus energy from the strips from molybdenum before (left) and after (right) the application of cuts.

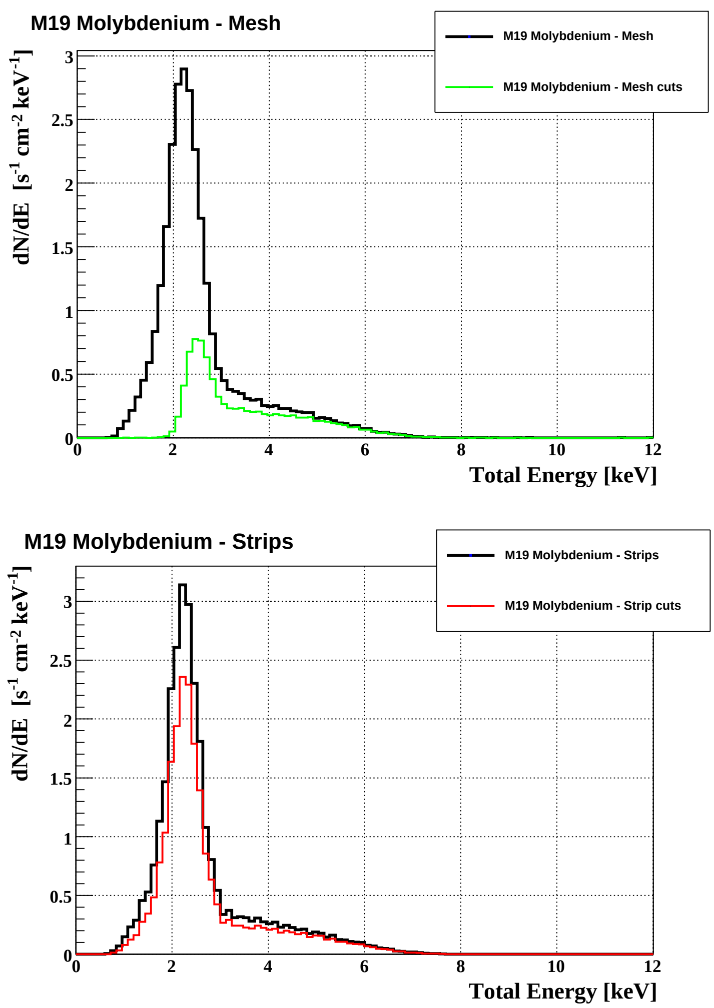

Figure 5.37: Energy spectrum of molybdenum acquired from the mesh (top) and the strips (bottom) before and after the cuts.

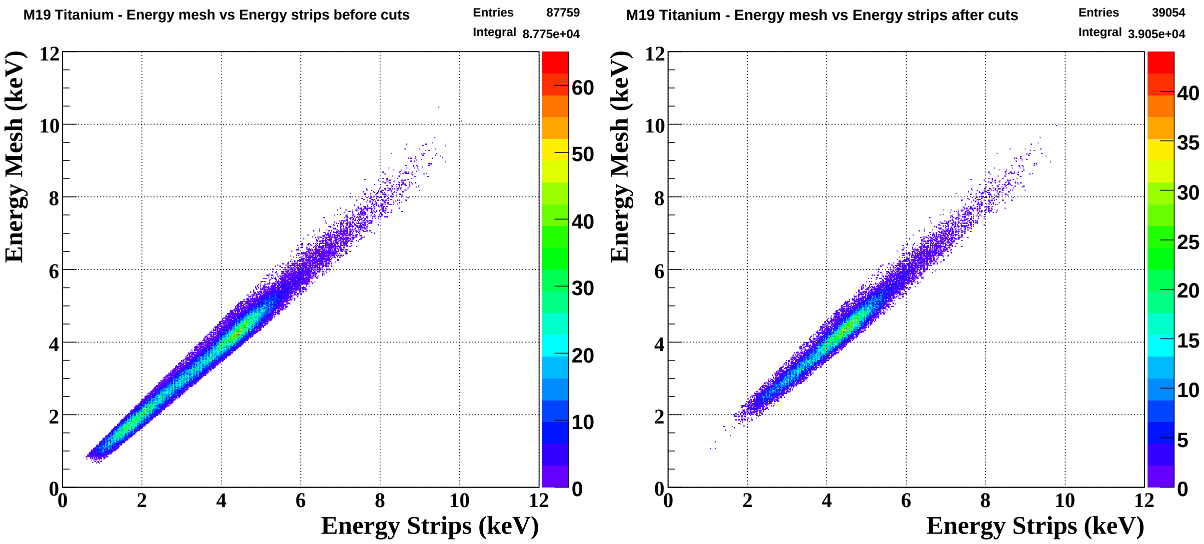

Figure 5.38: Energy from the mesh versus energy from the strips from titanium before (left) and after (right) the application of cuts.

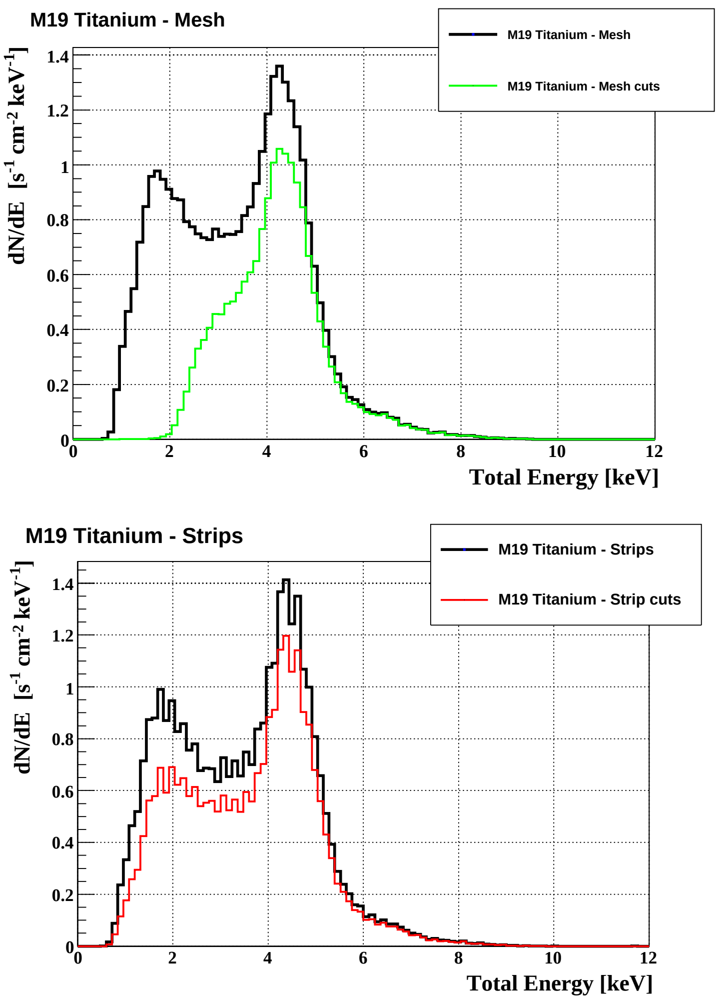

Figure 5.39 Energy spectrum of titanium acquired from the mesh (top) and the strips (bottom) before and after the cuts.

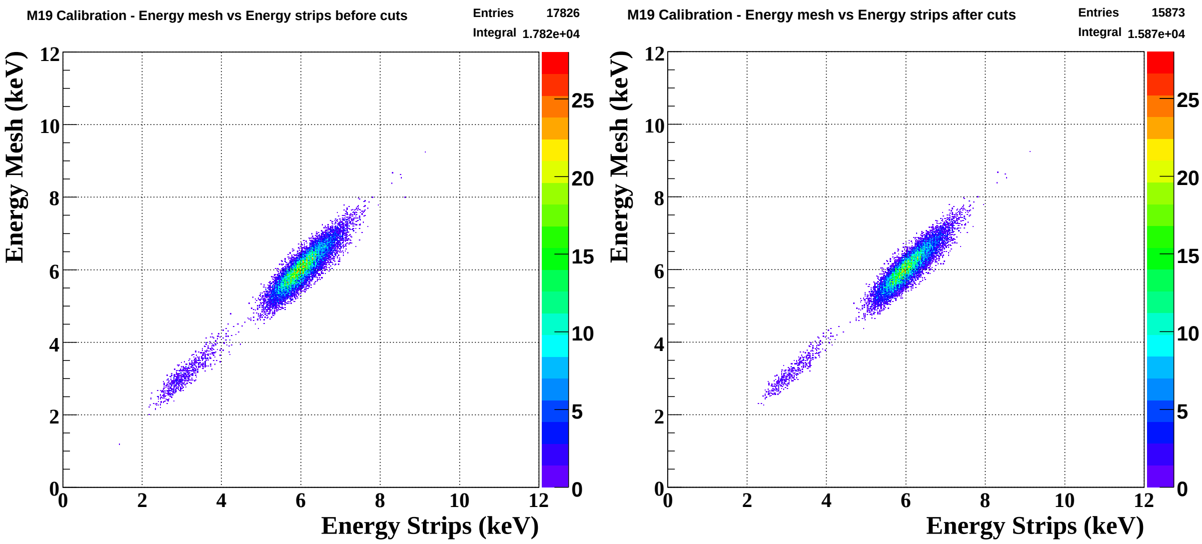

Figure 5.40: Energy from the mesh versus energy from the strips from a calibration with ^{55}Fe before (left) and after (right) the application of cuts.

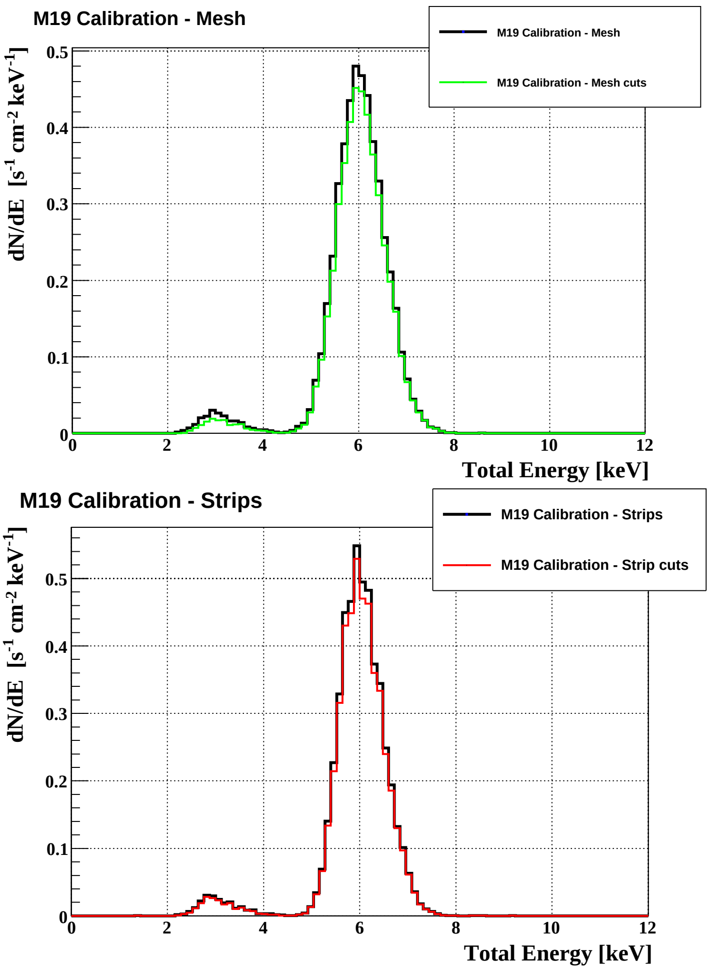

Figure 5.41: Energy spectrum of ^{55}Fe acquired from the mesh (top) and the strips (bottom) before and after the cuts.

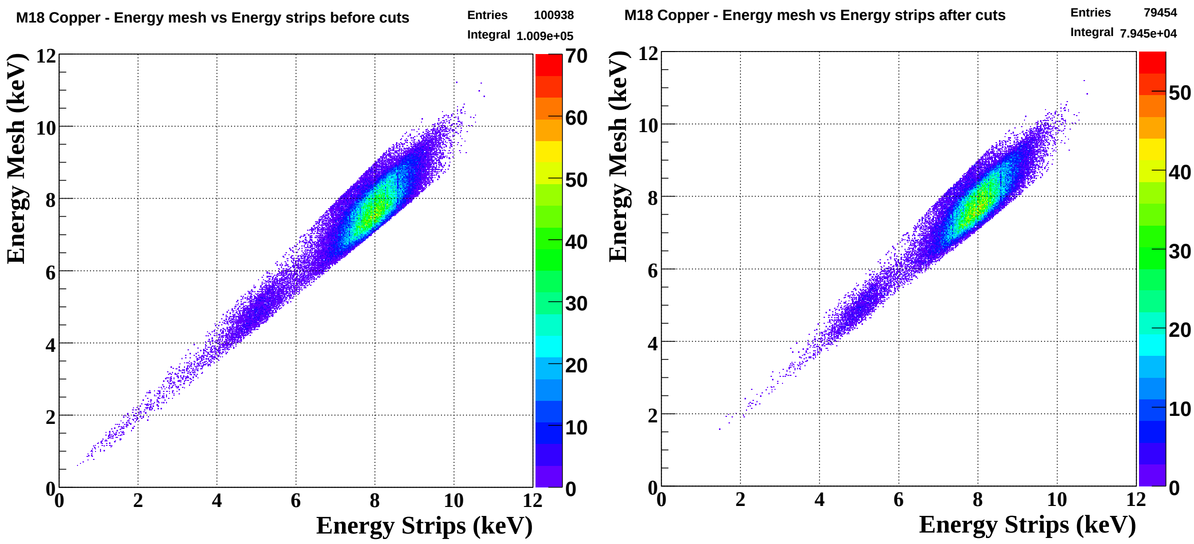

Figure 5.42: Energy from the mesh versus energy from the strips from copper before (left) and after (right) the application of cuts.

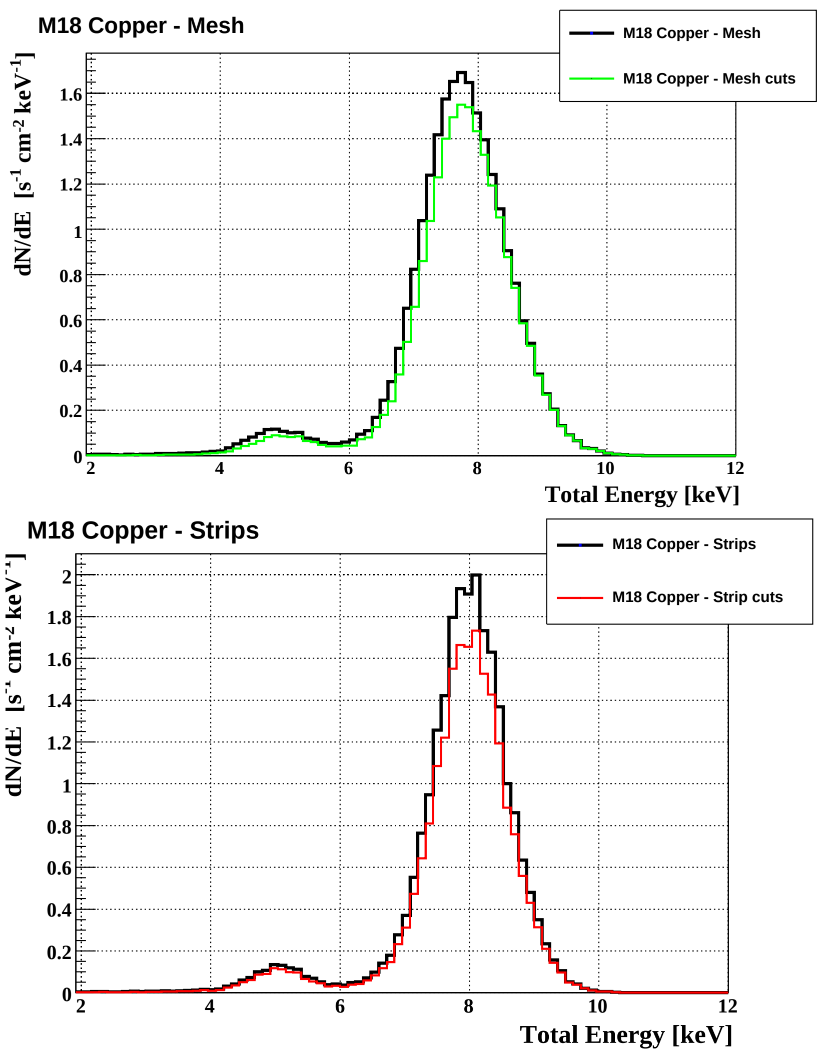

Figure 5.43: Energy spectrum of copper acquired from the mesh (top) and the strips (bottom) before and after the cuts.

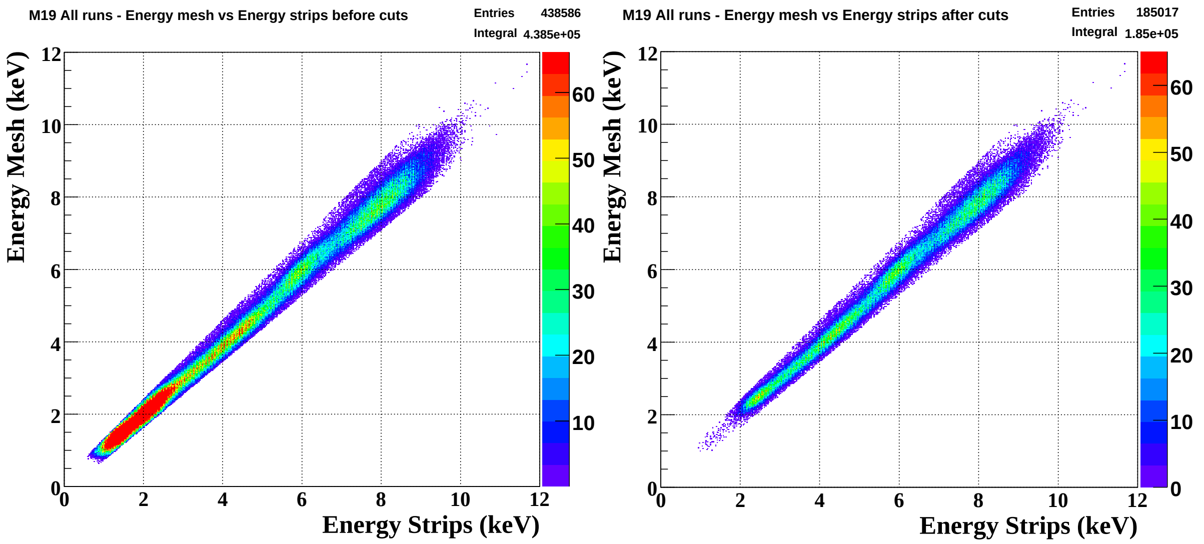

Figure 5.44: Superposition of the data acquired from all the targets and the ^{55}Fe source.

Target/source	Measured peak[keV]		Total efficiency %	
	Strips	Mesh	Strips	Mesh
Al	1.38±4.8×10^{-2}	1.40±4.8×10^{-3}	0.15±0.38	0.14±0.37
Au	2.09±1.0×10^{-1}	2.07±1.0×10^{-1}	7.0±2.6	5.3±2.3
Mo	2.25±1.1×10^{-1}	2.22±1.1×10^{-1}	13.6±3.7	11.8±3.4
Ti	4.40±2.6×10^{-1}	4.29±3.8×10^{-1}	66.3±8.15	66.4±8.16
^{55}Fe	6.00±2.7×10^{-1}	6.03±2.65×10^{-1}	88.0±9.5	91.1±9.6
Cu	7.98±2.64×10^{-1}	7.78±2.48×10^{-1}	81.68±7.9	81.2±8.3

Table 5.8: Summary of the efficiency of the software selection criteria for each target and the ^{55}Fe source.

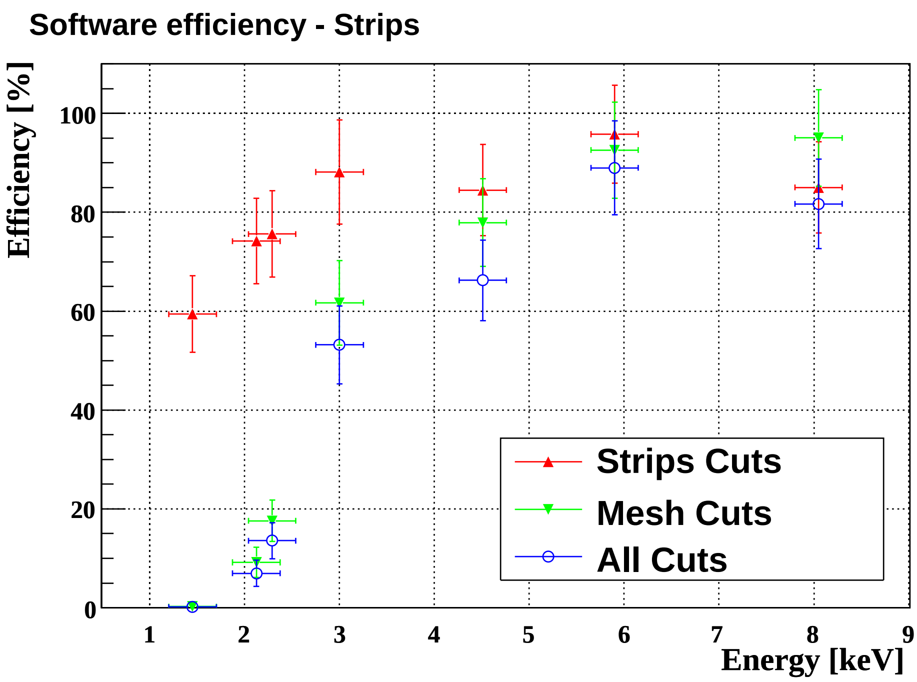

Figure 5.45: Software efficiency for the different energies of the targets with cuts applied to the mesh counts. The efficiency at 3 keV was derived from the escape peak of argon during an ^{55}Fe calibration.

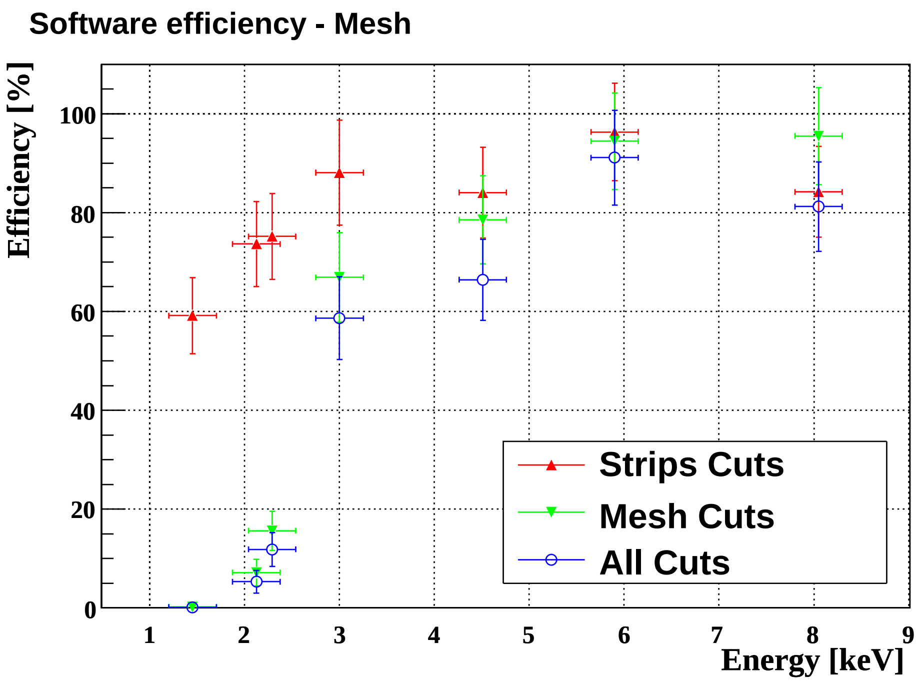

Figure 5.46: Software efficiency for the different energies of the targets with cuts applied to the strips counts.

5.5 Prospects and conclusions

In the CAST detector lab, for the first time, it was possible to test the efficiency, with respect to the energy, of the software selection criteria that are used in the offline analysis of CAST. Although the investigation of the software efficiency and the optimization of the analysis to obtain the best efficiency with the lowest possible background level, exceeds the scope of this thesis, some plots have been generated, which show the evolution of the selection criteria and characteristics of the pulses with the energy for the three detectors, M16, M18 and M19. These plots were created by the events that have ±0.5keV from the mean energy of the peak of each target and are presented in chapters 5.5.1-3.

From the results of the analysis it is evident that a calibration with the ^{55}Fe source illuminating the back of the detector does not fully match a calibration from the front. The reason is that when calibrating from the back of the detector, the majority of the primary electrons are created close to the amplification region, while during the calibration from the front, the majority of the photons are converted close to the drift window. In the first case the electrons travelling a shorter distance in the gas mixture, diffuse less, resulting in shorter pulses with shorter risetime, with respect to the ones that are produced when calibrating from the front of the detector (see figures in chapters 5.5.1 to 5.5.3). This phenomenon has an impact on the selection of the X-rays coming from the front, as seen in Figure 5.46. In practice this means that with the current configuration more events are rejected than if the calibration was done from the front of the detector. Therefore the first improvement that is considered for the X-ray generator is to install a manganese target to the X-ray wheel, which will give the same emission lines as the radioactive ^{55}Fe. In addition a combination of a number of targets and filters is going to be added, to have a variety of emission lines from a few hundred eV to 9 keV.

These first results of the CAST detector lab are just the beginning of a series of studies that will be carried out aiming to a better understanding of the behaviour of the detector and more efficient selection criteria.

5.5.1 M16 observables evolution with energy

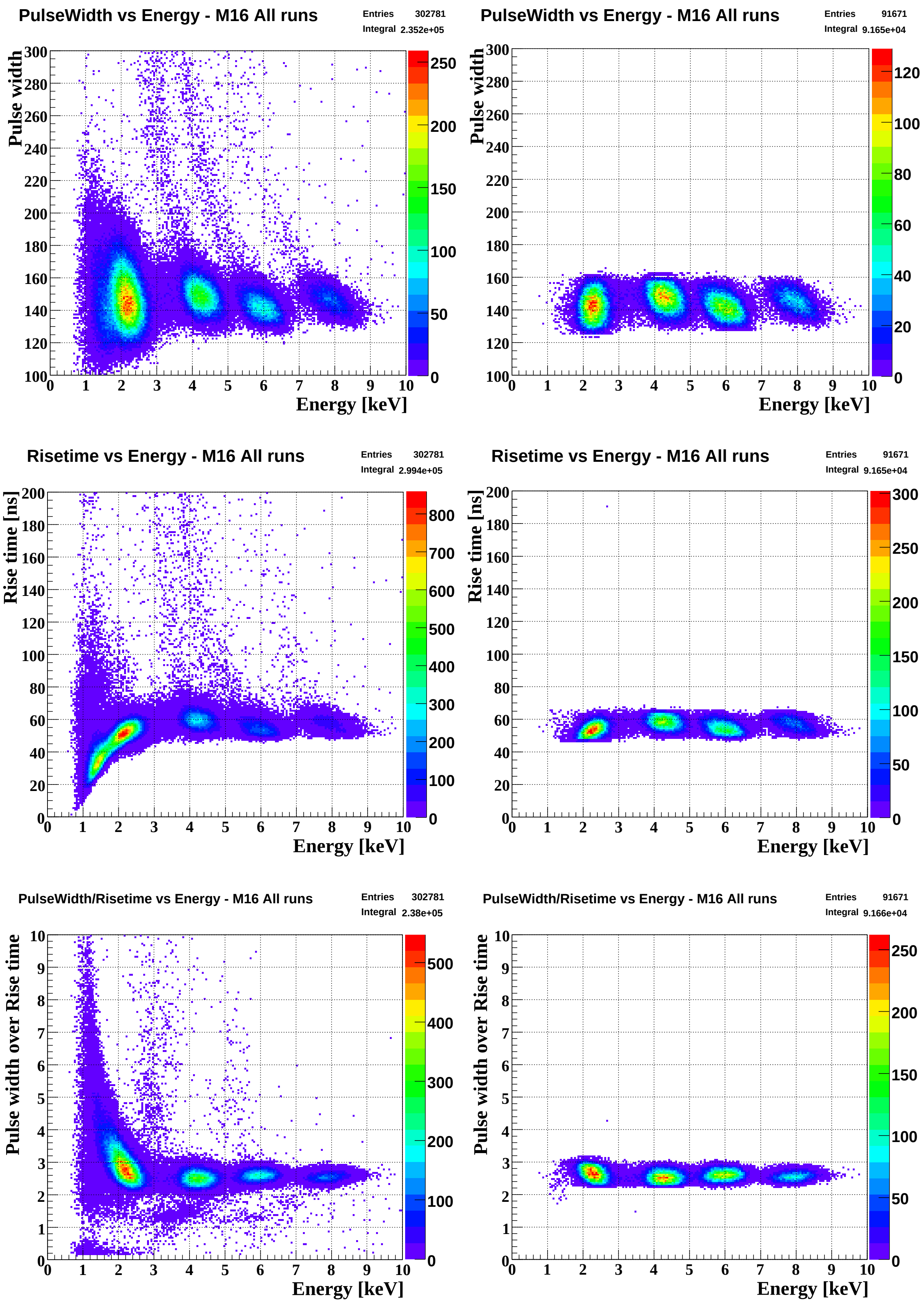

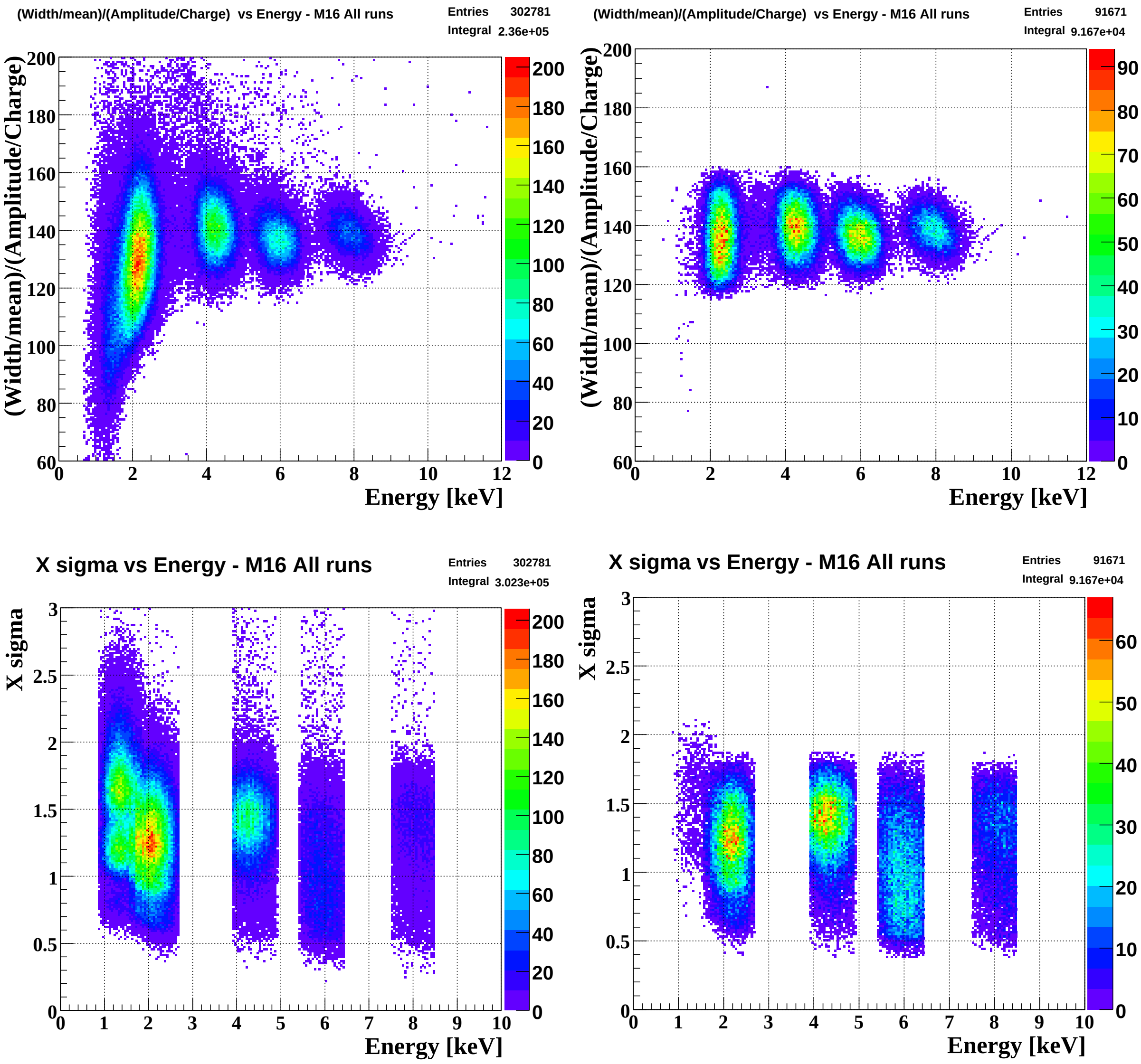
(Width/mean)/(Amplitude/Charge) vs Energy - M16 All runs
Entries 302781
Integral 2.36e+05
(Width/mean)/(Amplitude/Charge)
Energy [keV]
(Width/mean)/(Amplitude/Charge) vs Energy - M16 All runs
Entries 91671
Integral 9.167e+04
(Width/mean)/(Amplitude/Charge)
Energy [keV]
X sigma vs Energy - M16 All runs
Entries 302781
Integral 3.023e+05
X sigma
Energy [keV]
X sigma vs Energy - M16 All runs
Entries 91671
Integral 9.167e+04
X sigma
Energy [keV]

5.5.2 M18 observables evolution with energy

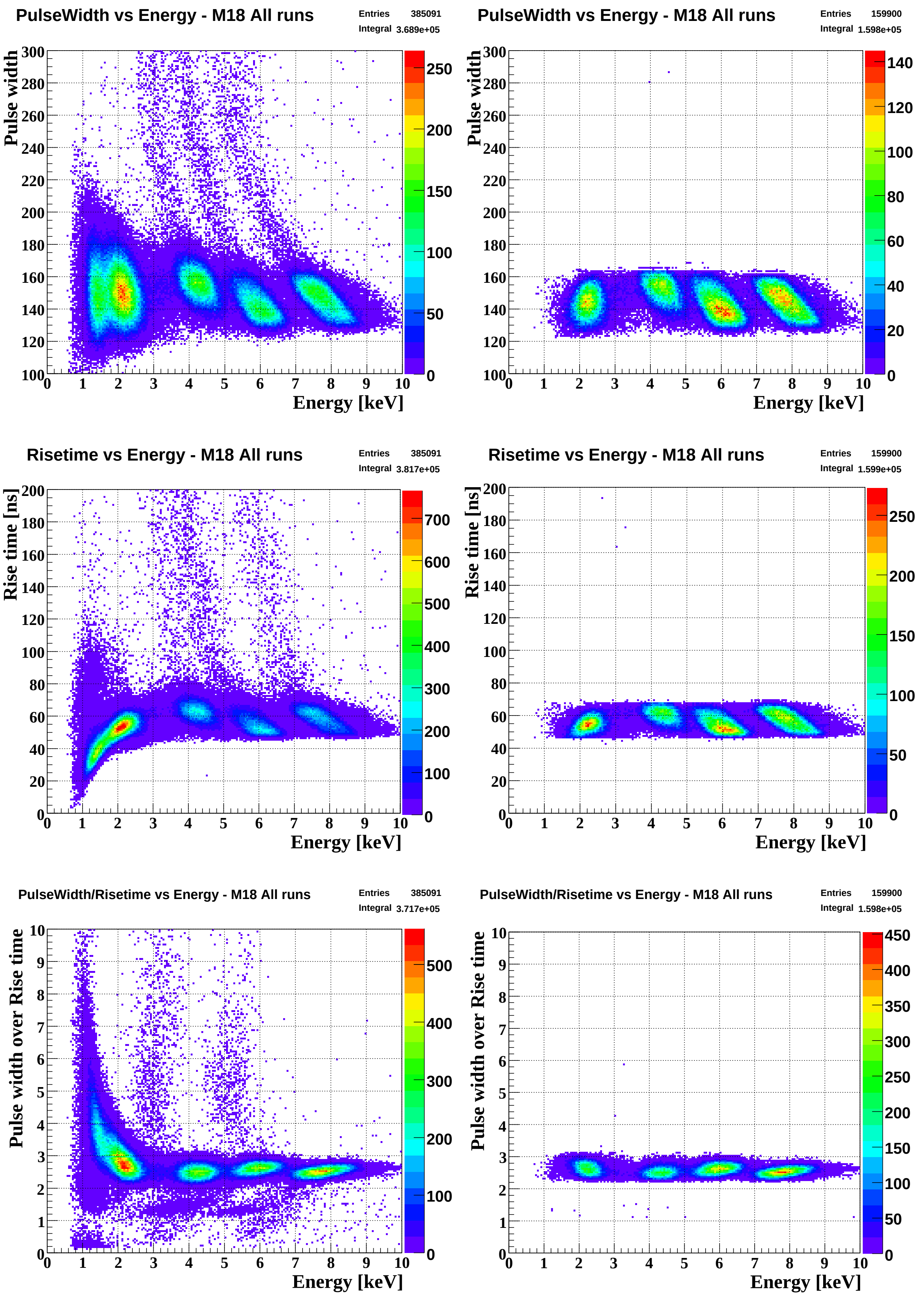

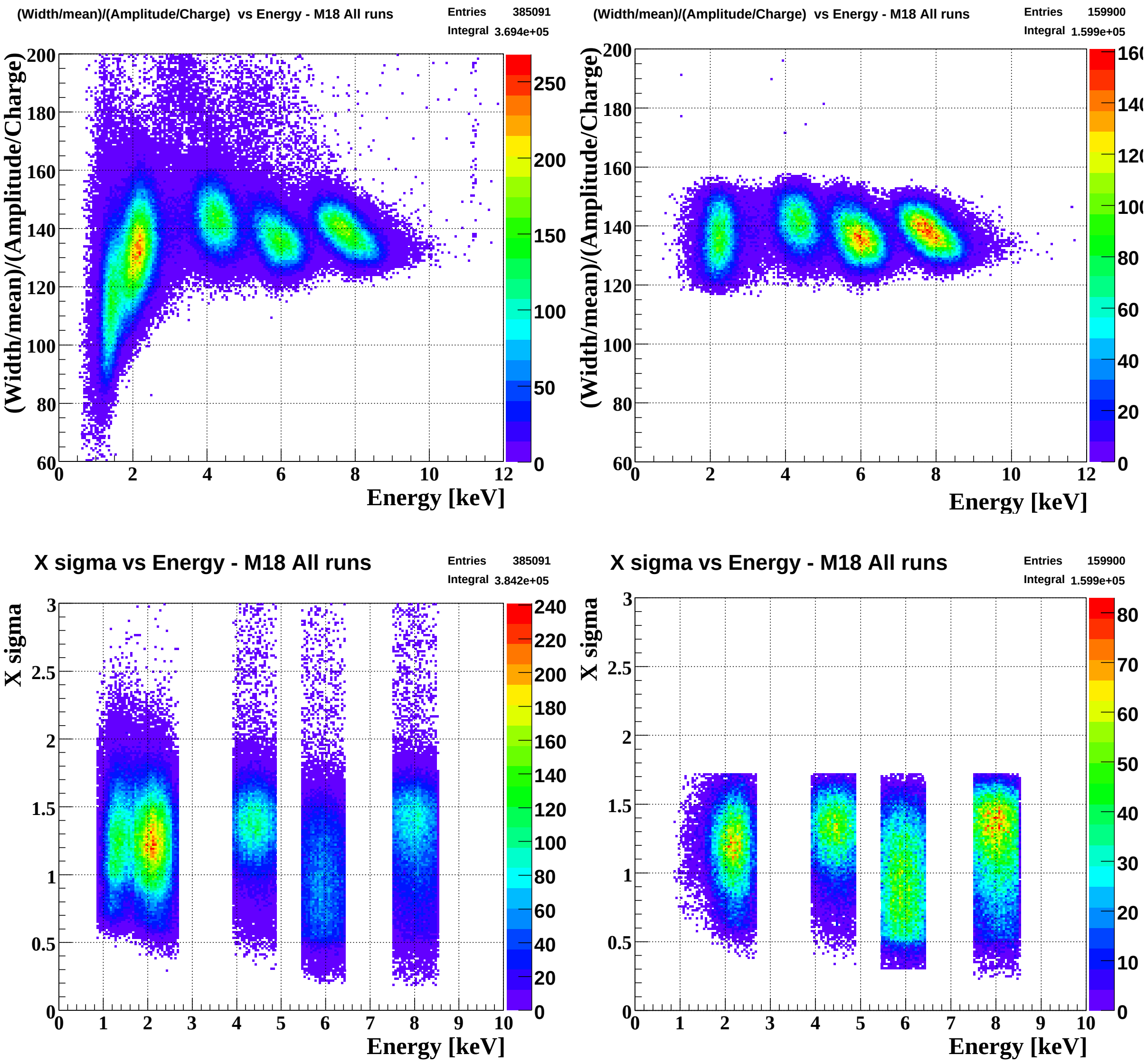
(Width/mean)/(Amplitude/Charge) vs Energy - M18 All runs
Entries 385091
Integral 3.694e+05
(Width/mean)/(Amplitude/Charge)
Energy [keV]
(Width/mean)/(Amplitude/Charge) vs Energy - M18 All runs
Entries 159900
Integral 1.599e+05
X sigma vs Energy - M18 All runs
Entries 385091
Integral 3.842e+05
X sigma
X sigma vs Energy - M18 All runs
Entries 159900
Integral 1.599e+05

5.5.3 M19 observables evolution with energy

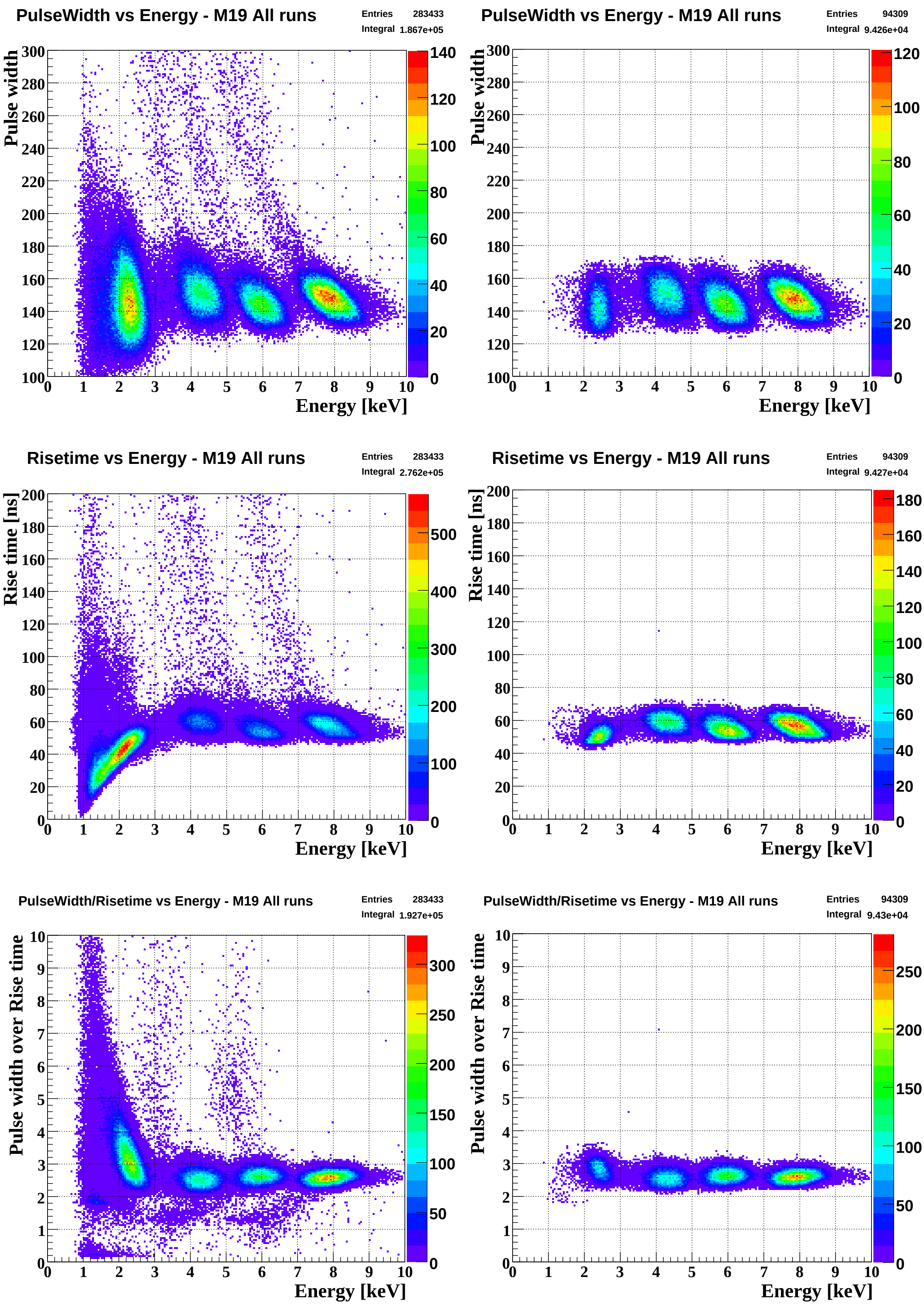

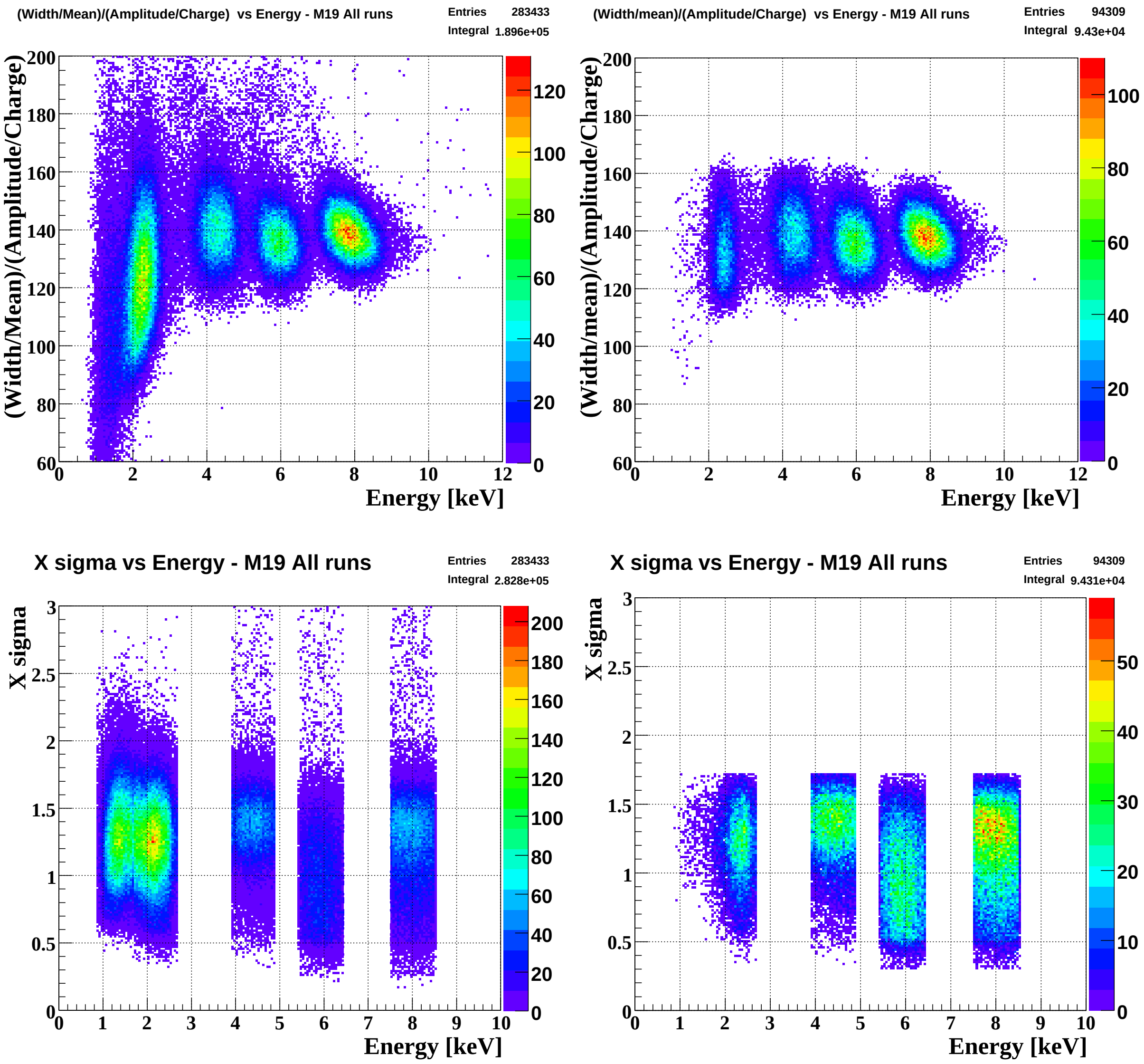

(Width/Mean)/(Amplitude/Charge) vs Energy - M19 All runs
Entries 283433
Integral 1.896e+05
(Width/Mean)/(Amplitude/Charge)
Energy [keV]
(Width/mean)/(Amplitude/Charge) vs Energy - M19 All runs
Entries 94309
Integral 9.43e+04
(Width/mean)/(Amplitude/Charge)
Energy [keV]
X sigma vs Energy - M19 All runs
Entries 283433
Integral 2.828e+05
X sigma
Energy [keV]
X sigma vs Energy - M19 All runs
Entries 94309
Integral 9.431e+04
X sigma
Energy [keV]

6. Sunrise Micromegas data taking

Contents

6.1 Discrimination of tracking and background data

During the data taking periods, each morning, the sunrise tracking takes place. Its start and duration depend on the season and the spacial restrictions to the movement of the CAST magnet. Furthermore occasionally there are short interruptions of the data taking period, due to accidents, malfunctions, quenches etc. Therefore it is not certain that every background run contains a tracking which has a specific start and duration, so the timings of the tracking have to be set dynamically.

In order to determine the tracking times a number of parameters that are recorded from the Tracking PC and the Slow Control are assessed. These parameters are:

Magnet Movement
During the tracking of the Sun, the magnet has to move in both directions (horizontal and vertical).

Tracking flag
A Boolean number that is recorded from the tracking program and it is 1 when the Sun is within the reach of the magnet and 0 when it is not.

Tracking precision
It is the precision with which the magnet follows the Sun. During a tracking, this parameter has to be smaller than 10^{-3} degrees in both directions of movement.

Magnet Current
During tracking the current of the magnet has to be 13000 A.

Magnetic Field
The Magnetic field should be above 8.9 T, in order to have the maximum conversion probability during tracking.

Gate valve open
This condition is essential, so that the axion conversion area of the cold bore is visible to the detector. During tracking the Boolean referring to the status of the gate valve should be 1.

When all these conditions are met the events recorded in the background runs are considered as events that occurred during tracking.

6.2 The 2009 run

6.2.1 CAST data taking overview

The 2009 data taking period lasted from the 13th of July to the 8th of December. During this period the CAST experiment visited 247 pressure settings (from #420 to #647), which correspond to pressures in the cold bores from 37.5 mbar at 1.8 K to 65.2 mbar at 1.8 K. The axion mass range covered is 0.66-0.88 eV/c^2. The full data taking period of 2009 is summarised in Figure 6.1, in terms of the pressure evolution of $P_{1.8}$ - the pressure in the cold bores corrected to 1.8K.

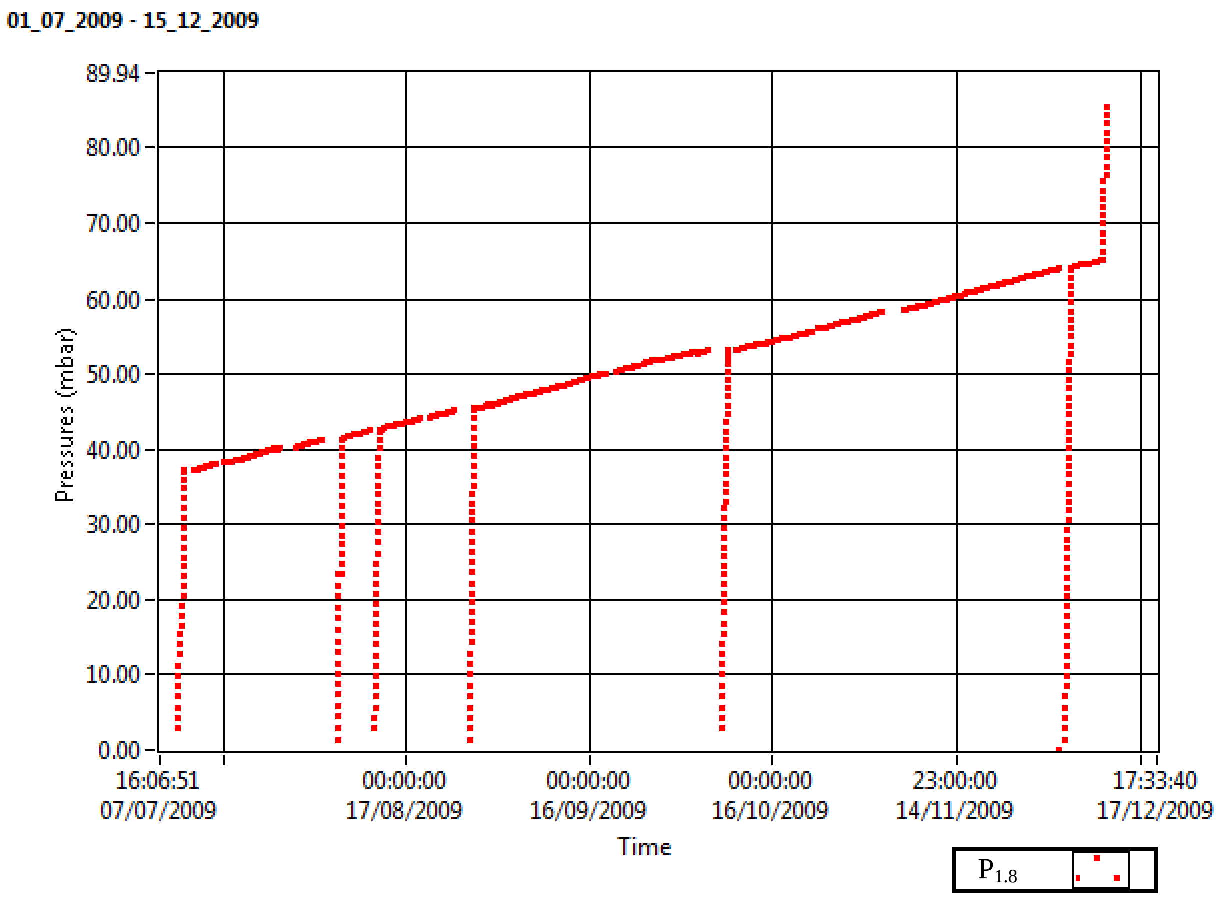

Figure 6.1: The full data taking period of 2009, in terms of the pressure evolution in the cold bores ($P_{1.8}$ refers to the pressure in the cold bores corrected to 1.8K). The gaps are due to several stoppages because to incidents like quenches, bake-outs of the cold windows or power cuts. Two test fillings were performed at the end of the run to 75 and 85 mbar at 1.8K.

The most significant events that resulted in the loss of more than 3 consecutive days of data taking are:

Programming bug in the PLC ^{3}He control program

A bug in the program that controls the ^{3}He circuit of the CAST experiment resulted in a false quench signal, opening the valves of the cold bores and evacuating the ^{3}He to the expansion volume.

Quench occurred on the 3rd of August

A power cut that took place in the building of the CAST experiment resulted in the discharge of the quench heaters to the magnet. The CAST team profited from this event to bake out the cold windows. The ^{3}He was refilled in the cold bores and the data taking was resumed on the 7th of August.

Natural Quench of 25th of August

The magnet quenched while it was taking position for the morning tracking. The data taking was resumed on the 29th of August

Planned stoppage from 5th to 8th of October

This stoppage was performed in order to transfer additional quantities of ^{3}He into the closed system of the system from a ^{3}He gas cylinder. The procedure included the evacuation of the cold bores and regeneration of the filters and cold traps of the ^{3}He system.

The famous "bird and baguette" incident [98] of the 3rd of November

The short circuit of the LHC 18 kV power supply, located in SR8, in the switchyard just outside the building of the CAST experiment resulted in the stoppage of the LHC and CAST cryogenics and the evacuation of the ^{3}He from the cold bores to the storage vessel. Three days were needed to recover the systems and refill the ^{3}He back in the cold bores.

Quench of the 2nd of December

A power cut in SR8 (the site of the CAST experiment) lead to the discharge of the quench heaters into the magnet. The ^{3}He was quickly recovered, to minimise the loss of data taking days and complete the 2009 data taking program.

6.2.2 Sunrise detector data taking

6.2.2.1 Overview

The sunrise Micromegas detector had a very stable performance during 2009. From a total of 249 pressure steps visited, the detector fully covered 240, plus one with half of the nominal exposure time. It recorded successfully a total of 198 hours of tracking and 3393 hours of background time. A summary of the pressure steps missed, and the incidents that caused the problems is given bellow.

Step Numbers 438, 439
Due to a problem in the data acquisition program, the background file that contained the tracking with the specific pressure steps was completely empty.

Step Number 574
Between 07:45 and 08:29 the trigger rate varied between 5 and 15 Hz, first increasing, and then decreasing again. Due to the high trigger rate (most probably induced by a pickup noise from the motors) the file completed 250000 events and stopped, causing the loss of 23 minutes of exposure time for this pressure step.

Step Numbers 586, 587
The background file from the tracking that corresponded to steps 586 and 587 was corrupted, therefore unreadable.

Step Numbers 592, 593
Approximately 10 minutes before the shift ended the shifters noticed from the event display of the data acquisition software that the strips were not read out properly due to a possible overflow. The NIM and VME crates and the PC were rebooted. The background file that was recorded was unusable.

Step Numbers 662, 663
A malfunction in the DAQ system resulted in the record of only 7000 events in the background file, whereas the normal number is 60000-70000. For this reason it was decided that this file will be excluded from the analysis.

6.2.2.2 Stability and Characteristics

In 2009 the M9 detector, installed in the sunrise side of the CAST experiment, showed an overall stable performance. More specifically:

Gain performance

The gain of the M9 detector showed remarkable stability. In Figure 6.2, the ADC unit which corresponds to the 6 keV peak during a calibration run is displayed. The big increase on the left occurred because the mesh voltage was increased from 320 V to 324 V on the 2nd of August. On the 28th of November due to a delay in the delivery of the gas mixture used in the detector (argon-2.3% isobutane), a mixture of argon-2% isobutane was used instead, for a total of 6 days. The smaller percentage in Isobutane as a quencher gas, caused the rise in the gain. The delivery was finally made on the 3rd of December and the detector gain returned to its nominal value.

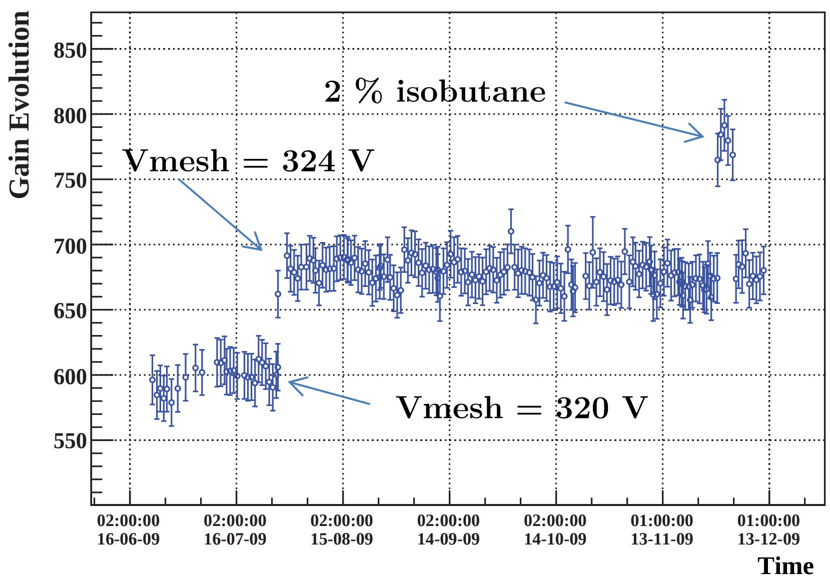

Figure 6.2: The ADC unit that corresponds to the 6keV peak of the calibration runs.

Energy resolution

The energy resolution of the detector was most of the time below 18% FWHM. After the 14^{th} of October, an increase to the noise levels, caused considerable fluctuations of the base line, which result in the deterioration of the resolution and the spikes in the right side of Figure 6.3.

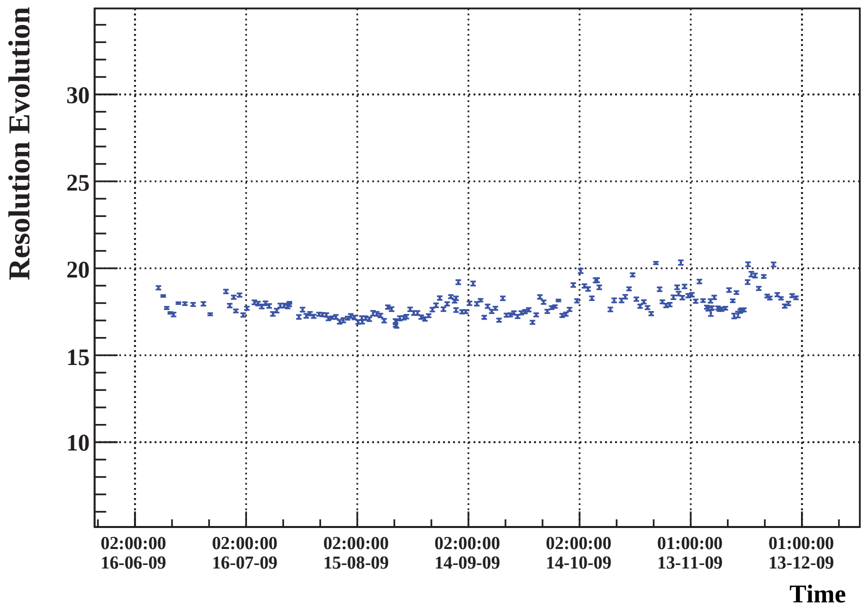

Figure 6.3: The evolution of the energy resolution during 2009.

The detector did not show any signs of aging or defects, except a known issue, which is a dead area along the X axis, in the upper part of the detector (Figure 6.4) .The reason is either that the Gassiplex that reads out the Y strips has a broken strip, or that the corresponding CRAM from the data acquisition system has a malfunctioning channel. The dead area accounts for less than 5% of the total sensitive area.

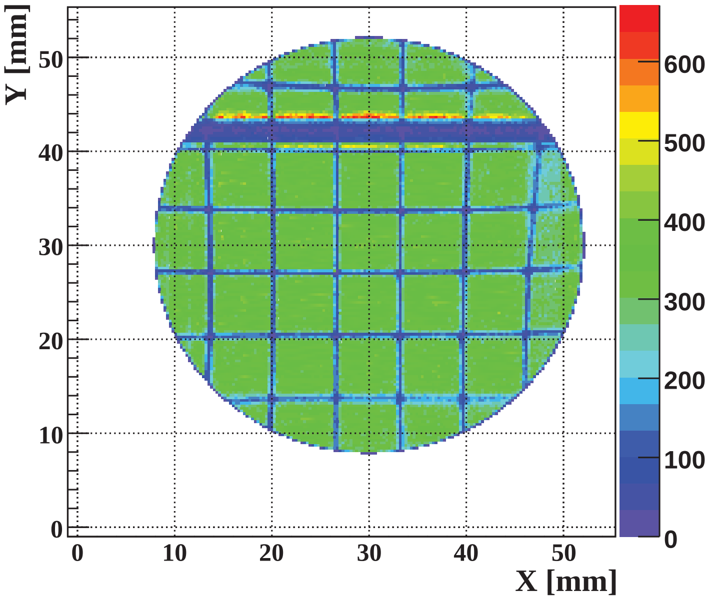

Figure 6.4: The Cold Bore area of the detector, as photographed from the X-rays of the calibration runs of 2009. The dead area in the upper semicircle accounts for less than 5% of the total area of interest.

Software efficiency at 6 keV

The software efficiency is defined for the calibration events as:

$$Efficiency = \frac{\int_{m-0.25}^{m+0.25} dN \text{ (after cuts)}}{\int_{m-0.25}^{m+0.25} dN \text{ (before cuts)}}\ , \tag{6.1}$$

where m=6 keV that corresponds to the peak of the ^{55}Fe calibration events.

The software efficiency is calculated separately for the events that are recorded from the mesh and the strips, applying the corresponding selection criteria. The total software efficiency is then given by:

$$Efficiency_{\mathrm{TOTAL}} = Efficiency_{\mathrm{STRIPS}} \cdot Efficiency_{\mathrm{MESH}} \tag{6.2}$$

The reason for separating the mesh from the strips events during a calibration, as explained in Appendix A, is a problem in the electronic configuration of the data acquisition system since the installation of the new calibrator in 2008. The gassiplex cards were not protected from triggering (veto) when the Matacq card was read; something that in high trigger rate conditions leads to the recording of uncorrelated mesh and strips characteristics for the same event.

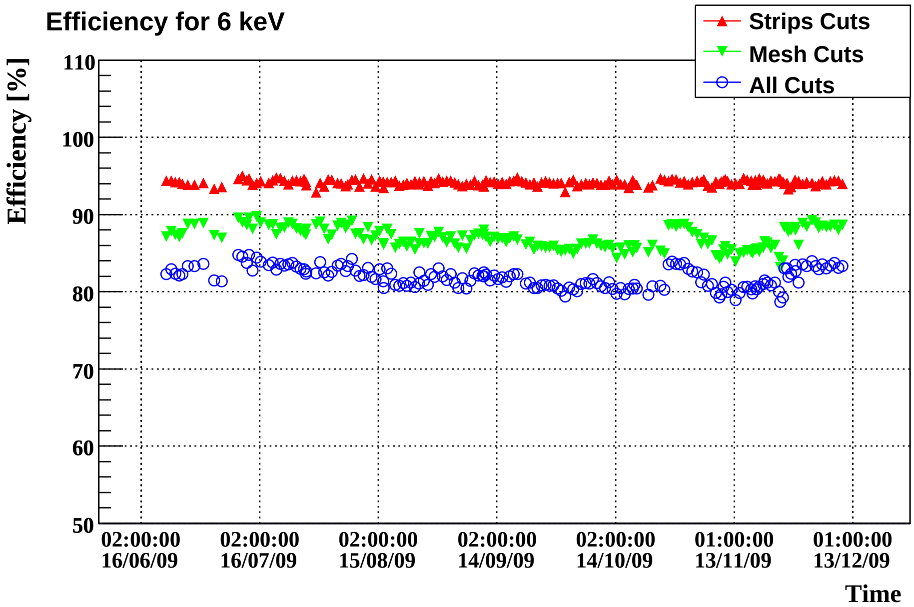

Figure 6.5: The software efficiency for the 6 keV events that were recorded from the strips.

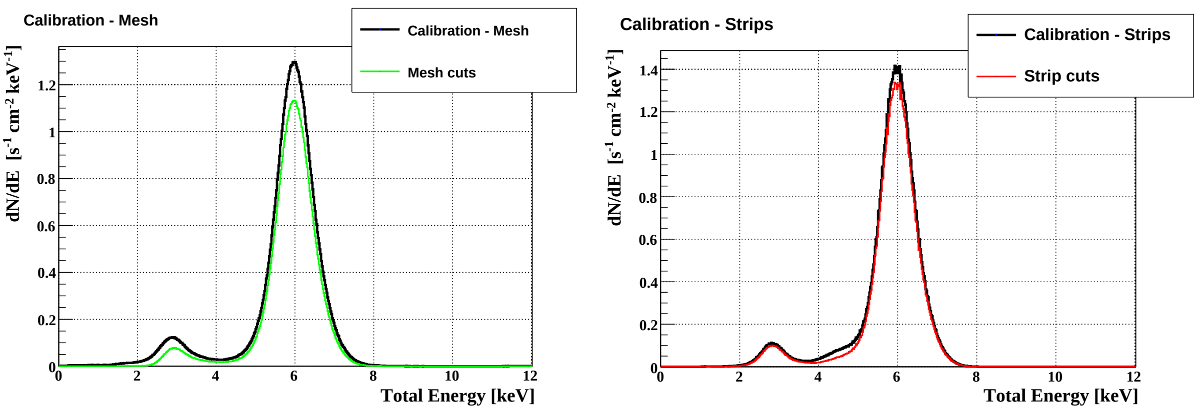

Figure 6.6: The original mesh (left) and strips (right) energy spectra and their shape after applying the corresponding cuts.

6.2.2.3 Background and Tracking distributions

After the definition of the selection criteria with the calibrations, the background and tracking events are distinguished with a series of criteria, formed from data recorded by the Slow Control and Tracking program.

In the middle of each tracking, a precise amount of gas is injected to the cold bores, so that two pressure settings are covered per tracking. The time spent in each step should be equal. In Figure 6.7, the coverage of each half tracking is shown, in respect to the run number of the file that contained the data. It is evident that the 1^{st} half of each tracking is only a maximum of 2 minutes longer than the 2^{nd} one. The red bars that extend above 80 minutes, indicate that in the specific tracking there was no gas change and only one pressure step was covered.

In order to eliminate the chance of systematic errors during tracking, as for example the excess of counts in the first half, in respect to the second, or inhomogeneity in the X and Y strips, several studies have being carried out. The result was that there is no statistically significant inhomogeneity during tracking or background in the events recorded by the detector, as can be seen in Figure 6.8 and Figure 6.9.

After applying the selection criteria and taking into account the timings of the background and tracking runs, the background energy spectra for the mesh and for the strips are produced, as seen in Figure 6.10. The most prominent peaks are the Copper fluorescence peak at 8 keV, the Iron peak at 6 keV, and the argon escape peak at 3 keV. The Iron contribution to the spectrum is due to the magnet, which is a large metallic mass in front of the detector, and all its stainless steel pipes that are in the field of view of the detector. The Copper peak is attributed to fluorescence of Copper components near the detector, such as shielding parts and Faraday cage.

The overall performance achieved during 2009 is summarised in Table 6.1.

	Tracking	Background
Time (h)	190.4	3478.8
Counts	421	7961
Mean Background (2-7 keV) ($\mathbf{keV^{-1}cm^{-2}\,s^{-1}}$)	$(8.08\pm0.39)\times10^{-6}$	$(8.36\pm0.06)\times10^{-6}$

Table 6.1: Summary of the 2009 sunrise Micromegas performance.

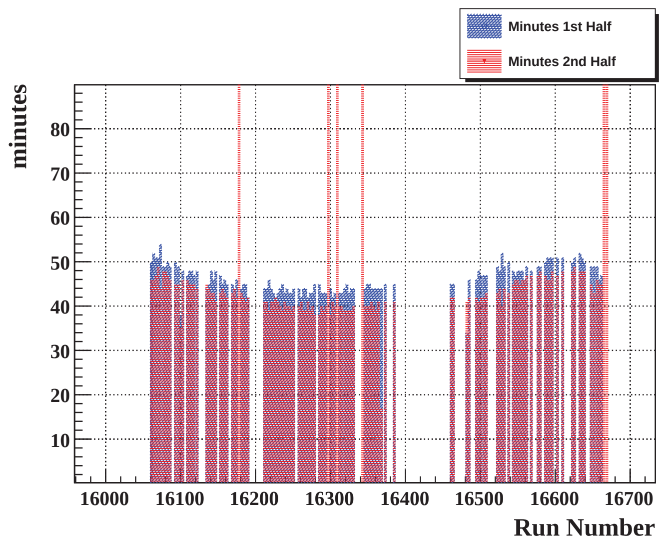

Figure 6.7: The time spent in each pressure step of every tracking during 2009. The red bars that extend above 80 minutes, indicate that in the specific tracking there was no gas change and only one pressure step was covered.

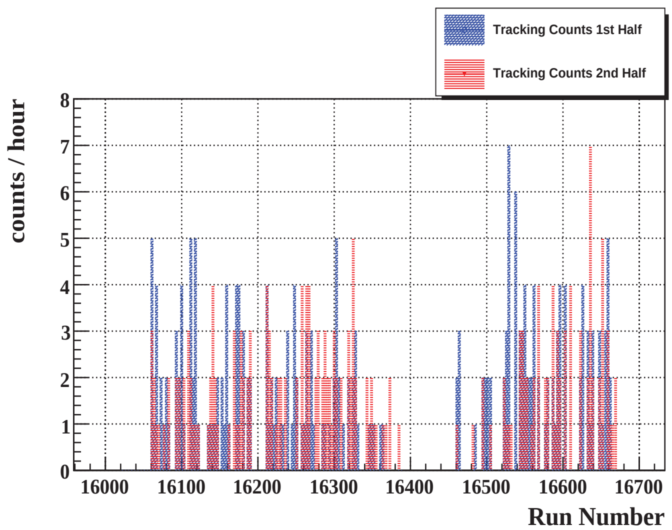

Figure 6.8: The tracking counts recorded in the first and second half of each tracking.

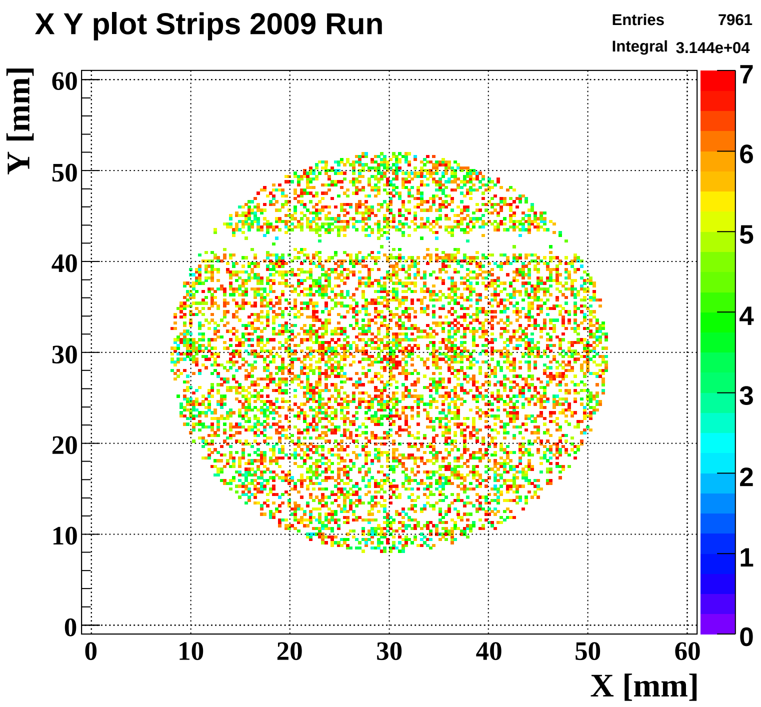

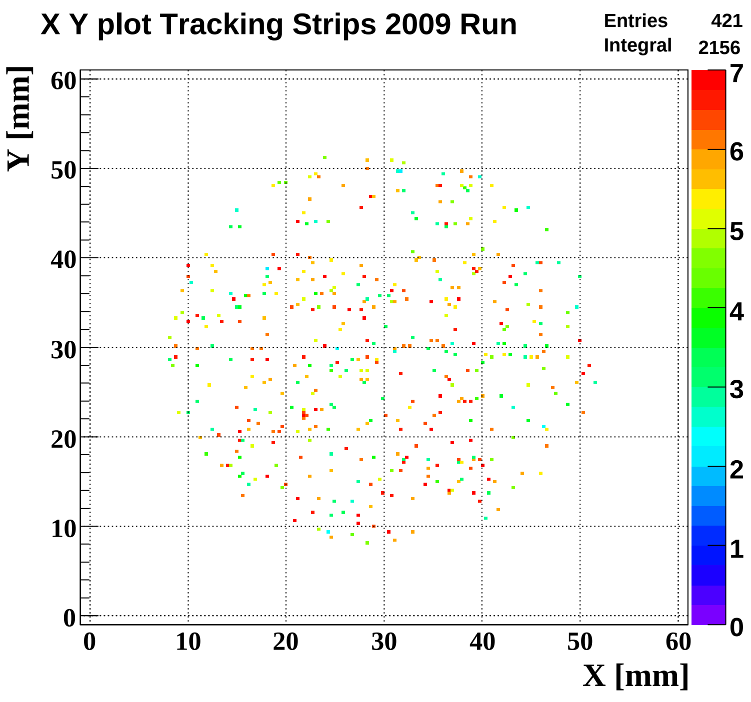

Figure 6.9: The background (top) and tracking (bottom) distribution of events in the strips.

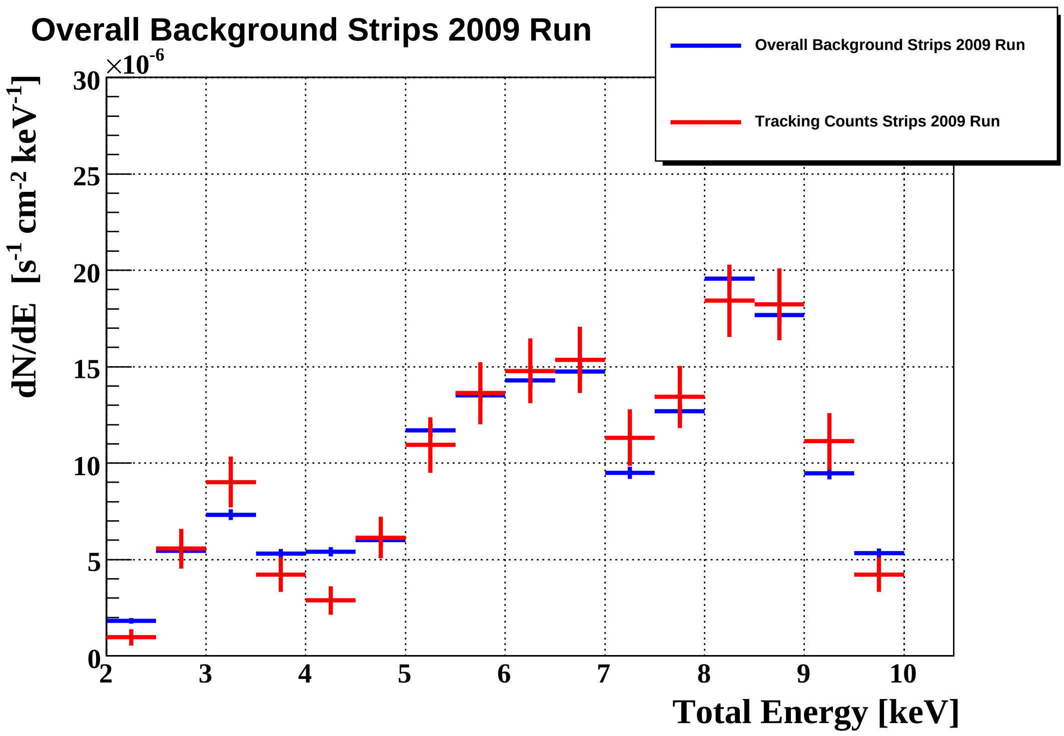

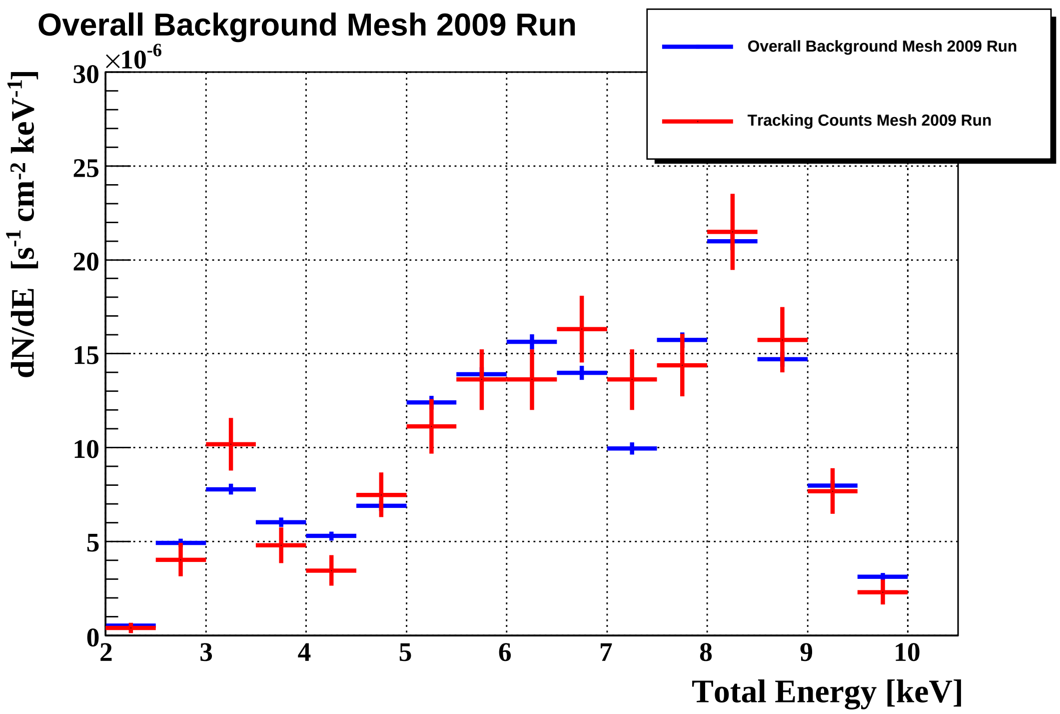

Figure 6.10: The background and tracking events energy spectra for the strips (top) and the mesh (bottom).

6.3 The 2010 run

The 2010 data taking period started on the 5th of May 2010, much later than previewed. The main reason of the delay was an extended maintenance of the cryogenics. The CAST team profited from this delay to upgrade the ^{3}He system with improved safety features, such as new interlocks and improved logic to the control program.

6.3.1 Interventions in the sunrise Micromegas line

Installation of a detector for visible X-rays in the Sunrise Micromegas line

A new detector system has been developed [99], under the BaRBE project and was installed in the sunrise Micromegas line on the 26th of January 2010. Low energy photons of the eV energy range are reflected by a mirror towards an optical telescope. Two pictures of the system are seen in Figure 6.11. The mirror consists of a 5 µm polypropylene foil with 10 nm of aluminum coating and is inclined by 45° with respect to the cold bore axis. It is aligned by a calibrator which shines LED light from the MRB side of the magnet. A scheme of the whole setup is shown in Figure 6.12. The whole construction and the materials of the mirror have been specially chosen so that they do not alter the efficiency of detection of incoming X-rays in the energy range of interest for axion detection.

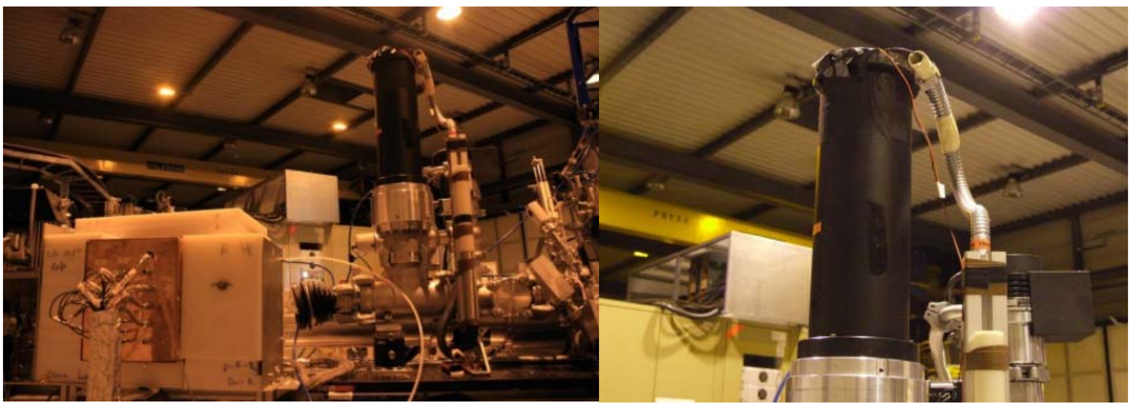

Figure 6.11: The BaRBE optical telescope set up in the Sunrise Micromegas line.

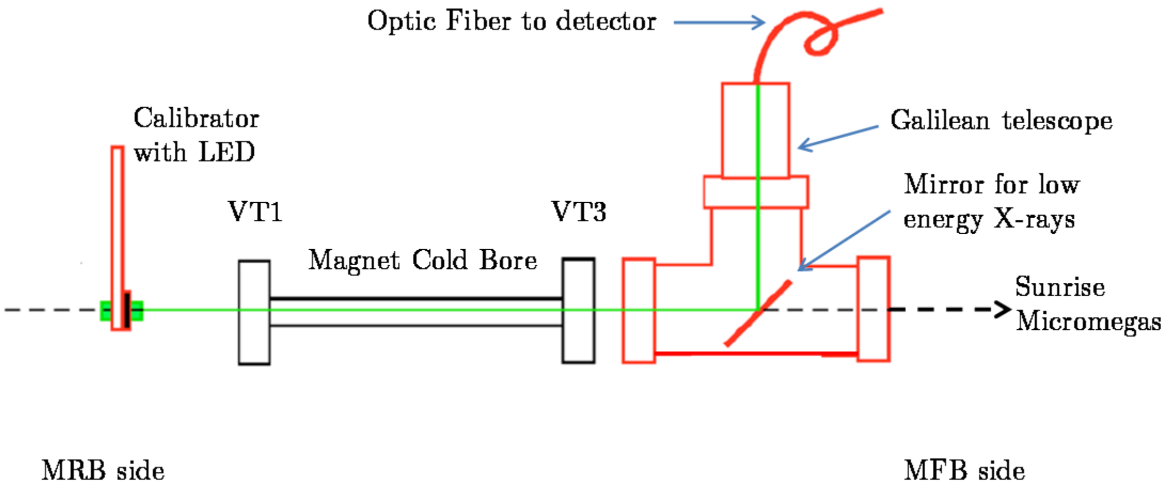

Figure 6.12: A scheme of the layout of the BaRBE detector system of CAST.

Installation of a new Faraday cage and revision of noise sources

On the 15th of April 2010, a new Faraday cage, made in CEA-Saclay, was installed, as seen in Figure 6.13. It includes feedthroughs for the signal and the high voltage power cables of the detector, improving the grounding and electronic noise of the system and thus its stability. In this intervention, the known sources of electronic noise in the data acquisition setup have been revised. A significant reduction in the electronic pickup noise levels was achieved by replacing the floating connector of the output of the Sequencer with a more sophisticated one that is connected to the same ground as all the VME modules, as seen in Figure 6.14.

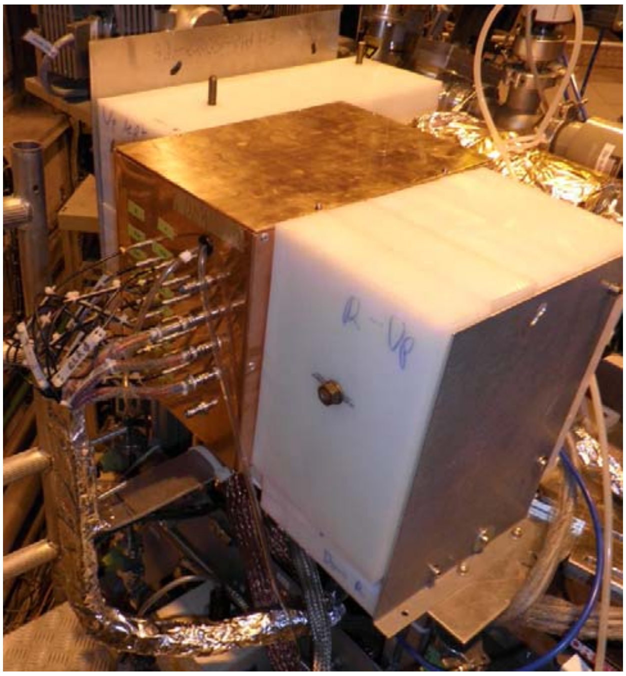

Figure 6.13: The new Faraday cage, which includes feedthroughs for the High Voltage and signal cables.

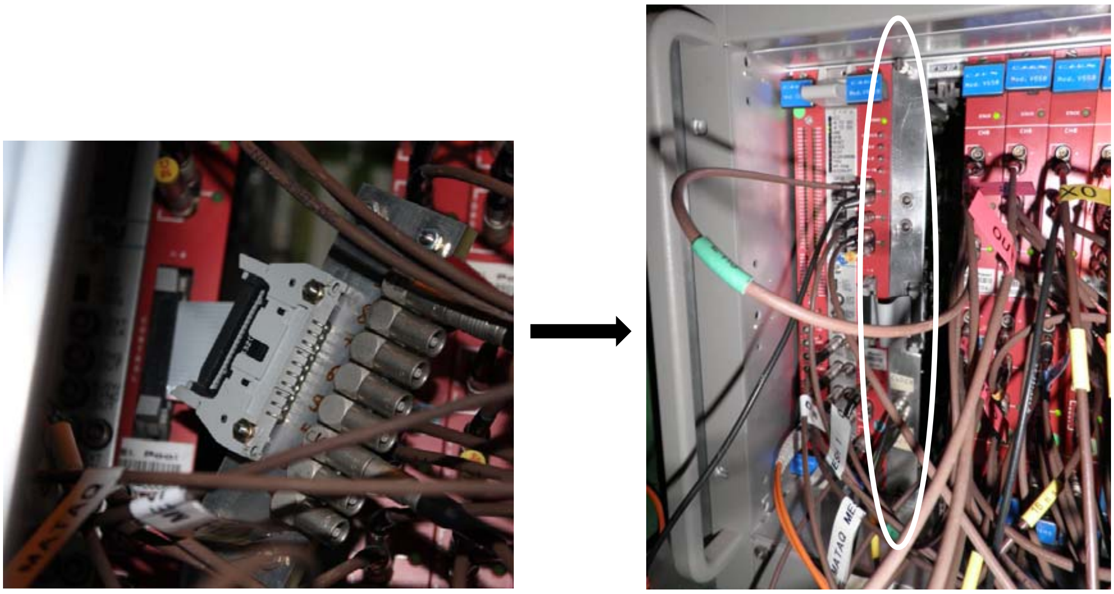

Figure 6.14: The old (left) and the new (right) connector of the Sequencer signals.

6.3.2 Data taking periods

6.3.2.1 Covering missing pressure settings

In the data taking period of 2008 a leak of ^3He occurred. It was discovered on the 27th of November 2008, when, after a two week shutdown, there was a clear drop in the pressure of ^3He inside the cold bores. At the end of January 2009, the magnet was opened and a leak of 1.1×10^{-3} mbar · l · s^{-1} was found on the MFB side. A smaller leak of 5×10^{-5} mbar · l · s^{-1} was found on the MRB side. The metal seals that were tightened by special chain clamps (Figure 6.15) were identified as the cause of the leak.

The leak was developed during the thermal cycle of the shutdown in Christmas of 2007, when the magnet was warmed up to room temperature. During 2008 the leak rate was increasing steadily with the increasing pressure in the cold bores and worsened with another thermal cycle of the magnet in September 2008.

Due to various reasons (quenches, bake-outs, cryogenics problems), the ^3He was evacuated from the cold bores and refilled 4 times during the 2008 data taking period. Because of the leak there was a pressure difference in the cold bores before and after each refilling, which created gaps in the axion mass coverage.

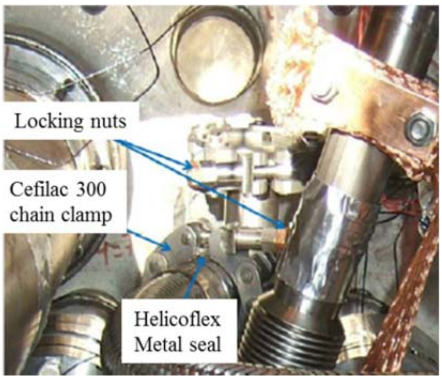

Figure 6.15: A picture of the replacement chain clamp of the MRB side, after the intervention of January 2009.

The first period of the 2010 data taking started on the 5^{th} of May and lasted until the 7^{th} of August. It was dedicated to covering these gaps that were created in the axion mass scan. In order to make sure that the repetition of the pressure settings would be successful, each missing gap was extended to have an overlap of 2 or 3 pressure steps with the original 2008 coverage. As a consequence the CAST experiment revisited 142 pressure steps, summarised in Table 6.2.

Gap #	Pressure in the CB (mbar)	Step Numbers
1	14.03-16.04	167-190
2	18.60-19.41	219-228
3	22.10-24.55	258-285
4	26.10-33.44	302-381

Table 6.2: Summary of the pressure settings visited in the first period of the 2010 data taking

6.3.2.2 New pressure settings

The data taking period with coverage of new pressure settings took place from the 10^{th} of August until the 30^{th} of November 2010. In this period 126 new pressure steps were covered (from #602 to #729). These pressure steps correspond to pressures in the cold bores from 65.1 mbar at 1.8 K (corresponding to axion mass of 0.85 eV/c^2) to 82.52 mbar at 1.8 K (axion mass of 1.01 eV/c^2).

6.3.3 CAST data taking overview

The 2010 run has not been uneventful. From the pressure evolution in the cold bore, seen in Figure 6.16, it is evident that a lot of events took place that were postponing the data taking. The most significant are:

Cryogenics problem and cold windows bakeout (11^{th} of June-17^{th} of July 2010)
A failure in the pump of the cryogenic system caused this extended stoppage. The cold windows were baked out during this period.

Quench occurred on the 1st of October

A quench signal was triggered by the maintenance of the external power converters in the CAST experimental hall. The shutdown was prolonged by several cryogenics problems until the 16th of October.

Natural quench on the 26th of October

A natural quench occurred while the shifters of the evening tracking were ramping up the current of the magnet.

Natural quenches on the 10th of October and 9th of November

These two quenches that occurred, were natural quenches and they had no correlation with any external parameter.

Quench on the 20th of October

A quench was triggered, as a precaution, due to the stoppage of the water that cools down the power cables that carry the 13000 A to the magnet.

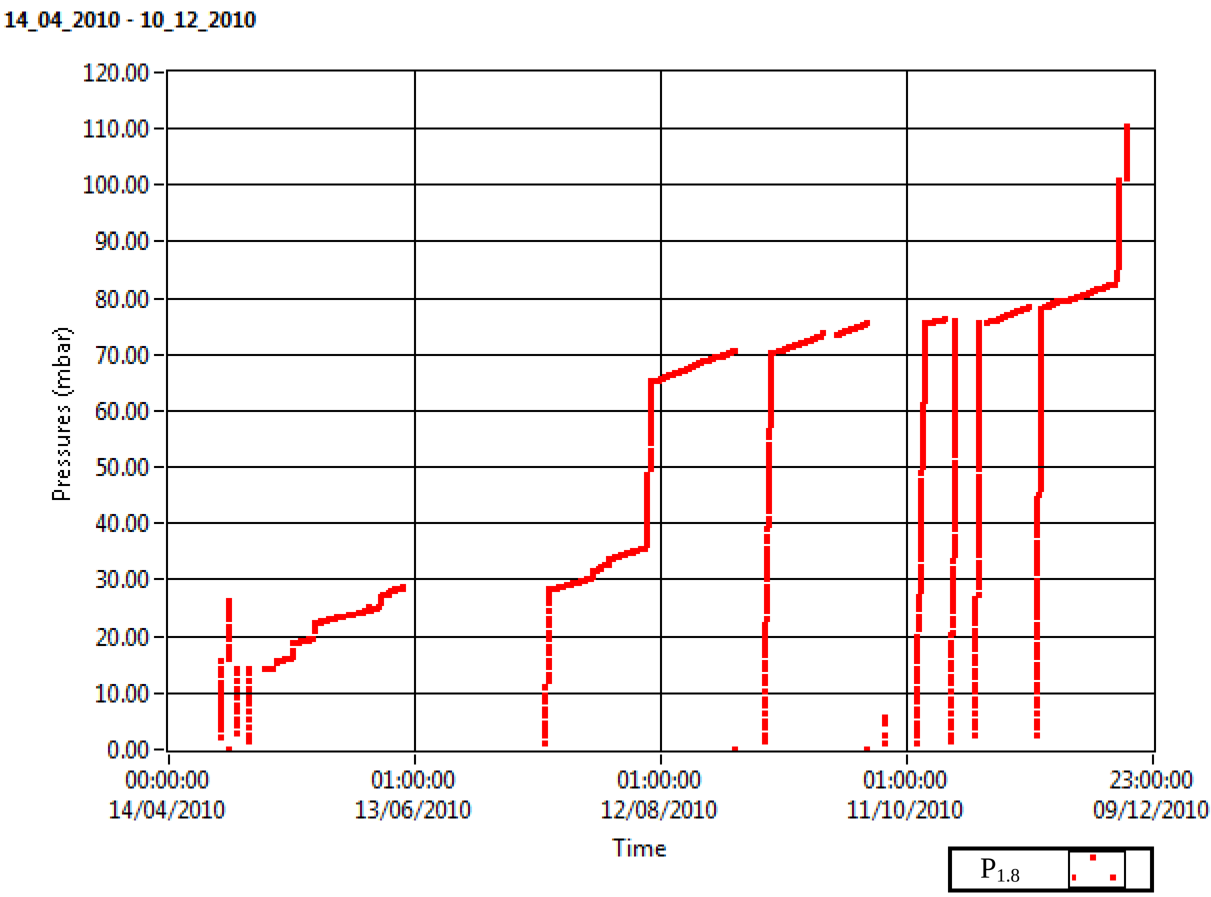

Figure 6.16: The evolution of pressure in the cold bores (at 1.8 K), throughout the 2010 run.

6.3.4 Sunrise detector data taking

6.3.4.1 Overview

Apart from all the cryogenics problems and the unusual number of quenches, the sunrise Micromegas 2010 run has been extremely smooth. The detector covered all the pressure steps with almost 100% efficiency. It recorded successfully 197 hours during 124 trackings and took approximately 6313 hours of background.

Some minor incidents that occurred during 2010 are:

Wrong position of the magnet caused a slight loss of tracking time
After each shift the magnet is driven to a predefined parking position which is close to the starting position of the tracking of the next shift. On the 15th of May 2010 the morning shifters found the magnet far away from the starting point of the tracking of the Sun. As a result they had to move it for a long time before the magnet could follow the Sun with the required precision and 15 minutes of tracking time were lost.

Leak tests on the manipulator of the ^{55}Fe source
On the 24th of August 2010, a minor leak was found in a T-junction of the compressed air inlet of the manipulator of the calibration source. The leak was cured by replacing the leaky T-junction and no tracking was lost.

Wrong manipulations of the shifters – minor bug of DAQ software
After each morning shift the shifters take a pedestal and a calibration run. If by mistake two consecutive pedestal runs are launched, the data acquisition software gets stuck. This incident has happened on the 8th of June, 27th of September and 6th of November. In each case the pc was restarted and new calibration runs were taken.

Accidental injection of 2 pressure steps during a morning shift
On the 17th of July the amount of gas that was injected in the cold bore, in the middle of the morning shift was double than the nominal, resulting in the coverage of steps 315 and 317, thus skipping 316.

6.3.4.2 Stability and Characteristics

The 2010 performance of the M9 detector was exceptional, especially after the intervention in the middle of April 2010. The improvement in the stability of the characteristics of the detector is visible in the following plots.

Gain performance

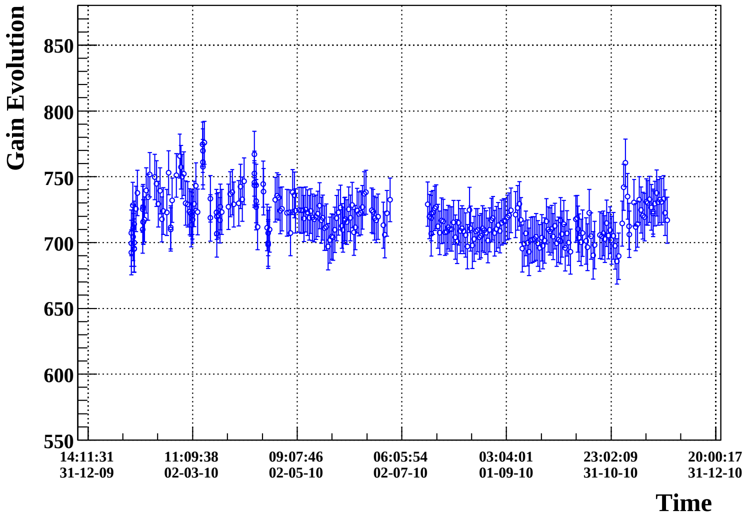

Figure 6.17: The gain performance of the detector was remarkably stable, especially after the intervention in mid-April.

Energy Resolution

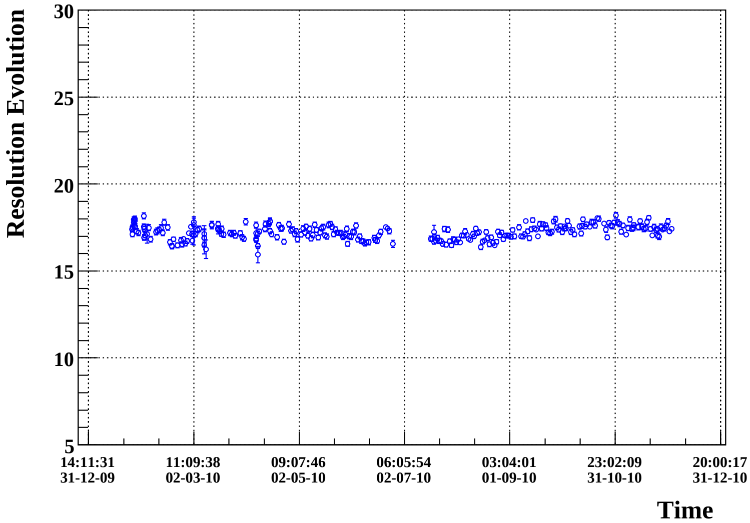

Figure 6.18: The evolution of the energy resolution of the detector during 2010.

This year as well, the detector did not show any signs of aging or defects, apart from the known issue of one Gassiplex that reads out the Y strips.

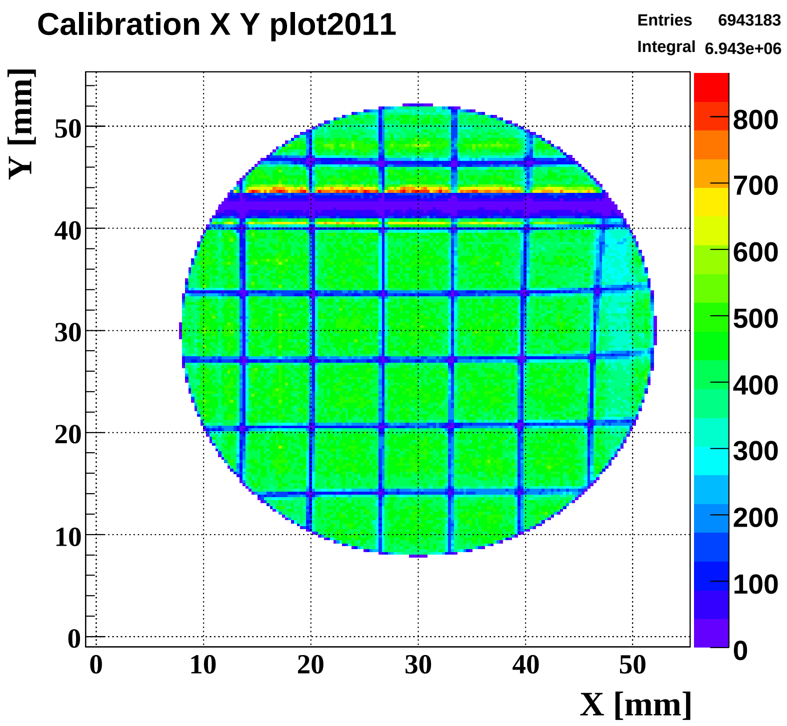

Figure 6.19: The cold bore area of the detector from the calibration runs of 2010. The dead area in the upper semicircle accounts for less than 5% of the total area of interest.

Software Efficiency at 6 keV

During 2010, the software efficiency of the analysis used, for the 6 keV peak, has an average higher than 80% for both the strips and the mesh, as seen in Figure 6.20 and Figure 6.21.

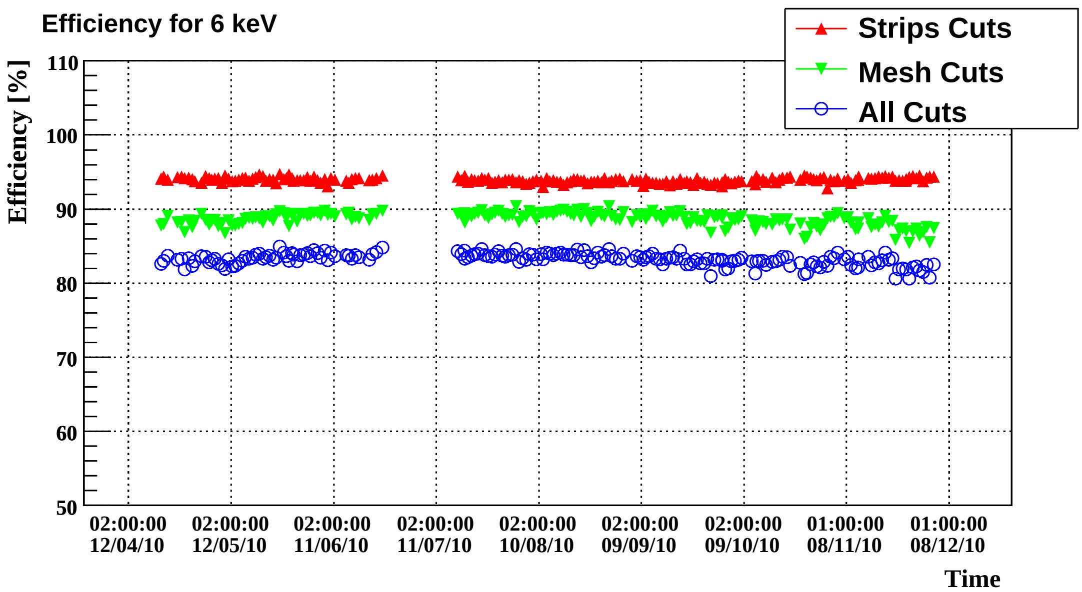

Figure 6.20: The software efficiency for the 6 keV events that were recorded from the strips.

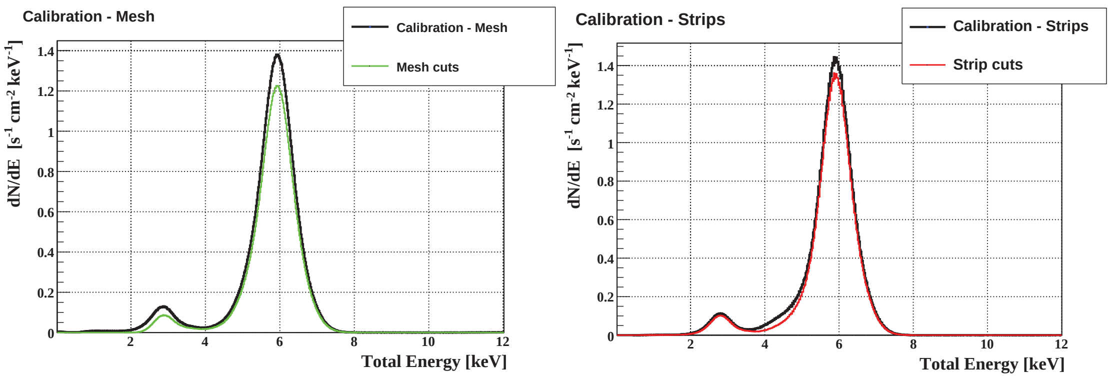

Figure 6.21: The original mesh (left) and strips (right) energy spectra and their shape after applying the corresponding cuts.

6.3.4.3 Background and tracking distributions

In the data of 2010, the same principles as in 2009 apply in order to classify the events that have passed the selection criteria. After applying these criteria and taking into account the timings of the background and tracking runs, the background energy spectra for the mesh and for the strips are produced, as seen in Figure 6.24, and Figure 6.25. The most prominent peaks are again the argon escape peak at 3 keV, the iron peak at 6 keV and the Copper peak at 8 keV.

The overall performance achieved during 2010 is summarised in the following Table:

	Tracking	**Background**
Time (h)	196.6	4496
Counts	443	10552
Mean background (2-7 keV) (keV^{-1}cm^{-2} s $^{-1}$)	$(8.24\pm0.4)\times10^{-6}$	$(8.58\pm0.09)\times10^{-6}$

Table 6.3: Summary of the 2010 Sunrise Micromegas performance.

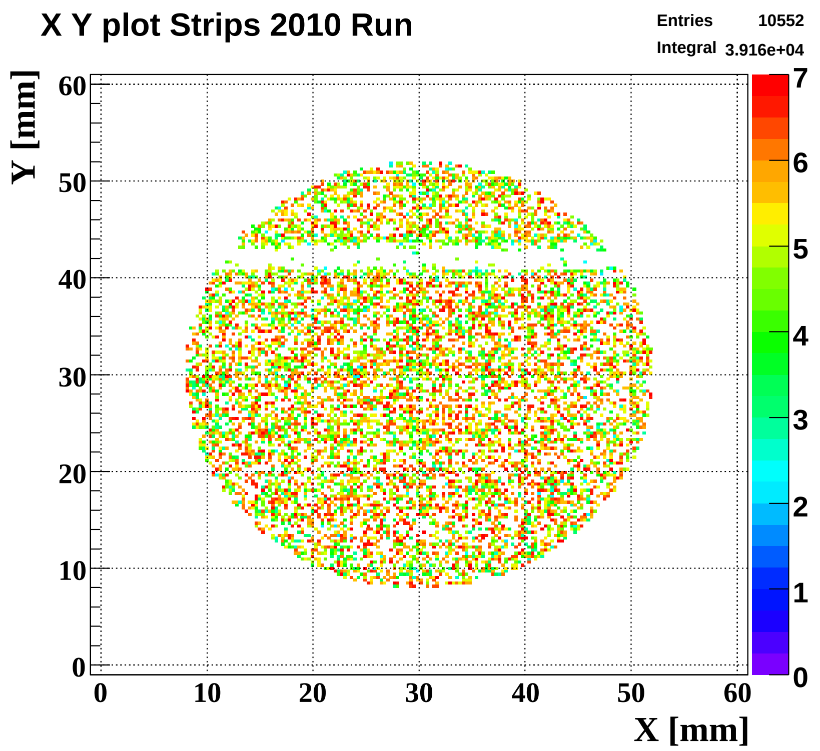

Figure 6.22: The X Y distribution of background events in the strips.

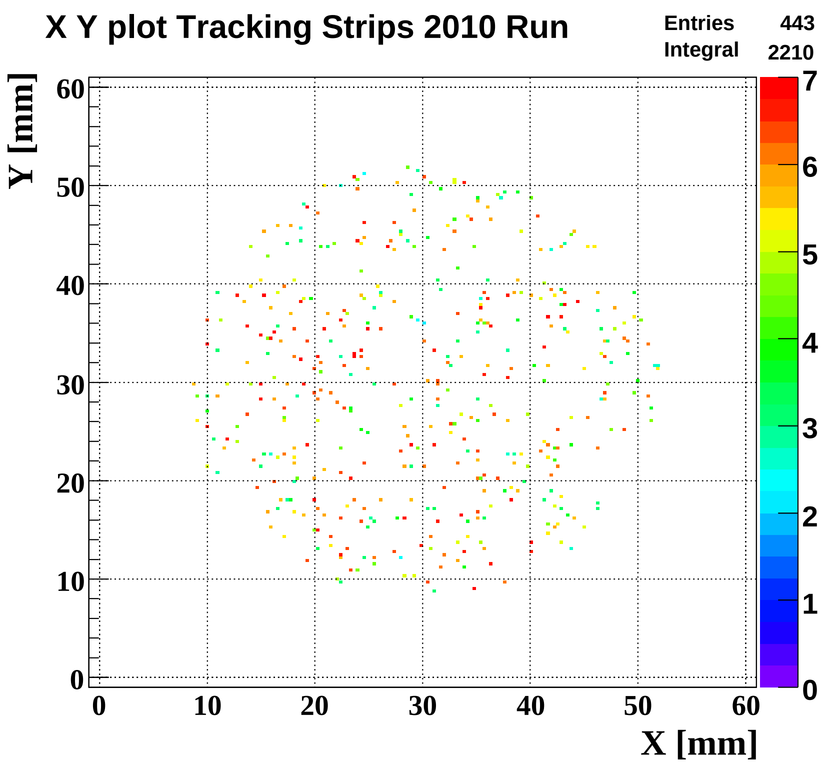

Figure 6.23: The X Y distribution of tracking events in the strips.

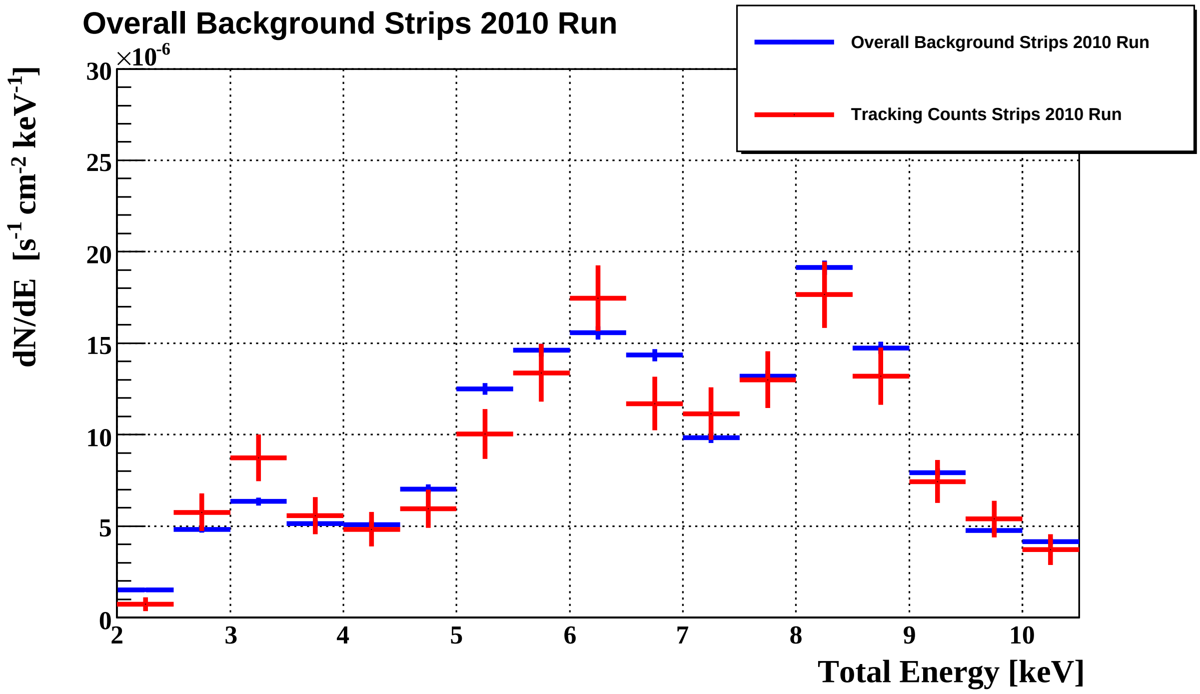

Figure 6.24: The energy spectra of the background and tracking events for the strips, during 2010.

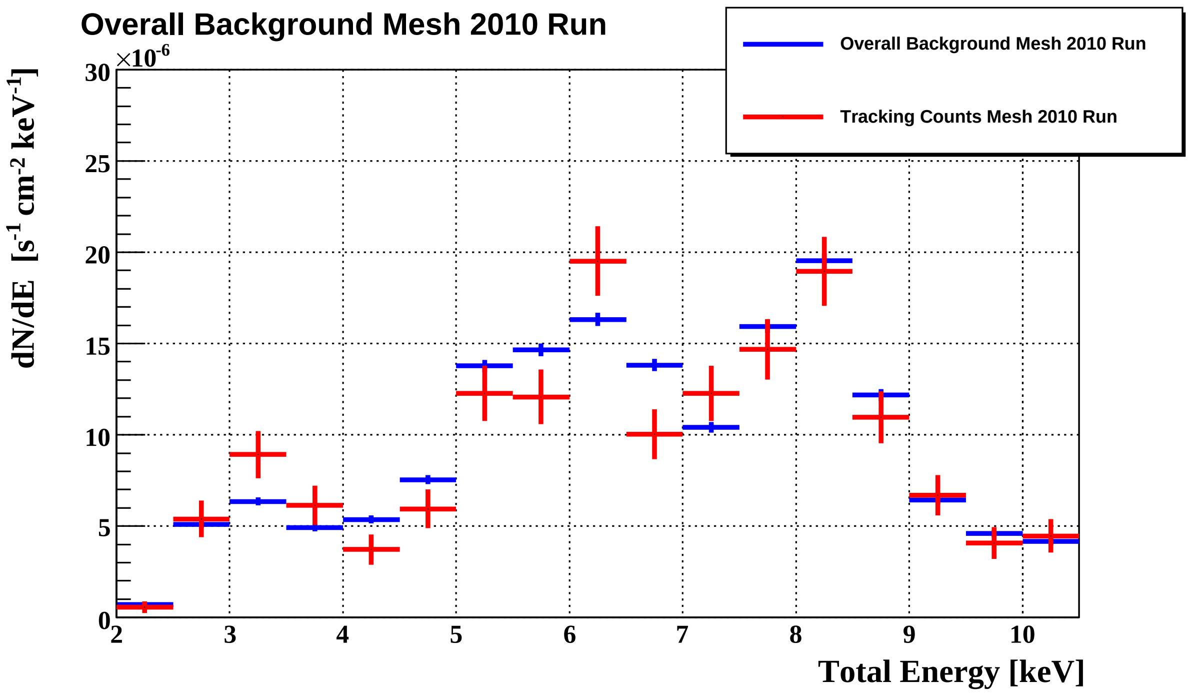

Figure 6.25: The energy spectra of the background and tracking events as recorded from the mesh, during 2010.

6.4 Count rate evolution and statistical evaluation of 2009 and 2010 data

During 2009 and 2010 data taking periods, the background rate, after applying the selection criteria, has been stable, at around 2.5 counts/h, as can be seen in Figure 6.26 and Figure 6.27.

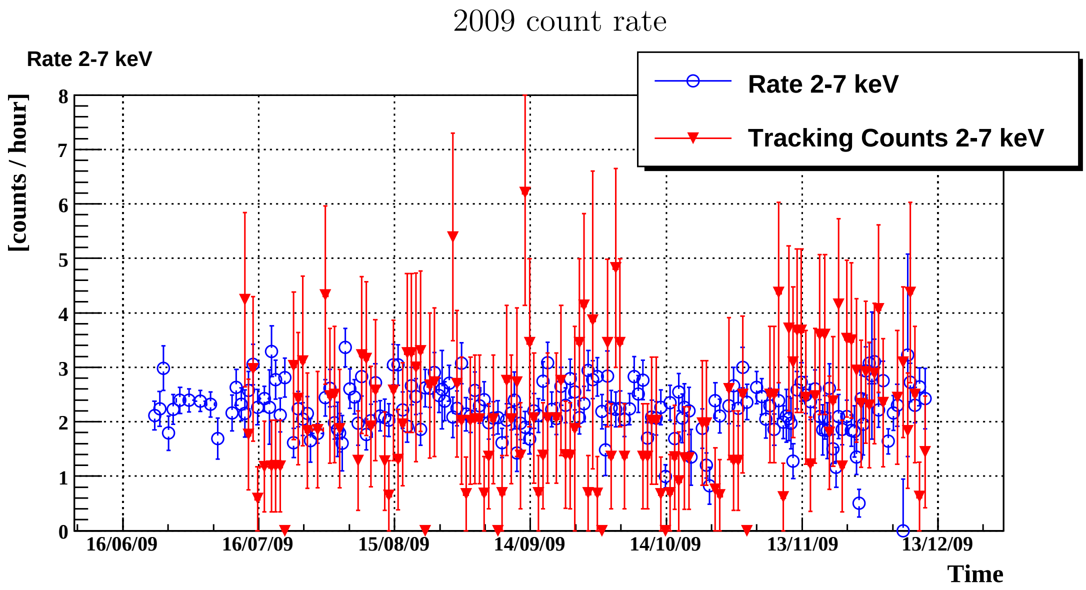

Figure 6.26 : The count rate evolution and the tracking counts recorded during the 2009 data taking period.

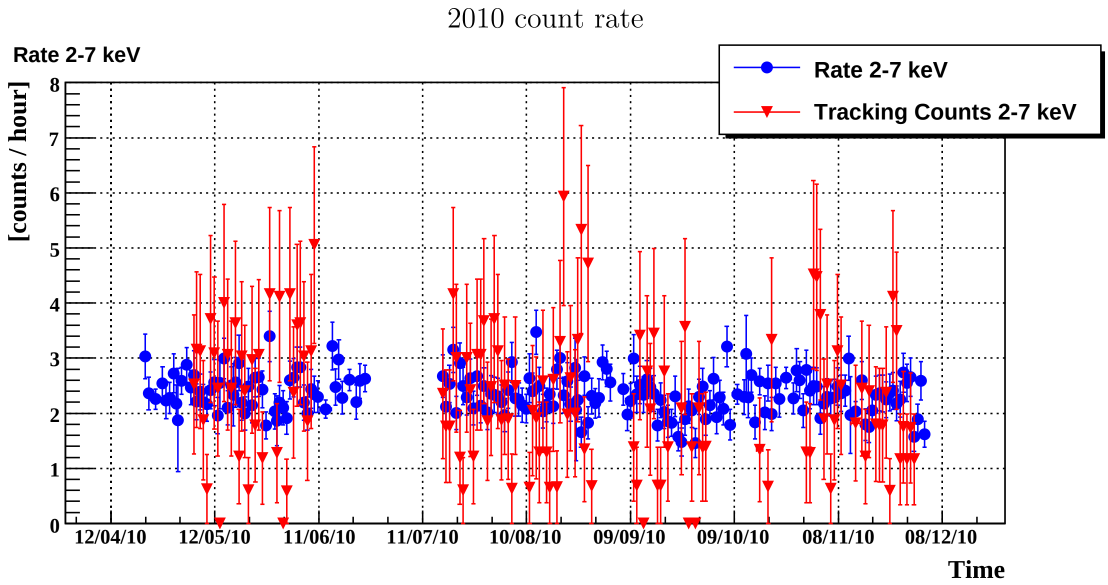

Figure 6.27: The count rate evolution and the tracking counts recorded in 2010.

6.4.1 Statistical evaluation of the 2009 and 2010 data

The low event rate of the detectors in CAST, indicates that the distribution of the number of events at a small time bin (i.e. 15-60 minutes) should follow a Poisson distribution. The statistical assessment of the compatibility of the background and tracking data has been performed, by comparing the distribution of the number of events that have been accepted from the selection criteria, to the Poisson distribution of their mean.

The time bin used for the analysis is 30 minutes and only full time bins were used. In Figure 6.28 the Poisson distribution is shown, for background (top) and tracking events (bottom) of 2009 respectively. The background events follow a Poisson distribution of mean μ_B=1.1637, while the tracking counts follow a distribution of a mean value μ_T=1.16, being in very good agreement with the background distribution.

In the case of 2010, the data of the whole data taking period were assessed and the Poisson distributions of the background and tracking data are shown in Figure 6.29. In the first case, the Poisson distribution has a mean of μ_B=1.1625, whereas the distribution of the tracking events has a mean of μ_T=1.1382, being in very good agreement.

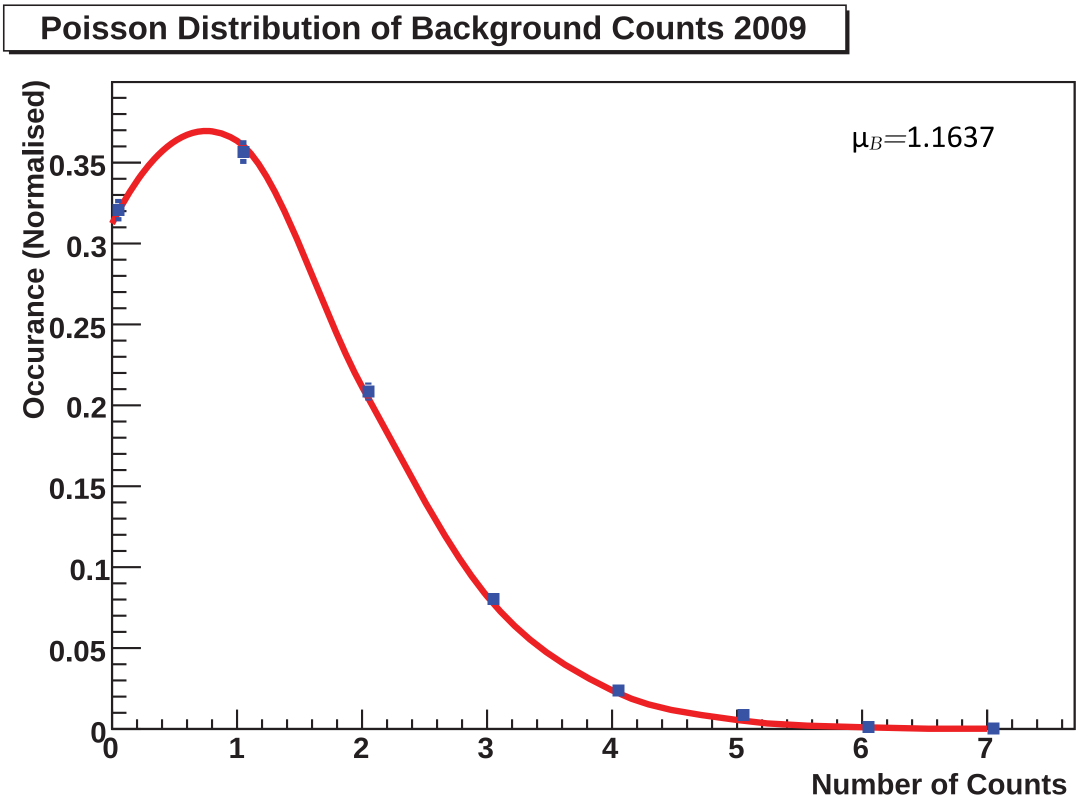

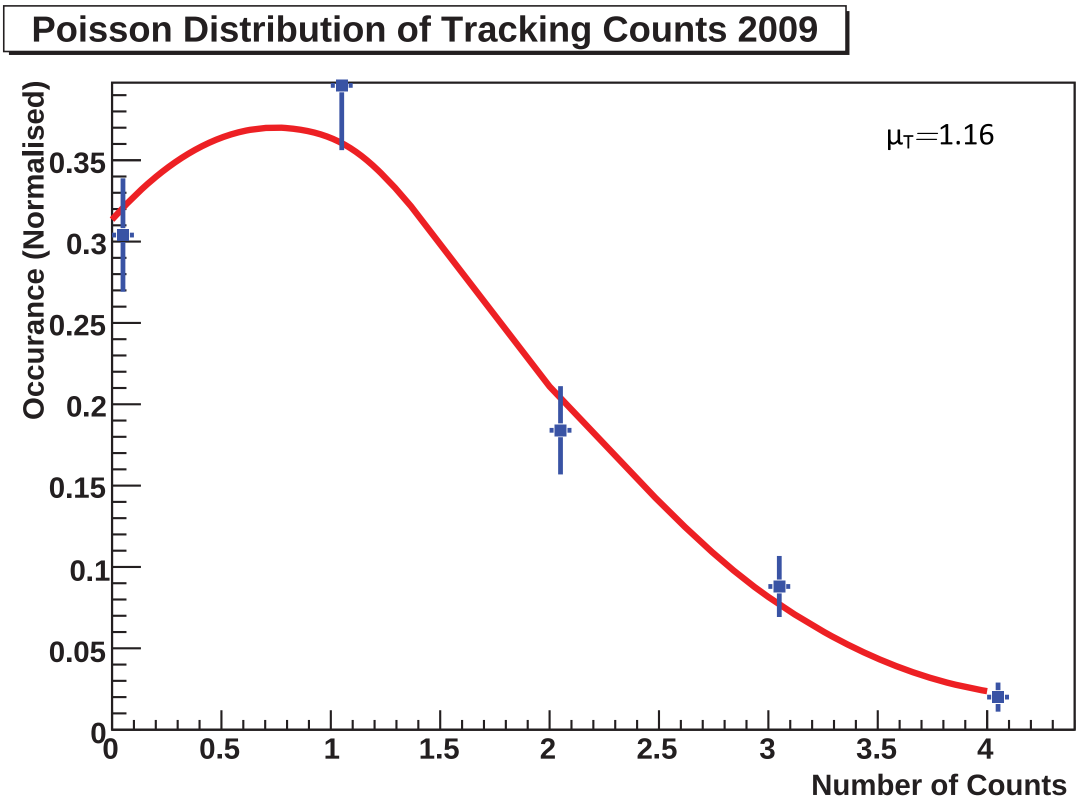

Figure 6.28: The Poissonian distribution of the number of events per 30 minutes, for the background (top) and tracking (bottom) events for the nominal background periods of 2009.

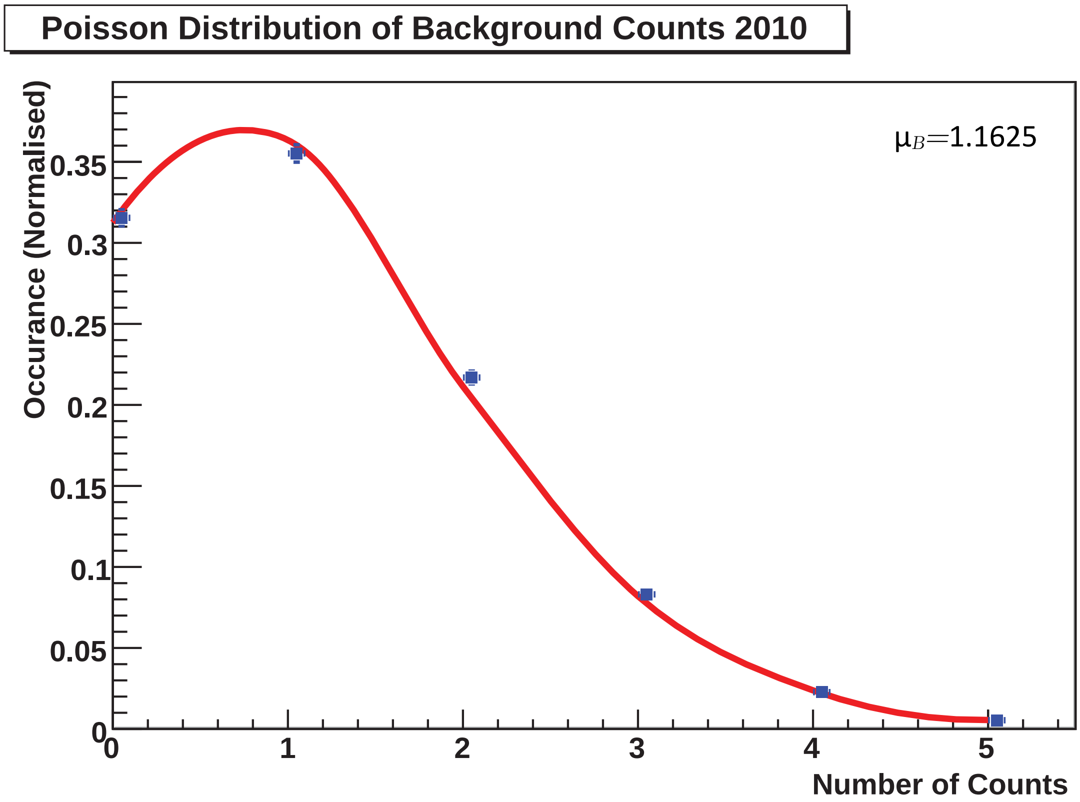

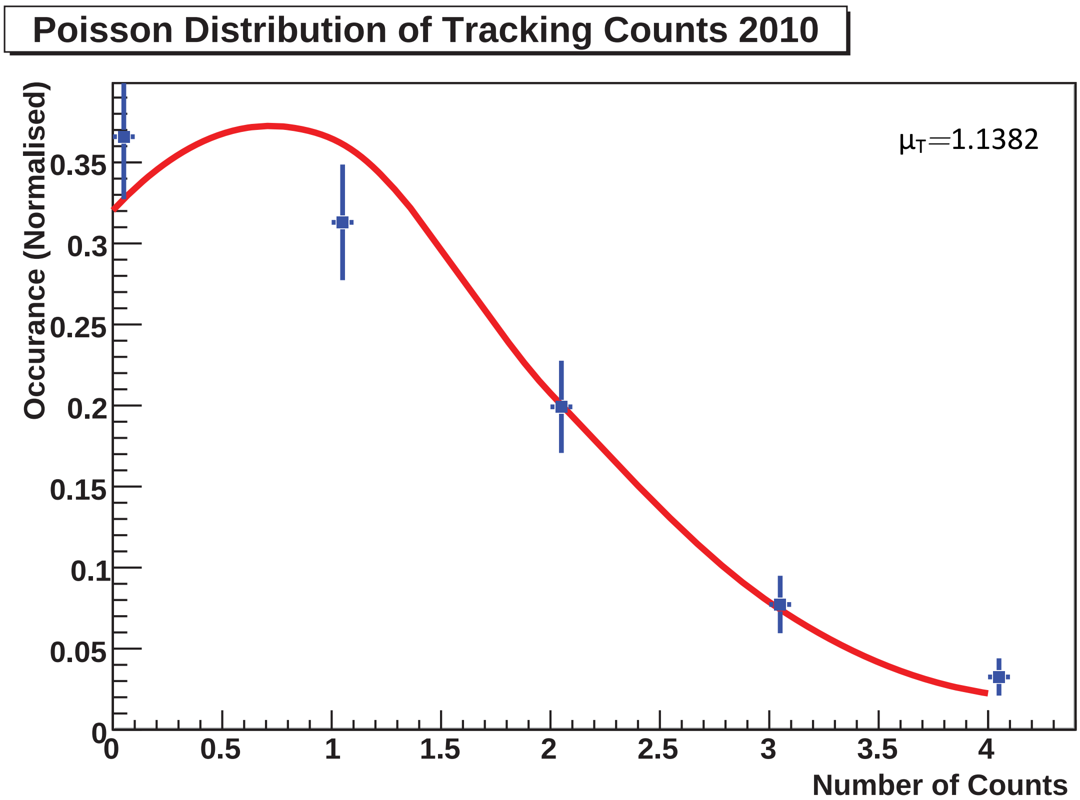

Figure 6.29: The Poissonian distribution of the number of events per 30 minutes, for the background (top) and tracking (bottom) events of the 2010 data taking period.

7. Calculation of the coupling constant limit

Contents

7.1 Coherence

As already mentioned in Chapter 2, the axions that reach the Earth have a differential flux that is described by:

$$\frac{d\Phi_a}{dE_a} = g_{10}^2\, 6.02 \cdot 10^{10}\, E_a^{2.481}\, e^{-\frac{E_a}{1.205}}\ [\mathrm{cm^{-2}s^{-1}keV^{-1}}]\ . \tag{7.1}$$

The probability of their conversion to a photon inside the CAST magnet is:

$$P_{a\to\gamma} = \left(\frac{B\, g_{a\gamma}}{2}\right)^2 \frac{1}{q^2 + \Gamma^2/4}\left[1 + e^{-\Gamma L} - 2e^{-\frac{\Gamma L}{2}} cos(qL)\right]\ , \tag{7.2}$$

with q the momentum transfer with a photon of effective mass m_γ, given by the expression:

$$m_\gamma = 28.77\sqrt{\frac{Z}{A}\rho}\ , \tag{7.3}$$

as a function of the density ρ, the atomic number Z and atomic mass A of the buffer gas, which in the case of ^{3}He are $Z = 2$ and A =3 g/mol respectively.

The number of photons N_γ, generated in the coherence length of the magnet is given by the expression:

$$N_\gamma = \int \frac{d\Phi_a}{dE_a} P_{a\to\gamma}\, A\, t\, dE_a\ . \tag{7.4}$$

Before advancing to further calculations, for the expected actual signal in the detector it is important to define the two main terms that influence the probability of conversion, the attenuation length Γ and the coherence length L. The magnetic field in the coherence length is well defined.

7.1.1 Attenuation length

The attenuation length inside a medium of constant density ρ is given by the formula:

$$\Gamma = \rho \left(\frac{\mu}{\rho}\right) , \tag{7.5}$$

where ρ is the density inside the conversion region and μ/ρ is the mass attenuation coefficient. In the case of the second part of CAST-PHASE II, ^{3}He is used as a buffer gas and μ/ρ is provided by the National Institute of Standards and Technology (NIST) database in [100]. The data of NIST have been fitted, in the energy range of 1 to 15 keV, and the dependence of μ/ρ from the energy was derived in [101]:

$$log\left(\frac{\mu}{\rho}\right) = -1.5832 + 5.9195\, e^{-0.353808\cdot E} + 4.03598\, e^{-0.970557\cdot E} , \tag{7.6}$$

with E, the energy of the photon in keV and μ/ρ expressed in cm^2/g. The evolution of μ/ρ in respect to the energy of the photon is shown in Figure 7.1.

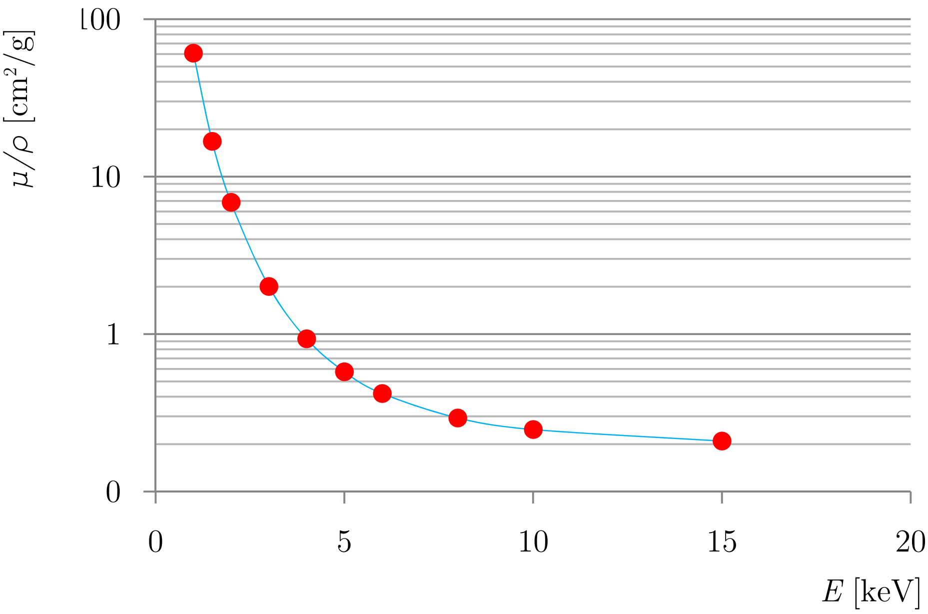

Figure 7.1: Representation of the evolution of the mass attenuation coefficient with respect to the energy of the photon. The red dots correspond to the points acquired from the NIST database and the blue line the fit to these points.

7.1.2 Coherence length

As already discussed in Chapter 2, in the presence of a buffer gas the coherence of the axion to photon conversion is restored for a very narrow mass range which corresponds to the density of the buffer gas. Therefore the stability and homogeneity of the density along the axion conversion region (coherence length, L) during the tracking of the Sun is crucial.

In order to achieve constant density the entire cold bore area is cooled down by liquid ^{4}He at 1.8 K, but there are parts linked to the cold bores which have a higher temperature. These are the cold windows. The temperature of the cold windows, is higher than the one of the parts inside the cryostat, due to heat conduction from the outer parts, through the steel pipes. The higher temperature of the windows is transferred, through natural convection, to the ^{3}He, and it heats it up. Then the hot gas enters deeper into the cold bores, it is cooled down, falls to the bottom of the pipes and comes back to the cold windows, where it is heated up, completing the thermal cycle. In Figure 7.2, the thermal cycle of the buffer gas is shown.

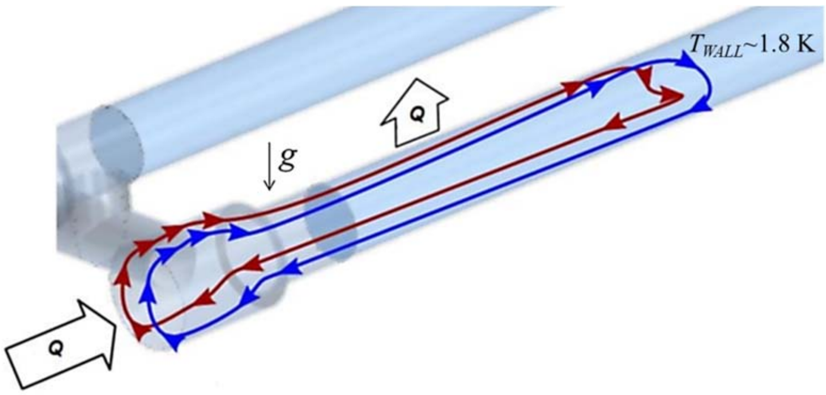

Figure 7.2: The thermal cycle of the ^{3}He buffer gas inside the cold bores, caused by the hig temperature of the cold windows [102].

Until the end of 2008 the cold windows were kept at a constant temperature of 70 K, much higher than the temperature of their environment. The reason was to ensure that residual gases in the vacuum side of the windows like Ar, N_2, O_2, H_2 would not be cryo-pumped to the windows' surface and reduce their transparency to X-rays. In the end of the 2008 run though, the cryogenics system of CAST could not cope with the additional heat load and after a vacuum upgrade and a series of tests it was decided to stop the heating. The windows were still kept at a temperature of 18 K to 20 K and frequent bake outs ensured their transparency.

In order to assess the effect of the higher temperature in the ends of the cold bores to the density profile and eventually the impact in the coherence length, the inputs of several temperature sensors placed in different parts of the magnet were fed as boundary conditions to a series of Computational Fluid Dynamics (CFD) simulations both in static (still magnet) and transient conditions (magnet moving as during a tracking).

7.1.2.1 Still magnet CFD Simulations

The first CFD simulations [102] helped to understand the real behaviour of the buffer gas and quantify effects such as buoyancy and convection due to the higher temperatures in the ends of the cold bores. In Figure 7.3 and Figure 7.4, the thermal profile of the area near the cold windows is shown.

The results revealed that hotter gas can penetrate the area of the magnetic field causing a density profile as seen in Figure 7.5 and Figure 7.6. Therefore, the length of constant density (coherence length) is shorter than expected and is decreasing at higher pressures, since the convection effects are higher. These effects are also amplified when the cold windows are heated.

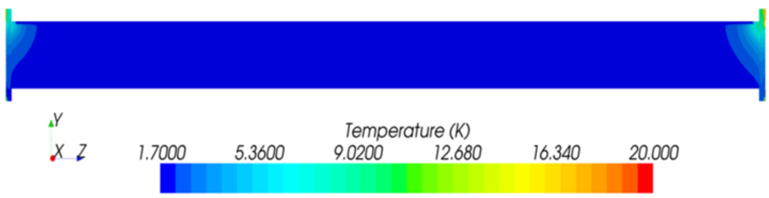

Figure 7.3: Characteristic temperature distribution along the cold bore due to convection of heat from the cold windows to the buffer gas.

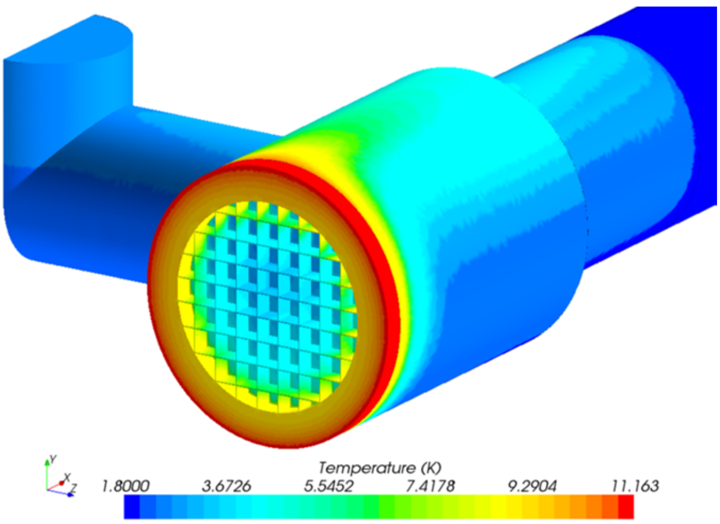

Figure 7.4: Detail of the temperature distribution in the cold window

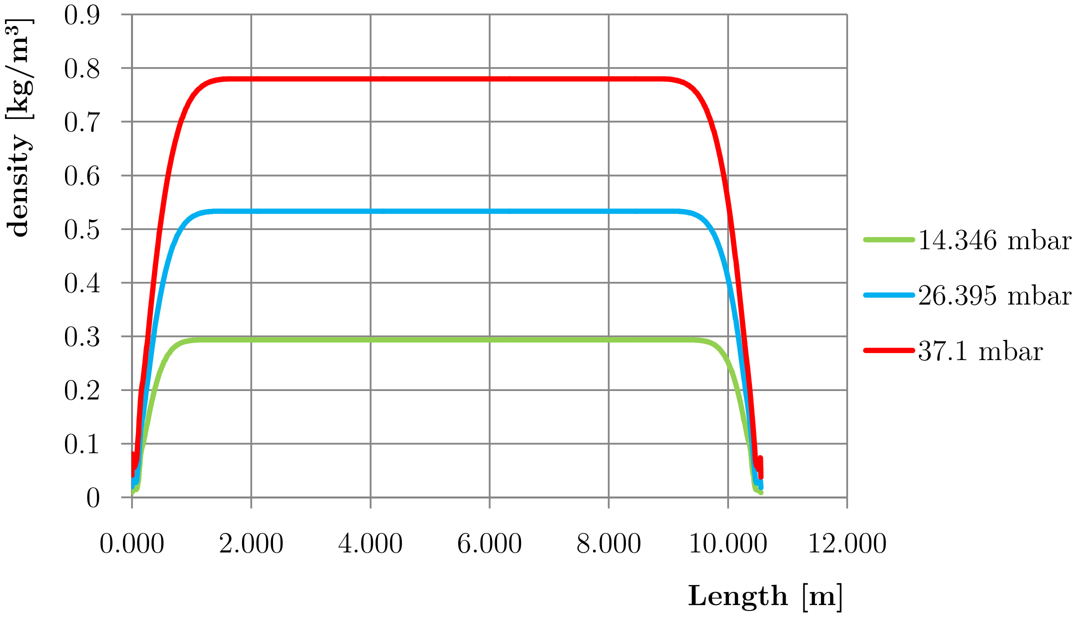

Figure 7.5: Density distribution along the cold bores, for heated windows and for three different pressures.

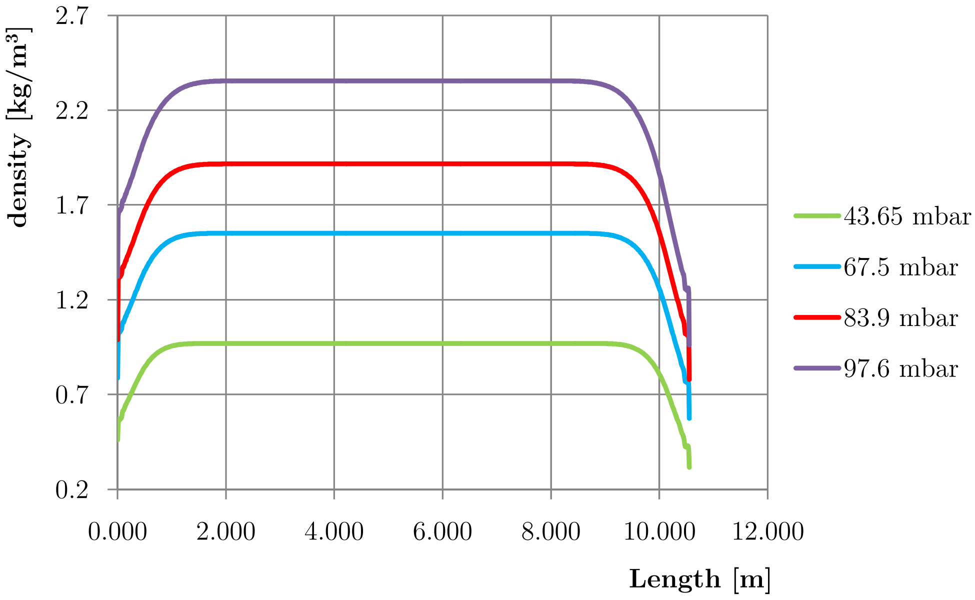

Figure 7.6: Density distribution along the cold bore, for the case of non-heated cold windows for four different pressures.

From the density profile of Figure 7.5 and Figure 7.6, it is evident that a threshold has to be set for the density fluctuations, in order to maintain the coherence effect over a length L. The density stability threshold [103], is directly related to the coherence length, since the stricter it is, the smaller the coherence length will be, resulting in a reduction to the overall CAST sensitivity. The density stability threshold was calculated expanding on [56]. The relative deviation in density can be expressed as:

$$\frac{d\rho}{\rho} = 2\frac{dm}{m} \equiv \frac{4\pi \cdot E_a}{L \cdot m_a^2} \ , \tag{7.7}$$

with E_a the axion energy, m_a the axion mass, L the coherence length and ρ the buffer gas density. When the axions are coherent with the photons in the buffer gas, then $m_a \equiv m_\gamma$ and:

$$\rho \equiv \frac{3}{2}\left(\frac{m_a}{28.77}\right)^2 \cdot 1000 \ [\text{kg/m}^3] \ , \tag{7.8}$$

with m_a expressed in eV. Substituting ρ in the above equation and rearranging the terms one gets:

$$d\rho \equiv 6.0518 \cdot 10^{-3} \cdot \frac{E_a}{L} \ . \tag{7.9}$$

The above formula shows that the allowed density fluctuation $d\rho$ is independent of the axion mass or gas density and depends only on the axion energy and the magnetic length. The allowed density variation $d\rho$, in respect to the axion energy is shown in n Figure 7.7.

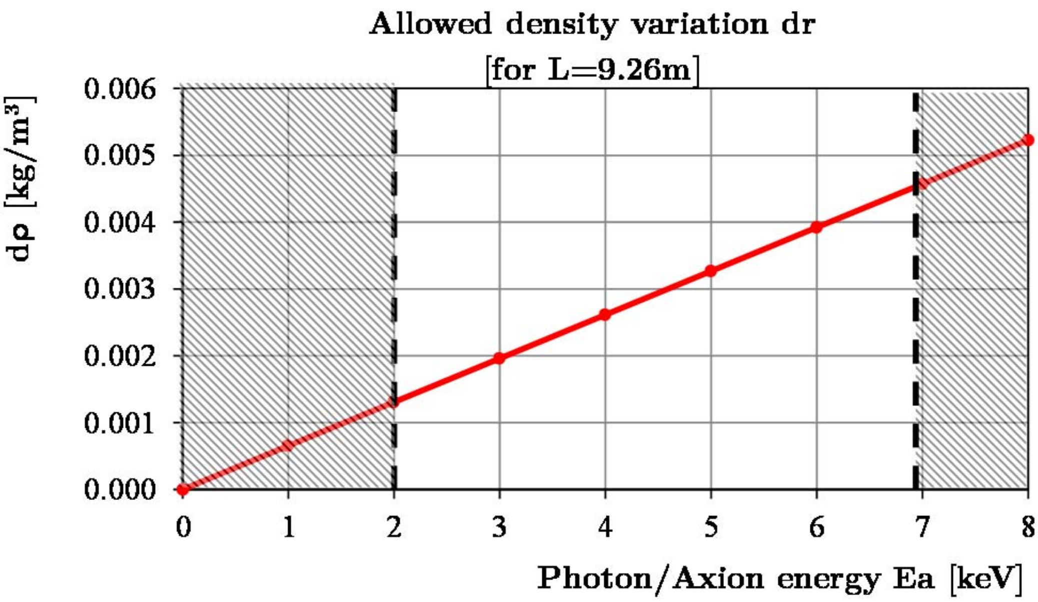

Figure 7.7: Allowed density fluctuation as a function of the axion energy (the dashed regions are outside the region of interest).

From the CFD simulations the effective length can be parameterised with respect to the density fluctuation and the pressure in the cold bore at 1.8 K [104]:

$$L_{eff} = \alpha \, d\rho^{\beta} \ , \tag{7.10}$$

with the parameters α and β, given by :

$$\alpha = -3.05801 \cdot 10^{-2} \, P_{1.8\mathrm{K}} + 10.3885 \qquad (heated\ windows) \tag{7.11}$$

$$\alpha = -1.0442 \cdot 10^{-2} \, P_{1.8\mathrm{K}} + 10.079 \qquad (non-heated\ windows) \tag{7.12}$$

$$\beta = -3.9461 \cdot 10^{-4} \, P_{1.8\mathrm{K}} + 1.6692 \cdot 10^{-2} \qquad \text{(heated windows)} \tag{7.13}$$

$$\beta = 2.57198 \cdot 10^{-4}\, P_{1.8\mathrm{K}} + 2.07989 \cdot 10^{-2} \;\; (\text{non}-\text{heated windows}) \tag{7.14}$$

The quantity $P_{1.8\mathrm{K}}$, is the measured pressure in the cold bores corrected by the temperature inside the cold bores.

Substituting eq. (7.10) to (7.9) one gets:

$$d\rho = \left(6.0518 \cdot 10^{-3} \frac{E_a}{\alpha}\right)^{\frac{1}{\beta+1}} \tag{7.15}$$

and finally

$$L_{eff} = \alpha \left(6.0518 \cdot 10^{-3} \frac{E_a}{\alpha}\right)^{\frac{\beta}{\beta+1}} \;. \tag{7.16}$$

From the density profile obtained by the simulations, it is evident that after the coherence length there is a length of decreasing density which extends until the cold windows.

The number of photons that reach the cold window can be expressed as:

$$N_{\gamma,W} = \int \frac{d\Phi_a}{dE_a} P_{a\to\gamma}\, A\, t\, dE_a \tag{7.17}$$

The static simulations also showed that during the ^{3}He phase, with increasingly higher pressure in the cold bores, the Van der Walls forces become significant and neglecting them could lead to variations in pressure even up to 11%. Therefore new formulas were generated, to include this effect and allow for a precise assessment of the density in the coherence length.

7.1.2.2 Tilted magnet CFD simulations

During tracking, the magnet moves from -8 to +8 degrees in the vertical direction. This movement affects the density distribution of the ^{3}He buffer gas. Therefore, the CFD simulations were extended to include the tilting of the CAST magnet.

In the case of the tilted magnet, the hydrostatic effect and a resulting convection mechanism are becoming significant as the density of the buffer gas increases. Due to the hydrostatic effect, the region of the cold bores which is in the lowest position has higher density than the one closer to the upper position, while the magnet is tilted. This enhances the heat transfer in the lowest position between the buffer gas and the cold windows and reduces it in the upper part. The effect in the density profile is dual, as seen in Figure 7.8 [105]. The coherence length is displaced further from the lowest part, due to the fact that hot gas penetrates deeper into the cold bore area and there is a small but measurable density gradient even in the coherence region, which increases with density.

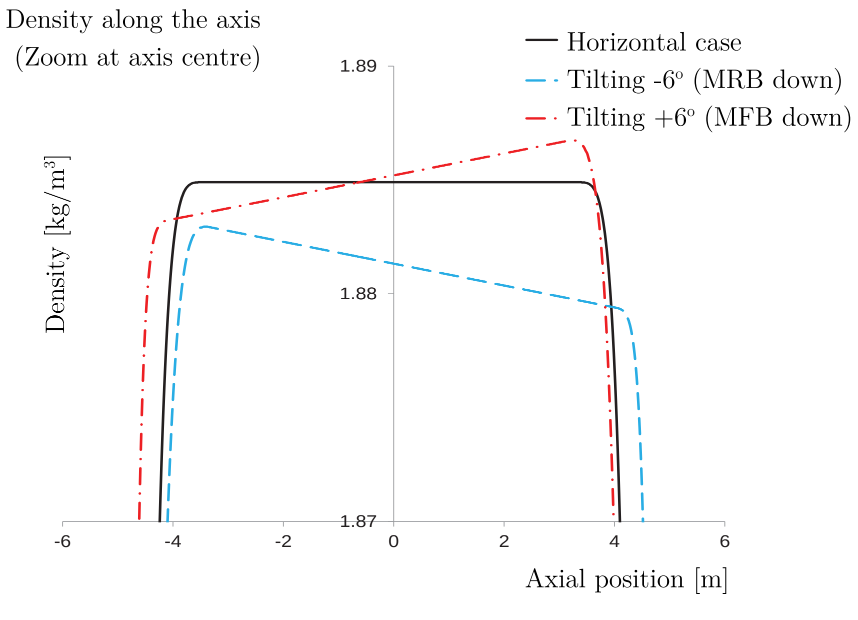

Figure 7.8: The density profile while tilting the CAST magnet for a given density in the Cold Bore.

7.1.3 Effective density

The CFD simulations, taking into account the effects of the tilting of the magnet, provided a relation between the density in the coherence length and the measured quantity $P_{1.8\mathrm{K}}$:

For heated cold windows:

$$\rho = \frac{(0.02099\, P_{1.8\mathrm{K}} - 0.004914)\cdot(1 + C_{\mathrm{angle}})}{1000} \quad [\mathrm{g/cm^3}] \tag{7.18}$$

and non-heated cold windows:

$$\rho = \frac{(2.87\ 10^{-5}\, P_{1.8\mathrm{K}}^2 + 0.02005\, P_{1.8\mathrm{K}} - 0.001571)\cdot(1 + D_{\mathrm{angle}})}{1000}\ [\mathrm{g/cm^3}]\ , \tag{7.19}$$

with C_{angle} and D_{angle} corrective terms for the tilting of the magnet.

Combining eq. (7.3) with (7.18) or (7.19), depending on whether the cold windows were heated or not, one derives the effective photon mass, that corresponds to the specific density and angle.

7.2 Software efficiency

Figures 5.45 and 5.46 of chapter 5 show the efficiency of the selection criteria for the different energies of the X-ray peaks for the M19 detector. This efficiency should be constant regardless of the detector, for a given set of operating conditions, such as:

- gas mixture,
- gas pressure,
- detector gain,
- amplifier settings.

Taking into account the compatibility of the efficiency at 6 keV of the sunrise Micromegas in CAST and the M19 that was tested in the lab, and given that M19 was operated in similar conditions, one can extract a rough estimate of the software efficiency used in the calculations of the coupling constant limit.

From the results of chapter 5, taking into account the performance of the CAST detector, a new dependence of the software efficiency with the event energy was created (Figure 7.9) which will be fed in the further calculations. It should be noted that due to the statistical nature of the coupling constant limit, it is very important not to overestimate the efficiency and less so it's exact value. Once the sunrise Micromegas detector will be dismounted from the CAST magnet, a full set of tests will be performed in the lab, the software efficiency will be extracted more precisely and the limit recalculated.

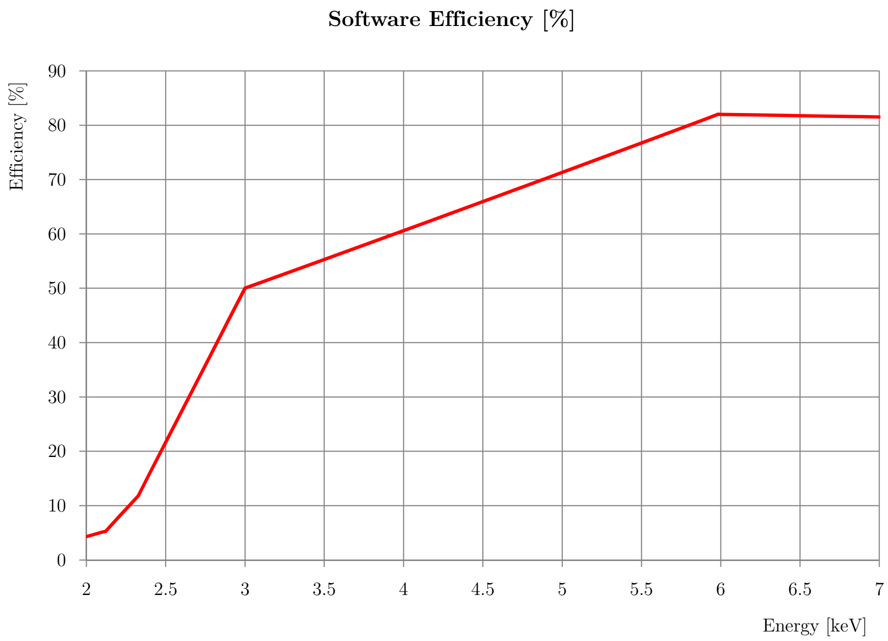

Figure 7.9: The estimate of the software efficiency of the detector.

7.3 Expected X-ray signal

The expected X-ray signal to the sunrise Micromegas detector, for an axion signal of energy E_a, in the time bin t can be expressed as:

$$R(E_a, t) = B(E_a, t) + S(E_a, t)\,, \tag{7.20}$$

where $B(E, t)$ is the background of the detector at the given energy and $S(E, t)$, the excess of counts that the detector will measure, due to an axion conversion:

$$S(E_a, t) = \frac{d\Phi_a}{dE_a} P_{a\to\gamma}\, A\, t\, \varepsilon_h\, \varepsilon_s \quad . \tag{7.21}$$

In this expression ε_h is the hardware efficiency to the detection of X-rays, described in Chapter 3.7.5 and ε_s the software efficiency, defined in Chapter 7.2. A is the area of the cold bore, $d\Phi_a/dE_a$ the differential flux of axions to Earth, from eq (7.1) and $P_{a\to\gamma}$ is the probability of their conversion to a photon. The integration of eq. (7.17) over the energy range of interest, and the total tracking time of a run gives the expected number of photons in the detector per axion mass, as seen in Figure 7.10.

$$N_{SRMM} = \int \frac{d\Phi_a}{dE_a} P_{a\to\gamma}\, A\, t\, \varepsilon_h\, \varepsilon_s\, dE_a \quad . \tag{7.22}$$

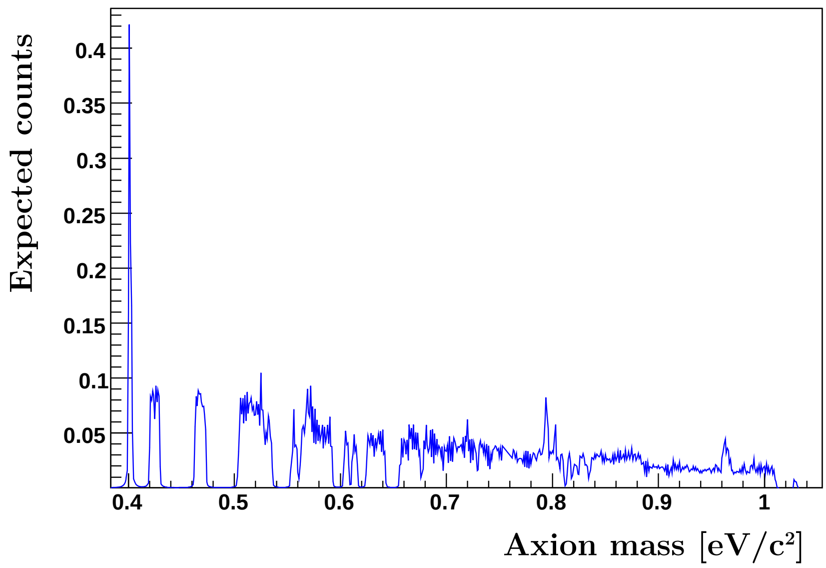

Figure 7.10: The expected X-ray signal in the Sunrise detector in the range 2-7 keV, for the 2009 and 2010 runs considering $g_{a\gamma}$=10^{-10} GeV^{-1} .

7.4 Unbinned likelihood

The most powerful method of finding limits in unknown parameters from experimental data is the Likelihood method. For data that follow a Poisson distribution it can be expressed as:

$$L_k = \frac{1}{L_{0k}} \prod_i e^{-r_{ik}} \frac{r_{ik}^{n_{ik}}}{n_{ik}!} \ , \tag{7.23}$$

for the event k. In this formula L_{0k} is the normalization factor:

$$L_{0k} = \prod_i e^{-n_{ik}} \frac{n_{ik}^{n_{ik}}}{n_{ik}!} \tag{7.24}$$

The index i runs over the energy bins around the energy of event k. The term r_{ik} is the expected number of counts in each energy bin, for the event k:

$$r_{ik} = b_{ik} + s_{ik} \ , \tag{7.25}$$

where b_{ik} is the expected background of event k in energy bin i and s_{ik} the expected signal, given by the expression:

$$s_{ik} = \int_{E_i}^{E_i+\Delta E} \frac{d\Phi_a}{dE_a} P_{a\to\gamma}\, A\, \varepsilon_h\, \varepsilon_s\, \Delta t_k\, dE_a \ , \tag{7.26}$$

with Δt_k being the time bin of event k.

In the CAST experimental conditions the density and length of the coherence region change during tracking, therefore the probability of conversion is not constant. This phenomenon and the low background rate of the sunrise Micromegas detector are the two main arguments in favour of forming an extended unbinned Likelihood for the data set of N events during 2009 and 2010. The unbinned limit corresponds to considering a Δt_k sufficiently small (ideally $\Delta t_k \to 0$ so that all the time bins contain either 0 or 1 event). The extended likelihood for a given axion mass can then be written:

$$L_{m_a} = \prod_{k_0} L_{k_0} \prod_{k_1} L_{k_1} \ , \tag{7.27}$$

where k now refers to the time bin Δt_k and the product includes all total exposure of all the trackings.

The distribution of the extended Likelihood L_{m_a} is tested with the χ^2 method. The relation of the two distributions is:

$$-\frac{1}{2}\chi^2 = log\left(L_{m_a}\right) \ . \tag{7.28}$$

Substituting eq. (7.26) to (7.27), considering the above discussion one gets after some calculations:

$$-\frac{1}{2}\chi^2 = -N_c - \sum_{k_{0,1}} r_{ik_{0,1}} + \sum_{k_1} log\left(r_{ik_1}\right) \ , \tag{7.29}$$

where N_c is the total number of counts measured in 2009 and 2010.

Expanding r_{ik} and simplifying the terms that do not contain $g_{a\gamma}$, since they do not contribute to the behaviour of the χ^2 eq. (7.24) becomes:

$$-\frac{1}{2}\chi^2 = -g_{a\gamma}^4 \, N_{SRMM} + g_{a\gamma}^4 \sum_{k_1} \left[log\left(\frac{\Delta b_{ik_1}}{\Delta t_{k_1}} + g_{a\gamma}^4 \int_{E_i}^{E_i+\Delta E} \frac{ds_{ik}}{\Delta t_{k_1} dE} dE \right) \right] \ , \tag{7.30}$$

or simpler:

$$-\frac{1}{2}\chi^2 = -R_{SRMM} + \sum_{i}^{N} logR(E_i t_i) \ , \tag{7.31}$$

where the sum runs over the detected tracking counts and $R(E_i t_i)$ is the expected signal to the sunrise Micromegas at the time t_i and energy E_i.

7.5 Sunrise Micromegas limit to $g_{a\gamma}$ for the data of 2009 and 2010

The results of the analysis of the sunrise Micromegas tracking and background data are consistent with no axion signal. Therefore they are used for the calculation of a limit for the $g_{a\gamma}$ in the range of axion masses visited in 2009 and 2010. The coherence length and the density of the buffer gas inside the cold bores as a function of the measured quantity $P_{1.8\mathrm{K}}$ were provided by the latest CFD simulations.

The extraction of the limit is done by maximizing the Likelihood function. The result is obtained by integrating the Bayesian probability with respect to $g_{a\gamma}^4$ from 0 up to 95%:

$$\frac{\int_0^{g_{a\gamma}^4} e^{-\frac{1}{2}\chi^2} dg_{a\gamma}^4}{\int_0^{\infty} e^{-\frac{1}{2}\chi^2} dg_{a\gamma}^4} = 0.95 \tag{7.32}$$

In Figure 7.12, the $g_{a\gamma}$ limit for the 2009 and 2010 data taking periods with the sunrise Micromegas is shown, as a function of the axion mass. It is divided in two parts:

- For the axion masses 0.4-0.64 eV/c^2 the CAST experiment in the first part of the data taking of 2010 was filling the gaps in the axion mass scanning, created by the leak of 2008.
- The nominal axion mass scanning during 2009 and the second part of the 2010 data taking period. The range of axion masses covered in this period is 0.66 - 1.01 eV/c^2.

Although the data obtained during the gap filling period of 2010 cannot be used by themselves to obtain a limit, they have been used in [106] in combination with the data obtained in 2008, to provide a limit in the range of 0.39-0.64 eV/c^2 of an average value of 2.27×10^{-10} GeV^{-1} at 95% confidence level.

In the present thesis a limit in the $g_{a\gamma}$ is provided with the data of the sunrise Micromegas detector in CAST, for the years 2009 and 2010. The exclusion plot is seen in Figure 7.11. The average value in the range 0.655 -1.01 eV/c² is:

$$g_{a\gamma} \leq 3.9\times10^{-10}\ \mathrm{GeV}^{-1}\ \text{at } 95\%\ \mathrm{CL} \quad , \tag{7.33}$$

which is expected to be slightly improved by the contribution of the rest of the detectors.

It is worth noting that at axion masses 0.812 eV/c² to 0.813 eV/c², there is less exposure because of the loss of two successive raw data files that were corrupted in the process of the "stageing" in the CASTOR system.

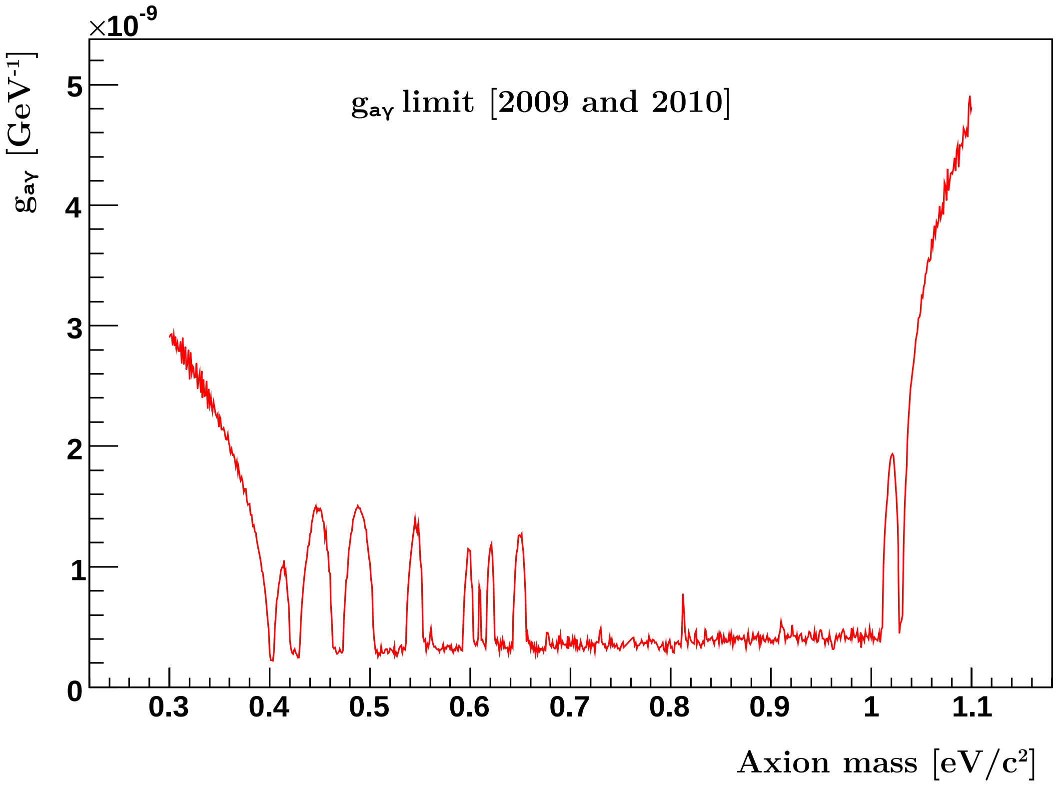

Figure 7.11: The coupling constant limit as a function of the axion mass, for the data taking periods of 2009 and 2010. The axion mass region 0.4-0.64 eV/c², corresponds to covering the gaps in the axion mass scanning created in the leak of 2008.

Conclusions

The present thesis was carried out in the CAST experiment at CERN. CAST is searching for solar axions using a decommissioned LHC dipole magnet with four low background X-ray detectors in each end of its cold bores.

The axion search that was performed during the 2009 and 2010 data taking periods with the sunrise Micromegas detector is compatible with the absence of axion signal in the axion mass range 0.655 -1.01 eV/c^2. A limit for the axion to photon coupling constant can be set:

$$g_{a\gamma} \leq 3.9\times10^{-10}\ \mathrm{GeV}^{-1} \text{ at } 95\%\ \mathrm{CL} \quad ,$$

which is expected to be slightly improved by the contribution of the rest of the detectors.

The first period of the 2010 data taking was dedicated to covering the gaps that were created in the axion mass scan during the 2008 run. The data of this period were analysed in this thesis and used in combination with the data from the rest of the detectors, to extract a limit in the axion mass range: 0.39 - 0.64 eV/c^2, [71]:

$$g_{a\gamma} \leq 2.27\times10^{-10}\ \mathrm{GeV}^{-1} \text{ at } 95\%\ \mathrm{CL}$$

This is the strictest experimental limit to date for this axion mass range, excluding part of the QCD-favoured axion model region.

This limit was the result of the responsibility for the maintenance and operation of the sunrise Micromegas detector during the periods of 2009 and 2010 and the analysis of its acquired data.

In parallel a new detector lab for CAST has been realized at CERN. In this lab, for the first time, it was possible to test the efficiency of the software selection criteria that are used in the offline analysis of CAST, in various energies. For this purpose a variable energy calibration system was used, having as targets, materials that have characteristic emission lines in the energy range of interest in CAST.

Of course the operation of this facility will not seize here. A significant upgrade is scheduled for the X-ray beam line, to accommodate more targets and filters, for a finer scan of a larger energy range between few hundred eV to 9 keV. The lab will be used for detector and software development and also for transmission tests for vacuum windows, to be used in the future phase of CAST and as a starting point for research and development for the future helioscope (IAXO).

Bibliography

[1] R. D. Peccei and Helen R. Quinn, CP Conservation in the Presence of Pseudoparticles, Phys. Rev. Lett., 38(25):1440–1443, Jun 1977.

[2] G.'t Hooft, Computation of the quantum effects due to a four-dimensional pseudoparticle, Phys. Rev. D, 14(12):3432–3450, Dec 1976.

[3] G.'t Hooft, Symmetry Breaking through Bell-Jackiw Anomalies, Phys. Rev. Lett., 37(1):8, Jul 1976.

[4] R. D. Peccei, QCD, strong CP and axions, J. Korean Phys. Soc. 29 (1996) S199.

[5] Michael S. Turner, Windows on the axion, Physics Reports, 197(2):67 – 97, 1990.

[6] S. Weinberg, A New Light Boson?, Phys. Rev. Lett. 40 (1978) 223.

[7]F.Wilczek, Problem Of Strong P And T Invariance In The Presence Of Instantons, Phys. Rev. Lett. 40 (1978) 279.

[8] R. D. Peccei, Tai Tsun Wu and T. Yanagida, A viable axion model, Physics Letters B Volume 172, Issues 3-4, 22 May 1986, Pages 435-440.

[9] L.M Krauss, F. Wilczek, A short-lived axion variant, Physics Letters 173B (1986) 189.

[10] R. D. Peccei and Helen R. Quinn, Constraints imposed by CP conservation in the presence of pseudoparticles, Phys. Rev. D 16, 1791–1797 (1977).

[11] Jihn E. Kim, Light pseudoscalars, particle physics and cosmology, Physics Reports Volume 150, Issues 1-2, June 1987, Pages 1-177.

[12] I. Antoniadis and Tran N. Truong, Lower bound for branching ratio of$K^+ \to \pi^+$ axion and non-existence of Peccei-Quinn axion, Physics Letters B Volume 109, Issues 1-2, 11 February 1982, Pages 67-72.

[13] G G Raffelt, Axions-Motivation, limits and searches, arXiv:hep-ph/0611118v1 9 Nov 2006.

[14] J. E. Kim, Weak interaction singlet and strong CP invariance, Phys. Rev. Lett. 43 (1979) 103.

[15] M. A. Shifman, A. I. Vainshtein and V. I. Zakharov, Can confinement ensure natural CP invariance of strong interactions?, Nucl. Phys. B 166 (1980) 493.

[16] M. Dine, W. Fischler and M. Srednicki, A simple solution to the strong CP problem with a harmless axion, Phys. Lett. B 104 (1981) 199.

[17] J. E. Kim, Light pseudoscalars, particle physics and cosmology, Phys. Rept. 150 (1987).

[18] S. L. Cheng, C. Q. Geng and W. T. Ni, Axion-photon couplings in invisible axion models, Phys. Rev. D 52 (1995) 3132.

[19] Gasser J and Leutwyler H, Quark masses, 1982 Phys. Rep. 87 77.

[20] H. Leutwyler, The ratios of the light quark masses, Physics Letters B Volume 378, Issues 1-4, 20 June 1996, Pages 313-318.

[21] H.Primakoff, Photo-production of neutral mesons in nuclear electric fields and the mean life of the neutral meson, Phys. Rev. 81, 899–899 (1951).

[22] Georg G. Raffelt, Astrophysical axion bounds, Lect. Notes Phys., 741:51–71, 2008.

[23] Leanne D. Duffy, Karl van Bibber, Axions as Dark Matter Particles, New J.Phys.11:105008,2009

[24] L. F. Abbott and P. Sikivie, A cosmological bound on the invisible axion, Phys. Lett., B120:133–136, 1983.

[25] J. Preskill, M. B. Wise, and F. Wilczek, Cosmology of the Invisible Axion, Phys. Lett., B120:127–132, 1983.

[26] M. Dine and W. Fischler, The not-so-harmless axion, Phys. Lett., B120:137–141, 1983.

[27] A. Dabholkar and J. M. Quashnock, Pinning down the axion, Nucl. Phys., B333:815, 1990.

[28] R. A. Battye and E. P. S. Shellard, Global string radiation, Nucl. Phys., B423:260–304, 1994.

[29] R. A. Battye and E. P. S. Shellard, axion string constraints, Phys. Rev. Lett., 73:2954–2957, 1994.

[30] S. Chang, C. Hagmann, and P. Sikivie, Studies of the motion and decay of axionwalls bounded by strings, Phys. Rev., D59:023505, 1999.

[31] D. H. Lyth, Estimates of the cosmological axion density, Phys. Lett., B275:279–283, 1992.

[32] M. Nagasawa and M. Kawasaki, Collapse of axionic domain wall and axion emission, Phys. Rev., D50:4821–4826, 1994.

[33] Frank Daniel Steffen, Dark matter candidates - axions, neutralinos, gravitinos, and axions, Technical Report arXiv:0811.3347. MPP-2008-130, Nov 2008.

[34] Xue-Lei Chen and Marc Kamionkowski, Particle decays during the cosmic dark ages, Phys. Rev., D70:043502, 2004.

[35] Raffelt, G.G., Stars as laboratories for fundamental physics. University of Chicago Press, Chicago (1996).

[36] G.G. Raffelt, Astrophysics probes of particle physics, Physics Reports 333-334 (2000) 593-618.

[37] E.P.S. Shellard, R.A. Battye, Cosmic axions, astro-ph/9802216.

[38] R. A. Battye and E. P. S. Shellard, Axion string constraints, Phys. Rev. Lett. 73 (1994) 2954 Erratum-ibid. 76 (1996).

[39] D. Harari and P. Sikivie, On the evolution of global strings in the early universe, Phys. Lett. B 195 (1987).

[40] C. Hagmann and P. Sikivie, Computer simulations of the motion and decay of global strings, Nucl. Phys. B 363 (1991).

[41] P. Sikivie, Experimental Tests Of The “Invisible” Axion, Phys. Rev. Lett. 51 (1983) 1415 Erratum-ibid. 52 (1984).

[42] R. Bradley et al., Microwave cavity searches for dark-matter axions, Rev. Mod. Phys. 75 (2003).

[43] C. Hagmann, D. Kinion, W. Stoeffl, K. van Bibber, E. Daw, H. Peng, Leslie J Rosenberg, J. LaVeigne, P. Sikivie, N. S. Sullivan, D. B. Tanner, F. Nezrick, Michael S. Turner, D. M. Moltz, J. Powell, and N. A. Golubev, Results from a high-sensitivity search for cosmic axions, Phys. Rev. Lett., 80(10):2043–2046, Mar 1998.

[44] S. J. Asztalos *et al.*, A SQUID-based microwave cavity search for dark-matter axions, Phys. Rev. Lett., 104:041301, 2010.

[45] Remy Battesti *et al.*, Axion searches in the past, at present, and in the near future, Lect. Notes Phys., 741:199–237, 2008.

[46] G. Ruoso *et al.*, Limits on light scalar and pseudoscalar particles from a photon regeneration experiment, Z. Phys. C 56 (1992) 505.

[47] R. Cameron *et al.*, Search for nearly massless, weakly coupled particles by optical techniques, Phys. Rev. D 47 (1993) 3707.

[48] R. Cameron, G. Cantatore, A. C. Melissinos, G. Ruoso, Y. Semertzidis, H. J. Halama, D. M. Lazarus, A. G. Prodell, F. Nezrick, C. Rizzo, and E. Zavattini, Search for nearly massless, weakly coupled particles by optical techniques, Phys. Rev. D, 47(9):3707–3725, May 1993.

[49] E. Zavattini *et al.* (PVLAS Collaboration), Experimental observation of optical rotation generated in vacuum by a magnetic field, Phys. Rev. Lett. 96, 110406 (2006).

[50] E. A. Paschos and K. Zioutas, A Proposal for solar axion detection via Bragg scattering, Phys. Lett. B 323, 367 (1994).

[51] A. Morales *et al.* (COSME Collaboration), Particle dark matter and solar axion searches with a small germanium detector at the Canfranc underground laboratory, Astropart. Phys. 16, 325 (2002) [hepex/0101037].

[52] F. T. Avignone *et al.* (SOLAX Collaboration), Experimental search for solar axions via coherent Primakoff conversion in a germanium spectrometer, Phys. Rev. Lett. 81, 5068 (1998) [astro-ph/9708008].

[53] R. Bernabei *et al.*, Search for solar axions by Primakoff effect in NaI crystals, Phys. Lett. B 515, 6 (2001).

[54] D. M. Lazarus, G. C. Smith, R. Cameron, A. C. Melissinos, G. Ruoso, Y. K. Semertzidis and F. A. Nezrick, A Search for solar axions, Phys. Rev. Lett. 69, 2333 (1992).

[55] S. Moriyama, M. Minowa, T. Namba, Y. Inoue, Y. Takasu and A. Yamamoto, Direct search for solar axions by using strong magnetic field and X-ray detectors, Phys. Lett. B 434 (1998) 147.

[56] K Zioutas *et al*, Axion searches with helioscopes and astrophysical signatures for axion(-like) particles, New Journal of Physics 11 (2009) 105020.

[57] S. Andriamonje *et al* (CAST Collaboration), An improved limit on the axion-photon coupling from the CAST experiment, 2007 J. Cosmol. Astropart. Phys. JCAP04(2007)010 (arXiv:hep-ex/0702006).

[58] J.N. Bahcall, M.H. Pinsonneault, What do we (not) know theoretically about solar neutrino fluxes?, 2004 Phys. Rev. Lett. 92 121301 [astro-ph/0402114].

[59] K. Van Bibber, P. M. McIntyre, D. E. Morris, G. G Raffelt, Design for a practical laboratory detector for solar axions, 1989 Phys. Rev. D.

[60] J. N. Bahcall, W. F. Huebner, S.H. Lubow, P. D. Parker, R. K. Ulrich, Standard solar models and the uncertainties in predicted capture rates of solar neutrinos, 1982 Rev. Mod. Phys.

[61] K. Zioutas *et al*, A decommissioned LHC model magnet as an axion telescope, NIM A425, 480, 1999.

[62] http://aa.usno.navy.mil/software/novas/novas_info.php .

[63] T.O. Niinikoski, B. Bellanger, M. Davenport, N. Elias, S. Aune, J. Franz, THIN CRYOGENIC X-RAY WINDOWS, Departmental Report CERN-AT-2008-034.

[64] N. Elias, Conversion and Operation of CAST as a massive axion detector, PhD thesis, Lisbon, Universidade Técnica de Lisboa : 2010.

[65] R. Kotthaus, H. Braeuninger, P. Friedrich, R. Hartmann, D. Kang, M. Kuster, G. Lutz, and L. Strueder, The X-ray Telescope of the CAST Experiment, ArXiv Astrophysics e-prints, November 2005.

[66] M. Kuster, *et al.*, The x-ray telescope of CAST, New Journal of Physics, 9:169, June 2007.

[67] J. Altmann *et al.* and W. J. Egle *et al.*, Mirror system for the German X-ray satellite ABRIXAS, parts I and II, Proceedings of SPIE , vol. 3444, pp. 350-358 and 359-368, 1998.

[68] L. Strüder *et al.*, The European Photon Imaging Camera on XMM-Newton: The pn-CCD camera A&A, Volume 365, Number 1, January I 2001 First Results from XMM-Newton.

[69] K Zioutas *et al.*, An improved limit on the axion-photon coupling from the CAST experiment, Journal of Cosmology and Astroparticle Physics, 2007(04):010, 2007.

[70] E. Arik *et al* [CAST Collaboration], Probing ev-scale axions with CAST, Journal of Cosmology and Astroparticle Physics, 2009(02):008, 2009.

[71] CAST Collaboration, CAST search for sub-eV mass solar axions with He^3 buffer gas, Jun 2011. e-Print: arXiv:1106.3919, to be published in Physical Review Letters.

[72] S. Hannestad, A. Mirizzi, G. G. Raffelt and Y. Y. Y. Wong, Neutrino and axion hot dark matter bounds after WMAP-7, JCAP 1008 (2010) 001 [arXiv:1004.0695].

[73] E. Rutherford, H. Geiger, An Electrical Method of Counting the Number of Alpha Particles from Radioactive Substances, Proc. Royal Soc. A81 (1908), 141.

[74] G. Charpak, Spark chambers, Proc. Int. Symp. Nuclear Electronics (Versailles 10-13 Sept 1968).

[75] A. Oed, Position sensitive detector with microstrip anode for electron multiplication with gases, Nucl. Instrum. Meth. A 263 (1988) 351.

[76] Y. Giomataris *et al.*, MICROMEGAS: a high-granularity position-sensitive gaseous detector for high particle-flux environments, Nucl. Instr. And Meth. A 376(1996)29.

[77] F. Sauli, GEM: a new concept for electron amplification in gas detectors, Nucl. Instr. And Meth. A 386(1997)531.

[78] W. R. Leo, Techniques for Nuclear and Particle Physics Experiments, Springer-Verlag Berlin Heidelberg, 1994.

[79] U. Fano, Ionization Yield of Radiations. II. The Fluctuations of the Number of Ions, Phys. Rev. 72 (1947) 26-29.

[80] Y. Giomataris *et al.*, Development and prospects of the new gaseous detector micromegas, Nucl. Instr. And Meth. A419(1998), Issues 2-3, Pages 239-250.

[81] A. Delbart *et al.*, New developments of Micromegas detector, Nucl. Instrum. Meth. A461(2001)84.

[82] J. Derre *et al.*, Spatial resolution in Micromegas detector, Nucl. Instrum. Meth. A 459 (2001) 523.

[83] Puill, G.; Derre, J.; Giomataris, I.; Rebourgeard, P., MICROMEGAS: high rate and radiation hardness results, Nuclear Science Symposium, 1998. Conference Record. 1998 IEEE , vol.1, no., pp.594-597 vol.1, 1998 doi: 10.1109/NSSMIC.1998.775211.

[84] I. Giomataris *et al.*, Micromegas in a bulk, Nucl. Instr. and Meth. A 560 (2006) 405.

[85] S Andriamonje *et al.*, Development and performance of Microbulk Micromegas detectors, 2010 *JINST* 5 P02001 doi: 10.1088/1748-0221/5/02/P02001.

[86] S. Andriamonje *et al.*, A new MicrOMEGAs line for the CAST experiment, Nucl. Instrum. Meth. A 581 (2007) 217.

[87] J. Galan Lacarra, Safety manual for special use of radioactive source ^{55}Fe (4253RP) for the sunrise Micromegas detector vacuum line in CAST, Internal documents, EDMS 903219.

[88] P. Abon *et al.*, The Micromegas detector of the CAST experiment, New J. Phys. 9:170,2007 DOI: 10.1088/1367-2630/9/6/170.

[89] J Galán *et al,* MICROMEGAS detectors in the CAST experiment, 2010 *JINST* 5 P01009 doi: 10.1088/1748-0221/5/01/P01009.

[90] J.C. Santiard, Gassiplex, a low noise analog signal processor for readout of gaseous detectors, CERN-ECP/ 94-17.

[91] D. Breton, E. Delagnes, M. Houry, Very High Dynamic Range and High-Sampling Rate VME Digitizing Boards for Physics Experiments, Proceed. IEEE 2004 Med. Imag. Conf., Rome, Oct 2004.

[92] T. Geralis *et al.*, The Data Acquisition of the Micromegas Detector for the CAST experiment, IEEE 2003, Vol5, p3455 - 3459 Nuclear Science Symposium.

[93] http://www.amptek.com/pdf/characteristic_xrays.pdf .

[94] Jean-Michel Laurent, Vacuum operation of the X-ray test stand, internal documents, CAST detector lab.

[95] E. Gatti, P. Rehak, Semiconductor drift chamber – an application of a novel charge transport scheme, Nucl. Instrum. Meth. 225, pp 608-614 (1984).

[96] http://www.amptek.com/drift.html .

[97] X-ray data booklet, http://xdb.lbl.gov/ .

[98] The “bird and baguette” incident, http://cdsweb.cern.ch/record/1221806 .

[99] Cantatore G *et al.*, Search for low Energy solar Axions with CAST, 2008 Proc. 4th Patras Workshop on Axions, WIMPs,WISPs (DESY, Hamburg, Germany, 16-21 June 2008) arXiv:0809.4581v2.

[100] NIST database http://www.nist.gov/pml/data/xraycoef/index.cfm

[101] J.Galan, Probing eV-mass scale Axions with a Micromegas detector in the CAST Experiment, PhD thesis, Laboratorio de Física Nuclear y Astropartículas.

[102] Manuel Gómez Marzoa, Análisis CFD del comportamiento del He-3 en el sistema de gas del Telescopio Solar de Axiones del CERN (CAST), Master’s thesis.

[103] Internal communication N.Elias, B.Lakic, T.Vafeiadis.

[104] N.Elias, B.Lakic, T.Vafeiadis, Notes on density stability threshold, 47th CAST collaboration meeting.

[105] Enrico Da Riva, CFD Team Simulations of CAST tilted magnet, 48th CAST Collaboration Meeting.

[106] CAST Collaboration, CAST search for sub-eV mass solar axions with He^3 buffer gas. Jun 2011. Phys.Rev.Lett. 107 (2011) 261302.

Appendix

2009 and 2010 software efficiency

Energy from the mesh vs energy from the strips

The data acquisition system is set up in a way such that we can calculate the energy of the pulse both from the mesh and from the strips. Ideally they should have a one to one relation. However in the 2009 and 2010 calibration data this was not the case, as seen in Figure 1.

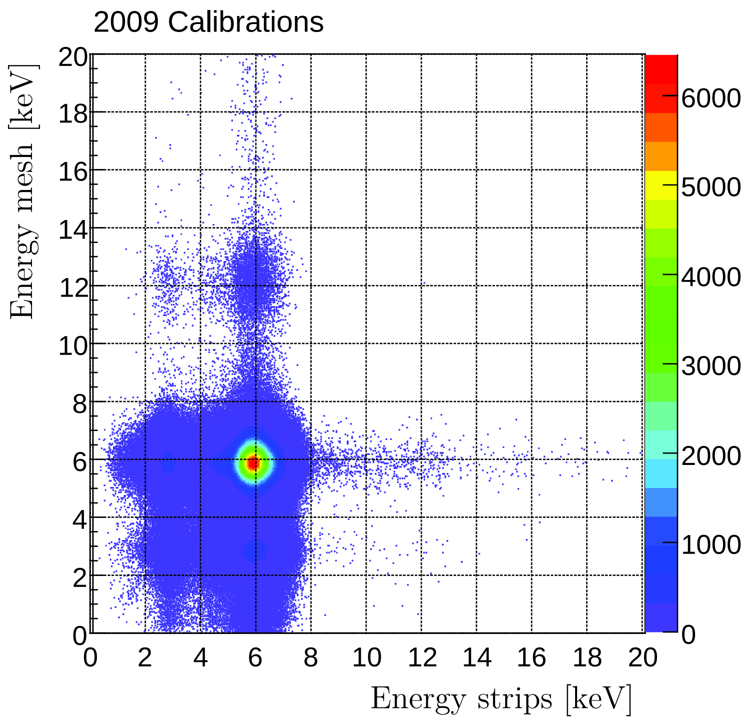

Figure 1: Energy calculated from the data of the mesh, versus energy calculated from the data of the strips for the calibrations of the 2009 data taking period.

Since the intervention for the installation of the new calibrator in 2008, there has been a leak in the veto system of the data acquisition. After the trigger, during the readout of the Matacq, (10-15 ms), the gassiplex cards were not protected and were recording signals, until they were read. This lead to uncorrelated mesh and strips events, in high trigger rate conditions such as calibrations. On the other hand the data acquisition system did not have any problem when operating in the low trigger rate of 1 Hz, during background measurements or while tracking the sun as seen in Figure 2. The probability of two events to occur within 10-15 ms and be accepted by the selection criteria, with a trigger rate of 1 Hz, is practically 0.

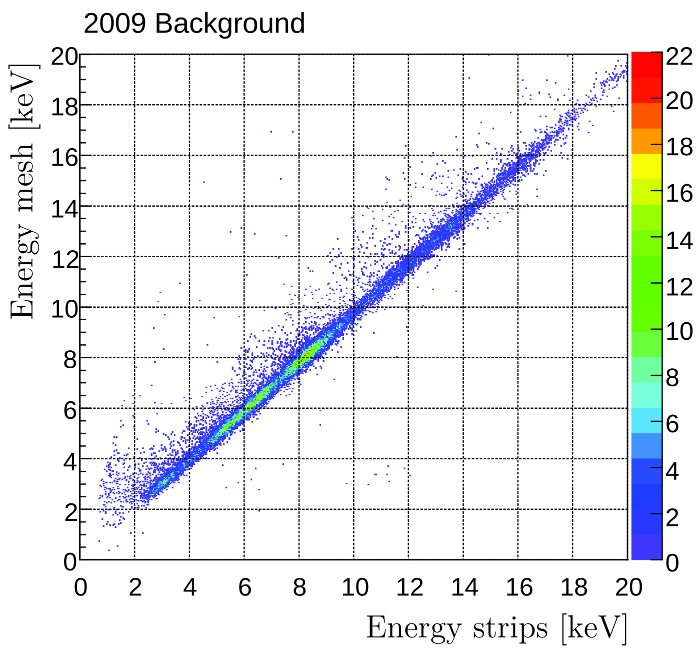

Figure 2 : During the background runs the correlation of the mesh pulses and the strip pulses is not affected.

The problem was identified and solved in the beginning of June 2011.From then on the busy from the sequencer is used as a veto to a dual timer which gets the start from the discriminator and gives as output a trigger to the Matacq.

After the intervention, the correlation between the mesh and strip pulses during a calibration was restored, as seen in Figure **3**.

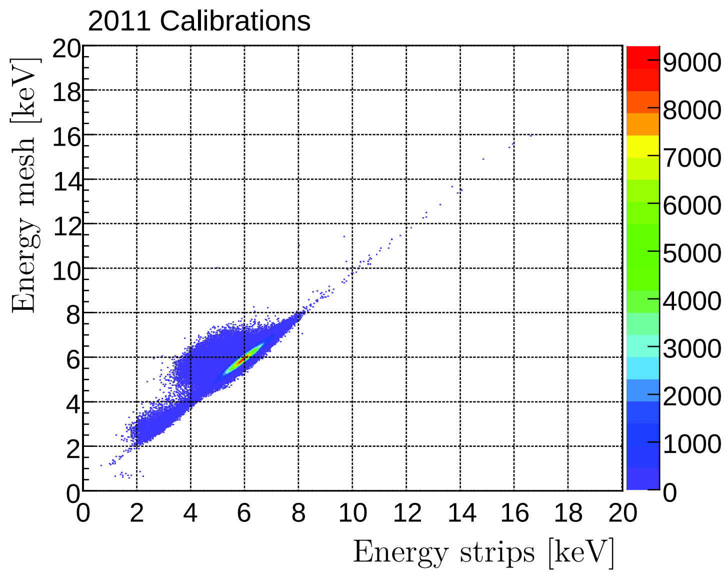

Figure 3: The correlation between the mesh and the strips pulses during a calibration run was restored in June 2011.

Calculating the software efficiency at 6 keV in 2009 and 2010

In order to calculate the software efficiency of the non-correlated calibration data during 2009 and 2010, the data of 2011, after the aforementioned intervention, were assessed. In Figure 4 one can see the effect of the mesh and the strips cuts in the efficiency. Although they both have an efficiency of ~92%, their combined application to the calibration data, reduces the efficiency to ~87%, meaning that in most cases the mesh and the strips cuts reject different events.

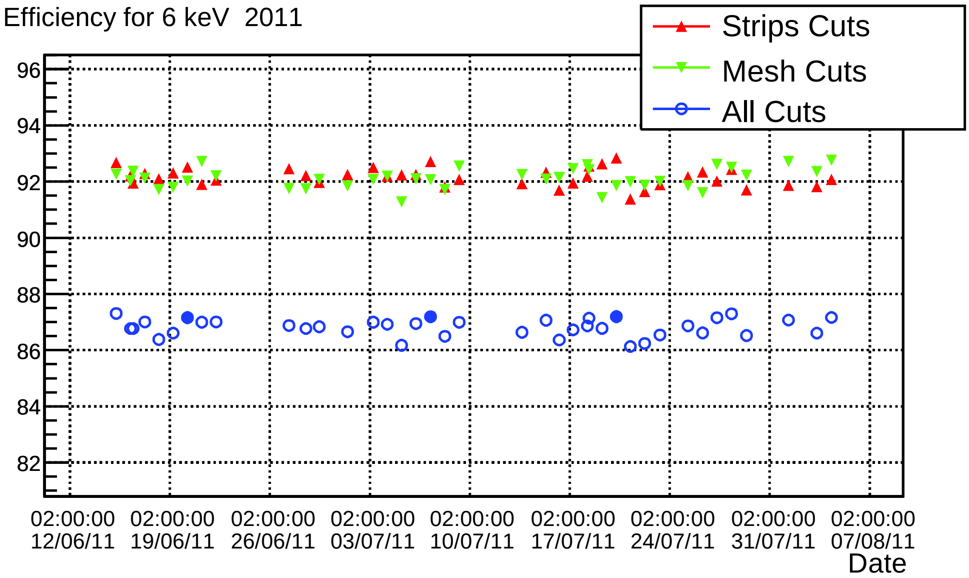

Figure 4: The software efficiency of the 2011 calibration data after the intervention that corrected the problem of the unprotected trigger of the gassiplex.

For the non-correlated data of 2009 and 2010 the strip cuts were applied only to the events recorded from the strips and the mesh cuts only to the events from the mesh. In order to find a software efficiency for the non-correlated data, keeping in mind the efficiency of the 2011 data, the efficiencies of the mesh and the strips cuts were multiplied.

$$Efficiency_{TOTAL} = Efficiency_{STRIPS} \cdot Efficiency_{MESH} \tag{1}$$

If Eq. (1) was applied for the 2011 data the result would be ~85%, slightly smaller than the actual average efficiency of 87% but nevertheless a safe result that can be used in an analysis which has the objective of finding a limit.